The Thesis Committee for Nicole Kristen Guinn
Certifies that this is the approved version of the following Thesis:

Using tree damage to characterize the evolution of dynamic pressure within the 18 May 1980 pyroclastic density current of Mount St. Helens

APPROVED BY
SUPERVISING COMMITTEE:

_____
James E. Gardner, Supervisor

_____
Timothy Goudge

_____
Mark Helper

Using tree damage to characterize the evolution of dynamic pressure within the 18 May 1980 pyroclastic density current of Mount St. Helens

by

Nicole Kristen Guinn

Thesis

Presented to the Faculty of the Graduate School of

The University of Texas at Austin

in Partial Fulfillment

of the Requirements

for the Degree of

Master of Science in Geological Sciences

The University of Texas at Austin

August 2020

Dedication

To my family, friends, and Dr. T

Acknowledgements

I wish to show my deep gratitude to Dr. Jim Gardner for his patience, support, and unlimited advice during the writing of this thesis and two-year long project. I would like to pay my special regards to Dr. Mark Helper for becoming a second mentor and his indispensable guidance. I wish to thank Dr. Tim Goudge for being a part of my thesis committee and for his informative and applicable teachings. I also thank my lab group – Wade Aubin, Nick Meszaros, and Sean O'Donnell – for their constant support and humor. I am indebted to Philip Guerrero; he is someone I can always count on. I would like to thank my family, who always believed in and encouraged me. My friends and classmates, I could not have done this without you. And finally, my husband, who was there for me without fail. I would like to recognize the invaluable assistance that you all provided during my study.

Abstract

Using tree damage to characterize the evolution of dynamic pressure within the 18 May 1980 pyroclastic density current of Mount St. Helens

Nicole Kristen Guinn, M.S.Geo.Sci.
The University of Texas at Austin, 2020

Supervisor: James E. Gardner

On 18 May 1980, Mount St. Helens erupted a laterally directed pyroclastic density current (PDC) that decimated ~600km^2 of forest, referred to as the blowdown zone. The head of the current contained the peak dynamic pressure, which uprooted or broke off many trees and stripped them of vegetation. The four main objectives in analyzing post-eruption aerial photos were to locate standing trees, calculate tree heights, calculate tree density, and calculate tree height from downed trees as a function of distance from the volcano. Clusters of 10 or more closely spaced trees were left standing throughout the blowdown zone. Clusters were categorized into stripped and foliage clusters based on their shadow shape. Stripped clusters are impacted by higher dynamic pressures than foliage clusters because trees were stripped of vegetation. Because stripped clusters are located closer to the volcano, the PDC is relatively denser, therefore has higher dynamic pressure. The increasing number of stripped, isolated trees with distances indicates that dynamic pressure was declining. Values of dynamic pressure can

be estimated using tree height and radius, the maximum stress at the height of tree failure, and the drag coefficient of the PDC. Two different datasets of dynamic pressure were derived, that constrain the minimum and maximum dynamic pressures of the PDC. The dynamic pressures estimated from toppled trees tended to yield lower values than those estimated from standing trees. Standing tree clusters were affected by dynamic pressures that were on average 12 kPa lower than the dynamic pressures that impacted isolated, standing trees. The dynamic pressure of isolated, standing trees decreased from 35 kPa in the last 30% of the distance traveled by the PDC to around 15 kPa near the edge of the blowdown zone. Tree damage can provide insights into internal dynamic pressure changes of PDCs.

Table of Contents

List of Tables

List of Figures

Introduction

Pyroclastic density currents (PDCs) are hot, tephra-laden flows that move at high speeds (Baxter, 1990; Auker et al., 2013, Baxter et al., 2017). PDCs are a frequent result and dangerous hazard of explosive eruptions (Druitt, 1998; Blong, 1984; Baxter et al., 2005; Auker et al., 2013, Benage, 2016; Baxter et al., 2017). Three main origins of PDCs are pyroclastic fountaining, lateral blasts, and the collapse of lava domes (Branney and Kokelaar, 2002). Pyroclastic fountaining forms when the initial explosive jet loses momentum and is not able to entrain enough air to become buoyant (Sparks et al., 1997, Branney and Kokelaar, 2002). This kind of eruption can feed large-volume ignimbrites, with examples including the Long Valley Caldera eruption that created the Bishop tuff and the Valles Caldera eruption that created the Bandelier Tuff (Bursik and Woods, 1996; Branney and Kokelaar, 2002). Lateral blasts form when a volcanic flank collapses. Examples of lateral blasts include the 1956 Bezymianny eruption (Bogoyavlenskaya et al., 1985) and the 1980 Mount St. Helens eruption (Hoblitt, 1986). In regard to the third type of eruption style, lava domes can become unstable and collapse under gravity, disintegrating to form PDCs (Branney and Kokelaar, 2002). Examples of this style of eruption include Santiaguito (Rose et al., 1977), Merapi (Bardintzeff, 1984), Mount Unzen (Yamamoto et al., 1993; Ui et al., 1999), and Montserrat (Cole at al., 1998, 2002). Few humans (Baxter, 1990) or structures (Valentine, 1998) survive these devastating flows, making it a challenge to investigate their mechanical evolution.

PDCs follow topography because they are denser than the atmosphere, leaving behind a path of destruction (Dobran et al., 1993; Sparks et al, 1997; Blong, 1984; Auker et al., 2013). As the PDC deposits sediment and entrains air, bulk density decreases (Bursik and Woods, 1996; Branney and Kokelaar, 2002). Density can decrease to less than that of the ambient atmosphere, at which point the PDC becomes buoyant and lifts off to form a co-ignimbrite plume or Phoenix cloud (Sparks and Walker, 1977; Woods and Wohletz, 1991; Dobran et al., 1993; Sparks et al., 1993; Woods and Bursik, 1994, Bursik and Woods, 1996; Sparks et al, 1997; Hoblitt, 2000; Branney and Kokelaar, 2002; Wilson, 2008; Andrews and Manga, 2012). The runout distance, or how far the PDC travels until liftoff, is controlled by the mass flux, pyroclast size distribution, topography, outside air entrainment, and sedimentation rate (Bursik and Woods, 1996; Branney and Kokelaar, 2002; Andrews and Manga, 2012).

The internal structure of a PDC is thought to consist of a dense underflow and a turbulent overcurrent (Fisher, 1966; Dade and Huppert, 1996; Baer et al., 1997; Branney and Kokelaar, 2002; Sulpizio et al., 2014). The current is typically composed of a leading nose, a head, and a body (Middleton, 1970; Simpson, 1997; Kneller and Buckee, 2000; Branney and Kokelaar, 2002) (Figure 1). The head forms behind the leading nose and is thicker (Branney and Kokelaar, 2002). The body follows the head and is dominated by particle-particle interactions (Cas and Wright, 1987; Branney and Kokelaar, 2002, Sulpizio et al., 2014). Kelvin-Hemoltz billows result from the shear along the boundary between the top of the head and the ambient air, and cause entrainment of that ambient air (Branney and Kokelaar, 2002) within the mixing zone (Figure 1). The entrained

ambient air is heated and expands, allowing the top part of the PDC to become less dense than the atmosphere (Dobran et al., 1993; Sparks et al., 1997a; Branney and Kokelaar, 2002; Sulpizio et al., 2014). The head and leading nose of PDCs are not well understood and their behavior is one of the main objectives of this thesis.

PDCs cause damage through their dynamic pressure, which is the lateral force applied to objects. Dynamic pressure (P_{dyn}) is expressed as:

$$P_{dyn} = \frac{1}{2}\rho v^2 \quad (1)$$

where ρ is bulk density and v is velocity (Valentine, 1998). Understanding how dynamic pressure variations correspond to certain levels of damage is important when planning hazard mitigation and engineering new structures to withstand such damage (Valentine, 1998). Valentine (1998) argued that damage resulting from PDCs is comparable to that resulting from nuclear explosions. Data of how a structure responds to and is damaged by the dynamic pressure of nuclear explosions has been extensively collected since the 1940s. Valentine (1998) qualitatively summarized damage observations of structures, trees, and vehicles under corresponding ranges of dynamic pressures. Other studies have used these analog observations of damage to compare dynamic pressures within PDCs (Baxter et al., 2005; Jenkins et al., 2013).

The deadly nature of PDCs, however, prevents anyone from investigating the real-time evolution of density and speed needed to estimate how dynamic pressure evolves. Some studies have used clues in the aftermath of eruptions (Valentine, 1998; Clarke and Voight, 2000; Kelfoun et al., 2000; Baxter et al., 2005; Pitarri, 2007; Jenkins et al., 2013; Brand et al., 2014). Clarke and Voight (2000) identified a quantitative

approach based on tree and pole blowdown to estimate the dynamic pressure of a PDC. The dynamic pressure within the PDC was estimated as a function of cylinder geometry, the PDC drag coefficient, and the stress needed to knock over a tree. Unbroken trees left standing in the blowdown zone provided an upper limit to estimate dynamic pressure within the PDC (Clarke and Voight, 2000). Brand et al. (2014) inferred dynamic pressures from the lengths of downed trees at isolated positions, whereas Kelfoun et al. (2000) mapped zones of tree damage to describe the evolution of damage. Another study concluded that the aerodynamic drag force applied to a boulder to move it is equivalent to the dynamic pressure within the PDC (Pitarri, 2007). None of these studies, however, provide a full picture of dynamic pressure evolution.

Many eruptions of volcanoes surrounded by forested areas, such as Unzen, Mount St. Helens, Lamington, and Merapi, have resulted in a tree blowdown zone. The damage to trees in these blowdown zones provides a means to estimate dynamic pressure using the method of Clarke and Voight (2000). Extensive aerial photography taken just months after the Mount St. Helens eruption in 1980 provides an invaluable dataset to allow a thorough analysis of tree damage for the entire blowdown zone, providing a more complete picture of the evolution of dynamic pressure.

In March 1980, Mount St. Helens reawakened by producing earthquakes, phreatic steam explosions, and a bulge on the northern flank of the volcano (Rosenfeld, 1980; Moore and Rice, 1984). This bulge expanded at an average of 2 m/day as a result of an intruding dacitic cryptodome. On 18 May 1980, a landslide was triggered by a magnitude 5+ earthquake. A large part of the unstable bulge failed and became a debris avalanche

(Moore and Rice, 1984), exposing a giant scarp of 700 m tall, 1 km wide, and sloping at 70° (Moore and Albee, 1981). This sudden decompression of the magmatic system generated a lateral blast through the scarp that developed into a PDC (Waitt, 1981; Moore and Rice, 1984). Three processes feeding the PDC were water flashing to steam, gases exsolving from the magma in the cryptodome, and the heating of all other fluids in close contact with the exposed, hot cryptodome (Moore and Sisson, 1981). The PDC was reported to have initial velocities of 250 m/s (Vortman, 1980) and 100 m/s (Kieffer, 1980) and levelled roughly 600 km^2 of forest, creating the blowdown zone (Rosenfeld, 1980).

Before the eruption on 18 May, the forest surrounding the volcano consisted mainly of Douglas Fir, True Fir, Hemlock, and Cedar (Hoblitt et al., 1981). Tree diameter averaged around 1 m and larger trees were typically 2 m in diameter (Hoblitt et al., 1981). Many areas had been logged whereas others consisted of old-growth forests. Zones of damaged trees that change with distance from the volcano describe the destructiveness of the Mount St. Helens' PDC. Within the first couple of kilometers, and extending up to 12 km to the north (Waitt, 1981), trees were completely removed from the "proximal zone" (Hoblitt et al., 1981; Moore and Sisson, 1981; Waitt, 1981). Farther away, trees were downed but not removed (Hoblitt et al., 1981; Waitt, 1981). In this "medial zone", trees were stripped of bark on the side facing the volcano, larger trees were broken off near the base or uprooted, and smaller trees were bent over (Hoblitt et al., 1981; Moore and Sisson, 1981). Most felled trees pointed radially way from the volcano; however, felled trees situated behind some hills pointed toward the volcano

(Waitt, 1981). Furthermore, the stripped tree trunk and tree roots were abraded. The degree of abrasion decreased with distance from the vent, which suggests that the size, velocity, and amount of material suspended in the PDC decreased (Moore and Sisson, 1981; Waitt, 1981). Beyond the blowdown zone, trees were left standing, but were burned and dead in the distal zone, also called the scorched zone (Hoblitt et al., 1981; Waitt, 1981).

Many eyewitness observations provide qualitative data about the behavior of the 1980 Mount St. Helens PDC (Rosebaum and Waitt, 1981; Waitt, 2015; Gardner et al., 2016). A handful of people survived being hit by the PDC and were able to tell their story (Rosebaum and Waitt, 1981; Waitt, 2015). Jim Scymanky was 19 km northwest of the volcano logging trees with three other loggers when he looked up and saw trees beginning to fall, watching the tops snap off some. A force of air pushed him to the ground and then it got unbearably hot. After the main part of the PDC passed, he noted that all the trees were down pointing in a north-west direction and that a couple of small trees were still standing (Waitt, 2015, p. 163-165). Bob Payne and Mike Hubbard were 26 km northwest of the volcano fishing. They saw the PDC as a 1000 ft wall traveling speedily towards them. They also described being knocked to the ground and indescribable heat. Hubbard said he was on all fours and the PDC picked him up from behind, so he was just on his hands. They cooled off by diving into Green River as the PDC passed and noted all the downed trees (Waitt, 2015, p. 169-172). Bruce Nelson and Sue Ruff were camping 20 km north close to Green River. They both were thrown on their backs and then it got very hot. Bruce said he was a baker and estimated the heat to

be 500-600°F. They tried to search for their fellow campers through downed trees but had no luck (Waitt, 2015, p. 172-178). Dan Balch and Brian Thomas were also camped by Green River, close to Sue and Bruce. Brian was able to wedge himself underneath a large, already fallen tree when he saw the PDC and did not get badly burned. Dan ran to a standing tree to hold on but was knocked to the ground. Dan, who is now very badly burned, saw that the tree he was running towards was now downed (Waitt, 2015, p. 178-182). And finally, Edward Smith and his two sons were camped 17 km north in a canyon. After seeing a black billowing cloud, the family took shelter in the roots of a large tree as the PDC went over their heads. The unscathed family began searching for water and realized they had been in a cluster of standing trees with "their tops sheared off", whereas the surrounding area contained toppled trees (Waitt, 2015, p. 182-186). There are many similarities between the accounts (Gardner et al., 2016). Everyone described their experience in the same order: seeing the PDC, getting knocked the ground, being burned, and then climbing over downed trees to find help.

To better understand the temporal evolution of dynamic pressure, tree damage is evaluated throughout the blowdown zone. It is thought that the head of the current contained peak dynamic pressure (Clarke & Voight, 2000; Gardner et al., 2018), which toppled and stripped trees of branches and foliage (Rosenfeld, 1980; Hoblitt et al., 1981; Waitt, 1981; Moore and Sisson, 1981; Snellgrove et al., 1983). Within the devastation, however, clusters of partially stripped trees were burnt but left standing (Lipman and Mullineax, 1981), 51 in total (Gardner et al., 2018). Most of the clusters identified by Gardner et al. (2018) match those earlier mapped by Lipman and Mullineaux (1981), all

of which were situated on the lee sides of hills and topography drop-offs. The clusters reflected where the density in the PDC declined towards atmospheric density, allowing the base of the PDC to detach from the ground and remain aloft to pass over a cluster of trees (Gardner et al., 2018). Individual trees were also left standing, although most were stripped and broken off (Snellgrove et al., 1983). This study examines both classes of standing trees: standing tree clusters (Figure 2, 6a, 6b) and isolated standing trees (Figure 6c). Trends in tree height and tree densities with distance and location from the volcano are used to characterize the progression of dynamic pressure.

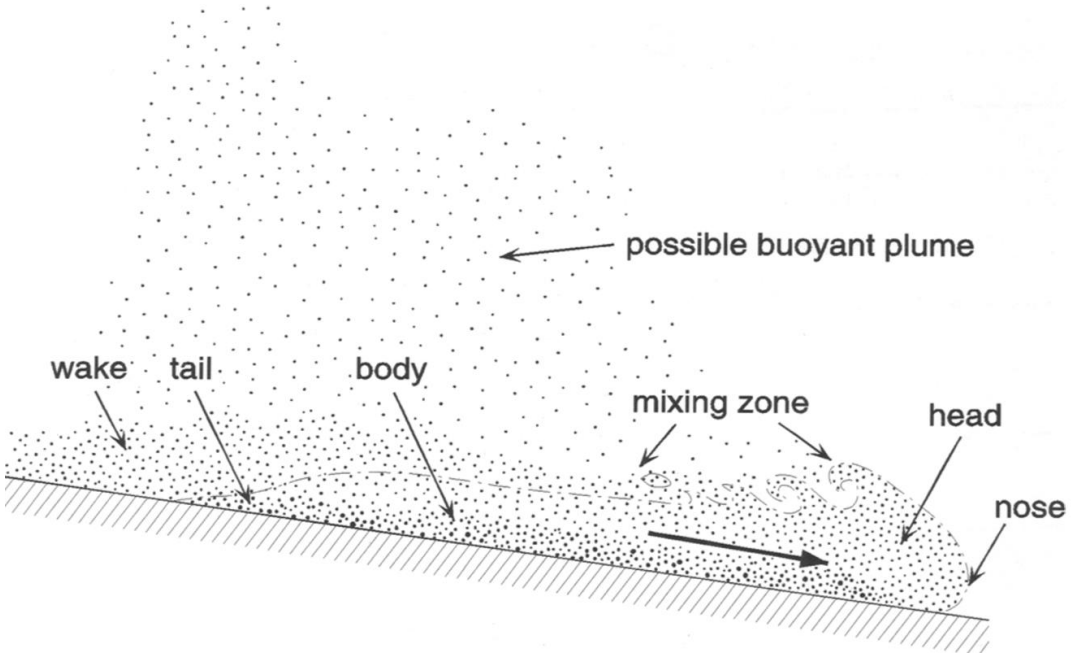

Figure 1. PDC anatomy (Branney and Kokelaar, 2002; modified from Simpson, 1997)

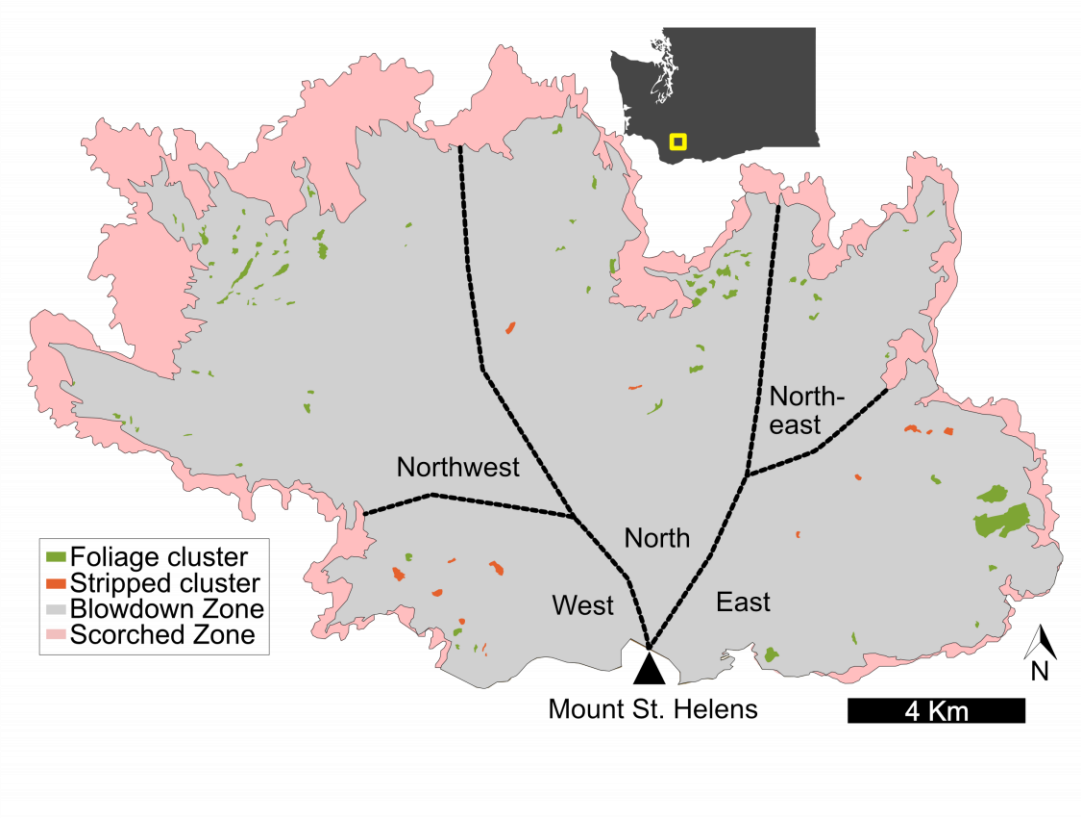

Figure 2. Map of the affected area, with location within Washington state indicated by a yellow box. The blowdown zone contains tree clusters, isolated standing trees, and fallen trees. The blowdown was separated into directional zones. The scorched zone contains only standing, burned trees. Outside the scorched zone are standing, living trees.

Methods

The four main objectives in studying post-eruption aerial photos were to locate standing trees, calculate tree heights, calculate tree density, and calculate tree height from downed trees as a function of distance from the volcano. Table 1 lists all variables, definitions, and units used in this work.

LOCATING CLUSTERS OF STANDING TREES

A 1/3 arc-second-resolution, ~10-meter digital elevation model (DEM) from the National Elevation Dataset (https://ned.usgs.gov) was re-projected in ArcMap from an original NAD83 geographic (i.e. decimal degrees) spatial reference to NAD 1983 UTM Zone 10N coordinate system, allowing all measurements to be in metric units. Hillshade (shaded relief), slope, and aspect rasters of 10 meter-resolution were constructed from the DEM using ArcGIS (https://www.esri.com/en-us/arcgis/about-arcgis/overview) tools. Single frame, 0.8 m-resolution, color-infrared aerial photographs acquired on 19 June 1980 by the U.S. Geological Survey were downloaded from Earth Explorer using the polygon search criteria and decimal degree coordinates. The images contain the damaged forest, where both standing and fallen trees are visible. The aerial photos were georeferenced to the DEM, and/or features visible in a detailed vector road layer, using 10 control points for each image. The control points were positioned using stream intersections or other distinct topographic features (Figure 3). Figure 25 in the Appendix shows the footprints of all the aerial photos with spatial reference to the blowdown and scorched zone. The extents of the blowdown and scorched zones (Figure 2) were traced

from a georeferenced copy of the map by Lipman and Mullineaux (1981). The blowdown zone was divided into five directional zones: West, Northwest, North, Northeast, and East. Zone boundaries conformed to similar distances the PDC traveled in each direction. The purpose was to spatially compare data to observe any effects from the radial spreading of the PDC.

Standing trees cast distinct shadows on the ground that provided a means to accomplish all of the earlier-stated objectives. A scorched zone of standing, dead trees that retained their foliage and branches encircled the blowdown zone (Figure 2; Rosenfeld, 1980; Tilling et al., 1990). In aerial photographs, trees in the scorched zone cast irregular, quasi-triangular shadows and appear grayish (Figure 4). The same shadows can be found in the blowdown zone, indicating that those standing trees also retained foliage and branches. In contrast, standing trees stripped of foliage and branches cast nearly linear shadows (Figure 5). Beyond the scorched zone, trees are reddish in color in the photos because they are photosynthetically active and reflect infrared light.

Clusters of 10 or more closely spaced trees were also left standing throughout the blowdown zone, as recognized by either groups of irregular, rounded and/or linear shadows. Clusters were surrounded by fallen trees. Clusters were numbered and categorized into two types: stripped and foliage. Stripped clusters contained distinct, linear shadows (Figure 6a). Foliage clusters contained wider, irregular, rounded shadows, very similar to shadows of standing trees with foliage within the scorched zone (Figure 6b). Figure 26 in the Appendix is a map of the numbered clusters. Cluster surface areas were calculated from the areas of polygons that were digitized to encircle each cluster.

Like surface area, slopes and aspects for clusters were derived from slope and aspect raster values, at 10 m spacings, that fell within cluster polygons. In brief, the GIS processing to derive these values involved: 1) creating a point, at the center of every slope and aspect raster cell, that stored the slope or aspect; 2) creating a spatial join between the slope and aspect point files so that a single point file contained them both; 3) successively selecting and exporting to individual cluster files only those points from the joined file that fell within each of the cluster polygons.

Paths along which the PDC traveled from the volcano, to each cluster, to the edge of the blowdown zone were mapped by following the alignment of fallen trees. A map of these cluster flow paths is in the Appendix (Figure 26).

Moore and Rice (1984) mapped the front of the PDC at 30 second intervals with satellite imagery. The resulting isochron map (Figure 7) has been used extensively in studies on Mount St. Helens as a proxy for PDC velocity. The velocity the PDC at each standing tree cluster was approximated by georeferencing the isochron map of Moore and Rice (1984) to the blowdown zone. The distance between each isochron along flow paths was measured by tracing the flow path over a specific cluster. PDC velocity was then obtained by dividing distance by the time difference between the isochrons.

TREE DENSITY

To characterize the density of standing trees, more paths along which the PDC traveled were traced by the same process from the volcano to the edge of the blowdown zone (Figure 8). There are now two sets of flow paths. The first set maps the path the

PDC took from Mount St. Helens, to the cluster, to the edge of the blowdown zone. The second set maps the path the PDC took from Mount St. Helens to the edge of the blowdown. The second set was used to analyze tree density. Because each flow path had a different length, distances along flow paths were normalized by the total distance traveled by the PDC along that path, where 0% began at Mount St. Helens and 100% ended at the edge of the blowdown zone. The lack of visible toppled trees in the northwest zone made it difficult to trace the PDC flow. To have a consistent area for measuring tree properties along flow paths, a 100 m buffer was created that extended 100 m on both sides of the flow paths. This buffer was sectioned into 200 by 200 m rectangles, centered along the flow paths, which had an area of 0.04 km^2. Rectangles were only created for areas along the flow path with visible standing and/or fallen trees. Tree density was obtained by counting all isolated, standing trees within the 200 by 200 m rectangles, and dividing by 0.04 km^2 (Figure 6c, Figure 9a-b). The last rectangle of a flow path typically overlapped the blowdown zone boundary. Tree density in this last rectangle was calculated by dividing the number of isolated, standing trees by the area of the portion of rectangle within the blowdown zone. Figure 114 in the Appendix contains all numbered flow paths for this study. Table 8-11 and Figure 115-135 in the Appendix contains tables with the number of trees per every 0.04 km^2 along each flow path as well as a figure for each path showing isolated standing trees, 200 by 200 m rectangles, and the flow path.

TREE HEIGHT

Heights for standing trees were derived from the shadows they cast. Tree shadows were digitized from start pixel to end pixel on each aerial photo. To find the height of a tree (z), the length of its shadow on flat ground (b) and the solar elevation (θ) is needed, calculated by (Figure 10a):

$$z = b * tan\theta. \quad (2)$$

Values for θ on 19 June 1980 can be estimated from an interactive sun path web application (http://solardat.uoregon.edu/SunChartProgram.html) maintained by the University of Oregon Solar Radiation Monitoring Laboratory (Figure 11). Solar azimuth and θ chart the path the sun took over of course of the day. It was inferred that the sun is directly aligned with and in the opposite direction from the tree shadow at the time the aerial photo was acquired; therefore, solar azimuth is found by subtracting 180° from the azimuth of a shadow (γ). Having solar azimuth, the sun path chart (Figure 11) provides θ. Values for γ, which ranged from 313° to 13°, were determined using ArcMap tools performed on the digitized shadow line. Thus, solar azimuth ranged from 133° to 193°, with a median of 158°, therefore θ had a median of 66°.

Eq (2), however, only applies when b is on flat ground. Most, if not all, tree shadows in the Mount St. Helens blowdown zone were situated on mountainous, sloping ground, therefore appearing longer or shorter in the aerial photography. To project the digitized length of the tree shadow (c) onto flat ground, another equation was needed to solve for b (Figure 10b):

$$b = \frac{c * \sin(\theta - \alpha)}{\sin(180 - \theta)} \quad (3)$$

where α is apparent slope, the slope in the direction of the shadow. Values for c were found using ArcMap tools performed on the digitized shadow. The resolution of the aerial photographs is 0.8 m per pixel; therefore, the uncertainty of c was estimated as ± 0.8 m. Values for α represent the slope of the tree shadow, which is not necessarily the same as the slope of the overall topography. The topographic slope (δ), as provided by the previously described slope rasters, is the maximum slope. Using a version of the apparent dip equation, α is solved (Figure 10c):

$$\alpha = \arctan[tan\delta * \sin(\gamma - \beta)] \quad (4)$$

where β is right-hand-rule strike (azimuth) of the hill, found by subtracting 90° from the ground aspect, available at 10 m ground spacings from the previously described aspect raster. Table 16 of the Appendix contains the heights of all standing trees in clusters.

In the above equations, topographic slope (δ) and aspect within 5 meters of a tree shadow are employed to find tree height. The slope and aspect rasters are 10 meter-resolution. If a tree shadow is less than 10 meters in length, it is possible for the shadow to reside within one pixel of the slope and aspect rasters. Setting a requirement for the tree shadow to be greater than 10 meters in length allows it to be spread across at least two pixels of the slope and aspect rasters. Having multiple values for slope and aspect allows for an average value of each and a better representation of the ground the tree shadow laid upon. Likewise, for consistency, the lengths of downed trees and tree densities also relied solely upon tree and shadow lengths greater than 10 m.

The 10 meter-resolution slope and aspect rasters propagated a ± 10 m error through both the δ and β variable. These lead ultimately to a very large theoretical error

in tree height that greatly diminishes the resolution of any true differences that might exist. Instead, to empirically evaluate the combined effects of slope and aspect resolution errors, tree heights derived from the 10 m DEM were compared to those derived the same way from a newer 3 meter-resolution DEM. The 3 meter-resolution DEM was collected 2 November 2002 by Fugro – EarthData Inc. The 3 meter-resolution DEM could not be used for more than this error comparison because it covers only a limited area of the blowdown zone. Comparing individual tree heights calculated from the 10 meter-resolution data to individual tree heights for those same trees derived from the 3 meter-resolution data show that, on average, heights agree within ± 3 m and show no systematical bias. The 0.8 m resolution of the aerial photographs used to measure shadow lengths (c) introduces an additional error that when propagated through equation 3, yields an average uncertainty of ± 2 m on height irrespective of slope and aspect errors. Combining these two uncertainties gives a total tree height error of ± 5 m. This is the height error used in this study.

Heights of standing trees and the lengths of fallen trees were compiled along the flow paths, within the 200 m by 200 m rectangles where tree density was acquired (Figure 9a-b). Heights were obtained from digitizing shadows, lengths from the digitized distance between the starting and ending points of a tree. Only isolated, fallen trees were measured because the energy needed to topple trees may be reduced when trees fall in groups (Clarke and Voight, 2000). Because shadows of standing trees were restricted to greater than 10 m in length, only fallen trees with lengths greater than 10 m were considered in order to not introduce bias. Fallen tree lengths have an error of ± 0.8 m, the

resolution of the aerial photographs. The length of a fallen tree was assumed to equal its height when standing. The Appendix contains tables of every isolated, standing tree (Table 12-15) and tree heights from fallen trees (Table 17) along each flow path.

CHARACTERIZING TOPOGRAPHY

Hill slope angles and heights (Figure 12) at tree cluster locations (Figure 2), as exhibited by topographic profiles, were collected to compare topographic relief. The procedure for creating topographic profiles was: 1) the ArcMap "feature to point" tool was run on a cluster polygon, placing a point at its center; 2) starting from this point, 500 m-long lines were digitized directly on the flow path of the cluster, both toward and away from the volcano, forming a 1000 m-long line along which the profile would be extracted; 3) using the "interpolate line" tool from the ArcMap 3D Analyst toolbar, the 1000 m line was traced, always starting at the point closer to the volcano; 4) the "profile graph" tool of the ArcMap 3D Analyst toolbar then created a topography profile of the 1000 m transect. For each hill in a profile (see Figure 12), the distance and elevations along the topographic profiles of the initial inflection point, crest, and last inflection point of the hill were collected. The slope of the stoss side which faces Mount St. Helens, here called the foreslope angle (θ_f; Figure 12), was calculated from the profiles by the addition of the angles between horizontal plane(s) and the topography of the localized hill (θ_1) and the angle created by a theoretical baseline connecting the upper and lower inflection points of the hill with the horizontal plane (θ_2; see Figure 12):

$$\theta_f = \theta_1 + \theta_2. \quad (5)$$

Both inflection points were identified by a sudden change of slope. In Figure 12, the upper inflection point changes from a negative to positive slope, whereas the lower inflection point changes from a strong negative slope to a weak negative slope. Hill height (h) was defined as the difference in elevation between the hill crest and the theoretical baseline, as measured at a right angle to the baseline (Figure 12):

$$h = L * \sin \theta_f \quad (6)$$

where L is the length of the stoss side of the localized hill. The crest of the hill was identified by a change from positive to negative slope.

The PDC of Mount St. Helens traveled over significantly variable topography before reaching sites where tree clusters were preserved. To quantify this variability, the foreslopes and hill heights upstream of every cluster and along its flow path were calculated (Figure 12). Starting at the beginning of each profile, every hill taller than 10 m with foreslopes greater than 1° were measured until reaching a hill with a cluster (Figure 13). The DEM is 10 meter-resolution, therefore, the hills had to be taller than 10 m to obtain an accurate portrayal of the topography. Part 28-113 in the Appendix includes all 1000 m topographic profiles for each upstream hill along a flow path.

A summary of topographic and other parameters for each cluster of standing trees is given in Table 3, which lists the cluster area, length, and width, average tree height, height of tallest tree, hill height, hill foreslope angle, and PDC velocity, all of which are separated by the type of cluster. Area is defined as the area that a cluster polygon encircles. Cluster length is the length of the cluster side parallel to the direction of the

PDC flow path. Cluster width is the side of the cluster perpendicular to the direction of the PDC. PDC velocity is the speed of the PDC when it went past the cluster.

Table 1. Notation

Symbol	Definition	Equation	Units
P_{dyn}	Dynamic pressure	1, 9	kPa
ρ	Density	1	$\frac{g}{m^3}$
v	Velocity	1	$\frac{m}{s}$
z	Tree height	2, 9	m
b	Shadow length on horizontal plane	2, 3	m
θ	Solar elevation	2, 3	°
c	Digitized shadow length	3	m
α	Apparent dip	3, 4	°
δ	Ground slope	4	°
γ	Shadow azimuth	4	°
β	Strike of hill	4	°
θ_f	Foreslope angle	5, 6	°
θ_1	Slope of localized hill	5	°
θ_2	Slope of main topography	5	°
L	Length of stoss side	6	m
h	Hill height	6	m
r	Tree radius	9	cm
σ_{ult}	Maximum stress at height of cylinder failure	9	$\frac{g}{ms^2}$
C_d	Drag coefficient	9	No unit

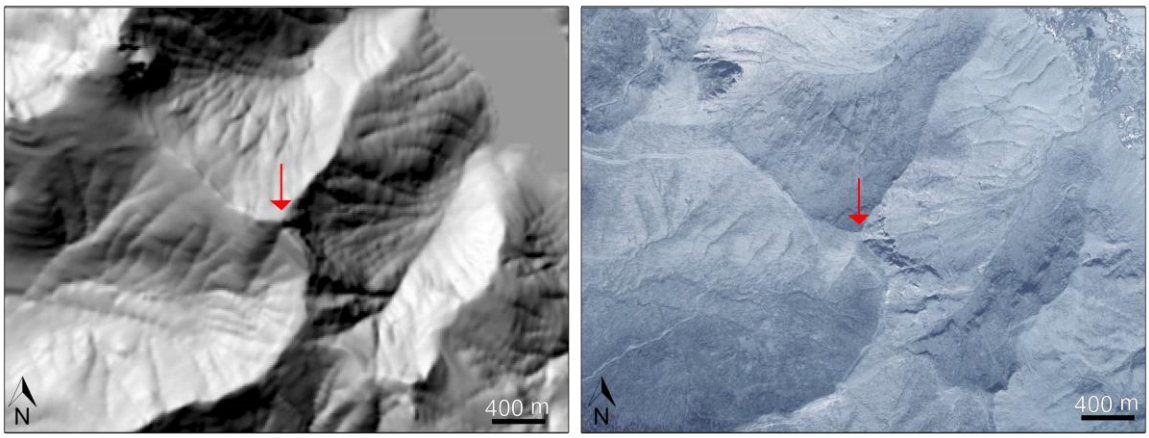

Figure 3. Example of distinct ridgelines seen in the 10 m-resolution hillshade on the left and the aerial photography on the right. The intersection of the ridges shown by the red arrow designates a great spot to add a control point for georeferencing.

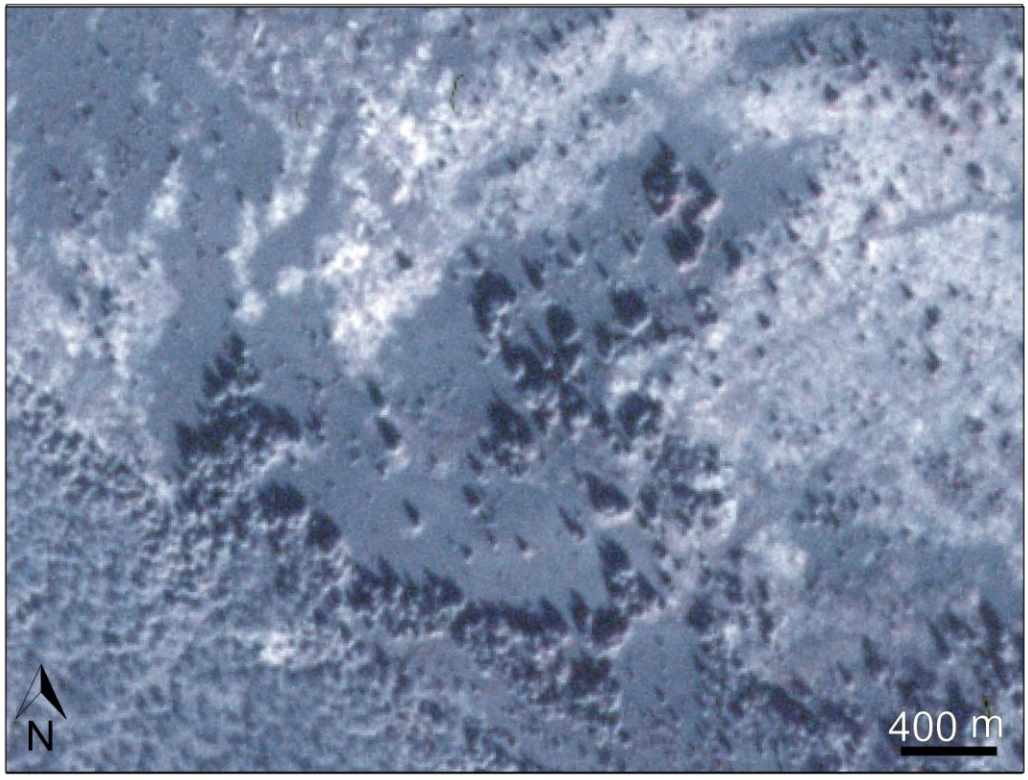

Figure 4. Tree shadows appearing rounded and thick are attributed to trees with foliage.

Figure 5. Tree shadows appearing thin, NW-oriented, dark linears are attributed to trees stripped of foliage and branches.

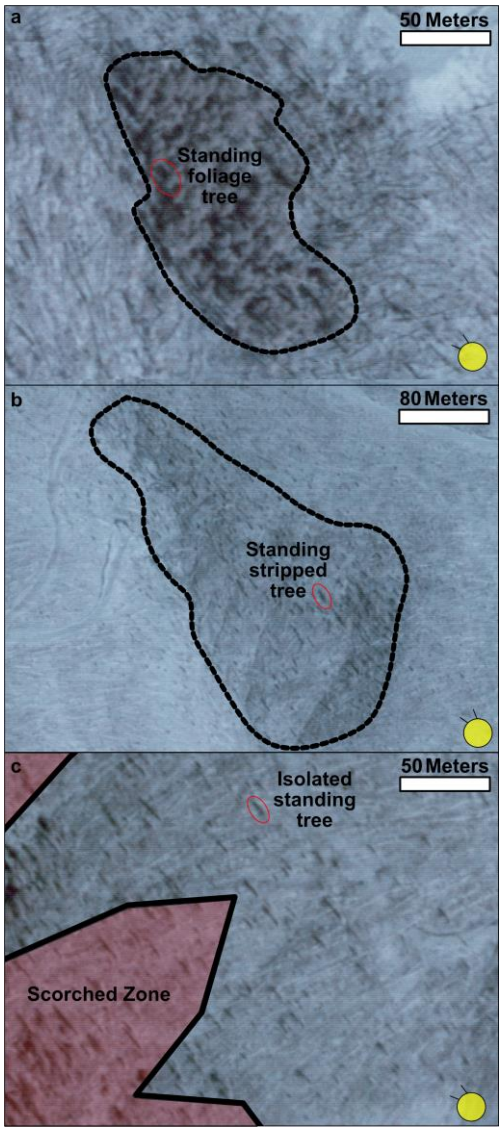

Figure 6a-c. The lack of color in this color infrared aerial photography indicates that all vegetation is dead. The yellow circle in the bottom right represents the sun and the direction of illumination. 6a) An example of a stripped cluster, encompassed by the thin black line. The red oval contains a single standing stripped tree with a linear shadow. 6b) An example of a foliage cluster, encompassed by the thin black line. The red oval contains a single standing tree with foliage, where the bottom of the oval is the fuzzy appearing tree top and the top of the oval shows an irregular shaped shadow. 6c) Isolated standing trees intermixing with fallen trees. The red oval contains a single standing tree, most likely stripped due to the linear shadow. The thick black line is the boundary between the blowdown zone and the scorched zone

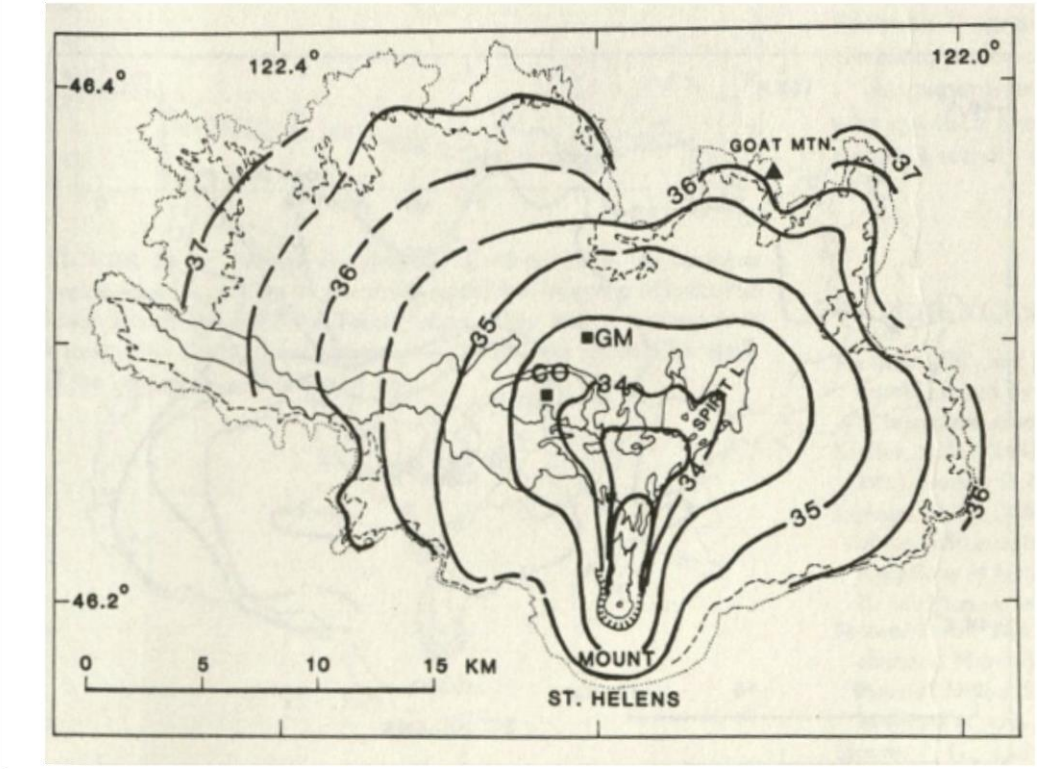

Figure 7. Taken from Moore and Rice (1984). The thick black lines represent the front of the PDC every 30 seconds. The thick, dashed black lines are hypothetical. These isochrons were used to derive velocity.

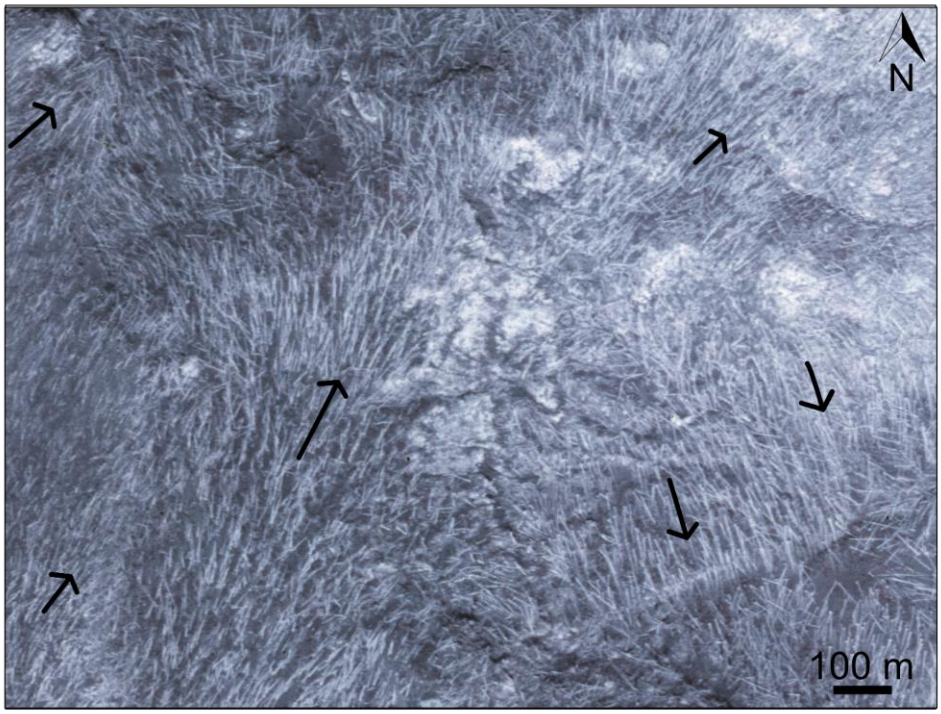

Figure 8. Arrows point to the direction of most of the downed trees. The volcano is directly south.

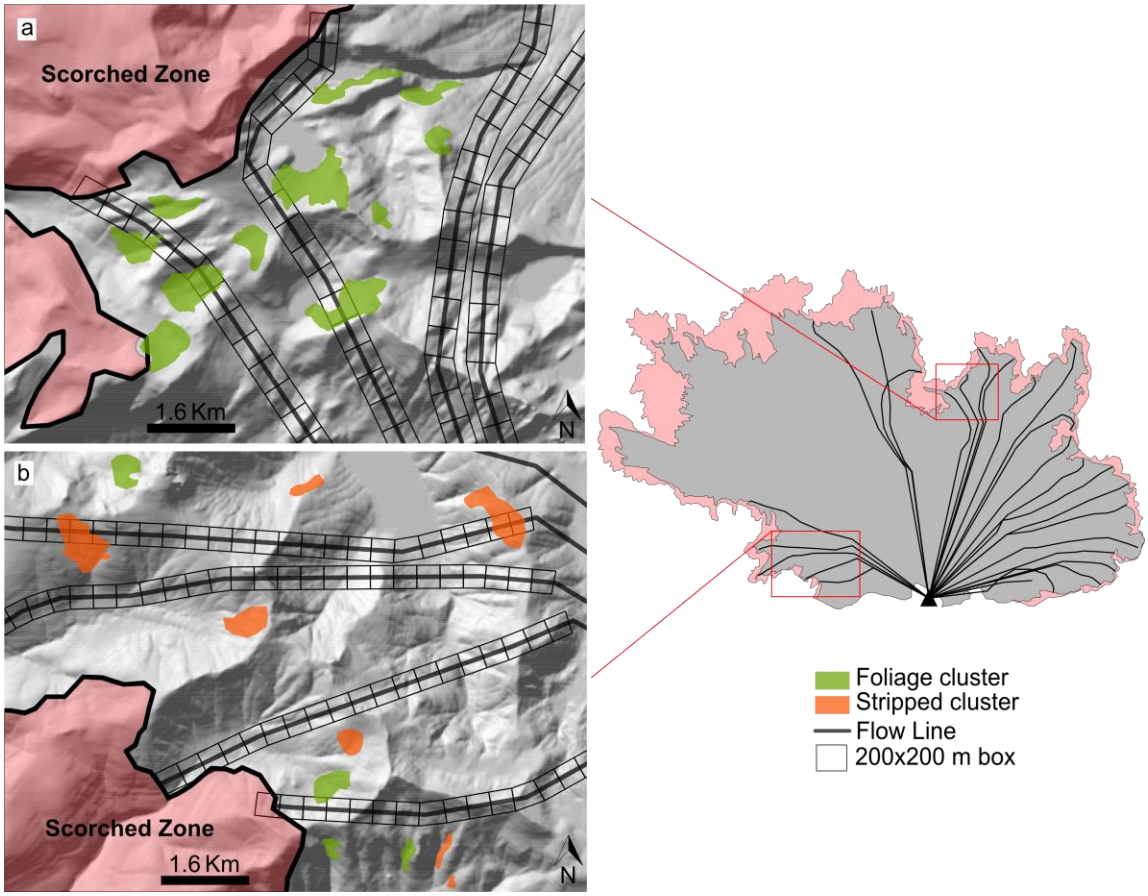

Figure 9a-b. Examples of tree clusters in the blowdown zone and their relationship to PDC flow paths, as mapped from orientations of fallen trees. The boxes on the flow paths designate a 200 m by 200 m area used to count the number of trees and calculate tree heights from tree shadows. The inset map illustrates all the mapped flow lines. 9a) Northern side of the blowdown zone where foliage clusters are clustered and located near the edge of the blowdown zone. 9b) Western side of the blowdown where most of the stripped clusters are located.

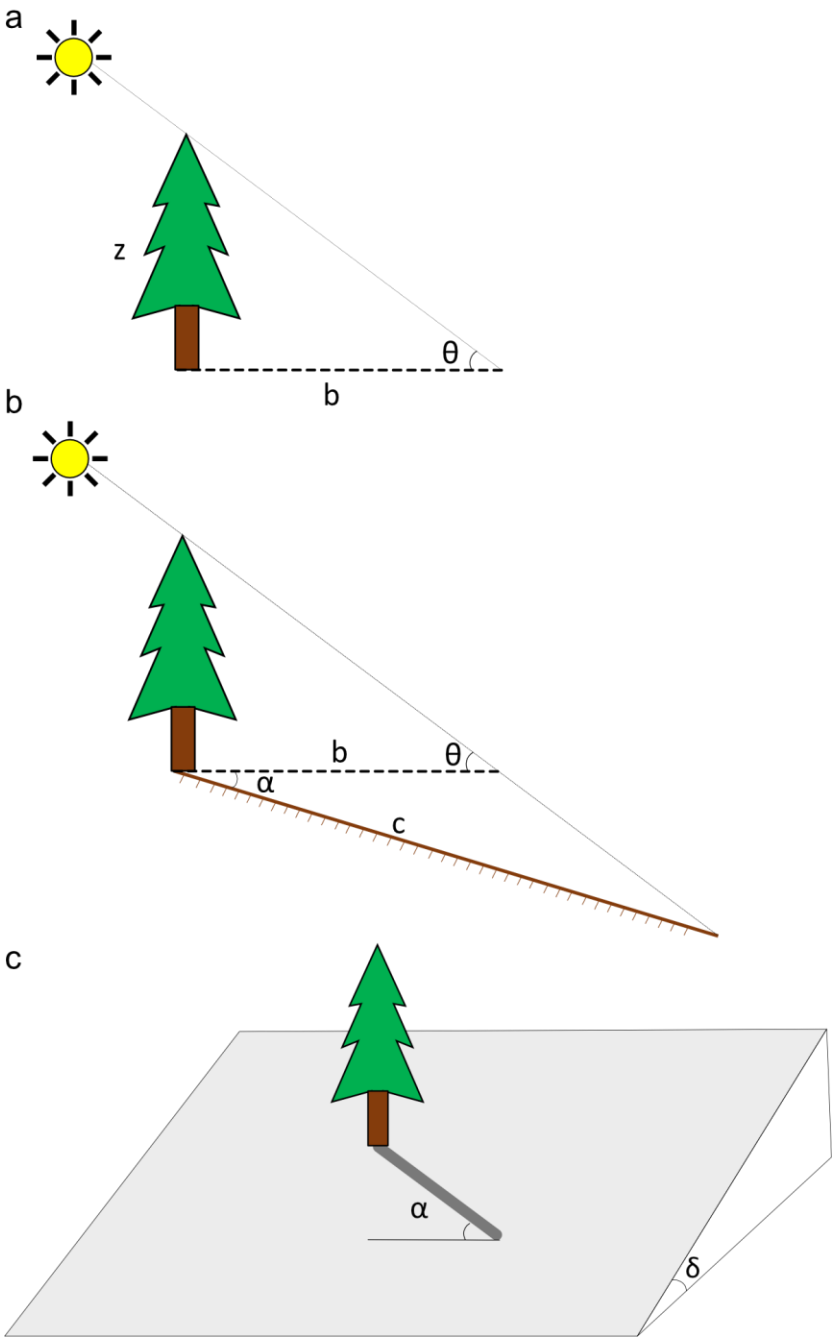

Figure 10a-c. 10a) Illustration of the parameters needed to find tree height (z) from tree shadow length (b) and solar elevation (θ). 10b) Illustration of the parameters used to calculate the tree shadow length projected onto a horizontal plane (b) using tree shadow length (c), the apparent slope (α), and the solar elevation (θ). 10c) Illustration of the difference between the slope of the ground (δ) and the apparent slope of the shadow (α)

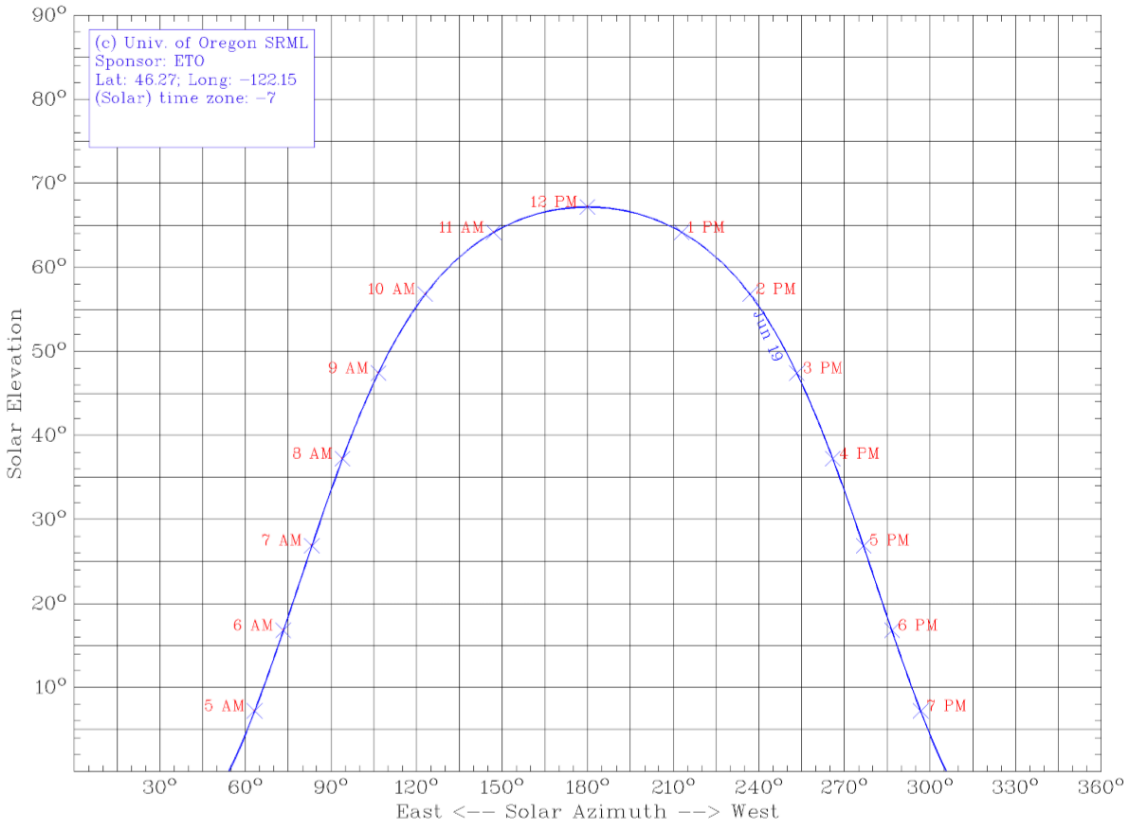

Figure 11. Sun chart plotting solar azimuth versus solar elevation (UO Solar Radiation Monitoring Laboratory, 2007). Latitude = 46.27. Longitude = -122.15. Date = 19 June 1980. Latitude and longitude were taken from the coordinates of the central aerial photo. Solar azimuth was found by subtracting 180° from the shadow azimuth.

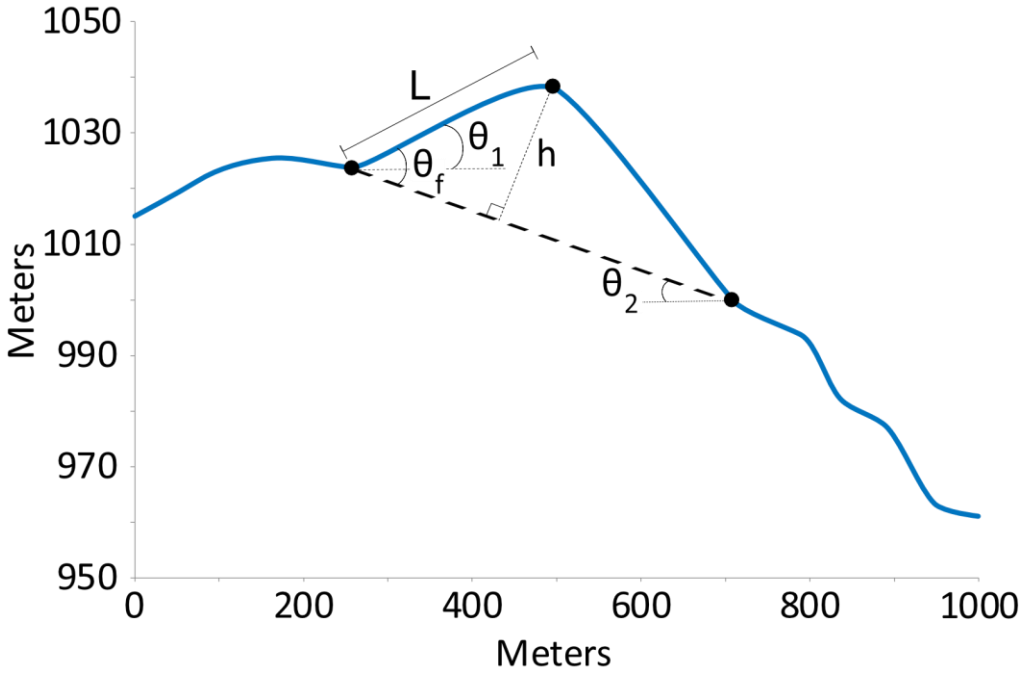

Figure 12. Schematic of a topographic profile that includes the parameters (θ_1, θ_2, L) needed to find the foreslope angle (θ_f) and hill height (h) of the localized hill.

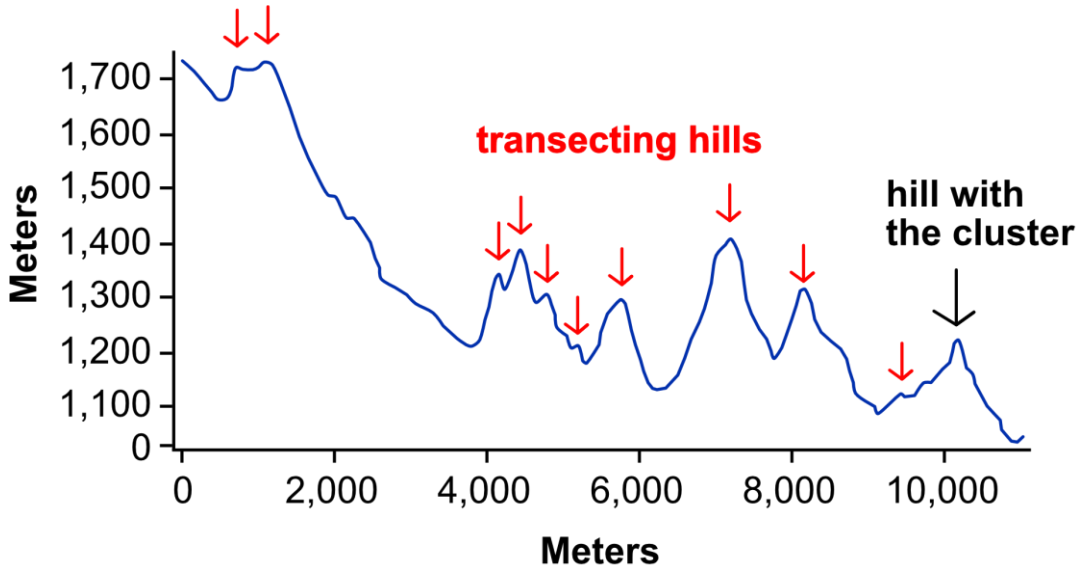

Figure 13. Example topography profile of a representative flow path beginning at the volcano (0 m) and ending at the hill with the cluster. The red arrows designate the hills that transect the flow path. The hill height and foreslope of each upstream hill was found. Vertically exaggerated x2.

Results

TREE CLUSTERS

A total of 92 tree clusters were identified. Of those, 41 were newly identified in this study with the other 51 reported in Gardner et al. (2018). Most of those 51 clusters are situated on lee sides of hills with respect to the PDC flow direction, as determined from the differential between the bearing of the flow path and the median aspect of the standing tree cluster hill slope (Gardner et al., 2018). By the same measure, the median aspects of stripped clusters exhibit a stronger parallelism with the local PDC direction than foliage patches (Figure 14). There are several foliage clusters in the North Fork Toutle River valley that appear to be in gulleys or directly behind a small outcrop, thus still being shielded from the PDC, but not located on hill lee sides or topographic drop-offs. None of the clusters are on slopes facing the local direction of the PDC.

Of the 41 new clusters, 14 are stripped. They are found in all but the northeast and northwest zones. Stripped clusters begin to appear at around 40% of the distance traveled by the PDC and persist until the edge of the blowdown zone (Figure 15). There are 79 total foliage clusters found distributed throughout all the blowdown zone, 27 of them newly identified by this study. Foliage clusters begin to appear only beyond 70% of the PDC runout distance (Figure 15). Therefore, stripped clusters were preserved nearer the volcano, whereas foliage clusters were only preserved farther away.

All standing trees with shadows in every cluster were measured to find tree height. The maximum average tree height in stripped clusters was 40.1 m ± 9 m, with a median of 16.1 m ± 9 m (Table 2). The maximum average tree height in foliage clusters

was 36.3 m ± 5.8 m, with a median of 10.3 m ± 5.8 m. The tallest tree in each stripped cluster had a maximum height of 73 ± 5 m, with a median of 29 ± 5 m. The tallest tree in each foliage cluster had a maximum height of 62 ± 5 m, with a median of 16 ± 5 m. Stripped clusters, therefore, contain taller trees.

Area is the ground covered by the cluster of standing trees. The area of stripped clusters ranged from 6,018 m^2 to 133,350 m^2, whereas foliage clusters ranged from 2,454 m^2 to 1,425,742 m^2 (Table 2). Width is the side of the cluster that is orthogonal to the PDC flow direction whereas length is the side that is parallel to the PDC flow direction. The width of stripped clusters ranged from 60 m to 686 m, with a median of 336 m, and the length ranged from 59 m to 498 m, with a median of 222 m. The width of foliage clusters ranged from 66 m to 1,343 m, with a median of 265 m, and the length ranged from 32 m to 2,017 m, with a median of 165 m. Even though the ranges of areas, widths, and lengths of foliage clusters are much broader, stripped patches generally cover more ground.

Hills that preserved stripped clusters range in height from 20 m to 147 m, with a median of 51 m, whereas foliage clusters have a maximum height of 417 m, with a median of 49 m (Table 2). The foreslopes that preserved stripped clusters range from 13° to 47°, with a median of 21°, whereas foliage cluster foreslopes range from 3° to 47°, with a median of 15°. Overall, stripped clusters were standing behind taller hills with larger foreslopes.

The medians of the height and foreslope of hills upstream of stripped clusters were 53 m and 19°, whereas the medians of hills upstream of foliage clusters were 66 m

and 16°, respectively (Table 2). A ratio was used to compare the attributes of hills traversed by the PDC before the hills with clusters. For hill height:

$$hill\ height\ ratio = \frac{height\ of\ upstream\ hill}{height\ of\ hill\ with\ cluster}. \quad (7)$$

For hill foreslope:

$$hill\ foreslope\ ratio = \frac{foreslope\ of\ upstream\ hill}{foreslope\ of\ hill\ with\ cluster}. \quad (8)$$

If the ratio is above 1, the upstream hill is taller or has a larger foreslope angle. If the ratio is between 0-1, the hill with the cluster is taller or has a larger foreslope angle. Table 4 and Table 5 summarizes all the ratio values for upstream hills. The ratios were plotted with distance to the cluster (Figure 16). About 68% of foliage clusters had upstream hills that were taller than the hill with the cluster, whereas 46% of stripped clusters had upstream hills that were taller than the hill with the cluster. About 46% of foliage clusters had upstream hills that had lower foreslope angles than the hill with the cluster, whereas 73% of stripped clusters had upstream hills that had lower foreslope angles than the hill with the cluster.

Table 6 summarizes all the ratio values for downstream hills. Only 13 hills downstream of clusters are greater than 10 m tall and steeper than 1° foreslope. Hills with these criteria only occur downstream of foliage clusters. Almost all heights and foreslopes of downstream hills are shorter and smaller in angle than the hills with clusters on the same flow path.

ISOLATED TREES

Isolated tree density increased with distance from the vent in all zones around the volcano (Figure 17a-d). Isolated tree density began to increase at 75% runout from 75 trees/km^2 to 426 trees/km^2 in the west zone (Figure 17a), at 65% runout from 125 trees/km^2 to 552 trees/km^2 in the east zone (Figure 17d) at 80% runout from 25 trees/km^2 to 775 trees/km^2 in the north zone (Figure 17b), and at 93% runout from 200 trees/km^2 to 1150 trees/km^2 in the northeast zone (Figure 17c). The preservation of isolated, standing trees varied with direction away from the volcano, with slightly taller trees more prevalent to the east and west of the volcano (Figure 17a-d).

Within the last 20% of the distance traveled by the PDC towards the west and east, there was an increase in the maximum tree height (Figure 17aa, 17dd). In contrast, the north zone (Figure 17bb) shows a decrease in the maximum height in the last 20% of distance, but a constant minimum height of 18 ± 5 m. A decrease in the maximum height with distance is also observed in the northeast zone (Figure 17cc).

The lengths of fallen trees do not change systematically with distance. In comparison with all the standing trees throughout the flow paths in the east zone, the downed trees were ~9 ± 5 m shorter than the isolated standing trees. The rest of the zones contained similar heights and lengths of isolated standing and downed trees.

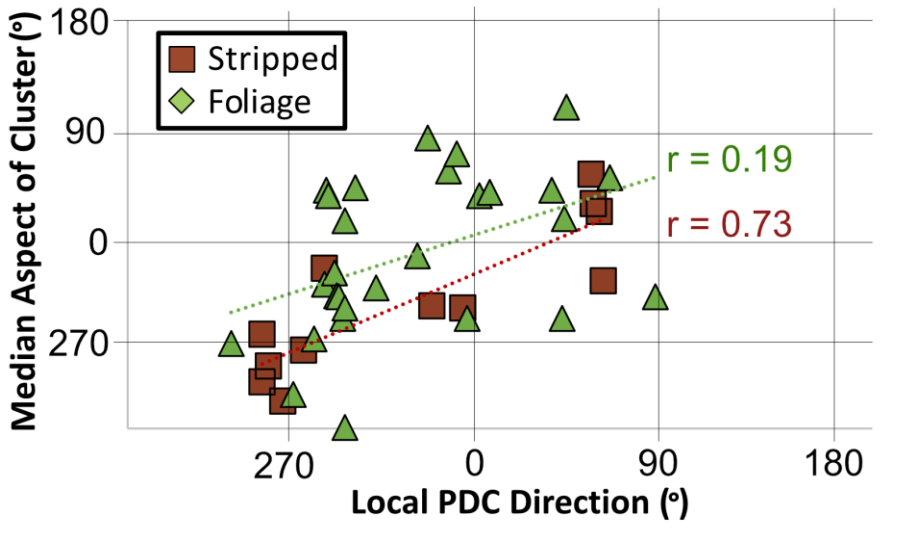

Figure 14. Stripped clusters have a higher r^2 value than foliage clusters when comparing the median aspect of the cluster to the local PDC direction at that cluster.

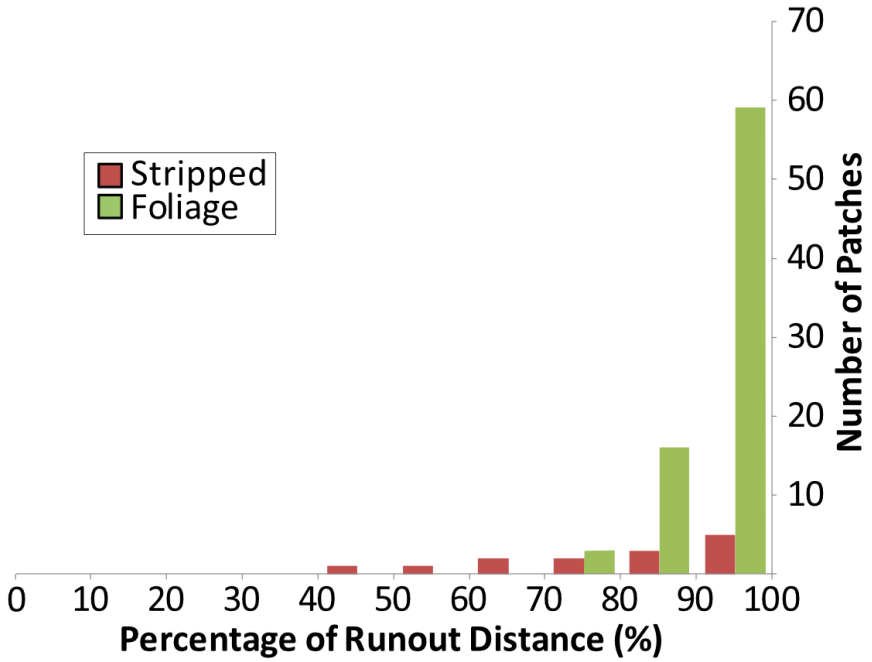

Figure 15. Histogram showing that stripped clusters are fewer in number and more proximal to the volcano than are those with foliage.

Table 2: Summary of results categorized by cluster type.

	Stripped Clusters (n=14)			Foliage Clusters (n=79)		
	Minimum	**Maximum**	**Median**	**Minimum**	**Maximum**	**Median**
Area (m^2) n=93	6,018	133,350	38,837	2,454	1,425,742	27,696
Cluster width (m) n=93	60	686	336	66	1,343	265
Cluster length (m) n=93	59	498	222	32	2,017	165
Average tree height (m) n=1,484	Less than 10	40.1 ± 9	16.1 ± 9	Less than 10	36.3 ± 5.8	10.3 ± 5.8
Tallest tree height (m) n=1,484	Less than 10	73 ± 5	29 ± 5	Less than 10	62 ± 5	16 ± 5
Hill height (m) n=93	20	147	51	Less than 10	417	49
Hill foreslope (°) n=93	13	47	21	3	47	15
Upstream hill height (m) n=226	Less than 10	250	53	Less than 10	259	66
Upstream hill foreslope (°) n=226	5	56	19	3	50	16

Table 3. All data collected for standing tree clusters regarding cluster location, trees, topography, cluster geometry, and PDC velocity.

Cluster Type	Cluster ID	Av Tree Ht	Tallest Tree Ht	Hill Ht	Hill For-slope	Cluster Area	Cluster Length	Cluster Width	PDC Velocity
Foliage									
	3	25	36.8	8.3	7.8	436079	1162	636	108
	22	16.8	33.6	40.4	14.5	23834	121	369	47
	28	12.2	22.7	167.6	47.3	38885	334	100	131
	29	13.3	21.3	183.3	25.8	90109	189	522	124
	32	23.8	40.9	10.4	15	68526	278	389	100
	35	9.1	13.7	17.9	8	24854	124	282	113
	36	8.8	12.6	14.1	8.2	12047	96	194	86
	37	9.2	12.4	39.5	6.9	25100	108	222	111
	41	11.3	20.1	80.8	15	21550	157	199	112
	43	11.1	24.6	88.2	11.6	165982	165	1343	112
	46	7	13.1	33.3	14.8	24534	172	329	90
	50	10.3	15.6	32.2	32.3	25010	273	96	109
	51	6.6	9.8	30.8	17.9	21663	228	144	115
	52	12.3	19.2	193.2	32.9	24310	238	126	100
	53	16.2	21.4	139.5	32.7	55933	187	390	100
	54	6	9.1	1.2	3.4	33438	210	179	134
	55	10.8	16.2	50.7	13.4	20296	182	115	128
	57	14.6	23.5	133.2	14.2	171189	409	438	110
	60	10.4	22.1	111.7	19.1	67429	233	838	101
	61	24.9	30.9			45290	200	213	123
	64	10.2	13.9	49.3	17.8	19256	112	177	74
	65	15.3	27.6	94	29.2	38440	187	224	94
	66	6.6	10.1	66	39.7	98614	115	573	72
	67	4.8	8.8	147.7	26.9	131504	235	477	71

Table 3 (continued)

Cluster Type	Cluster ID	Av Tree Ht	Tallest Tree Ht	Hill Ht	Hill For-slope	Cluster Area	Cluster Length	Cluster Width	PDC Velocity
Foliage	68	7.1	11.5	82.2	16.1	40906	230	161	61
	69	7	10	52	27.9	38857	161	356	46
	70	7.6	14.2	33.4	28.8	50311	338	196	130
	71	9.8	18	99.7	16.2	85619	218	405	130
	74	6.3	8.5	20.9	4.9	42853	127	482	129
	75	25.5	44.1	417.2	42.8	142574	2017	828	101
	76	6.5	9.4	152.9	29.6	15872	167	125	85
	77	12.8	18.3	58.4	9.7	16599	81	192	112
	78	19.9	30.6	58.8	6.5	85428	160	547	68
	79	12.7	16.2	31.3	31.4	27604	45	383	87
	80	7.2	9.9	124.5	12.1	143783	337	551	80
	81	9.5	13.8	19.6	12.8	8931	57	200	97
	82	8.2	11.5	19.7	16.6	11316	127	119	100
	83	10.6	14.3	20.4	7.8	57358	110	773	115
	84	9.2	14.3	6.6	5.4	8519	141	85	115
	85	10	17.2	25.3	5.6	83557	231	421	82
	86	9	12.5	208.2	25.7	74212	252	378	140
	87	33.8	62.4	69.6	25.4	46819	53	662	80
	89	11.2	17.5	94.6	12.7	38298	205	233	114
	91	9.8	13.3	24.1	10.7	7381	32	244	92
	92	9.3	11.6	25	4.9	8633	105	105	121
	94	13.9	18	11.6	13.4	108409	457	695	113
	95	9.4	13.1	39.9	6.5	7439	166	66	116
	96	10	16.8	49.4	12.9	49889	338	301	95
	97	14.2	21.7	56	27	18932	125	160	179
	98	11	17.5	70.1	13.1	102426	165	755	96
	99	9.6	14.3	34.7	11.3	28869	73	394	94

Table 3 (continued)

Cluster Type	Cluster ID	Av Tree Ht	Tallest Tree Ht	Hill Ht	Hill For-slope	Cluster Area	Cluster Length	Cluster Width	PDC Velocity
Foliage	101	6.9	16.2	128.1	20.4	67185	178	409	98
	106	14.4	22.2	14.1	11.8	18757	100	341	
	107	10.7	15	17.1	4.5	19667	92	255	111
	108	10.3	15.3	10.1	6.5	3698	58	117	94
	109	8.1	15.6	35.3	7.7	13840	91	339	133
	110	11.8	17.6	36.9	7.9	9421	69	172	
	111	10.2	16.4	13.3	6.9	17989	70	321	134
	112	8.4	14.6	21.7	6	14139	92	214	134
	113	12	17.3	48.4	35.7	23573	129	187	113
	119	16.6	22.1	69.3	8.3	13280	85	234	57
	120	19	36.1	50.4	23.7	35058	222	135	85
	121	15.5	28.2	41.9	41.9	48421	180	386	74
	122	10.4	15.8	73.3	20.6	26429	185	197	91
	123	36.3	58	51	38.2	35229	97	455	91
	124	13.1	29.6	146.9	27.4	44514	383	228	91
	125	9.6	22.3	25.9	11	56175	298	226	97
	126	10.2	16.5	74.4	14.6	20875	159	188	79
	127	10.9	22.5	27.7	23.9	27788	167	292	51
	131	14.1	24.8	21.5	32.2	60659	263	397	179
	133	7.2	13.2	70.5	33.9	21378	128	301	179
	138	13.8	48.5	86.7	45.5	57251	252	306	82
	141	6.4	11.1	35.9	8.6	3737	49	109	98
	143	10	19	20	7.3	22590	102	242	
	144	9.6	15.3	20.8	9.2	34245	195	274	
	145	8.9	14.6	50.2	11.6	21521	214	130	114
	146	8.9	12.2	15.6	4.6	16098	149	117	134
	147	3.8	9.4	38.7	27.3	2454	54	69	134

Table 3 (continued)

Cluster Type	Cluster ID	Av Tree Ht	Tallest Tree Ht	Hill Ht	Hill For-slope	Cluster Area	Cluster Length	Cluster Width	PDC Velocity
Foliage	102	4.6	9.8	53	20.8	36183	157	270	157
	104	40.1	72.9	38.1	20.4	79646	199	505	102
Stripped									
	115	5.3	13	118.4	13.3	25680	197	247	189
	116	24.7	56.1	22.8	46.7	72506	263	343	62
	117	19	32.1	27.6	22.8	25012	221	142	48
	118	15.7	40.9	64.3	41.7	94517	238	686	74
	128	17.2	26.8	48.2	13.8	38326	72	514	94
	129	13.1	35.8	61	17.5	129065	498	612	226
	130	16.1	23.8	147	18.7	26894	146	329	226
	132	8.6	16.4	91.7	26.5	39348	223	232	179
	134	16.3	30.7	20	29.8	16543	335	60	179
	135	6.9	11.2	21.7	21.1	6018	59	124	179
	137	16	23.2	43.9	13.3	133350	395	529	77
	139	16.8	37.9	141.1	22.7	71708	269	374	77

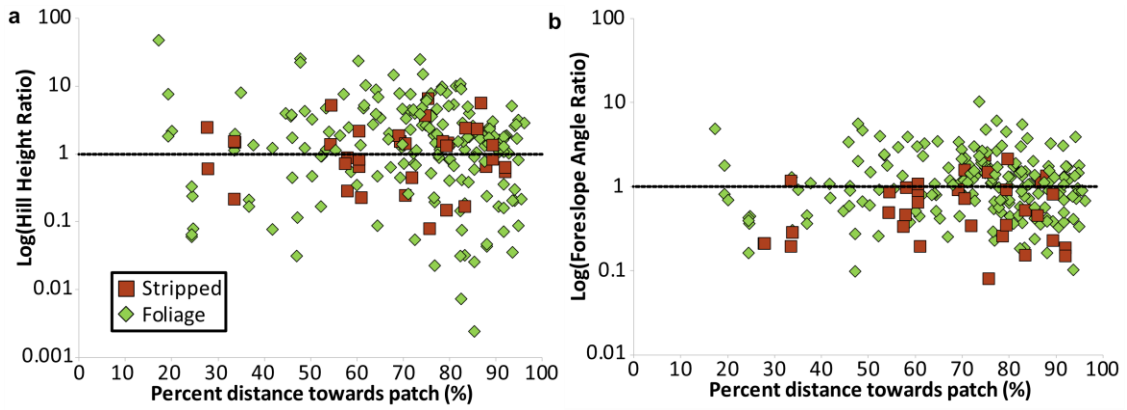

Figure 16a-b. The distances a upstream hill was along a topography profile were normalized to the total length of the topography profile. Topography profile is visualized in Figure 13. The dashed line at 1 splits the attributes of the hills. For data above the line, the attribute for the upstream hill is larger than the hill with the cluster. For data below the line, the attribute for the upstream hill is smaller than the hill with the cluster. 16a shows the hill height ratio of upstream hills for both foliage and stripped clusters. 16b shows the hill foreslope ratio of upstream hills for both foliage and stripped clusters.

Table 4. Summary of hill height ratios of hills upstream of clusters. Each row represents the flow path of a cluster. Hill1 through Hill8 represent the upstream hills. Hill1 occurs closest to the volcano. The last hill with a value is the last hill immediately before the hill with the cluster. The values are the hill height ratios defined in equation 7.

Cluster Type	Hill1	Hill2	Hill3	Hill4	Hill5	Hill6	Hill7	Hill8
Foliage								
	1.16	4.69	4.59	1.39	14.83			
	0.73	1.47						
	0.02	0.19	0.04	0.2				
	0.03	0.18						
	8.1	3.72	7.64	14.78	3.83	8.92	8.96	
	6.17							
	7.84							
	2.8							
	1.37							
	1.25	0.69						
	5.31	0.9	1.84	2.75				
	7.57	1.26	0.36					
	2.16	7.54						
	0.08	0.04	0.24	0.05				
	0.06	0.33	0.06					
	47.33	25.17	22.42	23.58	24.58			
	2.29	1.15	2.49	1.27	0.07	0.16		
	0.52							
	1.13	0.88	1.08					
	1.04	1.01						
	3.93							
	1.76							
	1.35	3.15						
	0.82	1.45	1.3	0.77	1.74			
	0.83	2.02						
	0.08	0.41	1.6					
	1.87	1.94	4.6	2.82				
	0.24	0.12	0.03	0.26				
	0.67	1.67						
	2.02	0.01	0.01	0.002	0.03	0.59		
	3.61	0.34	1.41					
	4	0.54	1.7	4.86				
	0.41							

Table 4 (continued)

ClusterType	Hill1	Hill2	Hill3	Hill4	Hill5	Hill6	Hill7	Hill8
Foliage	2.67	10.15						
	2.66	10.1						
	4.34	9.75						
	7.94	10.71						
	1.79	1.6						
	0.03	0.14						
	3.59							
	1.34							
	0.72	2.73						
	0.47	0.09	5	2.31				
	8.89	1.65						
	4.01							
	1.02	1.78						
	1.15	0.2	2.19					
	1.91							
	2.37	2.31						
	0.64	0.39	1.76	0.3				
	4.68	3.82						
	7.84							
	0.45	6.57	0.98					
	1.8							
	6.85							
	1.22	5.26	6.01					
	0.47	0.93	1.24	0.57				
	1.96	1.35	1.51					
	1.13	2.56						
	2.56	1.85						
	1.96	0.17						
	1.08	0.22	1.59					
	1.86	0.23	3.04	5.09				
	0.09	0.82						
	3.26	4.88	5.1					
	1.2	0.08	1.12	1.82				
	3.42	2.86						
	1.36	2.71						
	1.53							
	0.21	0.17						
	2.44	10.17	3.29					
	4.46	4.66						

Table 4 (continued)

ClusterType	Hill1	Hill2	Hill3	Hill4	Hill5	Hill6	Hill7	Hill8
Foliage	1.73	0.45	2.11					
	4.26							
	0.17	0.91						
Stripped	**Hill1**	**Hill2**	**Hill3**	**Hill4**	**Hill5**	**Hill6**	**Hill7**	**Hill8**
	0.28	0.88						
	6.56							
	0.24	0.07	0.45	0.11				
	2.48	0.6	0.72	0.17	2.42	2.31	0.54	0.63
	0.22	1.53	5.18	0.64	2.18	0.84		
	1.48	1.39	1.52	0.83	1.33			
	1.51	0.72						
	0.23	1.44						
	5.64							
	1.85	0.08						
	3.68							
	0.44	0.64						

Table 5. Summary of hill foreslope ratios of hills upstream of clusters. Each row represents the flow path of a cluster. Hill1 through Hill8 represent the upstream hills. Hill1 occurs closest to the volcano. The last hill with a value is the last hill immediately before the hill with the cluster. The values are the hill foreslope ratios defined in equation 8.

Cluster Type	Hill1	Hill2	Hill3	Hill4	Hill5	Hill6	Hill7	Hill8
Foliage								
	2.38	2.41	2.79	2.14	2.68			
	0.83	1.4						
	0.23	0.67	0.1	0.41				
	0.19	0.76						
	0.93	0.59	1.35	1.06	2.31	0.69	0.89	
	1.66							
	1.62							
	1.93							
	0.89							
	1.15	0.67						
	1.74	0.42	1.74	0.72				
	0.81	0.5	0.7					
	0.69	1.44						
	0.45	0.16	0.42	0.4				
	0.16	0.43	0.39					
	4.85	2	5.59	3.03	10.32			
	1.16	0.57	1.13	1.06	0.38	0.49		
	1.09							
	1.3	0.97	1.31					
	1.26	1.25						
	0.73							
	1.07							
	1.29	1.8						
	0.63	1.03	0.56	1.12	1.55			
	0.45	1.02						
	0.37	1.33	3.08					
	2.96	2.67	6.12	5.53				
	0.37	0.28	0.1	1.11				
	0.36	0.96						
	1.67	1.56	1.51	1.36	0.24	0.57		
	3.42	0.51	1.75					
	0.51	0.38	0.36	0.8				
	0.69							

Table 5 (continued)

ClusterType	Hill1	Hill2	Hill3	Hill4	Hill5	Hill6	Hill7	Hill8
Foliage	1.91	1.88						
	1.47	1.45						
	1.81	3.08						
	4.52	3.02						
	2.84	0.79						
	0.18	0.58						
	1.13							
	1.18							
	1.34	0.71						
	0.8	0.51	3.78	3.24				
	1.07	0.25						
	3.02							
	0.81							
	1.51	0.81	1.22					
	1.23							
	1.58	0.9						
	1.19	1.06	1.28	1.34				
	0.81	0.83						
	3.42							
	0.45	2.55	1.72					
	1.79							
	3.48							
	0.67	2.33	4.77					
	0.6	4	1.73	0.63				
	0.3	1.11	0.46					
	1.34	3.89						
	2.03	1.72						
	0.84	0.33						
	0.88	0.89	2.19					
	0.55	0.29	0.39	0.76				
	0.34	1.45						
	1.48	2.05	1.32					
	1.08	0.74	0.94	1.29				
	0.42	0.68						
	0.44	0.8						
	0.97							
	0.46	0.4						
	3.88	3.26	2.18					
	1.21	1.17						

Table 5 (continued)

ClusterType	Hill1	Hill2	Hill3	Hill4	Hill5	Hill6	Hill7	Hill8
Foliage	1.02	0.9	1.78					
	4.7							
	0.26	0.92						
ClusterType	**Hill1**	**Hill2**	**Hill3**	**Hill4**	**Hill5**	**Hill6**	**Hill7**	**Hill8**
Stripped	0.97	0.47	0.72	0.92	0.35			
	1.5							
	1.58	1.22	1.61	0.46				
	0.21	0.21	0.34	0.15	0.52	0.46	0.19	0.15
	0.19	1.17	0.86	0.89	1.08	0.65		
	0.28	0.49	0.26	0.23	0.81			
	0	0						
	0.2	2.12						
	1.13							
	0.91	0.08						
	2.38							
	0.34	1.36						

Table 6. Summary of hill height and foreslope ratios of hills downstream of clusters using equation 7 and 8, respectively. Each row represents a flow path of a cluster. HillHt1 through HillHt3 represent the hill height ratios. Foreslope1 through Foreslope3 represent the foreslope ratios. Hill 1 is closer to the patch and hill 3 is farther away.

Cluster Type	Cluster #	HillHt1	HillHt2	HillHt3	Foreslope1	Foreslope2	Foreslope3
Foliage	113	0.97	0.39	0.97	0.28	0.73	1.18
	119	0.3			1.57		
	121	0.41	0.41	1.29	0.19	0.36	0.26
	122	2.11			1.94		
	123	0.59	0.71		0.77	0.94	
	124	0.33	0.91		0.77	1.13	
	141	1.53			1.51		

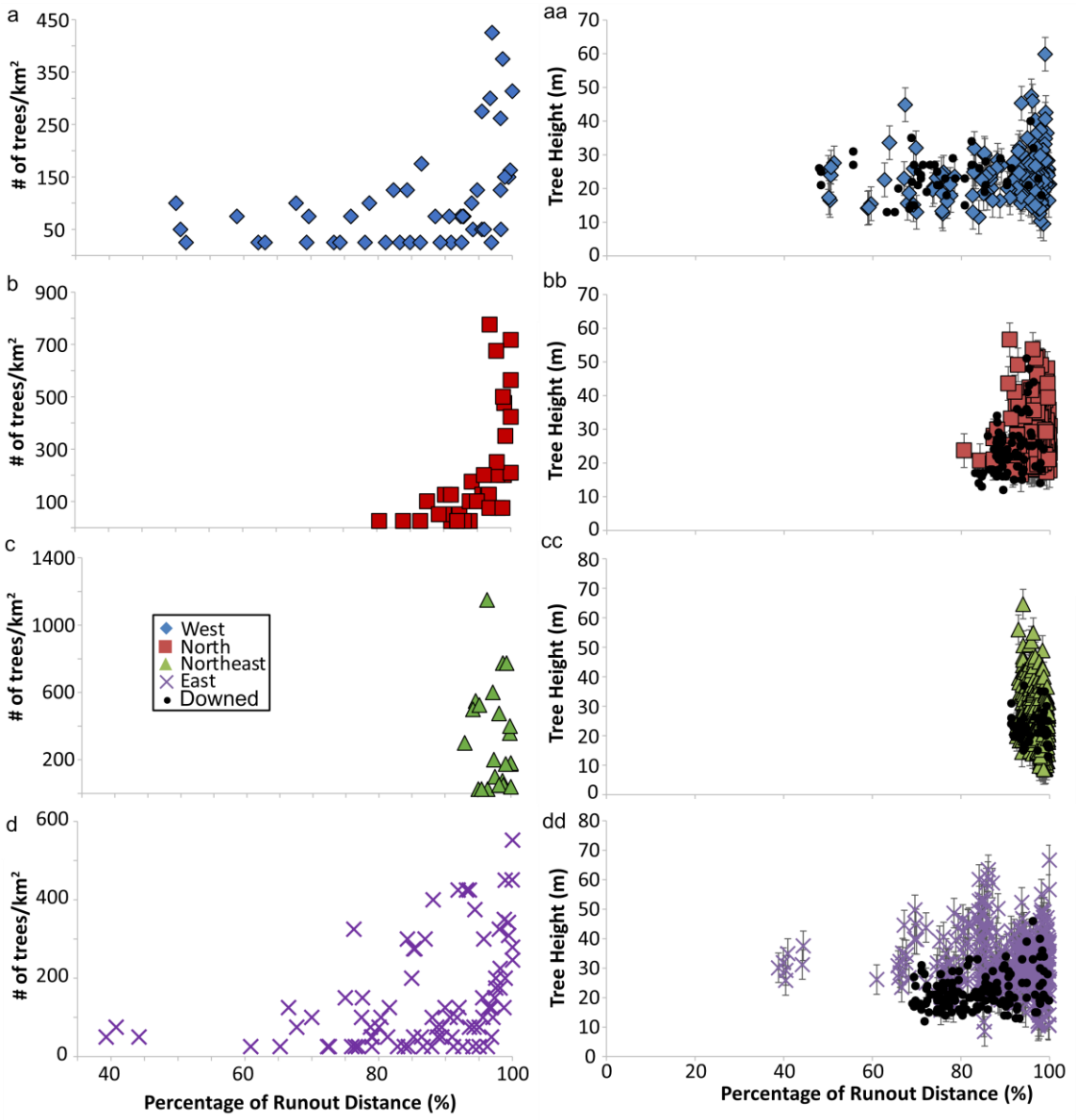

Figure 17a-d, 17aa-dd. The block dots represent the lengths of downed trees, which have errors of ± 0.8 m. The error bars on the colored shapes are ± 5 meters. 17a-d) Density of isolated standing trees in the blowdown zone within 100 m of a flow path. 17aa-dd) Heights of isolated standing trees in the blowdown zone within 100 m meters of a flow line.

Discussion

BALLISTIC TRAJECTORY

Isolated, standing trees with shadows longer than 10 m begin to be left standing at about similar runout distances as stripped clusters. It is at these distances where tall trees began to survive being hit by the PDC. As distance from the volcano increases, the number of isolated, standing trees also increase, indicating a drop in the dynamic pressure of the PDC.

Gardner et al. (2018) suggested that standing clusters of trees were preserved by the PDC following a ballistic trajectory path over them. That trajectory was shorter than a purely ballistic path because of expansion of the front of the PDC as it engulfed air. Stripped clusters and the new foliage clusters in this study were assessed to see if the PDC followed similar ballistic trajectories profiles by looking at hill height and foreslope, geometry of the cluster, and the velocity of the PDC. There is a positive relationship between the area and length of foliage clusters with their hill height (Figure 18a, 18b). There is also a slightly increasing trend of lengthening foliage clusters with the foreslope of the hill (Figure 18bb). The width of foliage clusters does not correlate (Figure 18c, 18cc). The area, length, or width of stripped clusters are not related to hill height, hill foreslope, or the velocity of the PDC (Figure 18a-b, 18aa-bb, 18aaa-bbb).

The PDC traveled past stripped clusters at speeds of 48 m/s to 226 m/s; for foliage clusters the speed ranged from 46 m/s to 179 m/s (Table 2, Table 3). Cluster area, length, and width do not correspond with speed for either cluster type (Figure 18aaa-ccc),

suggesting that velocity was not a controlling factor for tree preservation. This agrees with the conclusion of Gardner et al. (2018).

The geometry of foliage clusters thus appears to correlate with topographic relief, whereas stripped clusters do not; neither correlate with PDC velocity. This implies that part of the preservation of stripped clusters differs from foliage clusters. The process to form a cluster is most likely the same to the first order, namely a PDC taking a ballistic trajectory path over the cluster. However, another part of the PDC also affected stripped clusters because stripped cluster geometry does not relate to topographic relief.

DAMAGE

Tree damage varied as a function of distance (Figure 19). Nearest the volcano, no standing or fallen trees were present. Many studies describe this proximal area as the tree removal zone (Rosenfeld, 1980; Hoblitt et al., 1981; Moore and Sisson, 1981; Waitt, 1981). This zone exists generally within the first few kilometers around the volcano and up to 12 km to the north (Waitt, 1981; Figure 20).

As the PDC traveled farther, trees were broken at their bases and/or uprooted (Figure 19). All fallen trees were stripped completely and fell in alignment with the PDC flow. The dynamic pressures of the PDC in this damaged area were too high to leave any trees standing. Gardner et al. (2018) explains the lack of standing tree clusters close to the volcano. As the PDC surmounted a hill, the base of the PDC head became exposed to the outside air and entrained it, allowing it to expand downward. This downward expansion caused the PDC head to hug the lee side of hills, resulting in not a pure ballistic

trajectory. Because peak dynamic pressure is located in the PDC head (Clarke & Voight, 2000; Gardner et al., 2018s), trees are continually toppled. This failure of a pure ballistic trajectory is thought to be amplified in denser PDCs; PDC density is higher closer to the volcano (Gardner et al., 2018). This area of only stripped, downed trees generally exists within the first 40% of distance traveled by the PDC.

Moving farther out, isolated and clustered trees stripped of vegetation were left standing at distances greater than approximately 40% of the PDC runout throughout the blowdown zone (Figure 19). The appearance of stripped, isolated, standing trees indicates that they were affected by a lower dynamic pressure than the downed trees. Dynamic pressure was still great enough to strip trees of their branches and foliage. Stripped clusters suggest that they were affected by dynamic pressures even lower than that of the isolated, standing trees. These dynamic pressures are lower because of the effect of topography. Almost all stripped clusters are situated on the lee sides of hills. Because all trees are standing within stripped clusters, it can be inferred that the peak dynamic pressure followed a path above the cluster. Therefore, stripped clusters were most likely impacted by another part of the PDC. The dynamic pressure of this part still had to be high enough to strip the trees of branches and foliage.

Near the end of the PDC runout, foliage clusters and a larger number of stripped, isolated trees are left standing (Figure 19). More isolated trees left standing indicates that dynamic pressure was declining. That decrease also allowed shorter trees to be left standing in the last 20% of PDC runout. Foliage clusters were preserved in the last 30% of PDC runout, indicating that parts of the PDC did not contain a dynamic pressure high

enough to strip trees of foliage. Because the peak dynamic pressure most likely passed ballistically above foliage clusters, the basal part of the PDC that did affect the cluster did not have a dynamic pressure high enough to strip them. The trees in foliage clusters are scorched and dead, providing evidence that they were affected by some part of the PDC.

In all areas except in the northwest, the damage mentioned above is extant. The northwest zone is slightly different because toppled trees still had their branches and foliage at the end of the PDC runout (Figure 21b), whereas in other zones the downed trees were stripped (Figure 21a). Downed trees with foliage suggest that they were affected by dynamic pressure lower than those affecting stripped, downed trees; therefore, the northwest zone was subjected to the lowest dynamic pressures. The heights and density of isolated, standing trees in the other zones cannot be compared to the northwest zone because all tree shadows there were less than 10 m in length. Standing trees in clusters in the northwest zone are also shorter than the rest of the standing tree clusters. The lack of tall trees suggests that the northwest zone was heavily logged prior to the 1980 eruption.

In summary, foliage clusters were not stripped by the PDC because the cluster was affected by lower dynamic pressures than what affected stripped clusters. The increased number of stripped, isolated standing trees with distance indicates a decline in dynamic pressure. Downed trees with foliage were impacted by lower dynamic pressures than stripped, downed trees and occur farther from the volcano. Overall, standing tree clusters were affected by lower dynamic pressures than isolated, standing trees.

THE PRESERVATION OF CLUSTERS

The head and the body of PDCs are density stratified because of sedimentation and entrainment of ambient air (Dobran et al., 1993; Sparks et al., 1997a; Branney and Kokelaar, 2002; Sulpizio et al., 2014). The base of both is denser than the upper portions, suggesting that dynamic pressure is higher here (Branney and Kokelaar, 2002; Sulpizio et al., 2014; Gardner et al., 2017). The head, however, travels faster than the body (Fisher 1990, Andrews and Manga 2012, Andrews 2014, Gardner et al., 2017). Because velocity is squared in the dynamic pressure equation, the head has a significantly higher dynamic pressures than the body. Peak dynamic pressure most likely occurs at the base of the head because of the density stratification and higher speeds (Clarke and Voight, 2000; Gardner et al., 2017). To leave a standing tree cluster, the head partially follows a ballistic trajectory path over the cluster. The slower trailing body of the PDC continues to hug topography, flows up and over hills, and scorches everything. Because the body of the PDC is slower, dynamic pressure is lower and not strong enough to topple trees.

The difference between the processes of generating stripped versus foliage patches is the dynamic pressure of the PDC body. The body contains most of the mass and heat of the PDC (Branney and Kokelaar, 2002; Gardner et al., 2017). Because stripped clusters are located on hill lee sides closer to the volcano, they are affected by a relatively denser PDC body, and therefore, a higher dynamic pressure. This dynamic pressure has a large enough magnitude to strip trees of vegetation but not topple them. Farther from the volcano, the bulk density of the PDC body decreased from prolonged

sedimentation and the entrainment of air. This relatively less dense body has a dynamic pressure below the threshold needed to strip lee side trees, but still scorches them.

In section 4.1, it was concluded that stripped cluster geometry is not influenced by topographic relief; therefore, stripped clusters are most likely affected by a part of the PDC. This part, the PDC head, is assumed to not have taken a purely ballistic projectile path over stripped clusters. Instead, the head reattached to the ground sooner, affecting the size of the cluster. Gardner et al. (2018) said that a denser PDC reattaches sooner. Stripped patches are located closer to the volcano, where the density of the PDC is of larger magnitude.

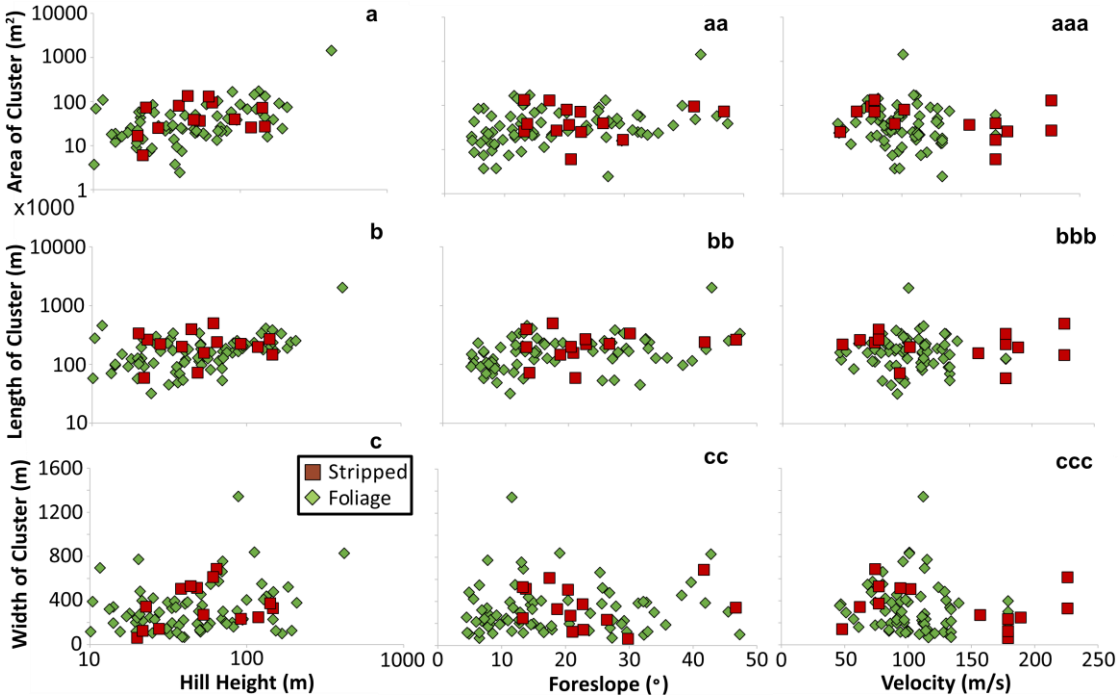

Figure 18a-c, 18aa-cc, 18aaa-ccc.18a-c) Plots comparing the height of a hill by the area of a cluster, length of a cluster, and width of a cluster. 18aa-cc) Plots comparing the foreslope of the hill by the area of the cluster, length of the cluster, and width of the cluster. 18aaa-ccc) Plots comparing the velocity of the PDC as it traveled past a cluster and the area of the cluster, length of the cluster, and width of the cluster.

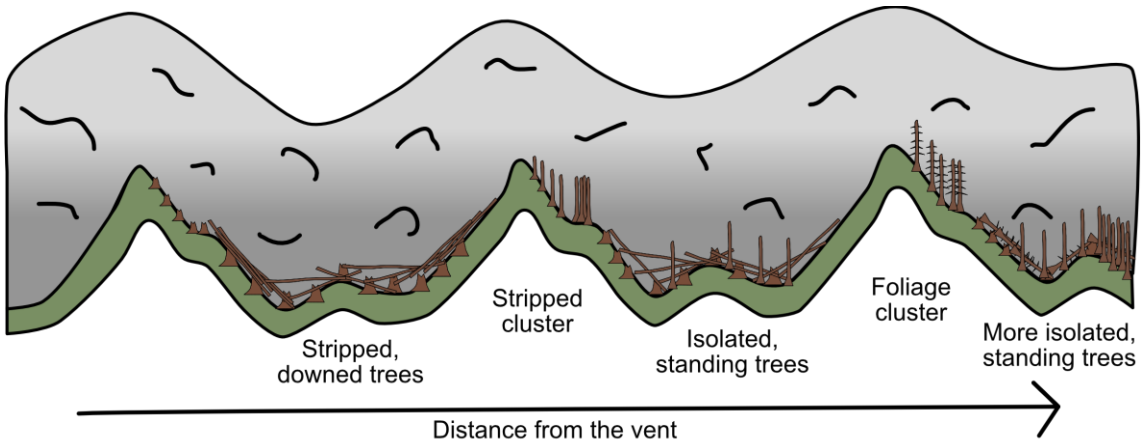

Figure 19. This topographic profile simplifies the terrain the PDC traversed from the vent to the edge of the blowdown zone to illustrate how tree damage evolved. Beginning at the left, the first hill shows no clusters and no isolated standing trees. Between the first and second hill are stripped, downed trees. The second hill contains stripped, standing clusters on its lee side. Between the second and third hill are isolated stripped standing trees and stripped fallen trees. The third hill contains standing, foliage clusters. Beyond the third hill are isolated stripped standing trees and downed trees with foliage.

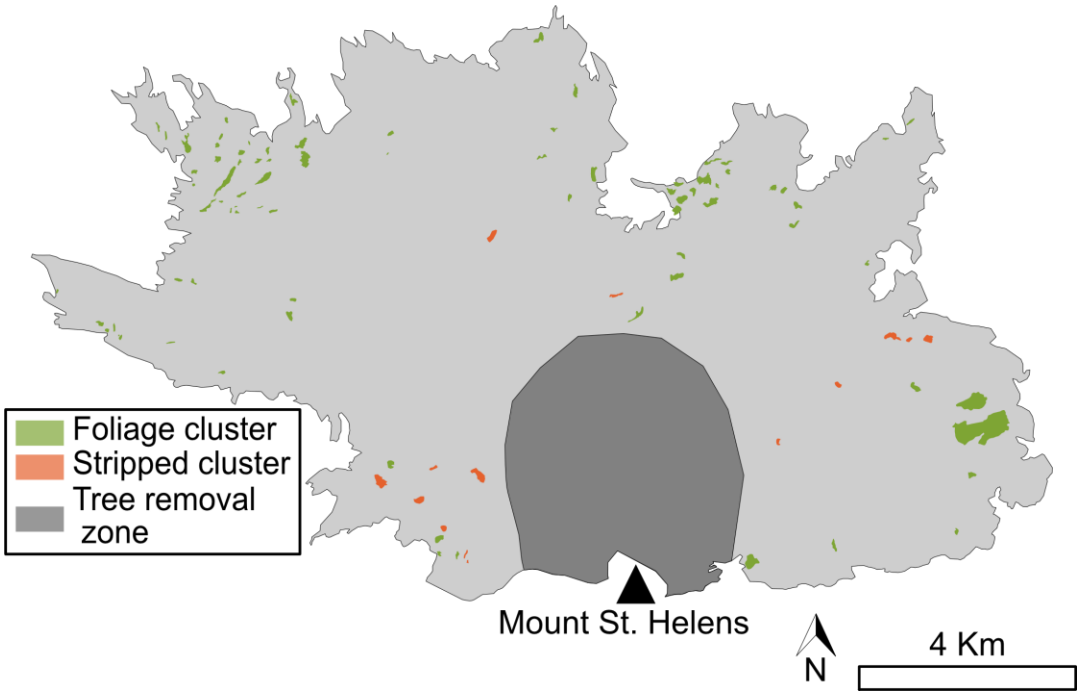

Figure 20. Map showing the tree removal zone, which is the area with no standing or fallen trees.

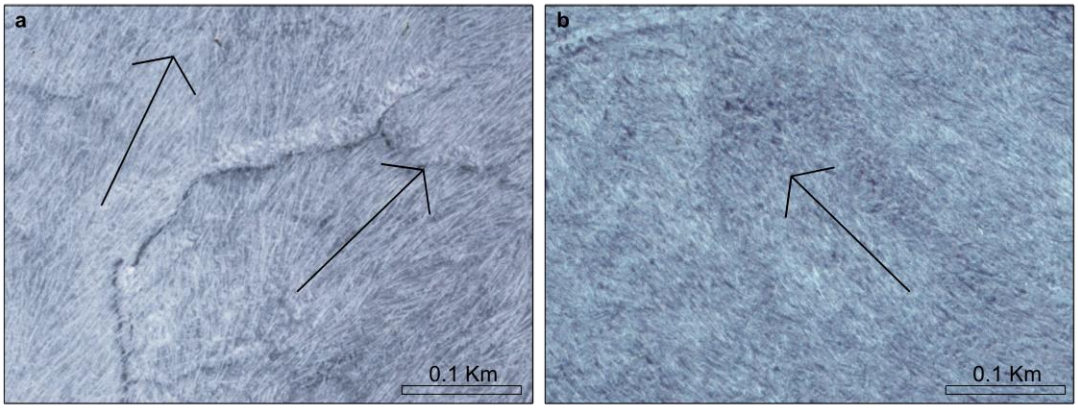

Figure 21a-b. Side by side comparison of downed trees. Black arrows point the main direction the PDC was traveling. a) Stripped, downed trees in the northeast zone. The trees appear distinctly linear. b) Downed trees with foliage in the northwest zone. The trees appear obscurely linear.

Quantifying dynamic pressure

ESTIMATE DYNAMIC PRESSURE FROM TREE GEOMETRY

The increasing number of isolated standing trees and the transition of stripped to foliage clusters argues that P_{dyn} decreased with distance. Following Clarke and Voight (2000), the P_{dyn} required to topple a tree of a given size by treating limbless trees as cylinders is given by:

$$P_{dyn} = \frac{\pi r^2 \sigma_{ult}}{4z^2 C_d} \quad (9)$$

where z and r are tree height and radius, σ_{ult} is maximum stress at the height of failure, and C_d is the aerodynamic drag coefficient. Maximum stress at the height of failure, σ_{ult}, is assumed to be 63,800 ± 800 kPa, which is the average tensile strength of Douglas Fir and Western Hemlock trees (Iangum et al., 2009). C_d is assumed to be 1.1 (Rae and Pope, 1984; Anderson, 1991; Panton, 1996; Clarke & Voight, 2000). Radius can be inferred from the study by McPherson et al. (2016), who collected urban tree growth data from 1998 to 2012 across the United States (https://www.fs.usda.gov/rds/archive/catalog/RDS-2016-0005). 14,000+ trees and 171 different species were measured, from which a relationship between tree radius and tree height can be inferred (Figure 22). This relationship is used to determine tree diameters from heights estimated from the shadow analysis for trees with shadows longer than 10 meters.

The principal errors on dynamic pressures calculated from equation 9 and Figure 22 are the ± 5 m error on shadow-derived tree heights and a ± 800 kPa error for σ_{ult}. Substituting minimum and maximum tree heights into equation 9 by subtracting and

adding 5 m to shadow-derived heights and 800 kPa to σ_{ult} produces a dynamic pressure variation of ± 0.3 kPa. Similarly, substituting ± 0.4 m for downed trees whose height were directly measured and ± 800 kPa for σ_{ult} also produces a dynamic pressure variation of ± 0.3 kPa.

DYNAMIC PRESSURE RESULTS

Two different datasets of dynamic pressure were derived from tree heights greater than 10 m (Figure 23a-d). The first dataset estimates dynamic pressures that toppled trees of a given size, as estimated from downed tree lengths that were measured directly in aerial photos. These dynamic pressure values are minimum values for the PDC because these trees are toppled. These data do not show an overall trend of dynamic pressure with distance in any of the zones around the volcano (Figure 23a-d). When compared to dynamic pressures of standing trees, however, the dynamic pressures that topple trees concentrate at lower values. The dynamic pressure that toppled trees in the east and northeast zones have medians of 13 ± 0.3 kPa, whereas the dynamic pressure of standing trees in the east and northeast zones have medians of 18 ± 0.3 kPa and 16 ± 0.3 kPa, respectively (Figure 23c, 23d). The median dynamic pressures that toppled trees in the north and west zones are within the range of the median dynamic pressure of standing trees (Figure 23a, 23b). The dynamic pressures in this dataset constrain the lower bound for the dynamic pressure of the PDC.

The second dataset estimates maximum dynamic pressures from standing trees (Figure 23a-d). These dynamic pressure values are maximum values for the PDC because

these trees are still standing. The maximum dynamic pressures of standing trees decreased in the last 10% of the distance traveled by the PDC from 10 ± 0.3 kPa to 7 ± 0.3 kPa in the west zone (Figure 23a), from 12 ± 0.3 kPa to 7 ± 0.3 kPa in the east zone (Figure 23d), and from 10 ± 0.3 kPa to 7 ± 0.3 kPa in the northeast zone (Figure 23c). In the north zone, the maximum dynamic pressures of standing trees stayed roughly the same at 12 ± 0.3 kPa in the last 20% of the distance traveled by the PDC (Figure 23b). Therefore, the dynamic pressures in this dataset constrain the upper bound for the dynamic pressure of the PDC.

Calculated maximum dynamic pressures of the isolated, standing trees along flow paths (i.e. pressures that were not reached or exceeded) were contoured to create a maximum dynamic pressure map of the distal area of the blowdown zone (Figure 24). The dynamic pressure of isolated, standing trees decreased from 35 ± 0.3 kPa in the last 30% of the distance traveled by the PDC to around 15 ± 0.3 kPa near the edge of the blowdown zone.

The dynamic pressures that impacted isolated, standing trees represent the values in the PDC head, whereas the dynamic pressures that impacted standing tree clusters represent the values in the PDC body. Median dynamic pressure of trees in clusters were compared to the nearest maximum pressure contour from Figure 24. The median dynamic pressure of trees in clusters were in every instance less than the dynamic pressure of the nearby contour (Table 7), and were, on average, 12 kPa ± 0.3 lower than the maximum dynamic pressures estimated from isolated, standing trees.

COMPARISON WITH OTHER STUDIES

Clarke and Voight (2000) estimated that the dynamic pressure in the Mount St. Helens blowdown zone 8 km northeast of the vent that toppled a 15 m tall, 50 cm-radius tree was 40 kPa. The tree was downed, indicating their estimate was a minimum. The maximum dynamic pressure estimated from our standing tree height data in the northeast zone was 34 ± 2.6 kPa at 16 km away from the volcano, suggesting that the dynamic pressure of the PDC dropped from 40+ kPa to below 34 kPa within 8 km.

Some isolated standing trees are within the area of the three-dimensionally modeled dynamic pressure map of Esposti Ongaro et al. (2011). The maximum dynamic pressure calculated ranges from 8-34 kPa, which is within the 0-35 kPa interval on their 3-D map. As demonstrated by this study, trees are damaged to the edge of the blowdown zone, yet the dynamic pressures of Esposti Ongaro et al. (2011) decrease to 0 kPa significantly before that. Dynamic pressure in Esposti Ongaro et al. (2011) is speculated to decrease to zero because modeled the speed and dynamic pressure of the PDC dropped to 0 m/s at the blowdown zone edge. It is also worth noting that the velocities derived in this study from the isochrons of the mapped PDC front (Moore and Rice, 1984) do not appear to diminish near the edge of the blowdown zone. Additionally, Gardner et al. (2017) demonstrated that the PDC did not stop at the end of the blowdown zone.

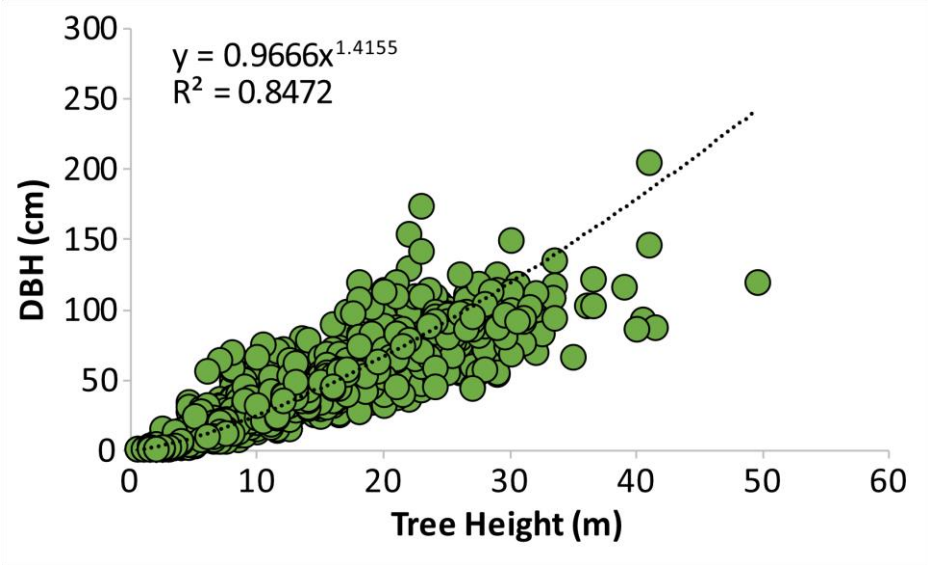

Figure 22. y is the best fit line equation for the relationship between tree height and the diameter of a tree at breast height (DBH). Dividing the DBH by 2 and then by 100 yields the tree radius in meters. Data from McPherson et al. (2016), for trees from Washington state.

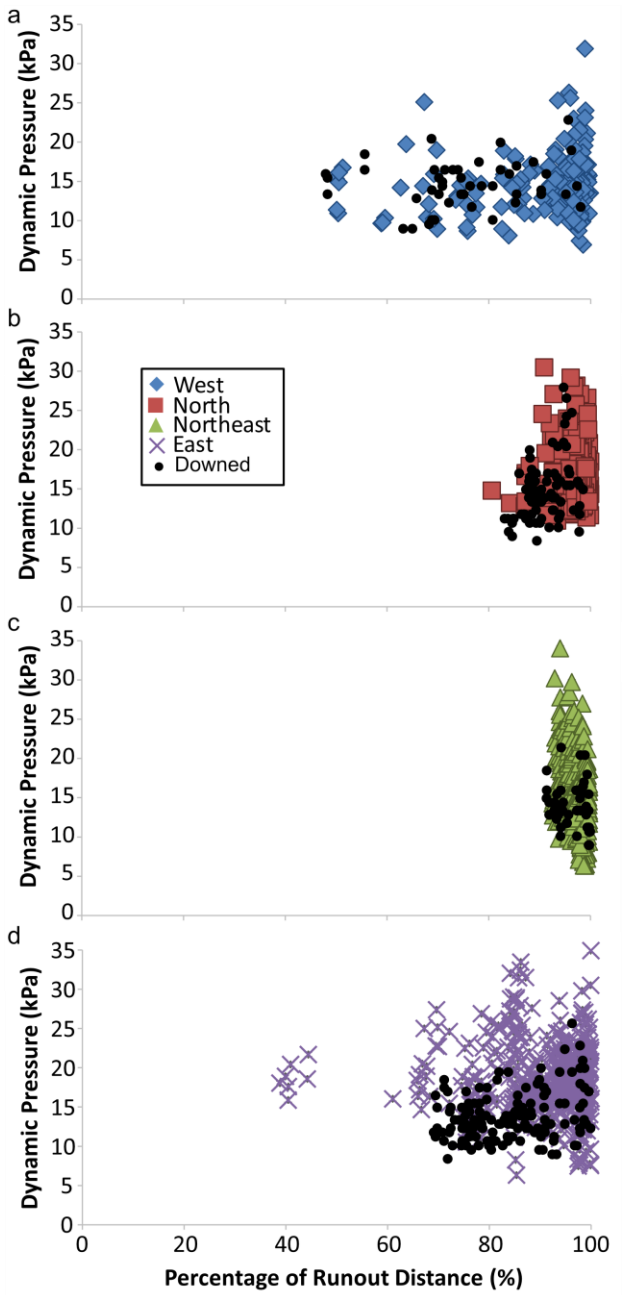

Figure 23a-d. The diamond, square, triangle, and x symbols show the dynamic pressure needed to topple isolated standing trees based on tree height, tree radius, failure stress, and aerodynamic drag coefficient (see equation 7) in separate zones around the volcano. These are estimated maximum pressures because these trees remained standing. Black circles show the dynamic pressure that toppled measured downed trees, and are thus minimum dynamic pressures within the PDC.

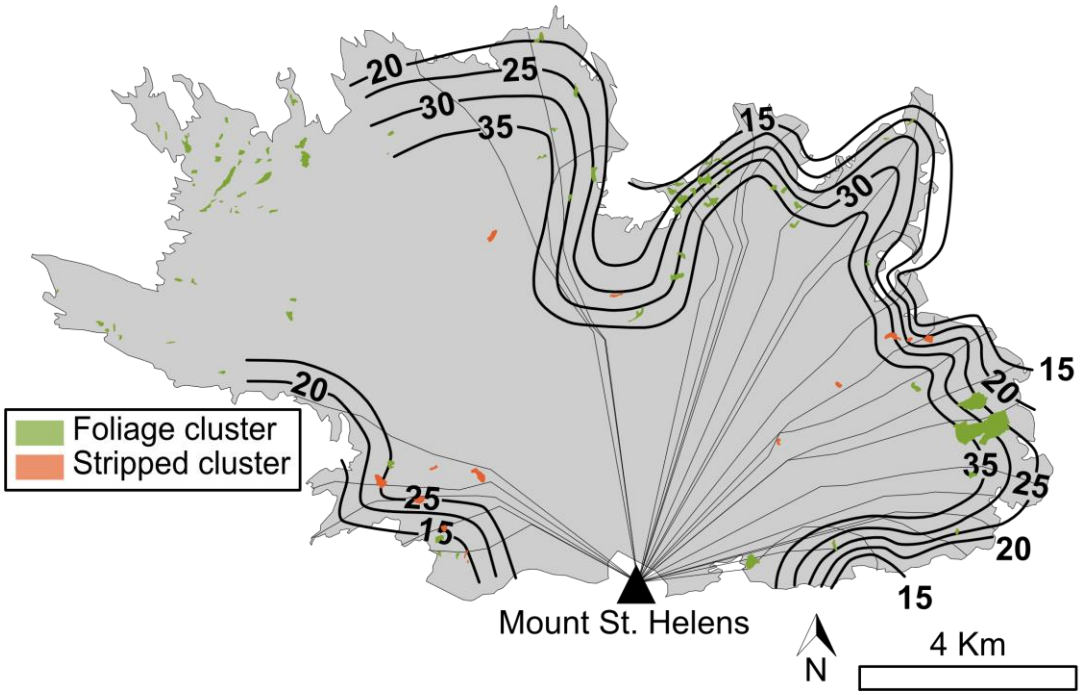

Figure 24. Map of contoured maximum dynamic pressures within the blowdown zone (gray area). Black contours show maximum dynamic pressures (kPa), those needed to topple an isolated, standing tree of a certain size, pressures that were not reached or exceeded. The northwest area is missing contours because of the lack of isolated, standing trees. Tree clusters overlie the contours. The thin black lines are the flow paths where isolated tree height and density analysis were made.

Table 7. Comparing the dynamic pressure needed to topple trees in clusters to the nearby contour of dynamic pressure that is needed to topple isolated, standing trees.

Cluster	Median P_{dyn} of Cluster ± 0.3 (kPa)	P_{dyn} Contour ± 0.3 (kPa)
135	8	15
134	13	15
97	10	15
131	11	15
139	10	25
129	10	25+
137	12	25
130	15	25+
138	10	25
104	25	35+
32	17	20
125	10	25
79	10	35
78	14	25
127	10	30
128	16	25
60	12	32
29	11	30
28	11	30
71	8	22
70	10	17
87	22	17
123	25	23
65	13	35
120	16	32
121	13	32
124	18	35+
119	14	23
22	11	20
118	12	30
117	17	24
116	16	21
3	17	27
75	15	30
61	16	35+
57	11	35+

Conclusions

A standing tree cluster is created when the PDC head follows a ballistic trajectory path over top of trees. The PDC body continues to hug topography, scorches everything, yet its dynamic pressure is not high enough to topple trees. The difference between stripped and foliage clusters depends on the dynamic pressure of the PDC body. Because stripped clusters are located closer to the volcano, the PDC is relatively denser, therefore has higher dynamic pressure. This dynamic pressure is high enough to strip trees of vegetation. Further away from the volcano, the dynamic pressure drops below the threshold to strip trees.

While the primary formation of tree clusters entails that the PDC head follows a ballistic trajectory path, stripped clusters are altered by a secondary effect. Because the PDC at the locations of stripped clusters is likely denser, the reattachment of the PDC head is hastened, resulting in modification of the stripped clusters geometries.

Tree damage as a function of distance from the volcano reflects the impact of dynamic pressure. Downed trees with foliage were impacted by lower dynamic pressures than stripped, downed trees and occur farther from the volcano. The increasing number of stripped, isolated standing trees with distance from the volcano indicates a decline in dynamic pressure. Standing tree clusters are affected by lower dynamic pressures than isolated, standing trees. Isolated, standing trees provide insight to overall variation of dynamic pressure whereas clusters show local variations.

The dynamic pressure of a tree can be estimated using tree height and radius, the maximum stress at the height of failure, and the drag coefficient. Dynamic pressures

estimated for fallen trees and standing trees constrain a minimum and maximum for the dynamic pressure of the impacting PDC. The contour map of maximum dynamic pressures demonstrated that values decreased from 35 kPa to 15 kPa in the distal area of the blowdown zone. The median dynamic pressures of trees in clusters were 12 kPa lower, on average, than the closest contour value. Tree damage can be used to qualitatively and quantitatively describe the evolution of dynamic pressure within the 1980 Mount St. Helens PDC.

Appendix

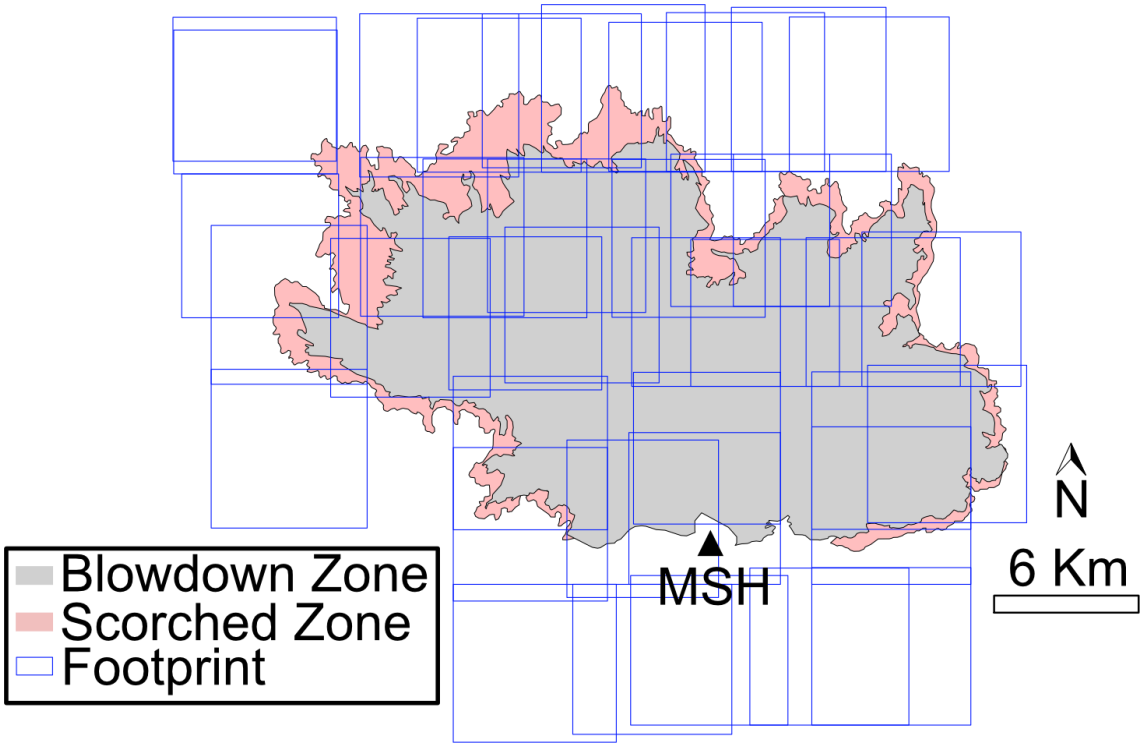

Figure 25. Blowdown and scorched zone with footprints of all aerial photos used in this study on top. MSH is Mount St. Helens.

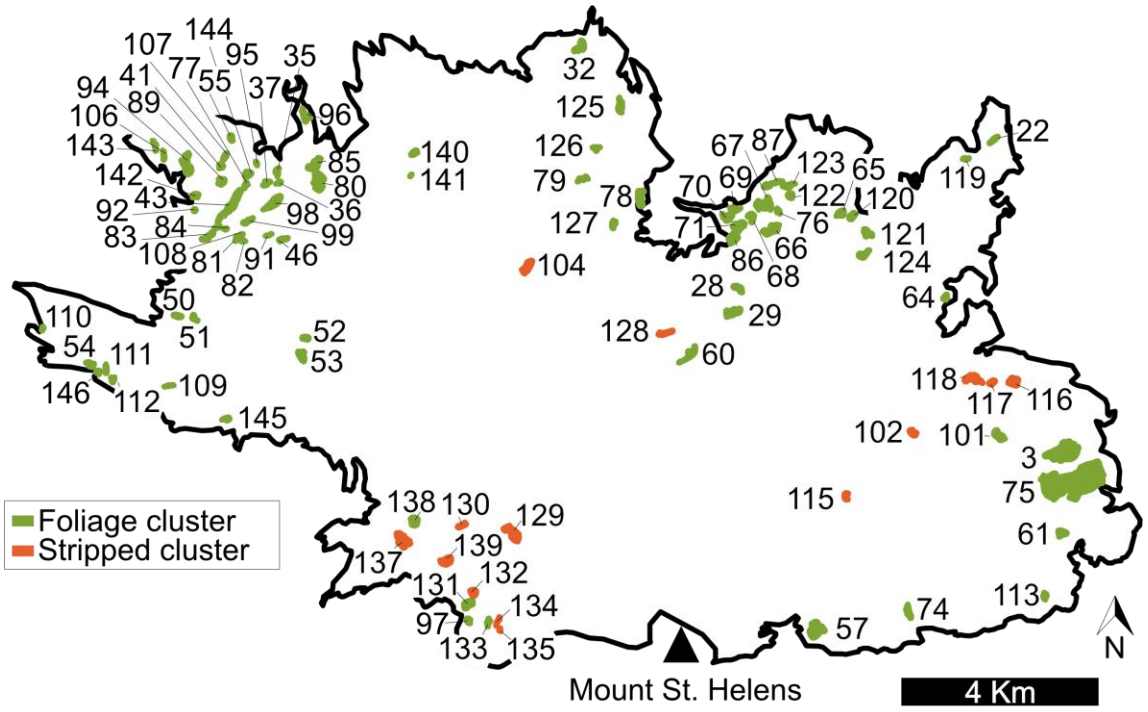

Figure 26. Numbered clusters.

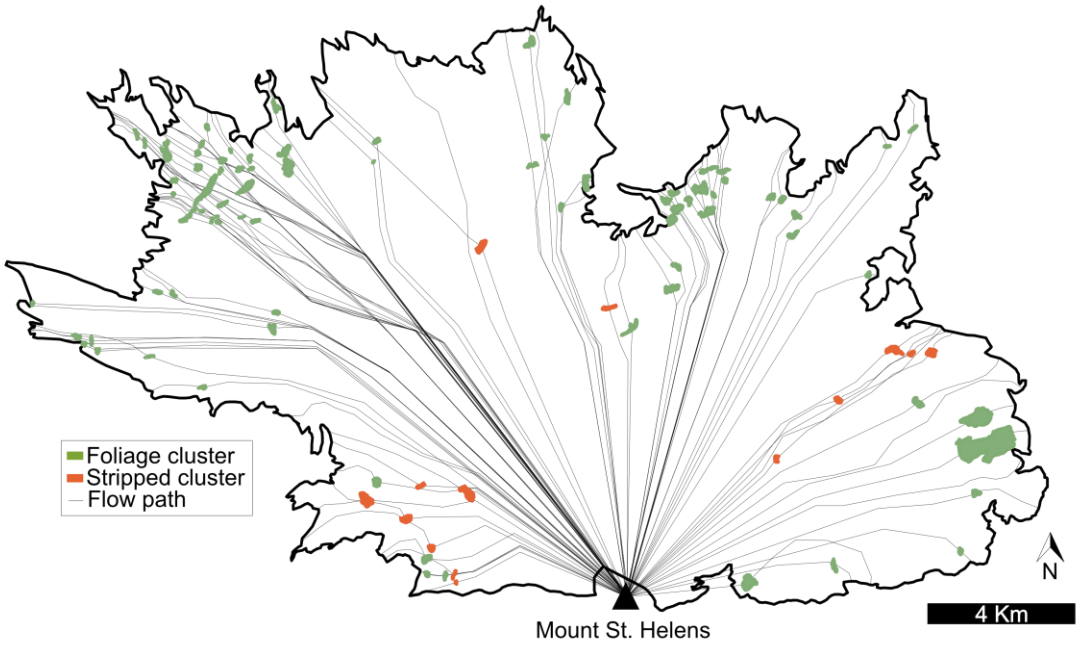

Figure 27. Map of clusters and the corresponding paths the PDC traveled to and from these clusters.

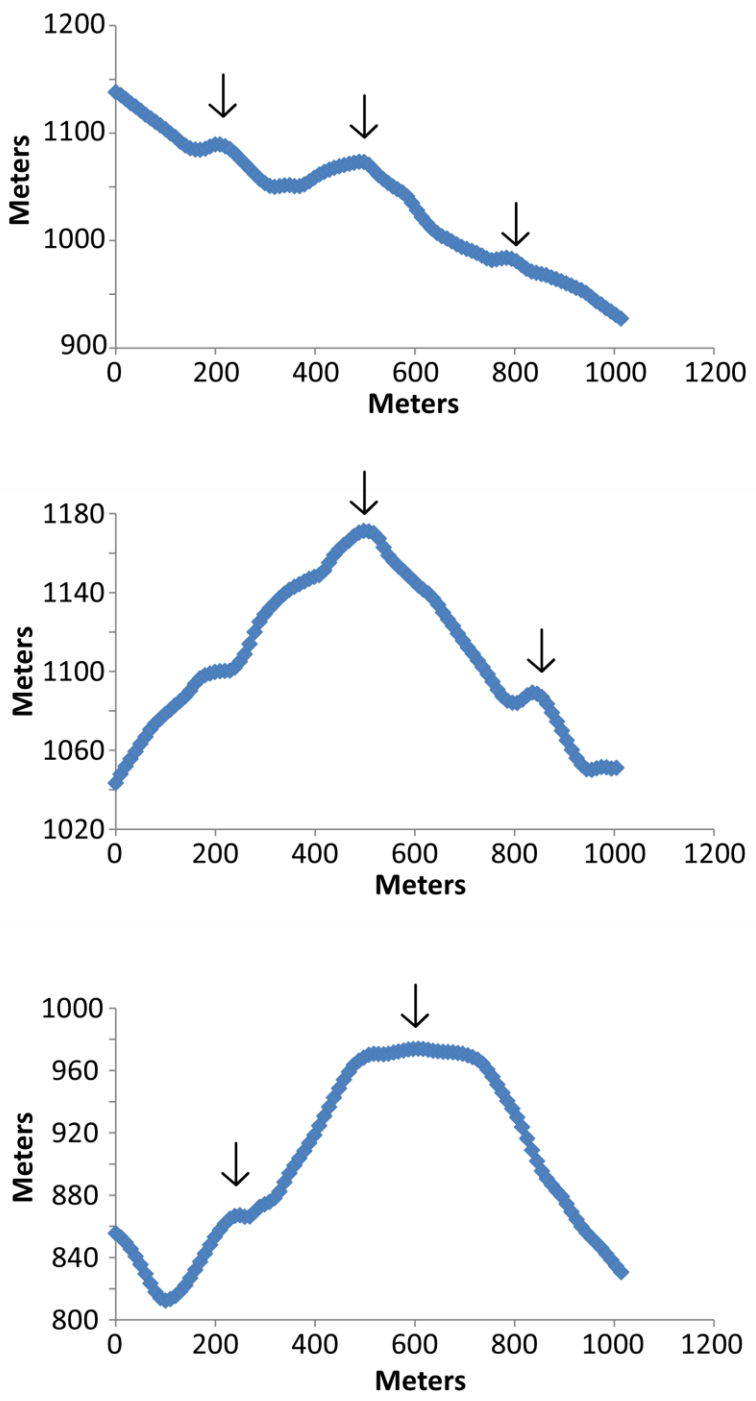

Figure *28*. Topography profiles of the transecting hills of Cluster 3. Hills are denoted with a black arrow.

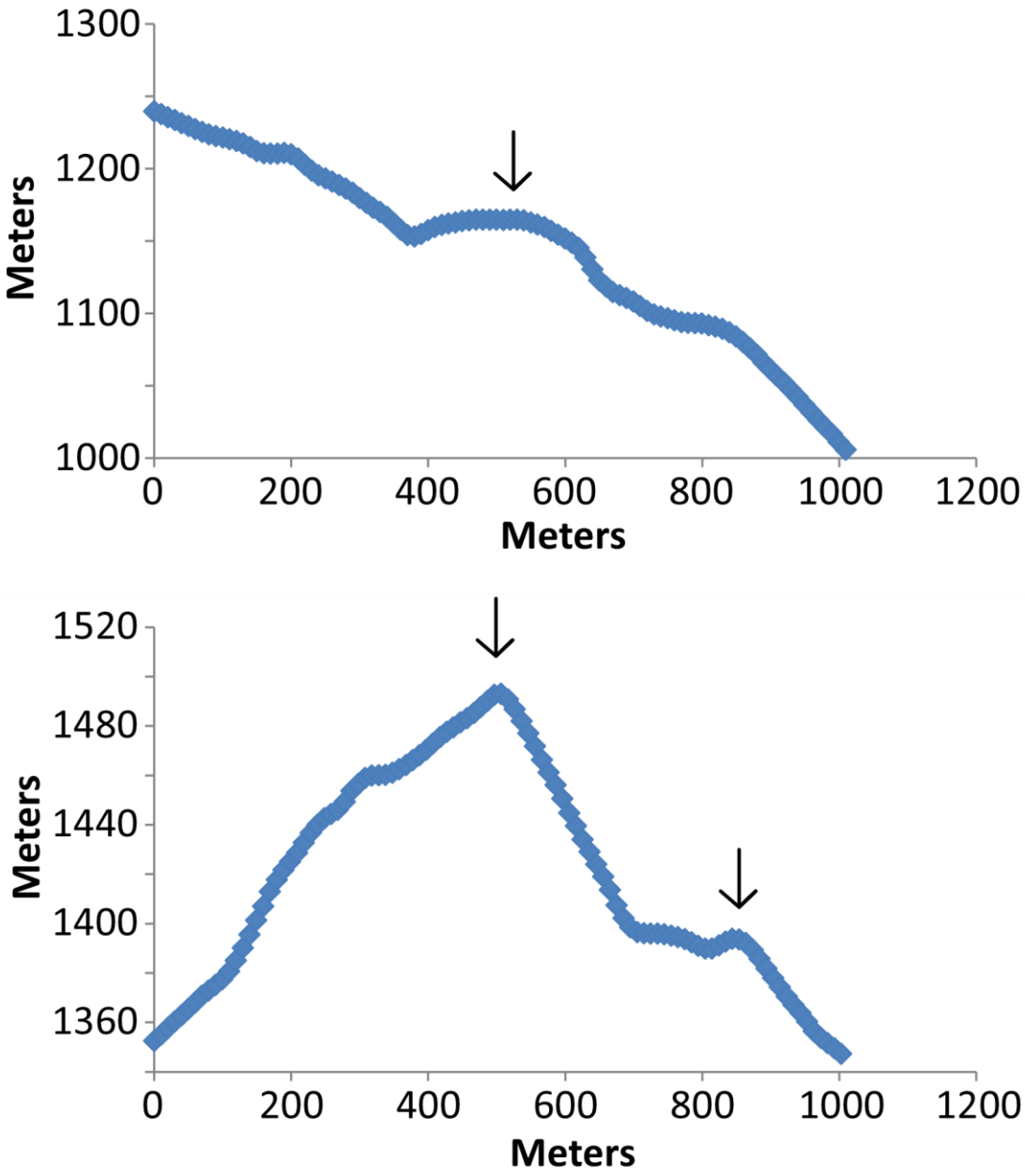

Figure *29*. Topography profiles of the transecting hills of Cluster 22. Hills are denoted with a black arrow.

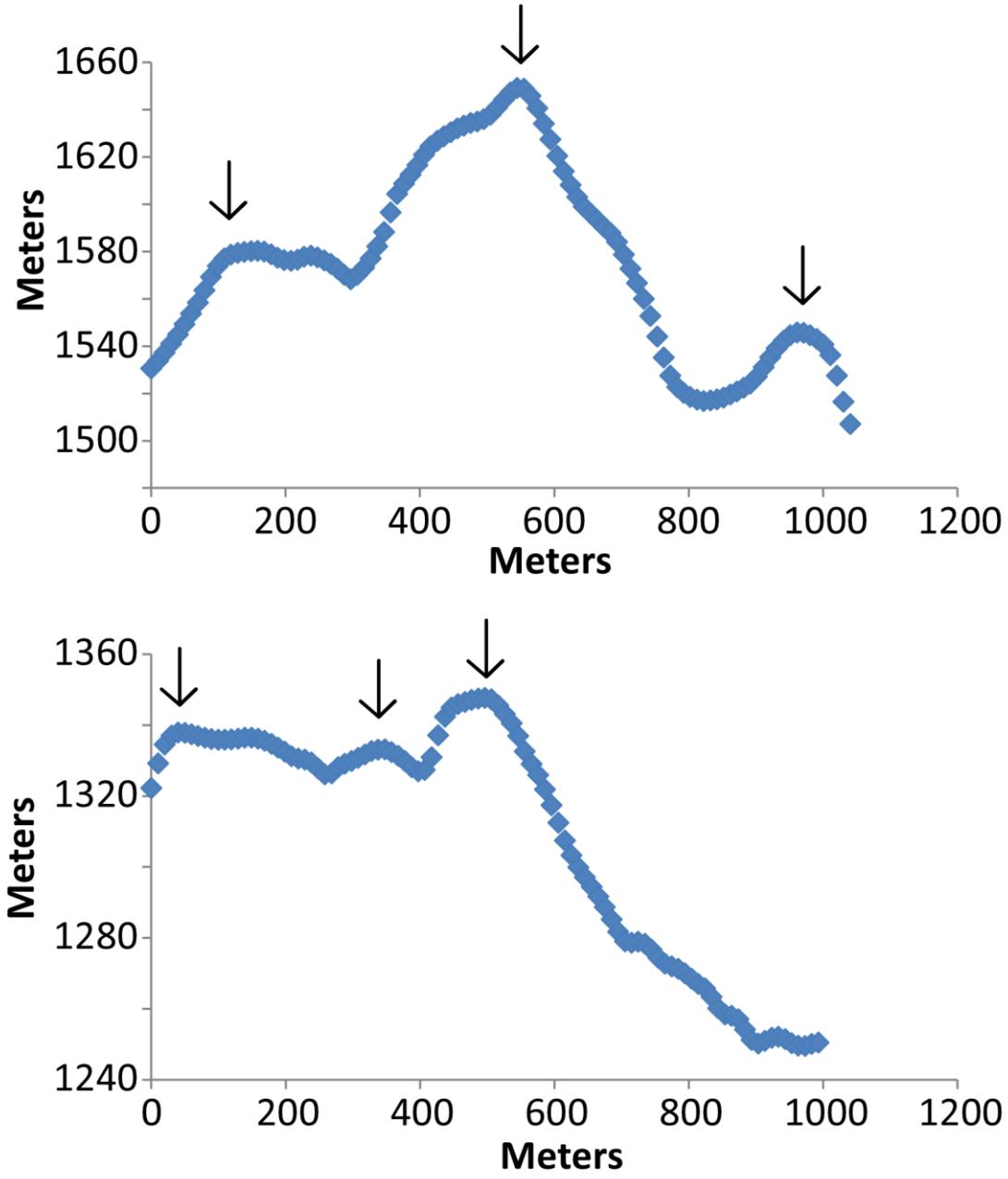

Figure *30*. Topography profiles of the transecting hills of Cluster 28. Hills are denoted with a black arrow.

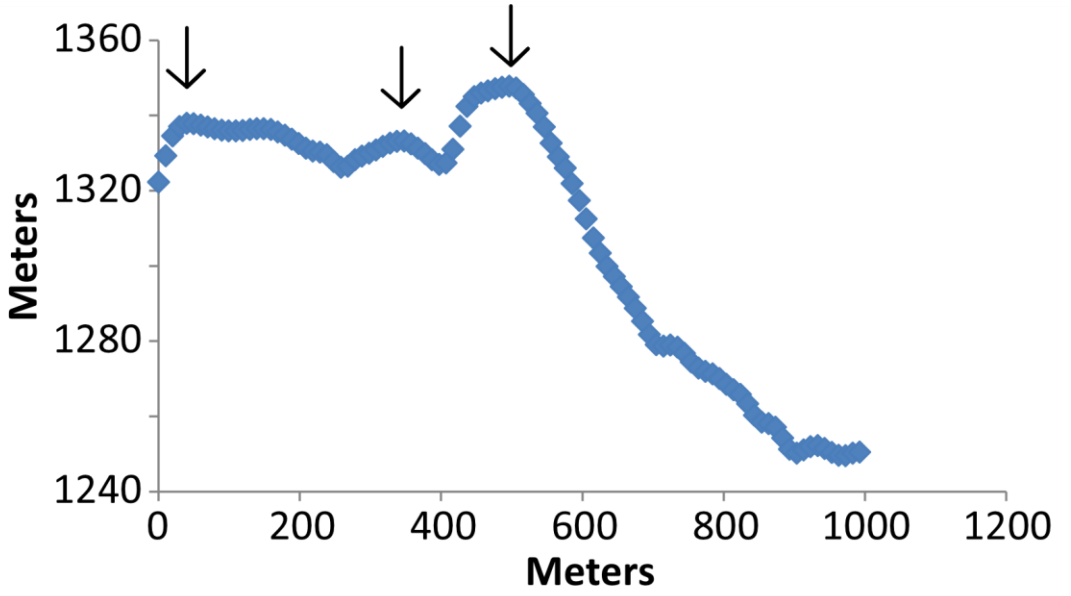

Figure *31*. Topography profiles of the transecting hills of Cluster 29. Hills are denoted with a black arrow.

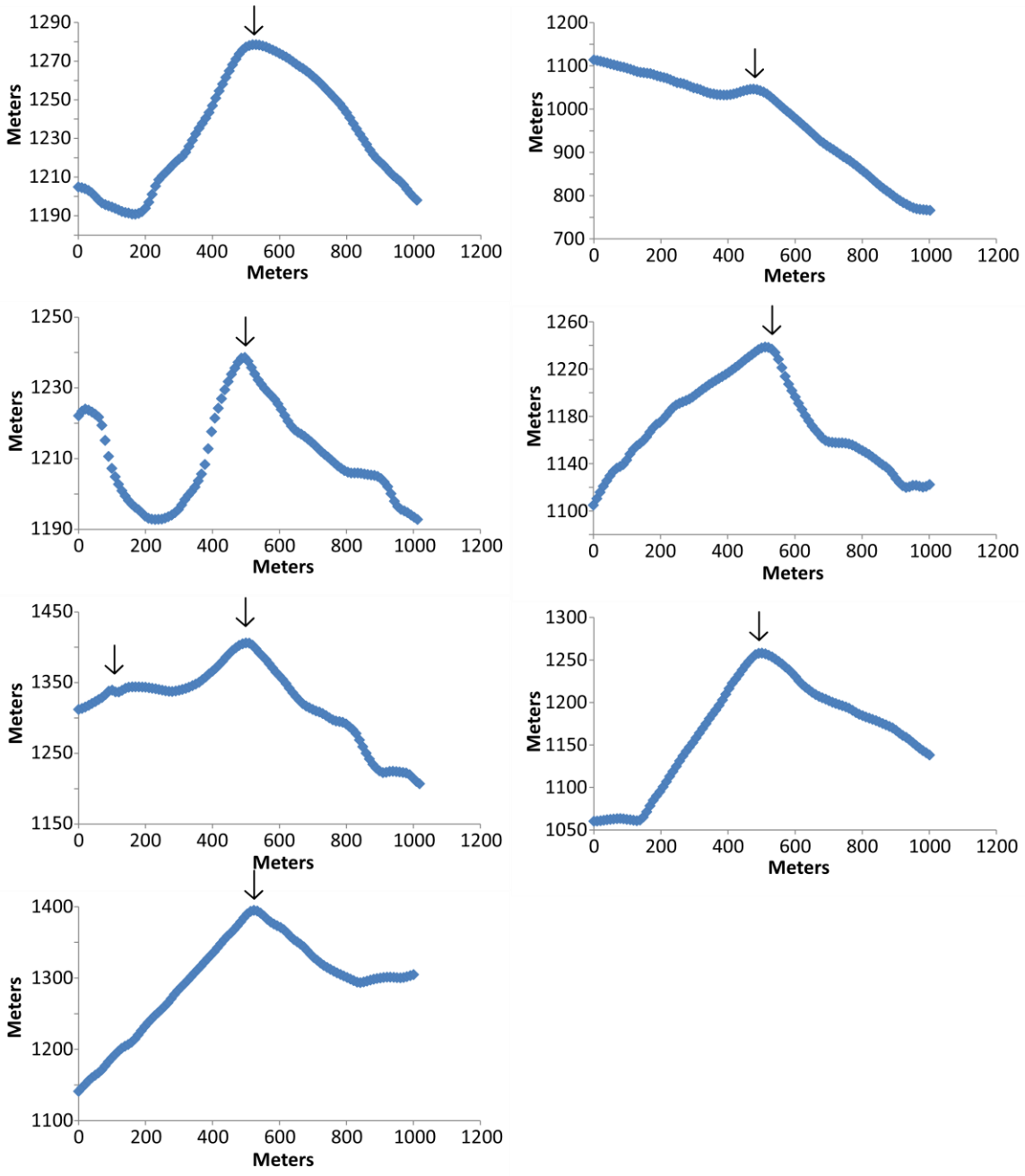

Figure *32*. Topography profiles of the transecting hills of Cluster 32. Hills are denoted with a black arrow.

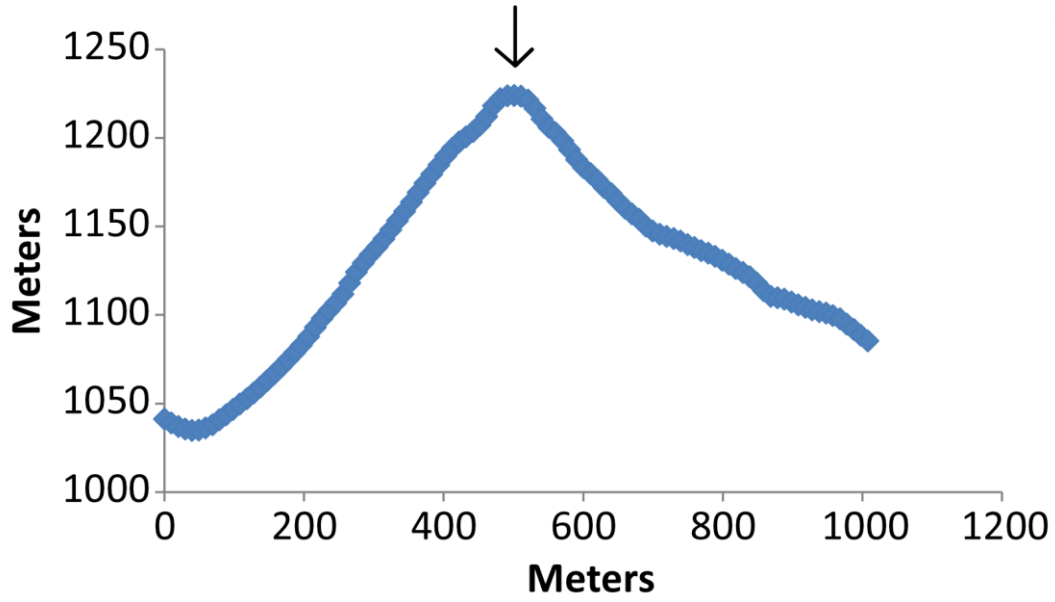

Figure *33*. Topography profiles of the transecting hills of Cluster 35. Hills are denoted with a black arrow.

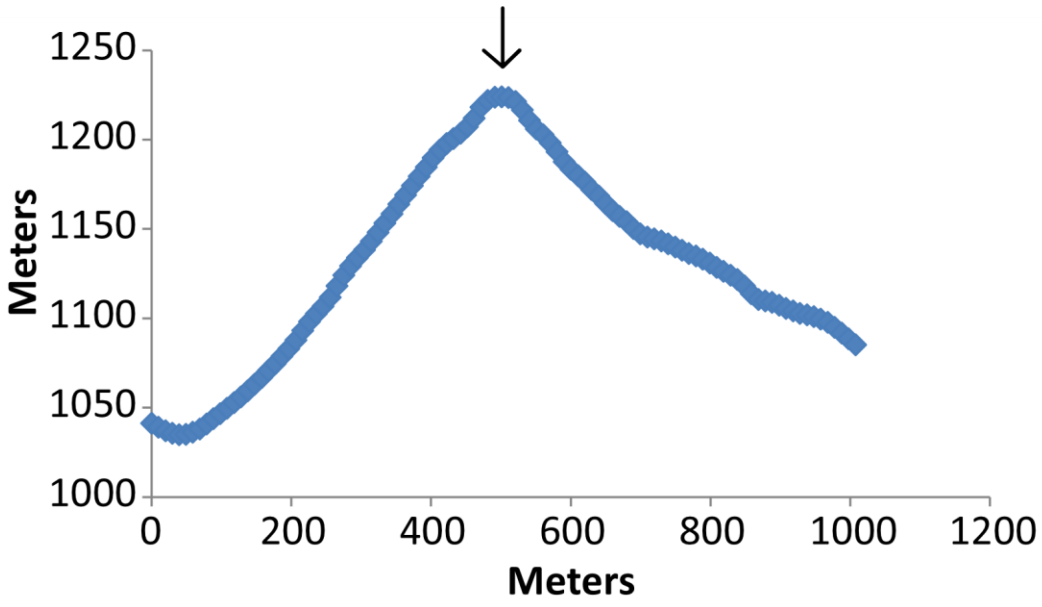

Figure *34*. Topography profiles of the transecting hills of Cluster 36. Hills are denoted with a black arrow.

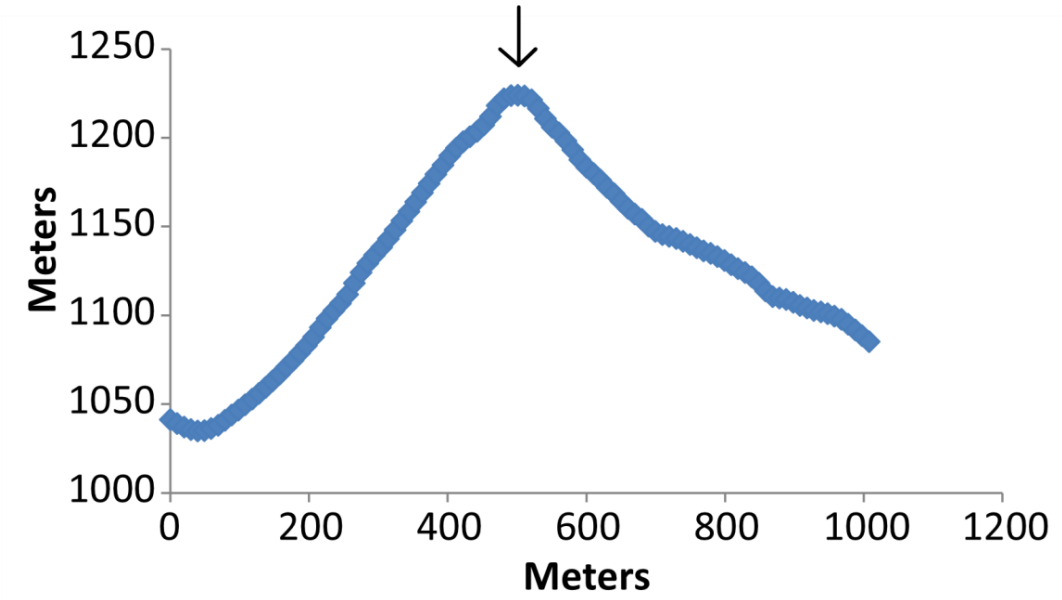

Figure *35*. Topography profiles of the transecting hills of Cluster 37. Hills are denoted with a black arrow.

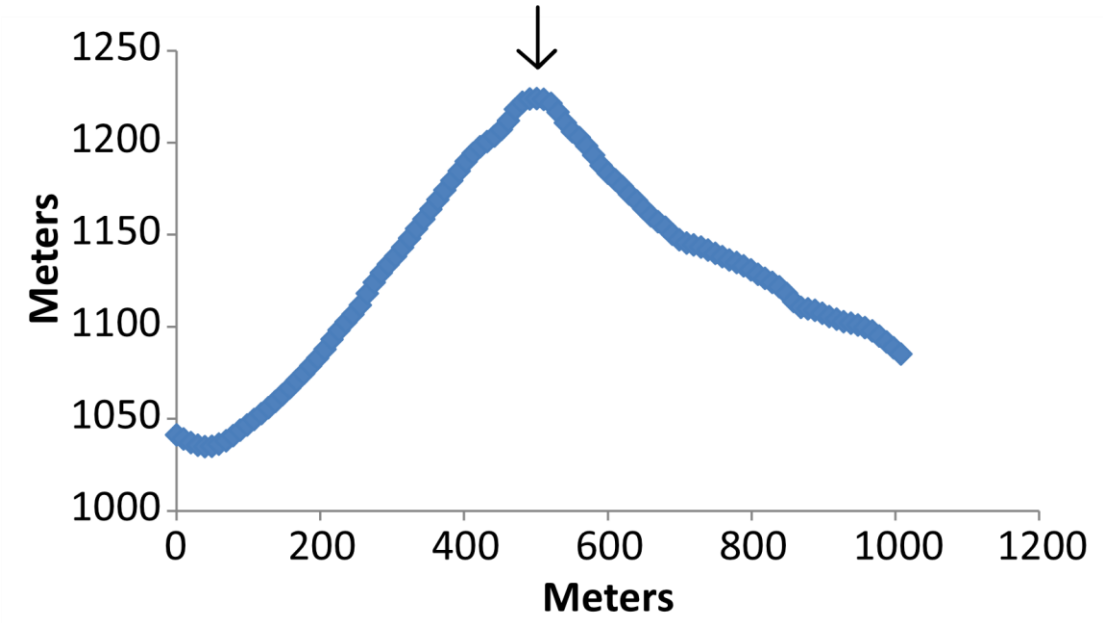

Figure *36*. Topography profiles of the transecting hills of Cluster 41. Hills are denoted with a black arrow.

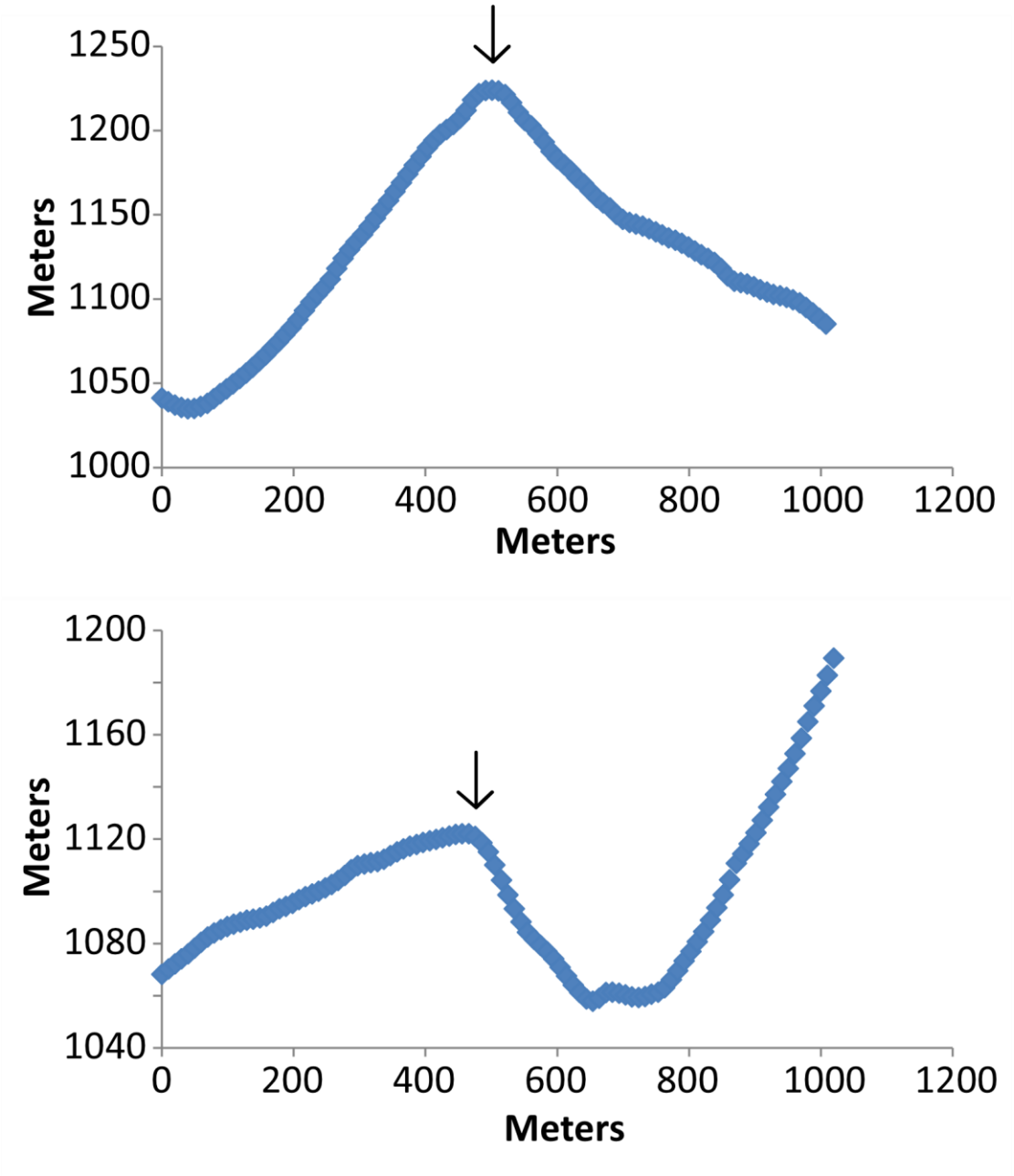

Figure *37*. Topography profiles of the transecting hills of Cluster 43. Hills are denoted with a black arrow.

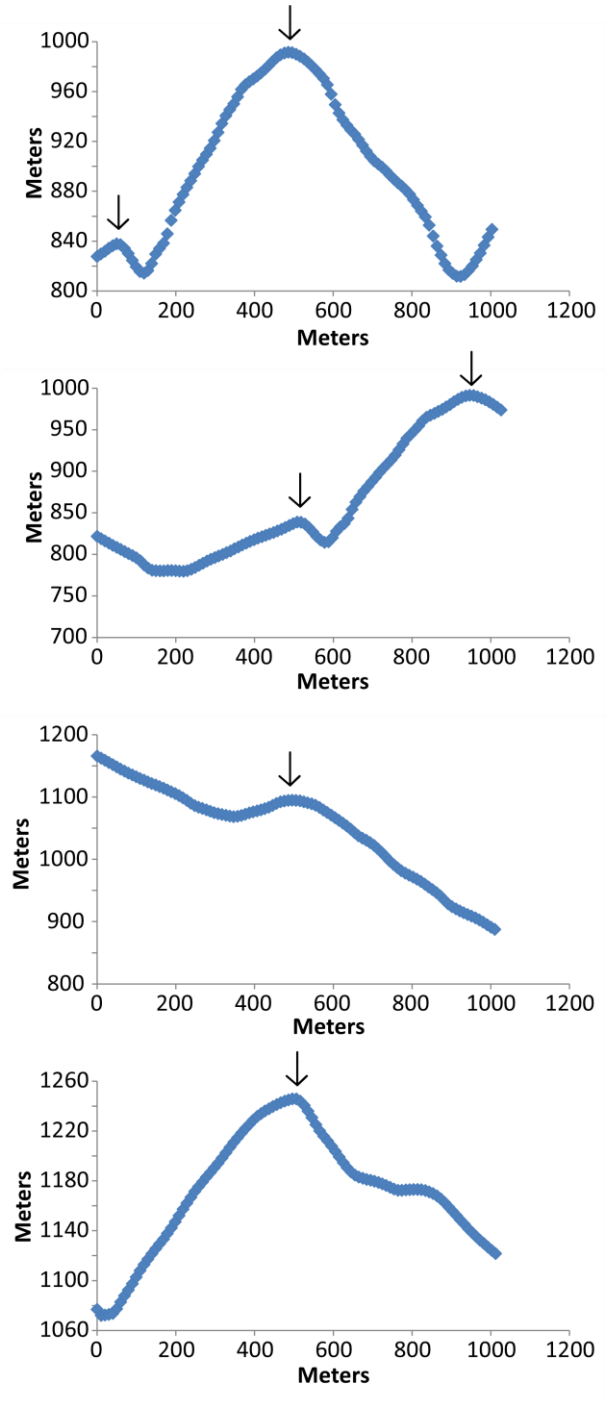

Figure *38*. Topography profiles of the transecting hills of Cluster 46. Hills are denoted with a black arrow.

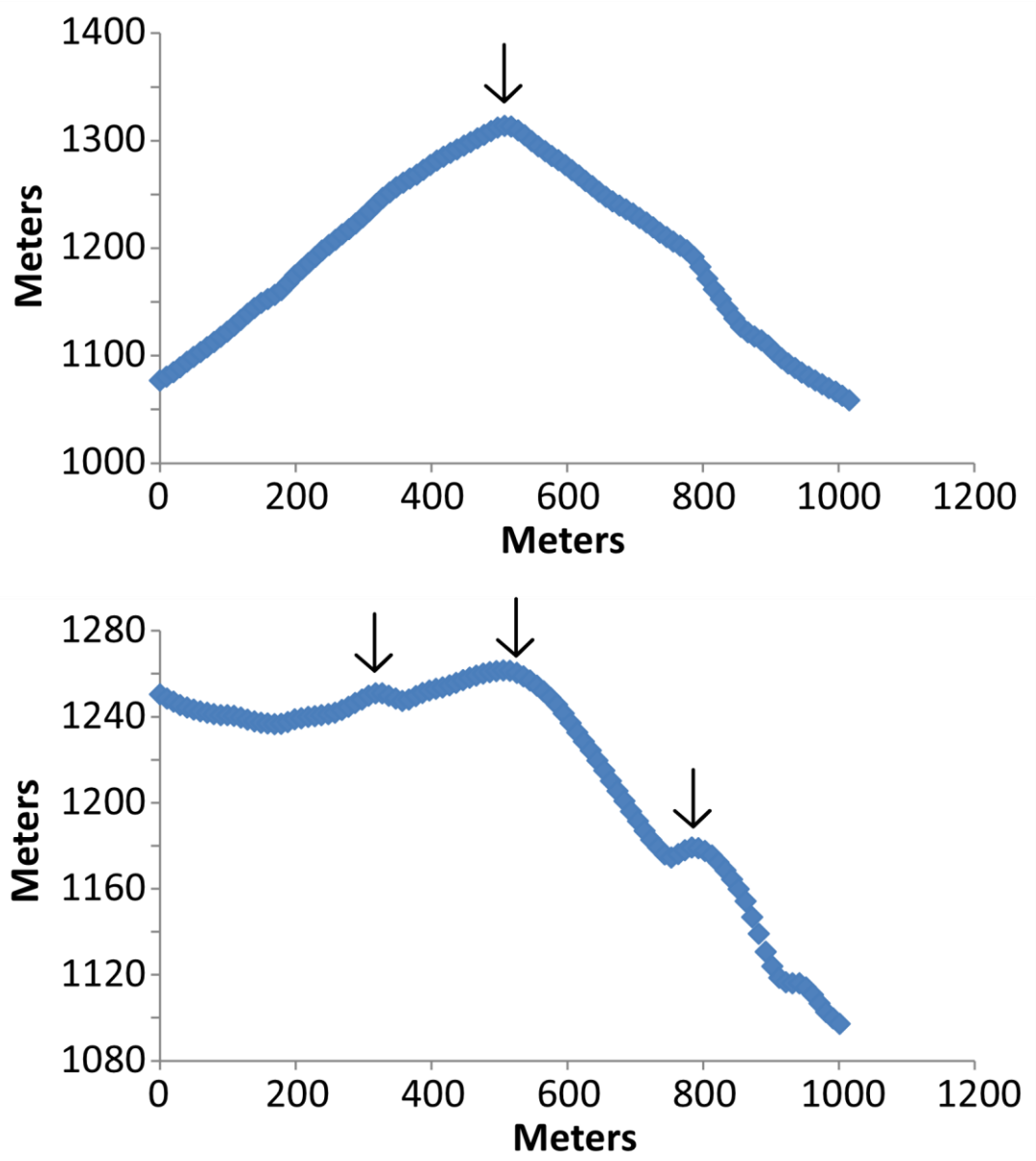

Figure *39*. Topography profiles of the transecting hills of Cluster 50. Hills are denoted with a black arrow.

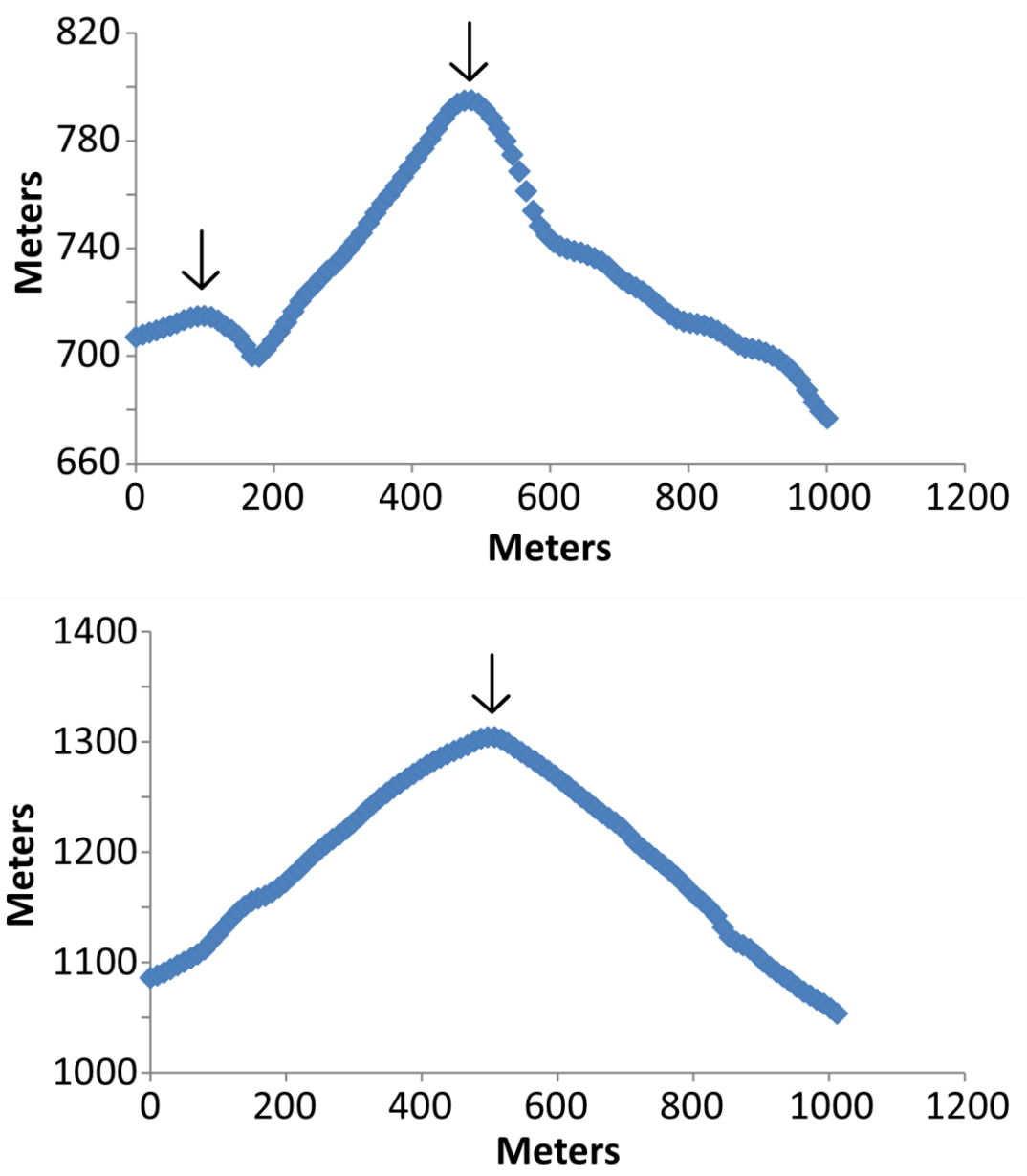

Figure *40*. Topography profiles of the transecting hills of Cluster 51. Hills are denoted with a black arrow.

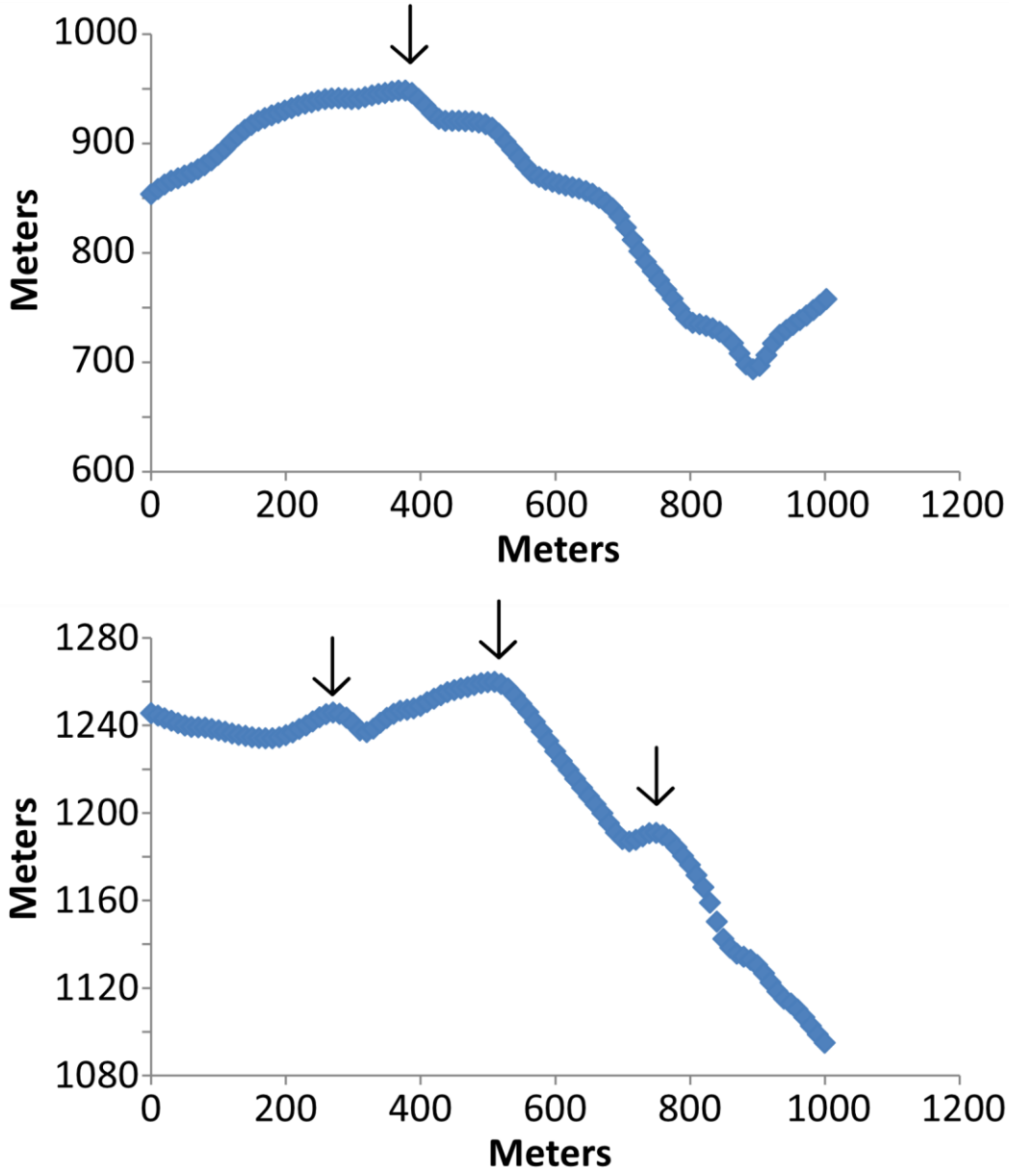

Figure *41*. Topography profiles of the transecting hills of Cluster 52. Hills are denoted with a black arrow.

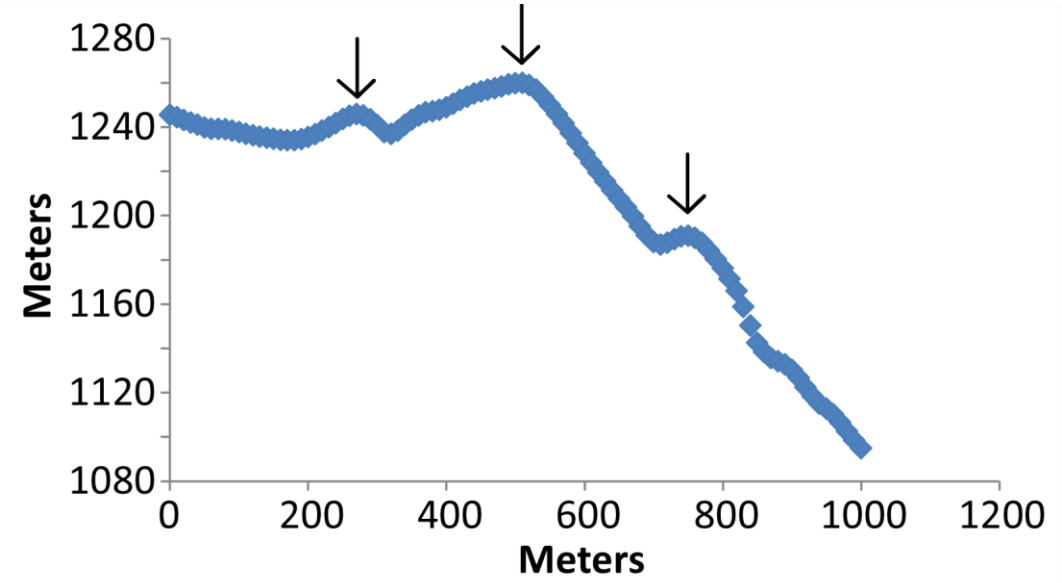

Figure *42*. Topography profiles of the transecting hills of Cluster 53. Hills are denoted with a black arrow.

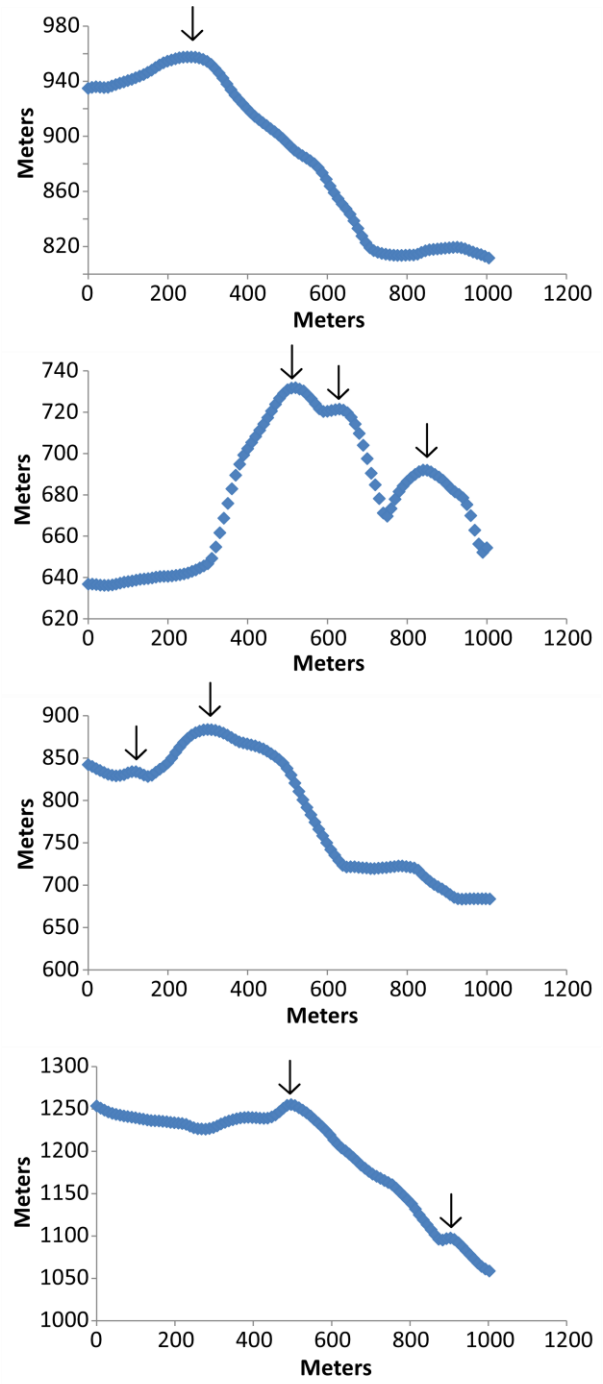

Figure *43*. Topography profiles of the transecting hills of Cluster 54. Hills are denoted with a black arrow.

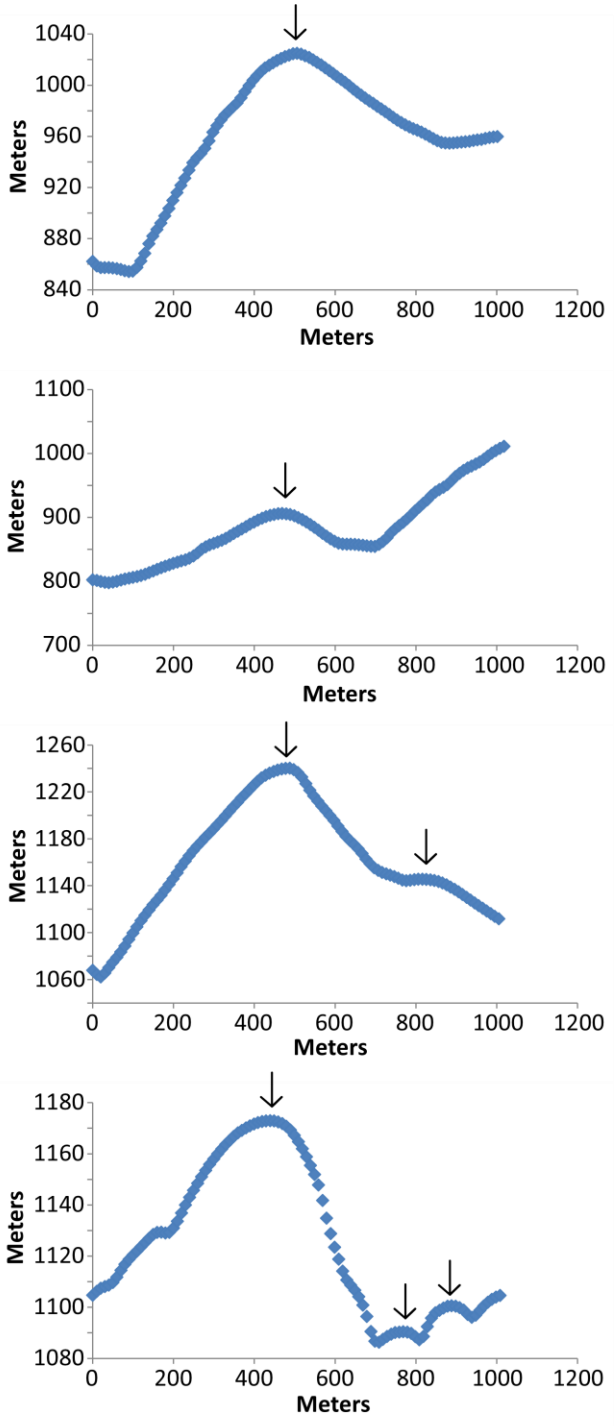

Figure *44*. Topography profiles of the transecting hills of Cluster 55. Hills are denoted with a black arrow.

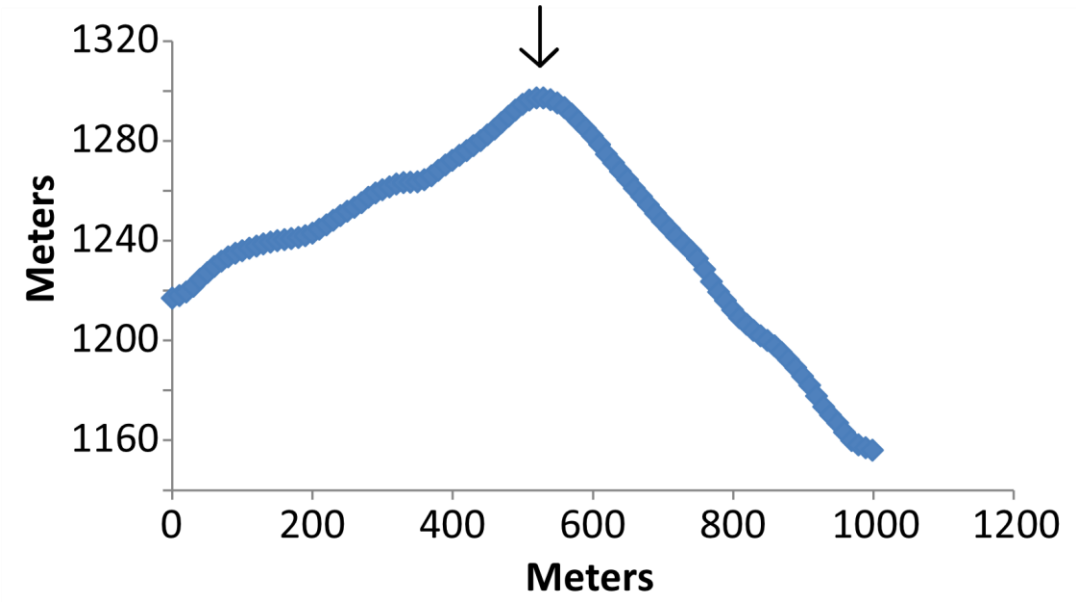

Figure *45*. Topography profiles of the transecting hills of Cluster 60. Hills are denoted with a black arrow.

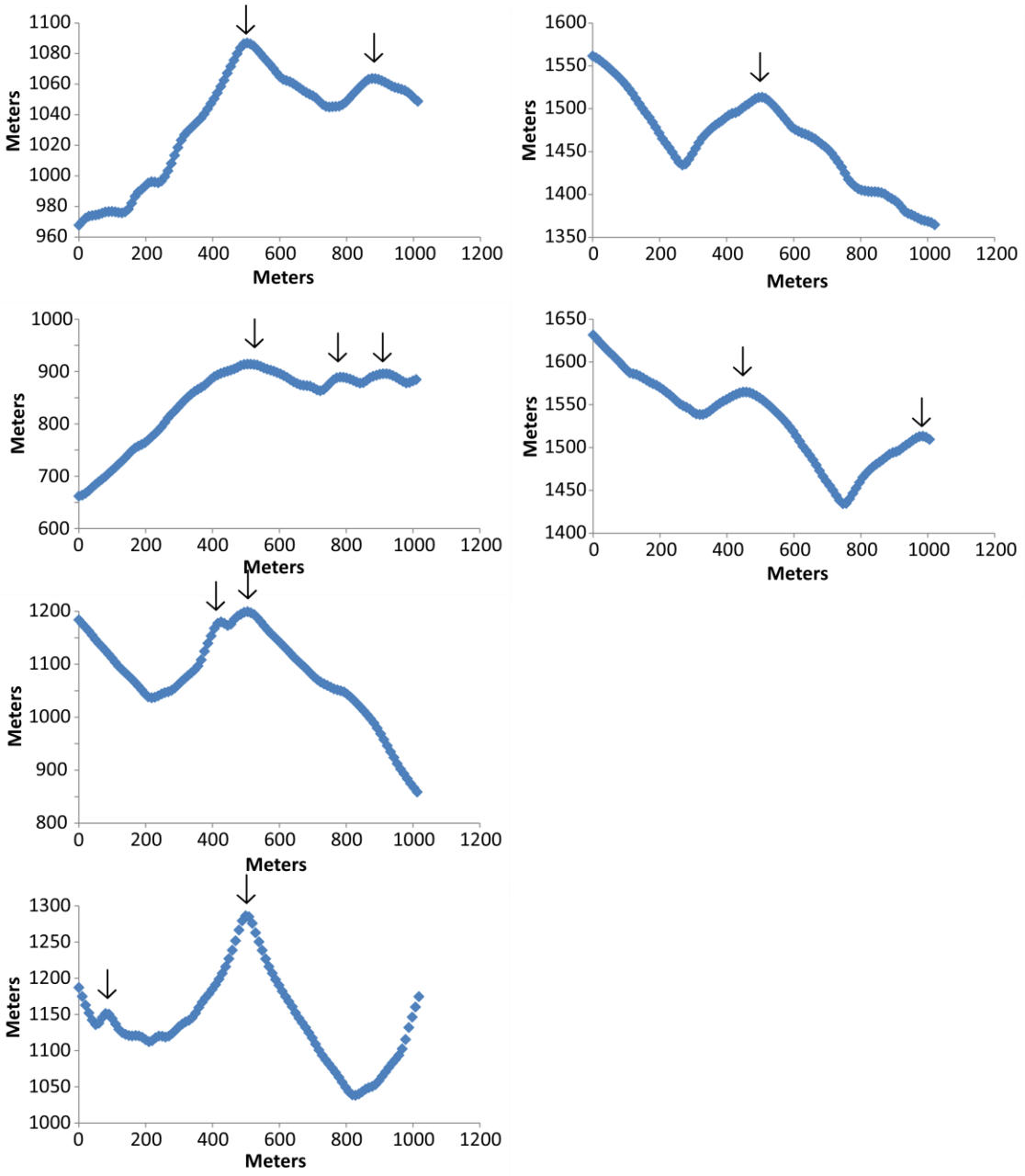

Figure *46*. Topography profiles of the transecting hills of Cluster 61. Hills are denoted with a black arrow.

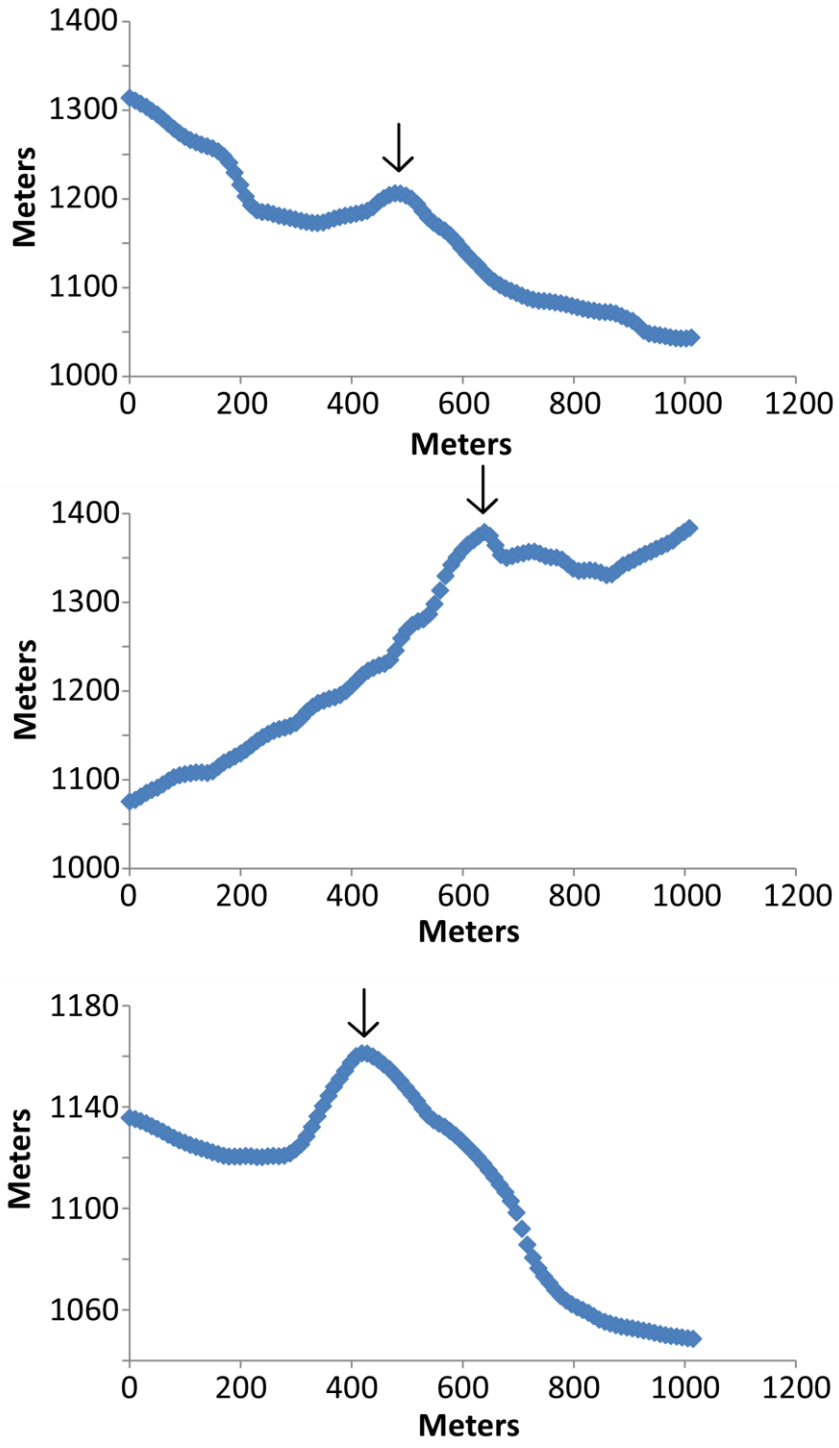

Figure *47*. Topography profiles of the transecting hills of Cluster 64. Hills are denoted with a black arrow.

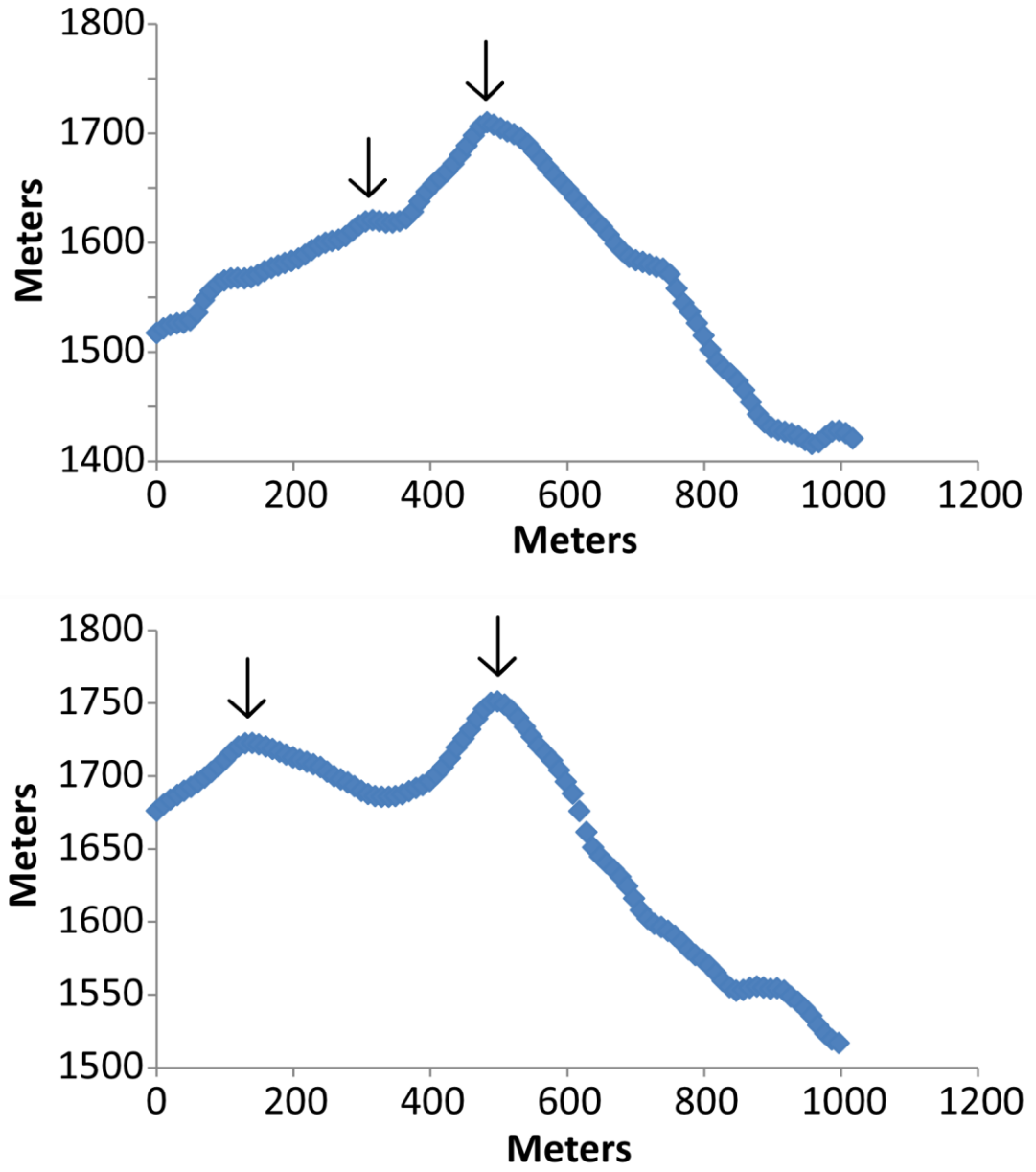

Figure *48*. Topography profiles of the transecting hills of Cluster 65. Hills are denoted with a black arrow.

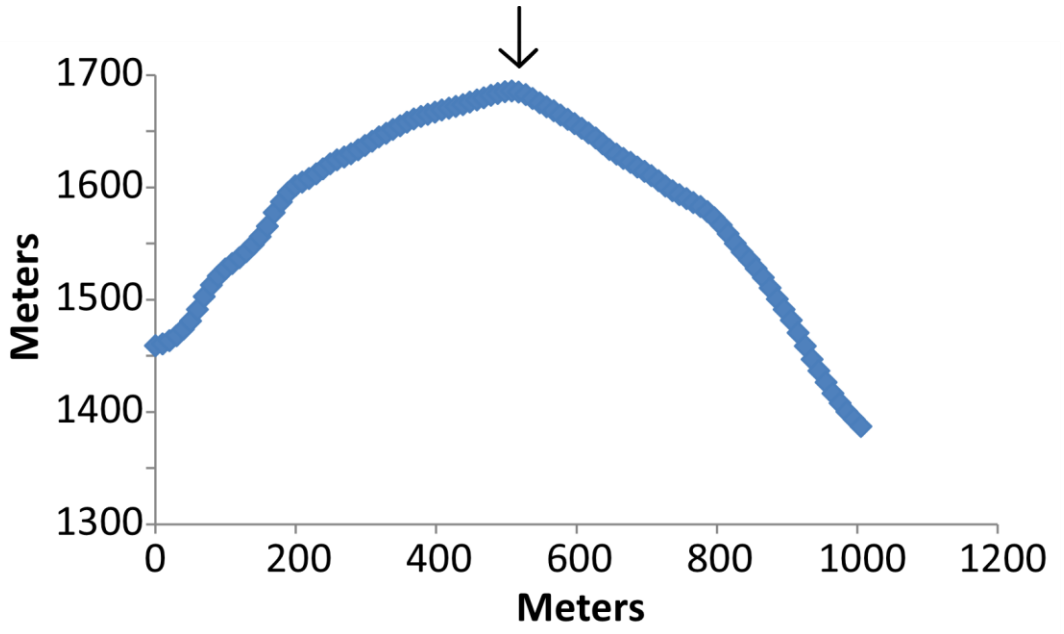

Figure *49*. Topography profiles of the transecting hills of Cluster 66. Hills are denoted with a black arrow.

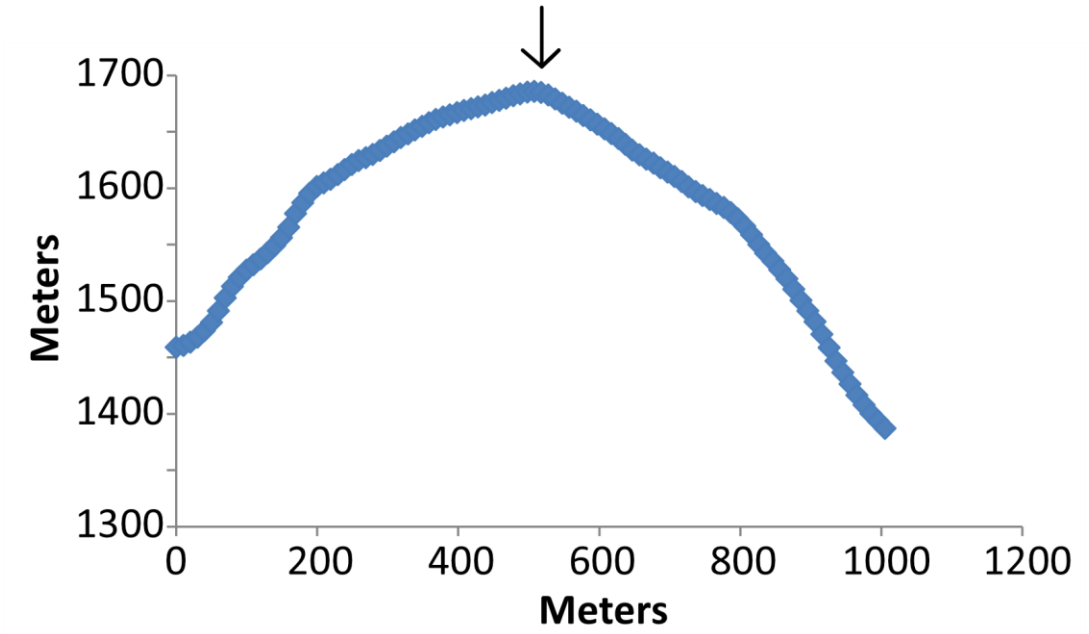

Figure *50.* Topography profiles of the transecting hills of Cluster 67. Hills are denoted with a black arrow.

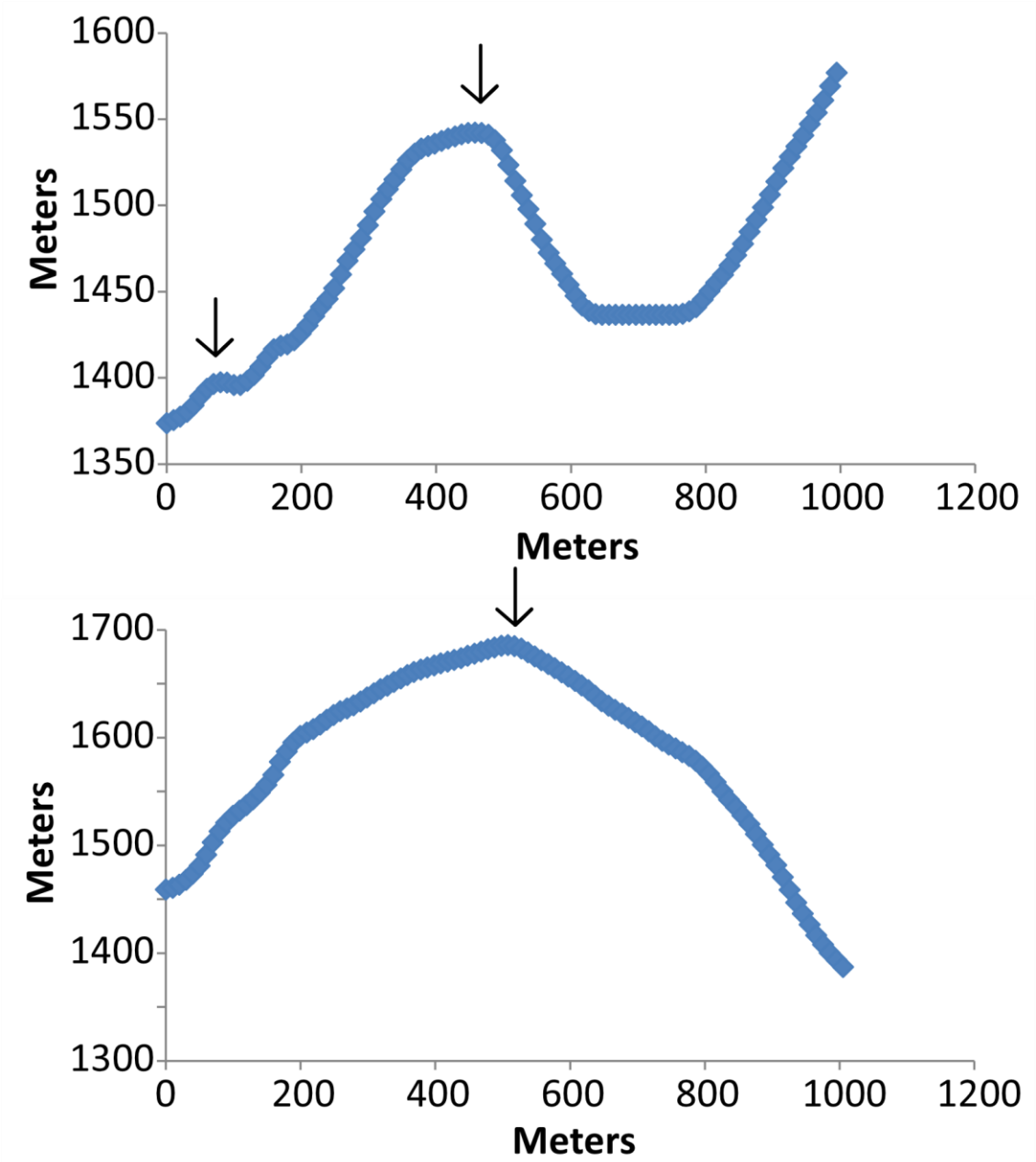

Figure *51*. Topography profiles of the transecting hills of Cluster 67. Hills are denoted with a black arrow.

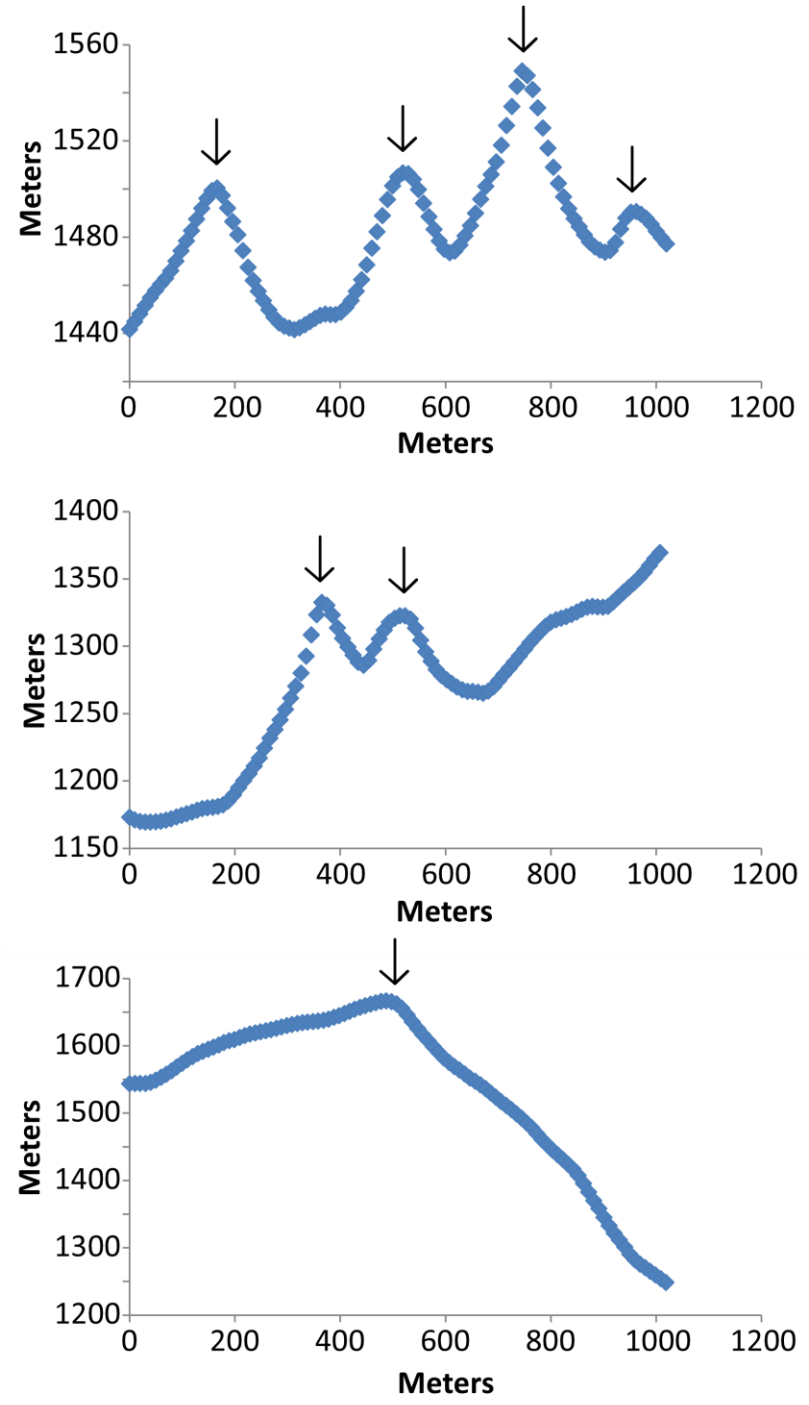

Figure *52*. Topography profiles of the transecting hills of Cluster 69. Hills are denoted with a black arrow.

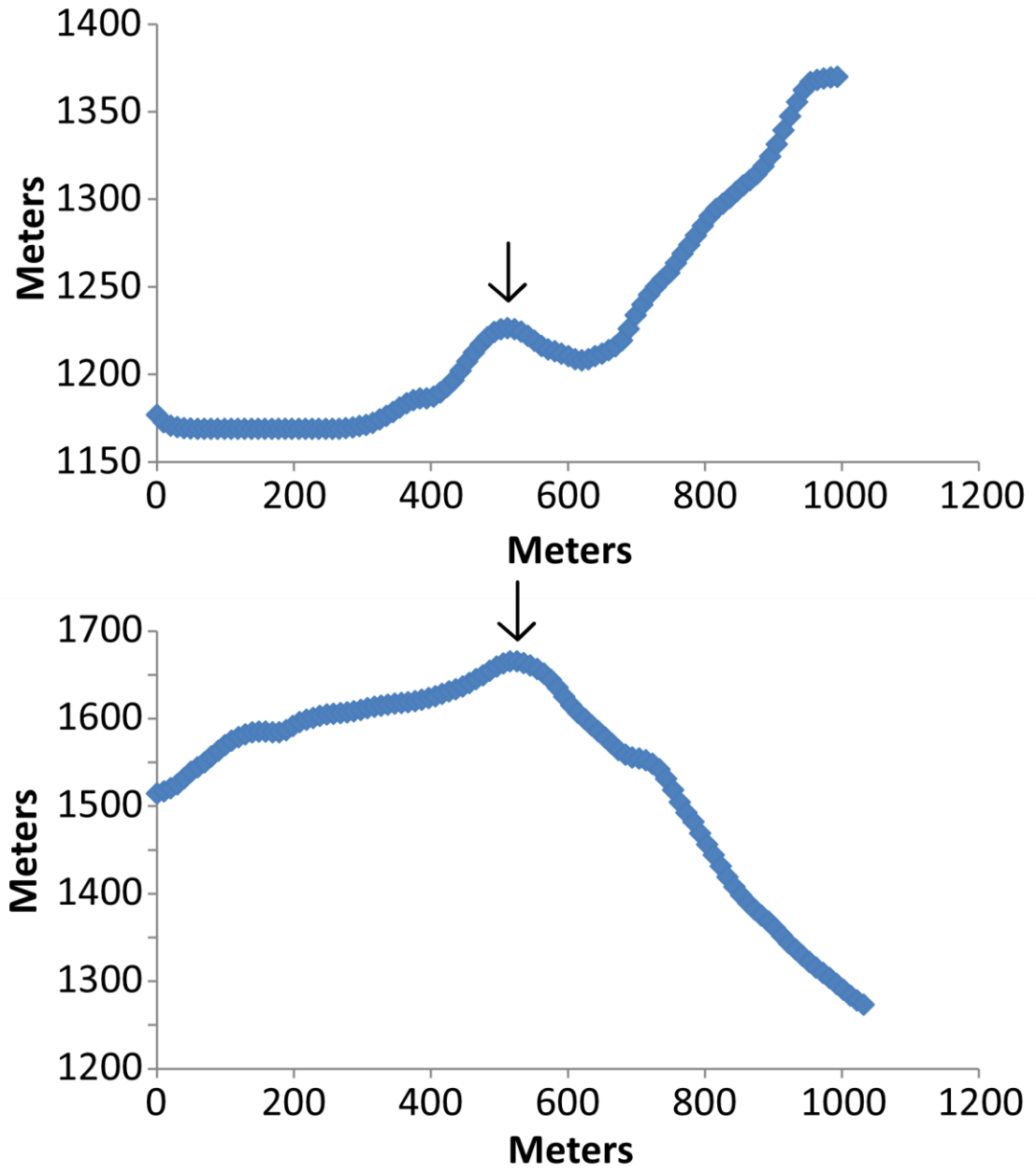

Figure *53*. Topography profiles of the transecting hills of Cluster 70. Hills are denoted with a black arrow.

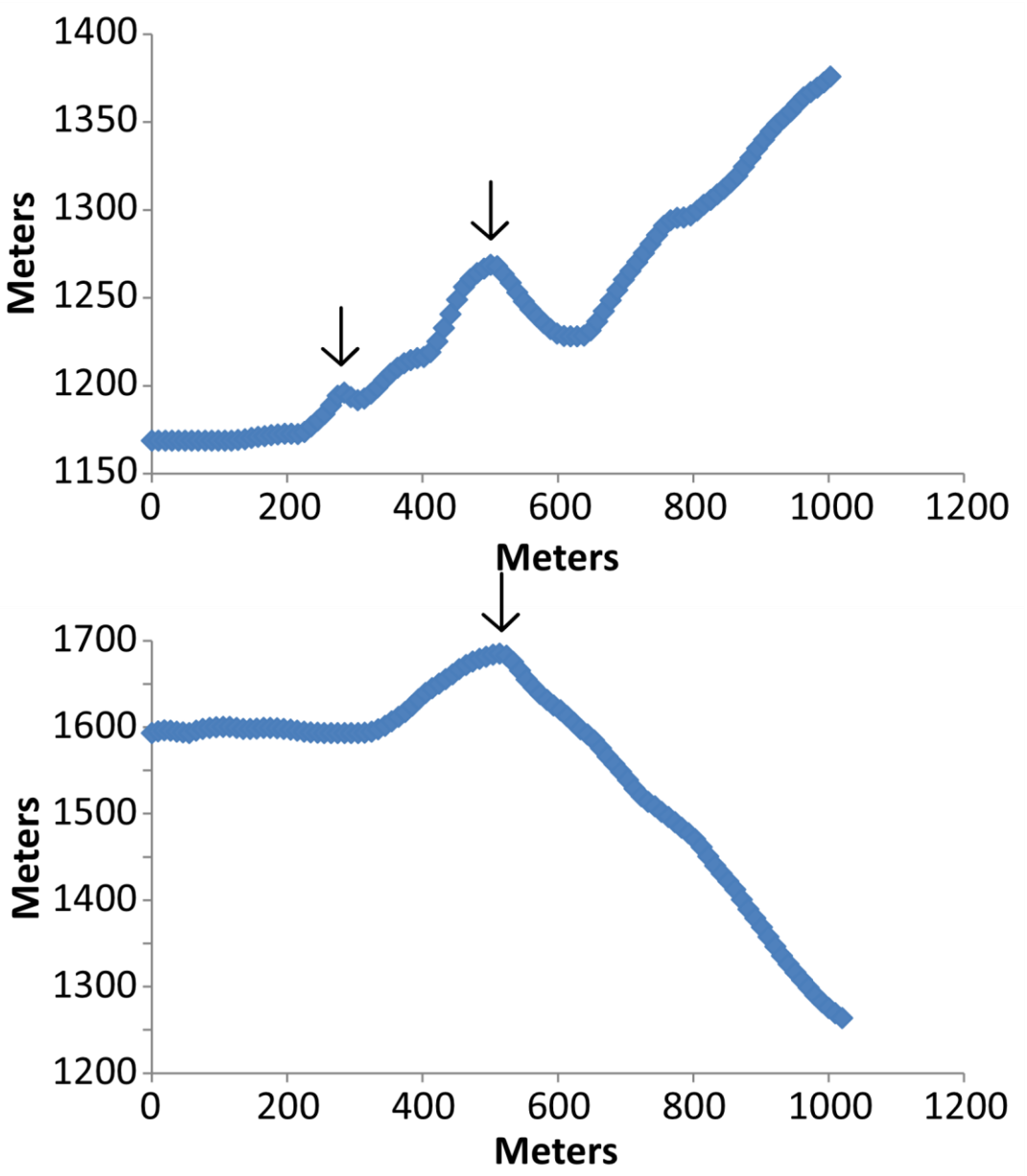

Figure *54*. Topography profiles of the transecting hills of Cluster 71. Hills are denoted with a black arrow.

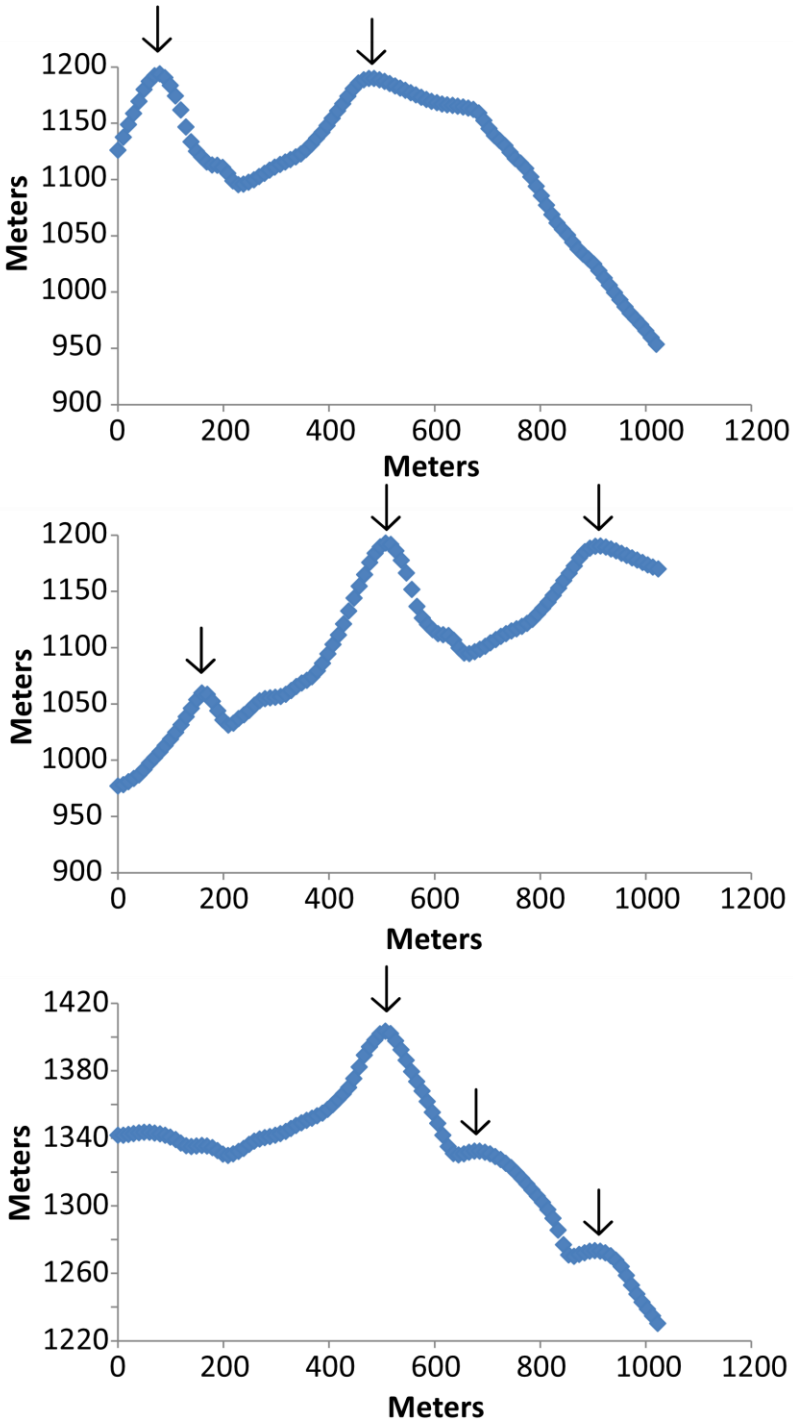

Figure *55*. Topography profiles of the transecting hills of Cluster 74. Hills are denoted with a black arrow.

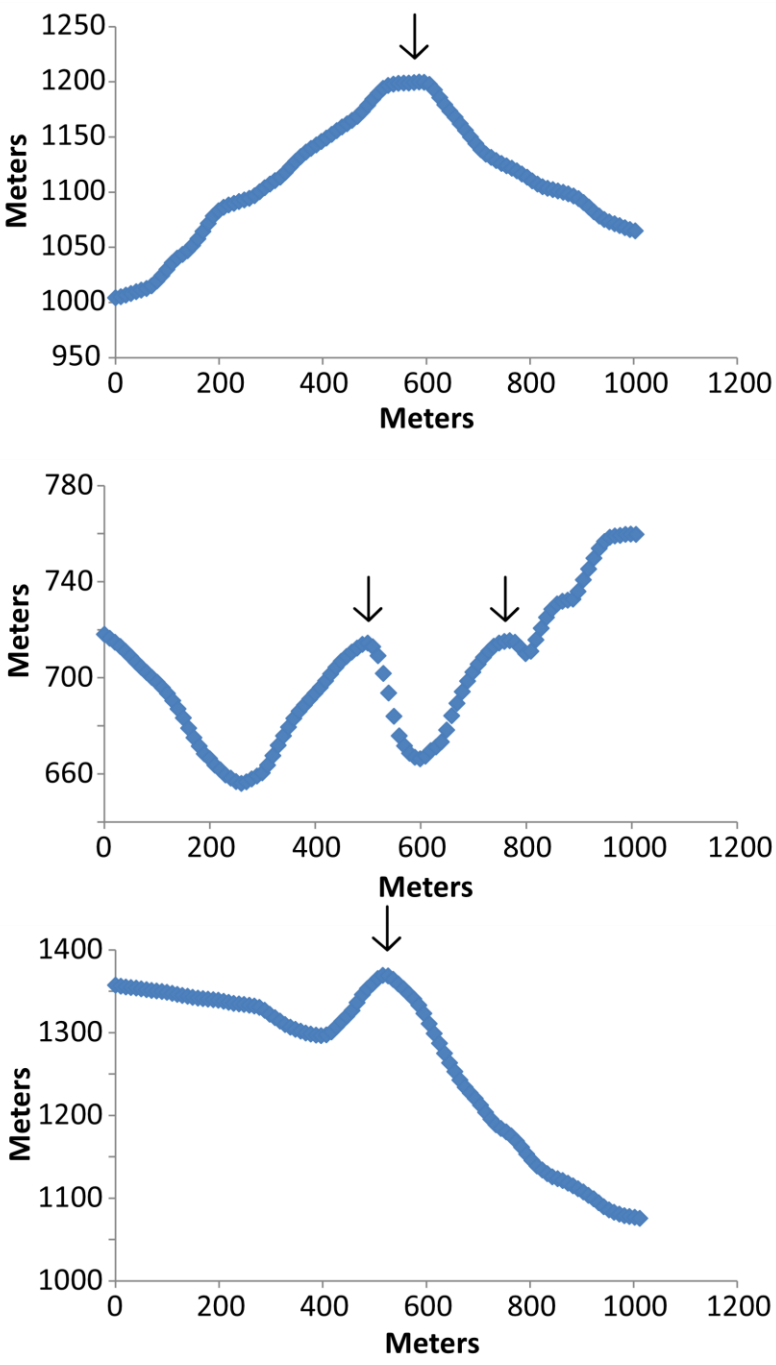

Figure *56*. Topography profiles of the transecting hills of Cluster 75. Hills are denoted with a black arrow.

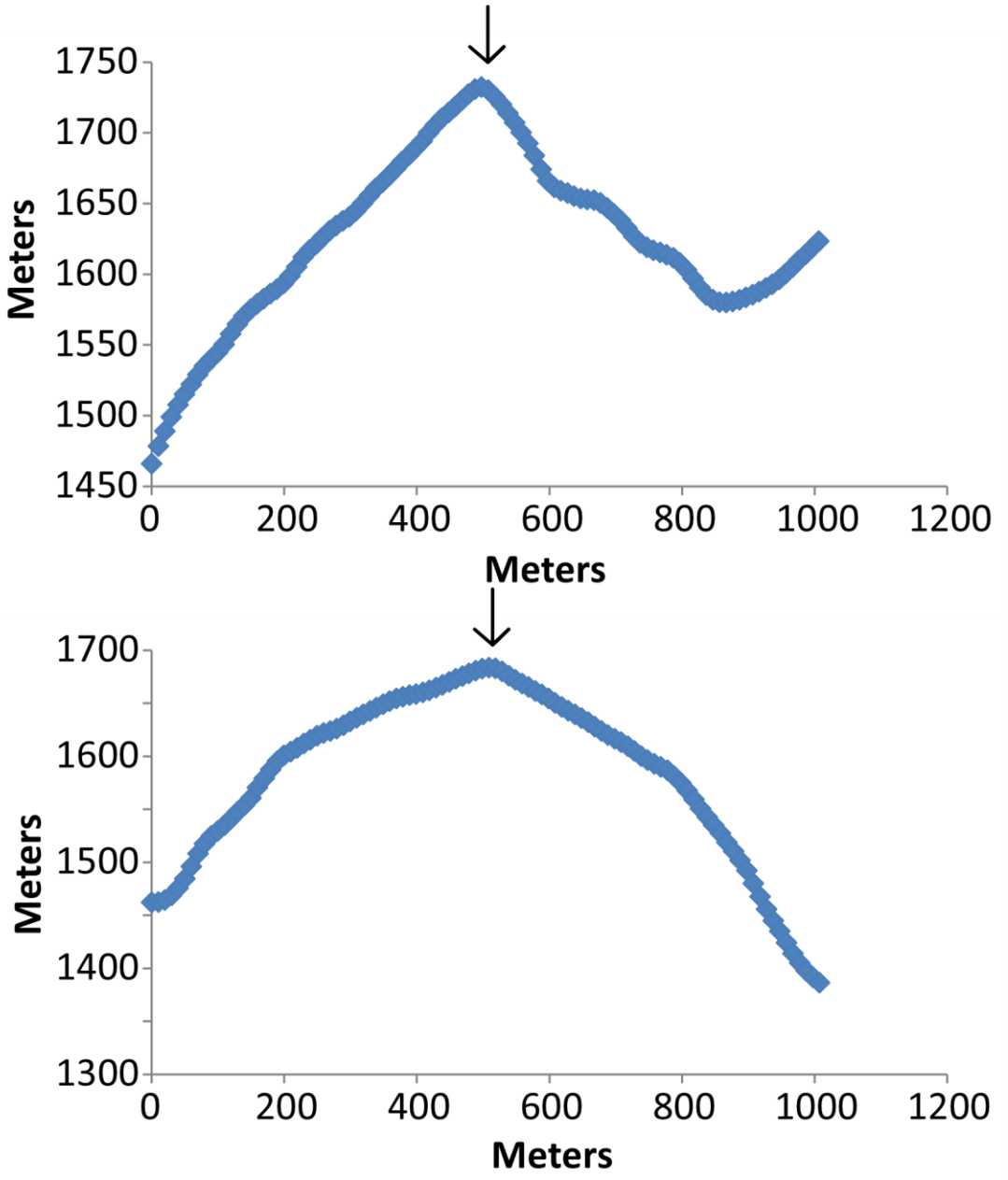

Figure *57*. Topography profiles of the transecting hills of Cluster 76. Hills are denoted with a black arrow.

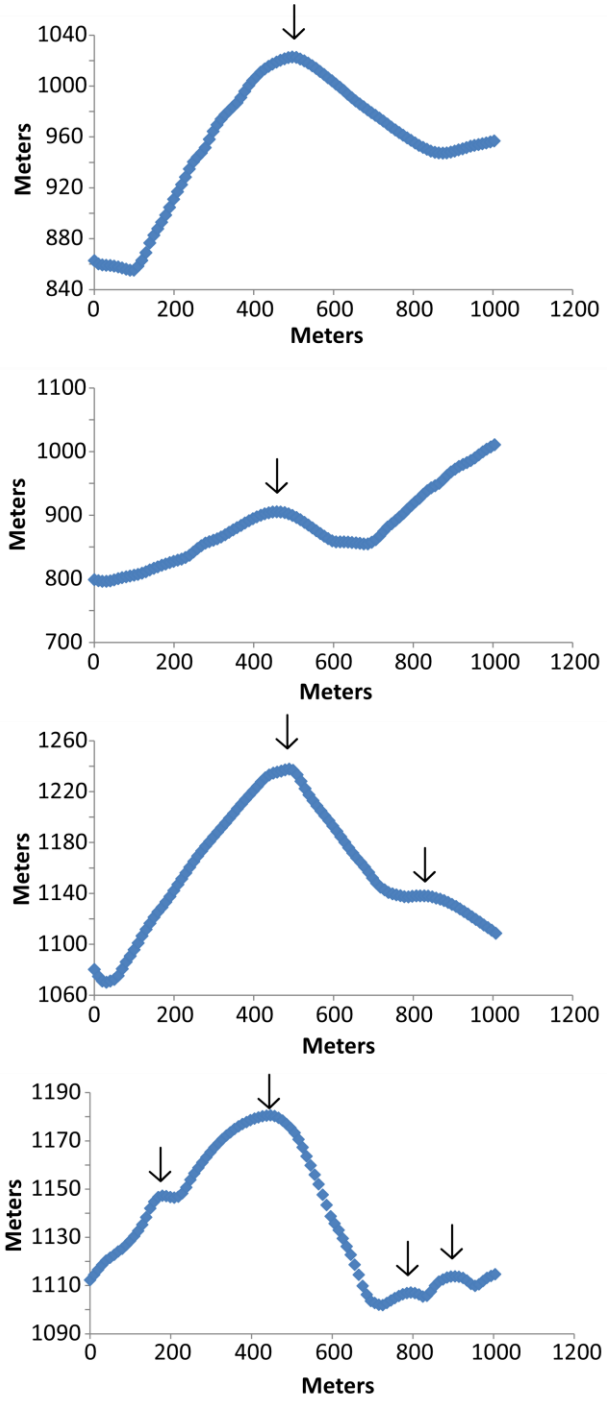

Figure *58*. Topography profiles of the transecting hills of Cluster 77. Hills are denoted with a black arrow.

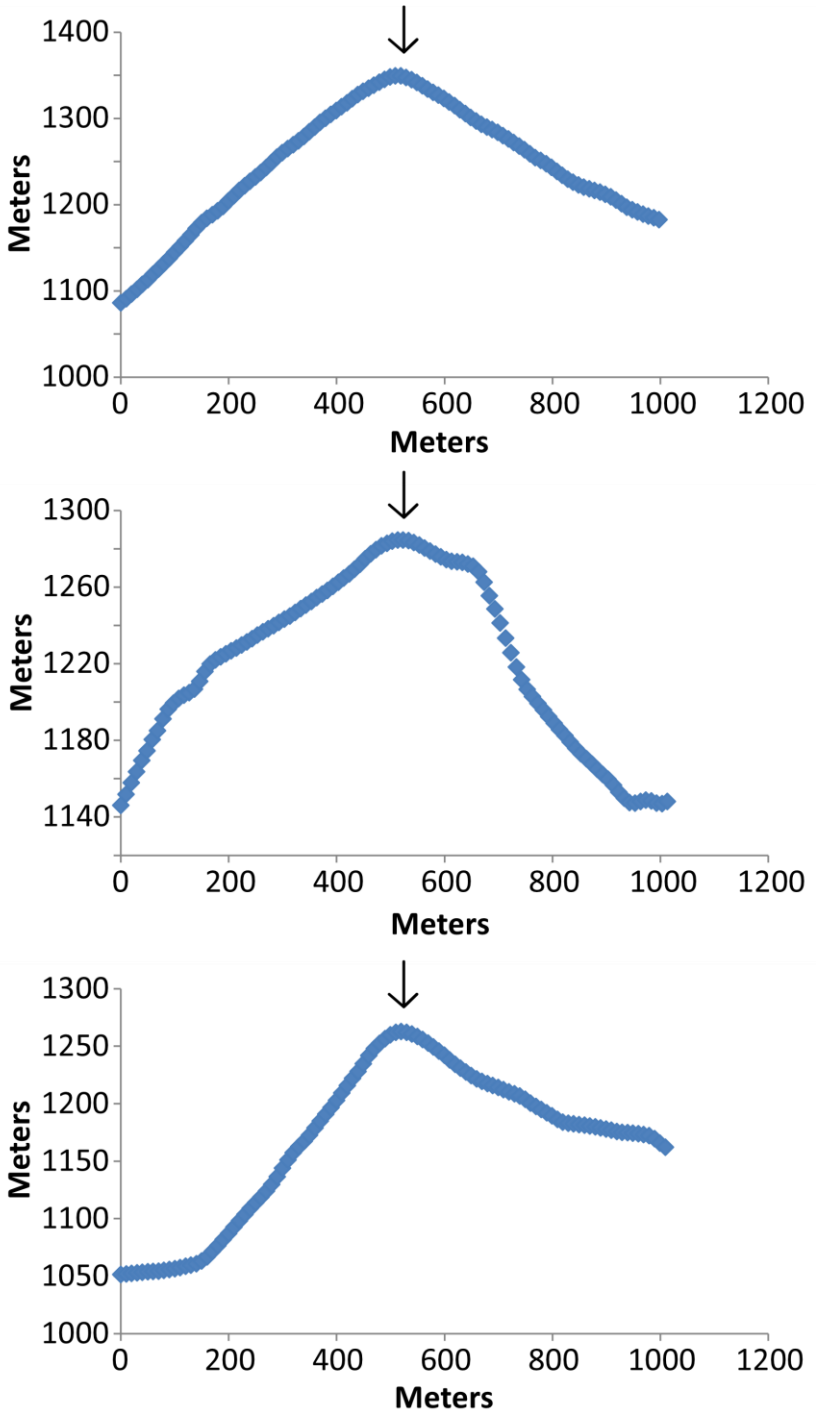

Figure 59. Topography profiles of the transecting hills of Cluster 78. Hills are denoted with a black arrow.

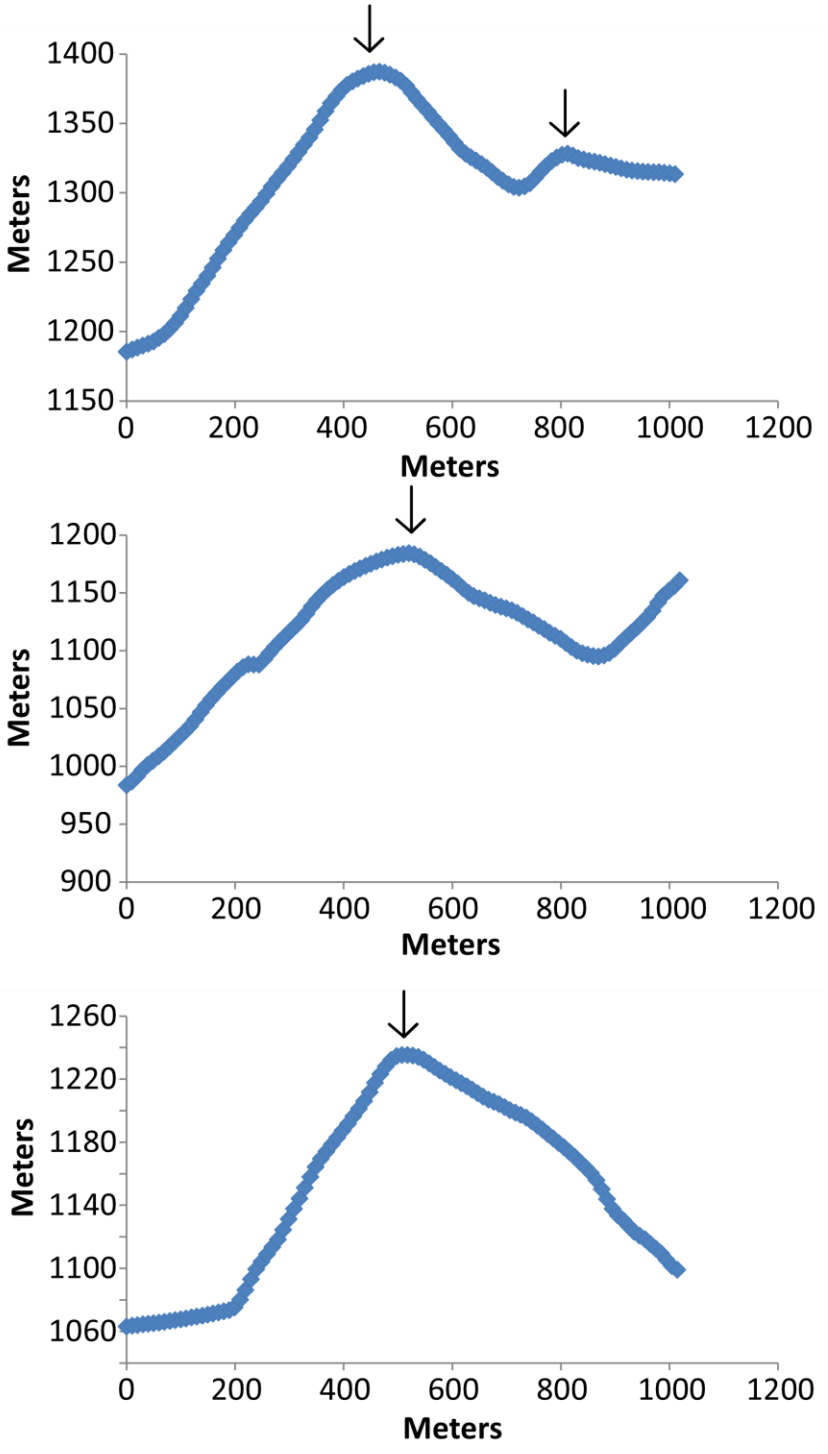

Figure *60*. Topography profiles of the transecting hills of Cluster 79. Hills are denoted with a black arrow.

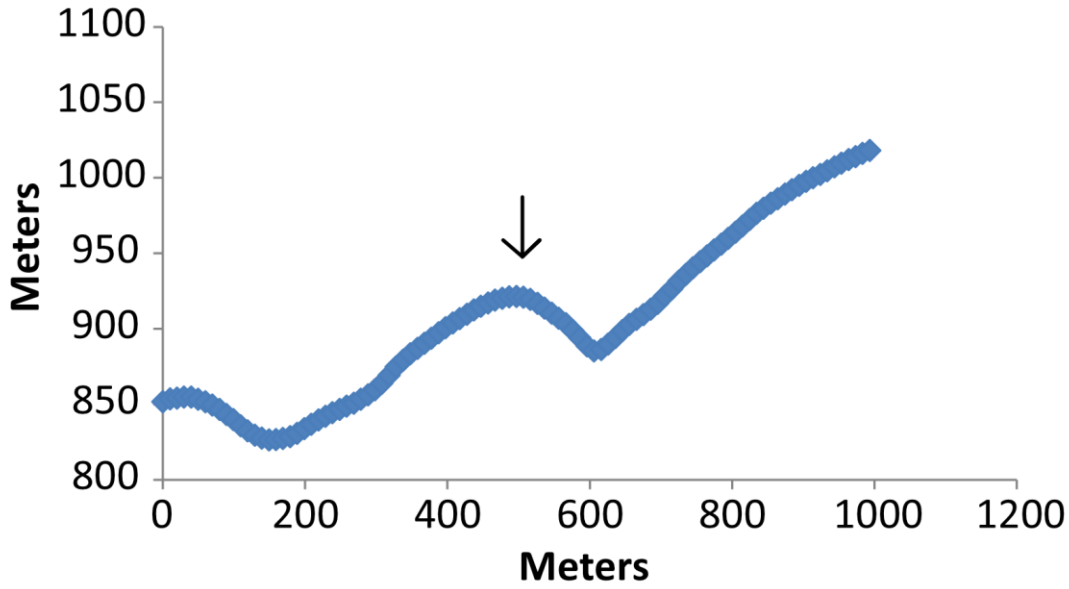

Figure *61*. Topography profiles of the transecting hills of Cluster 80. Hills are denoted with a black arrow.

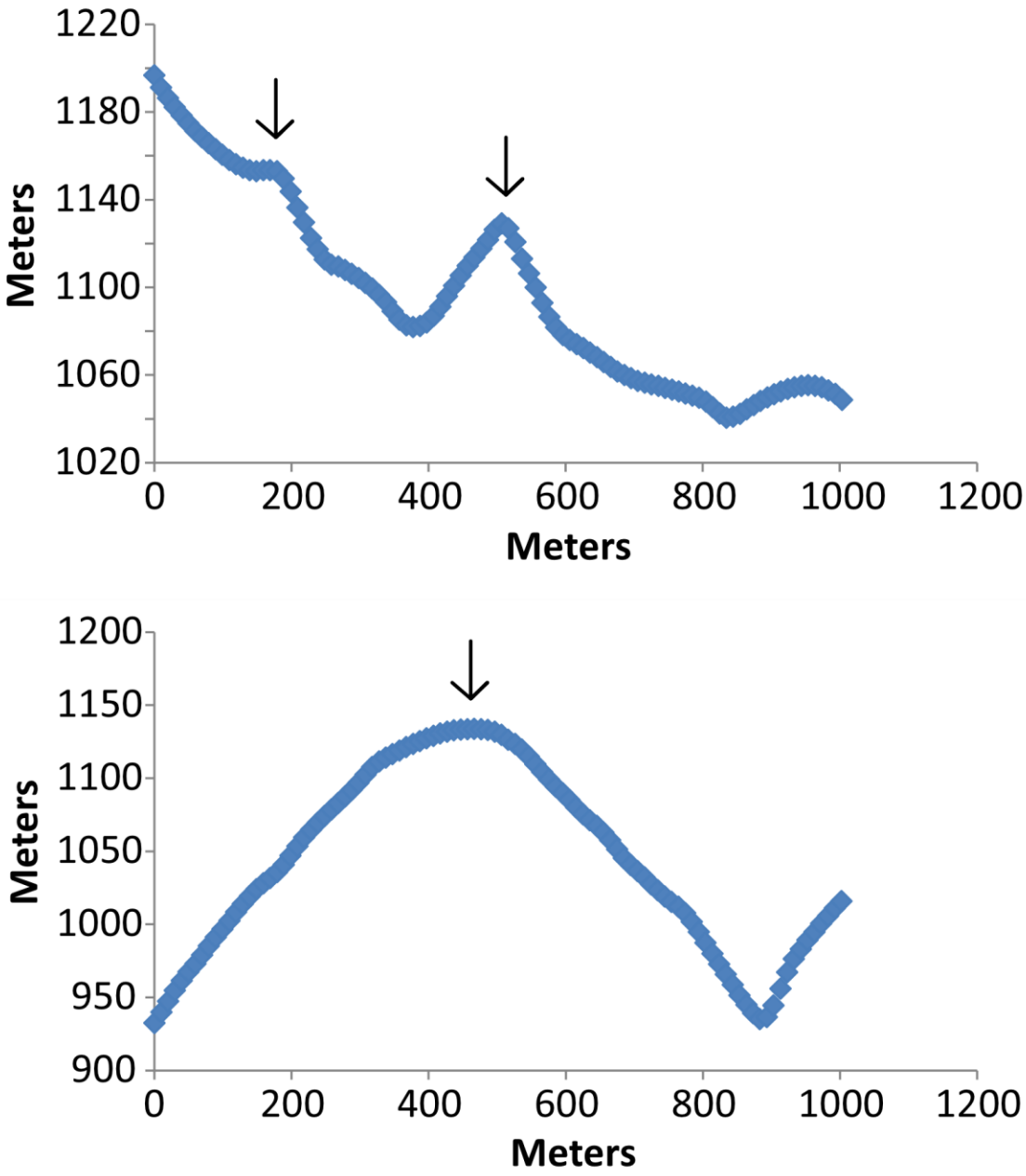

Figure *62*. Topography profiles of the transecting hills of Cluster 81. Hills are denoted with a black arrow.

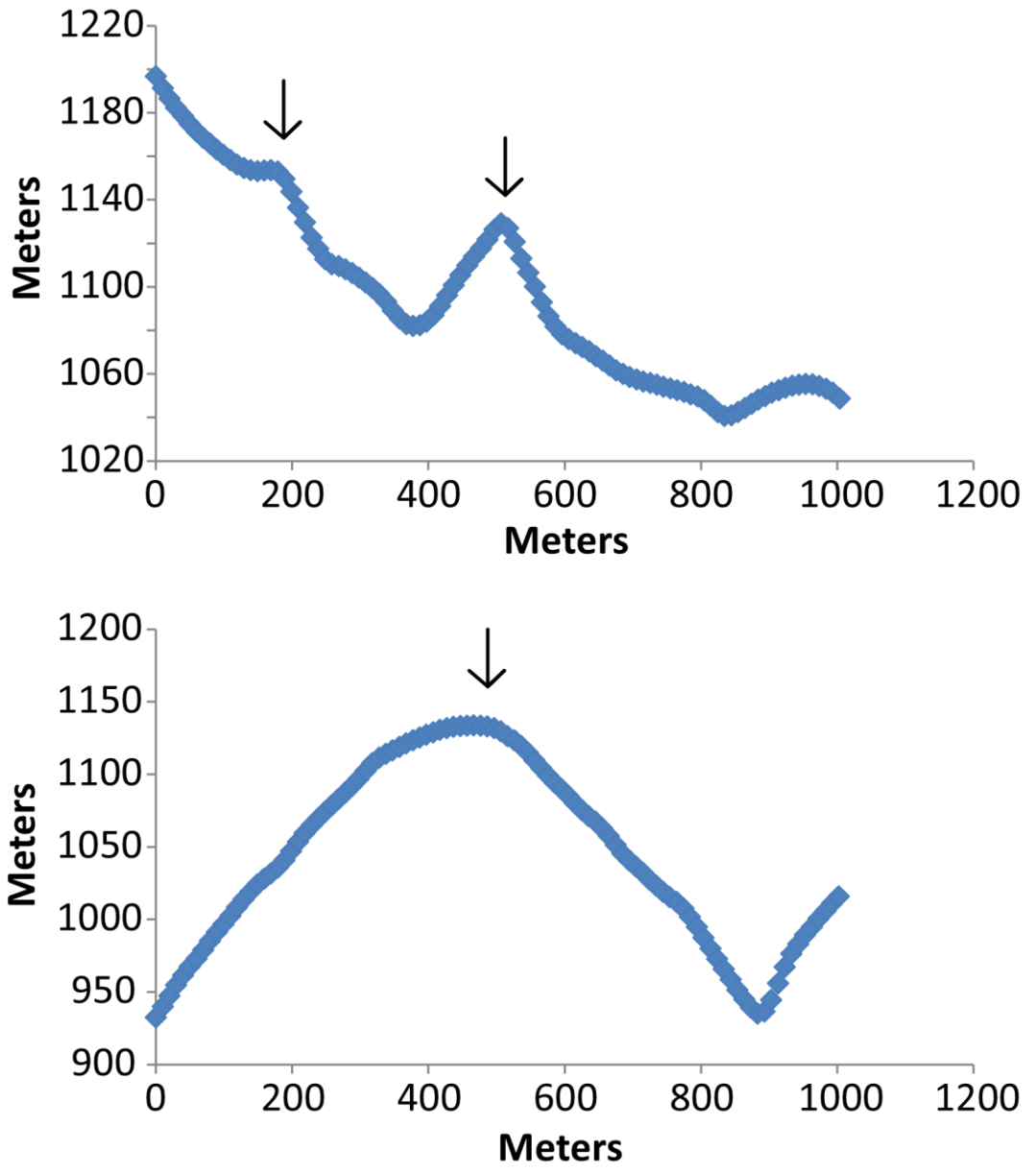

Figure *63*. Topography profiles of the transecting hills of Cluster 82. Hills are denoted with a black arrow.

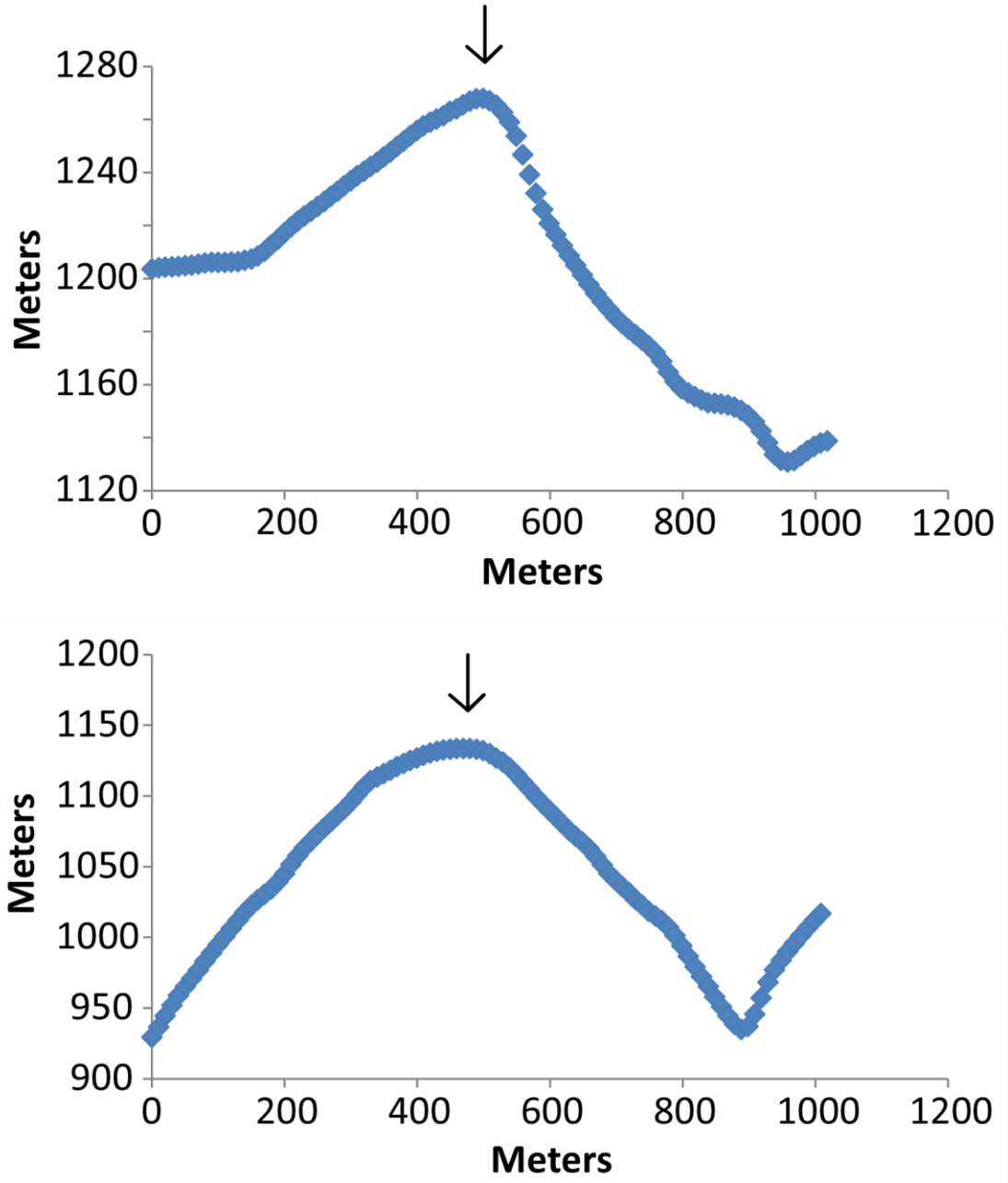

Figure *64*. Topography profiles of the transecting hills of Cluster 83. Hills are denoted with a black arrow.

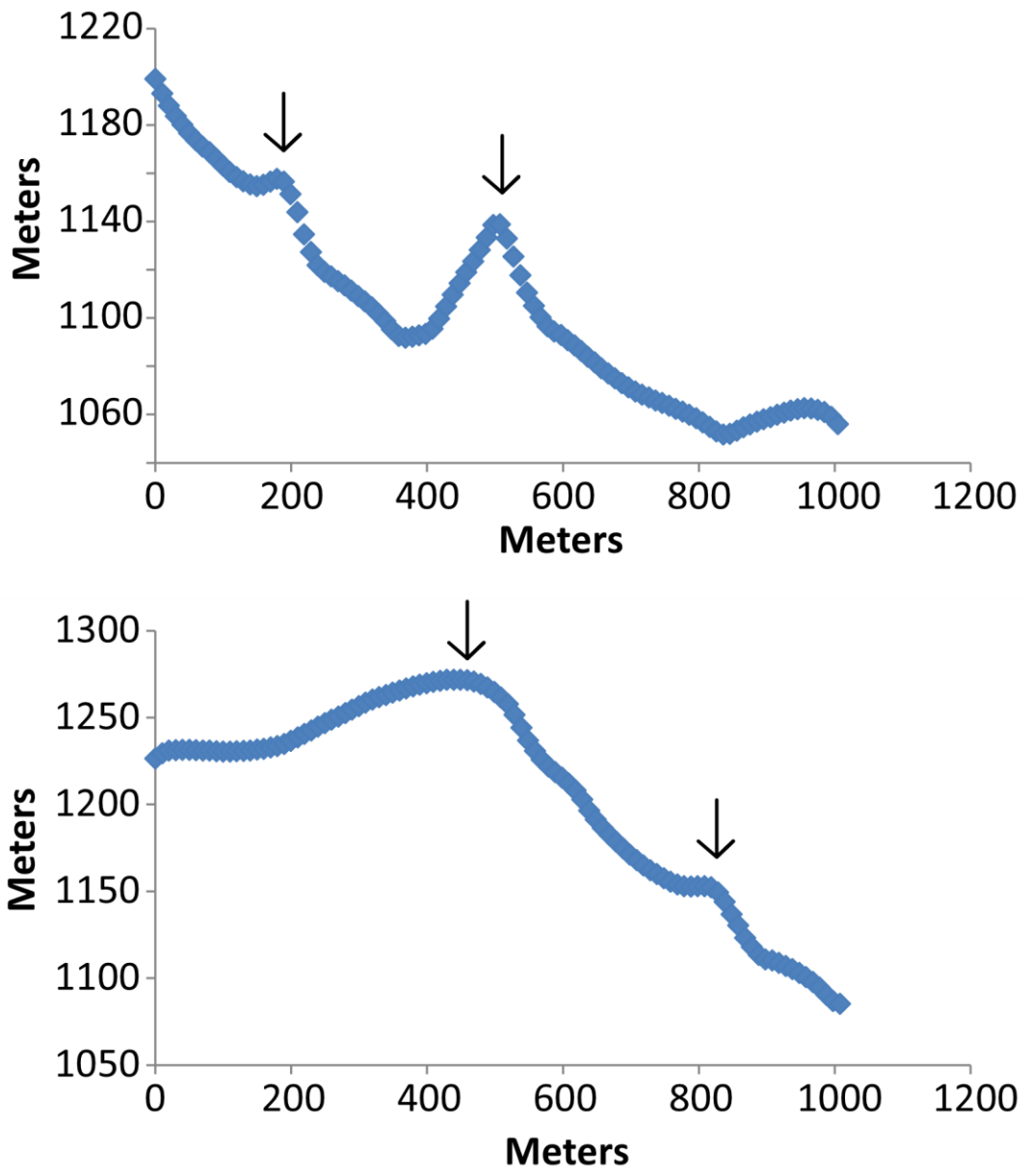

Figure *65*. Topography profiles of the transecting hills of Cluster 84. Hills are denoted with a black arrow.

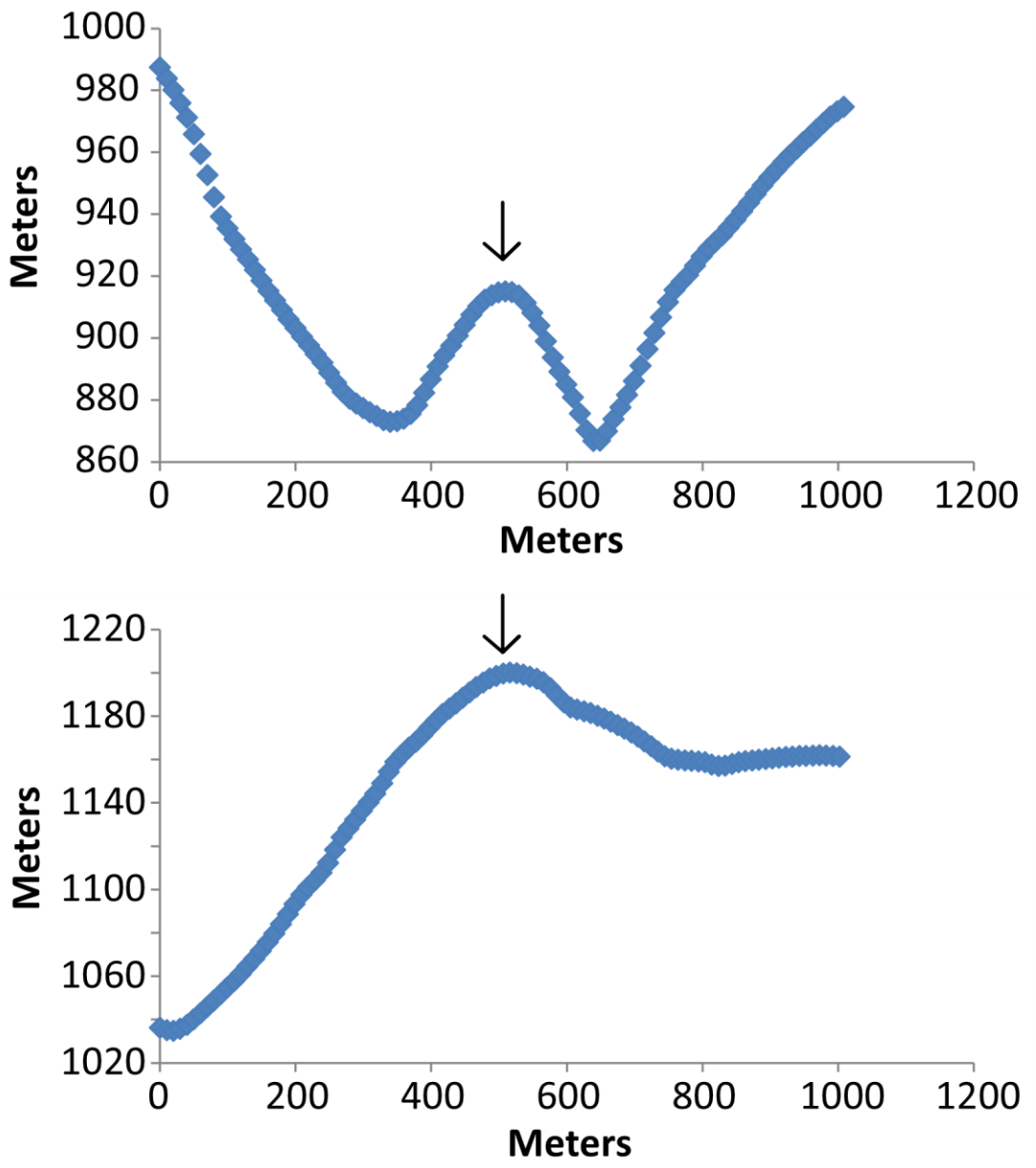

Figure *66*. Topography profiles of the transecting hills of Cluster 85. Hills are denoted with a black arrow.

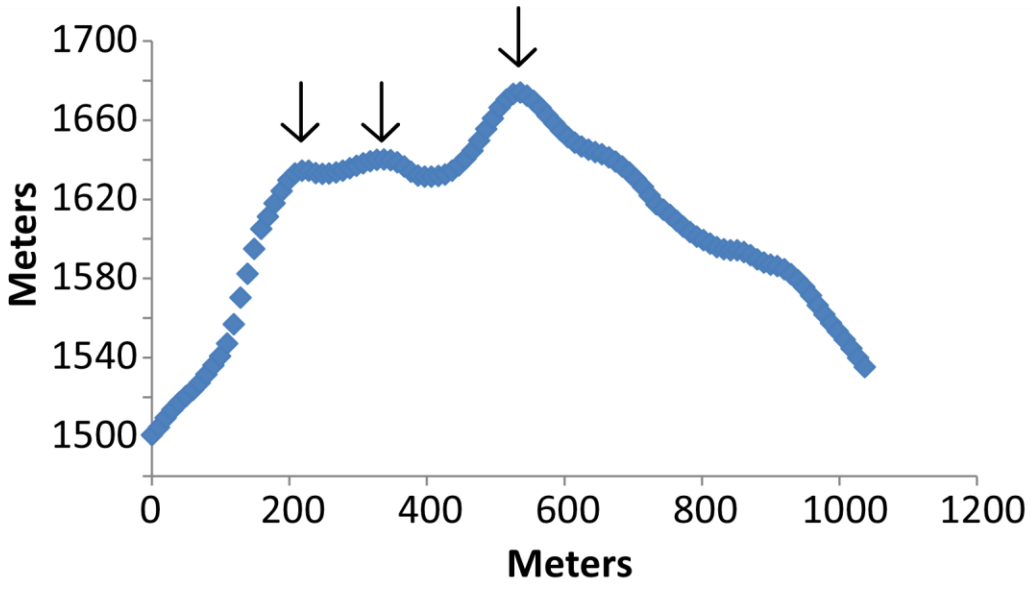

Figure *67*. Topography profiles of the transecting hills of Cluster 86. Hills are denoted with a black arrow.

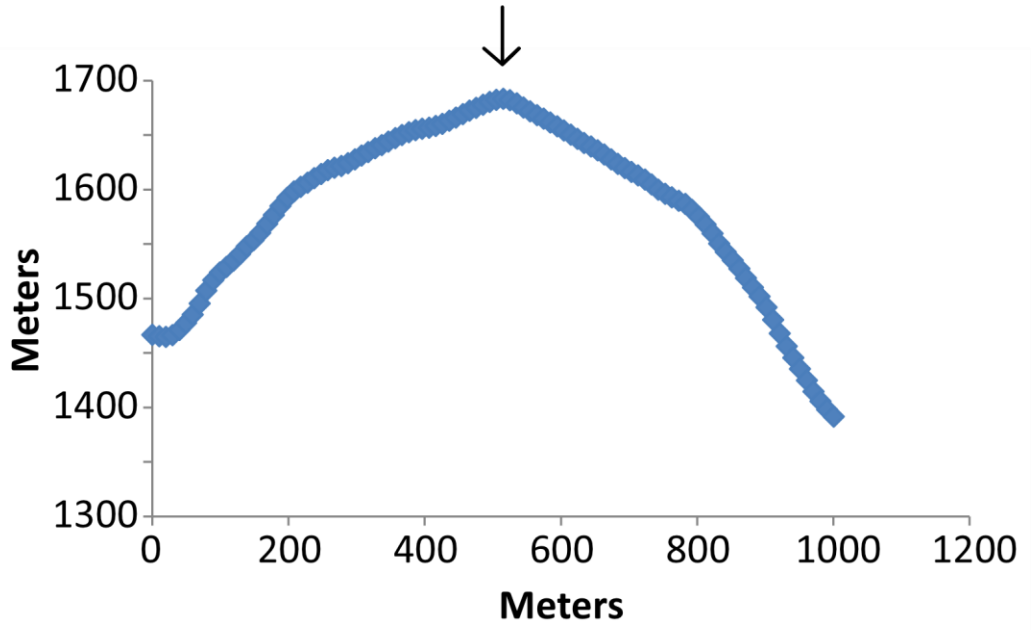

Figure *68*. Topography profiles of the transecting hills of Cluster 87. Hills are denoted with a black arrow.

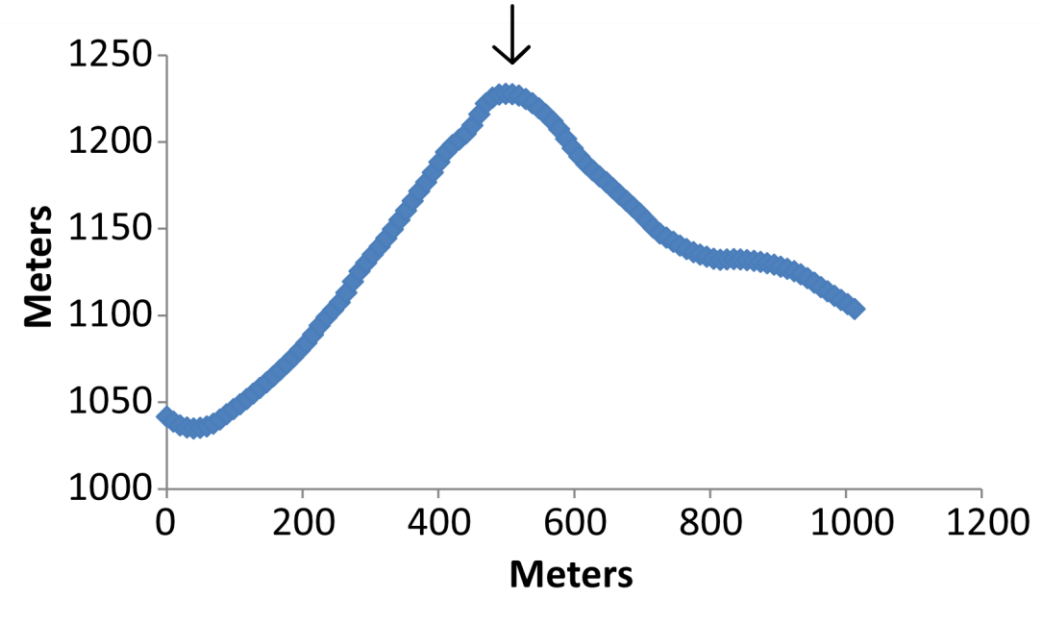

Figure *69*. Topography profiles of the transecting hills of Cluster 89. Hills are denoted with a black arrow.

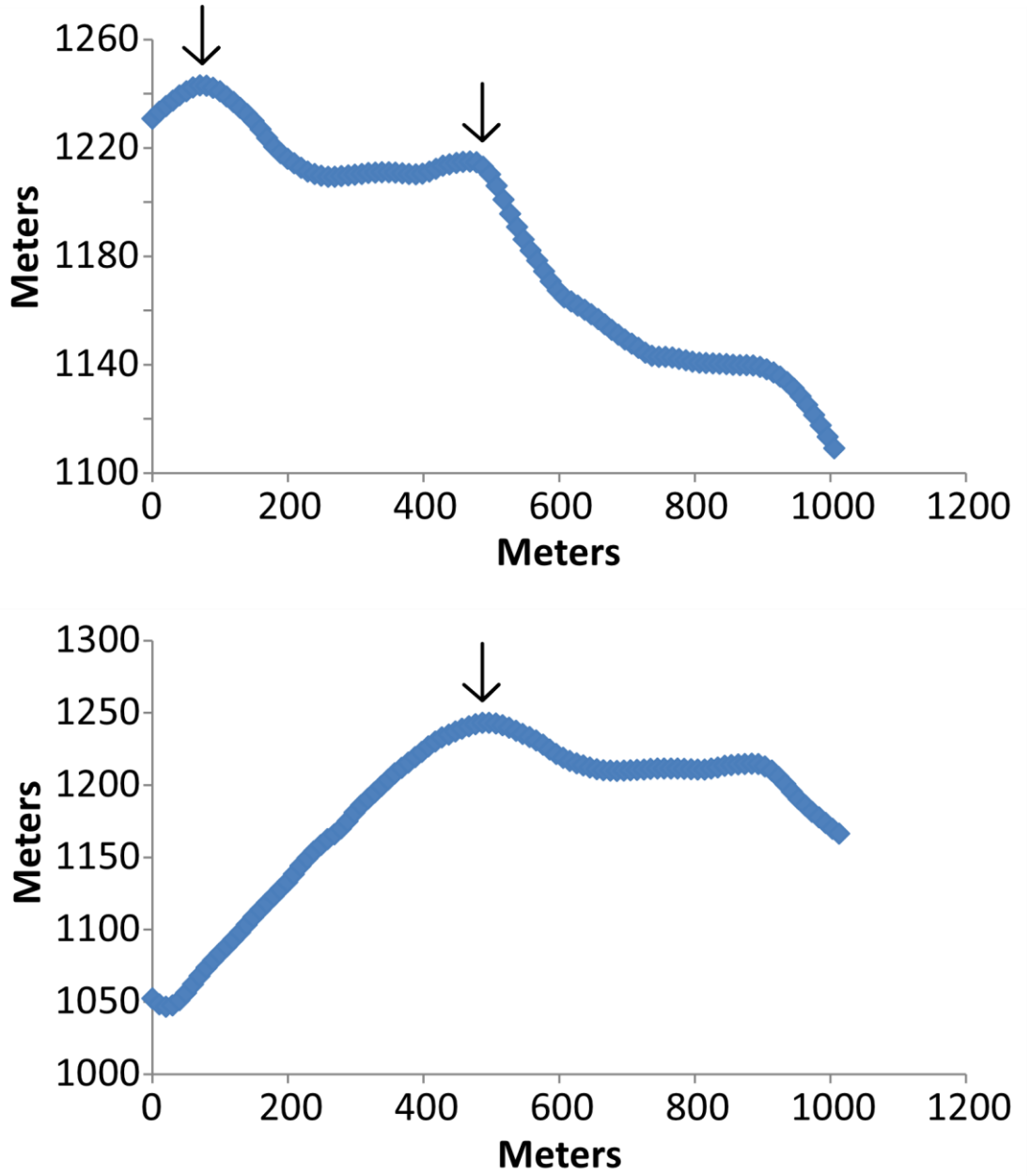

Figure *70*. Topography profiles of the transecting hills of Cluster 91. Hills are denoted with a black arrow.

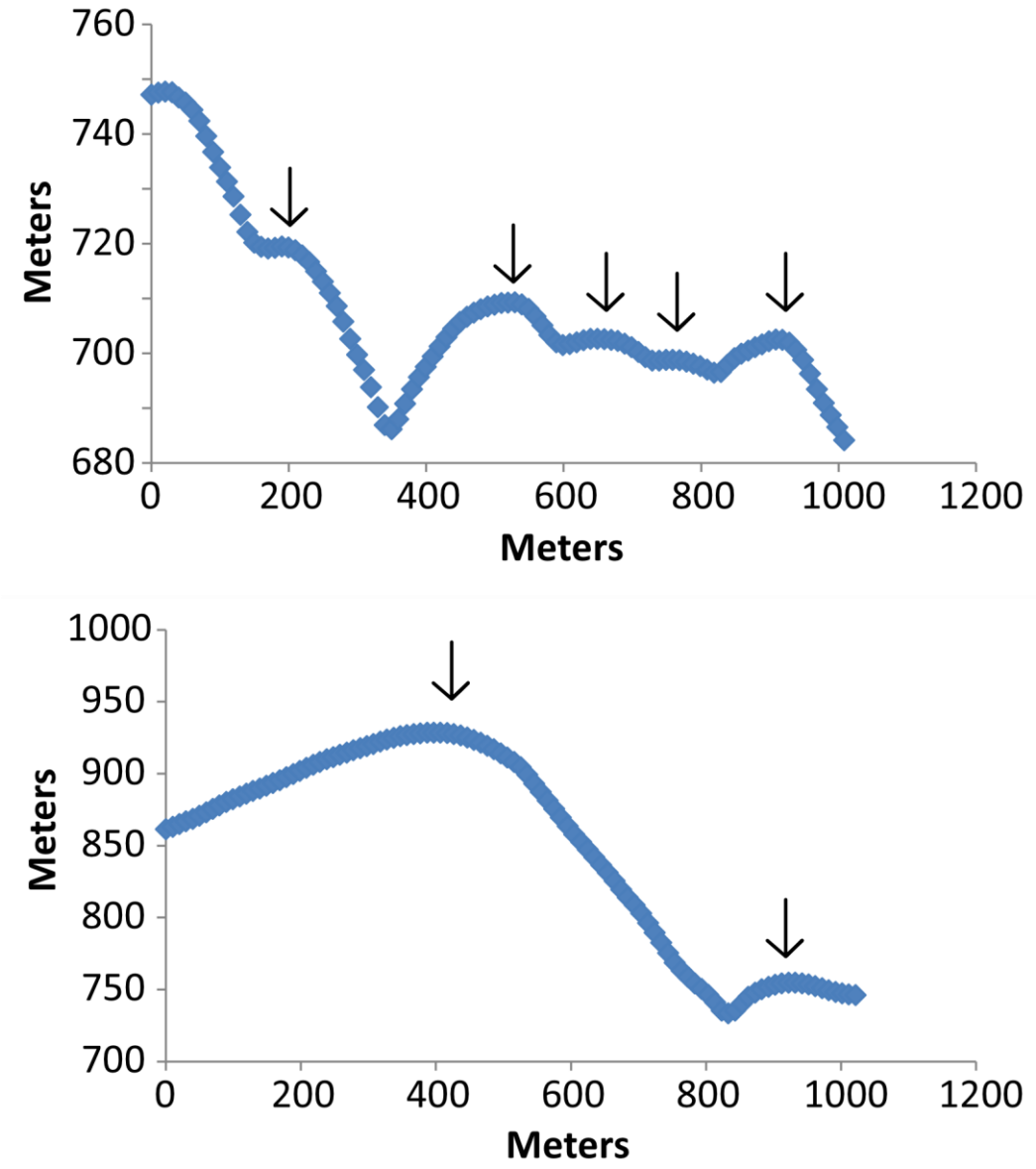

Figure *71*. Topography profiles of the transecting hills of Cluster 92. Hills are denoted with a black arrow.

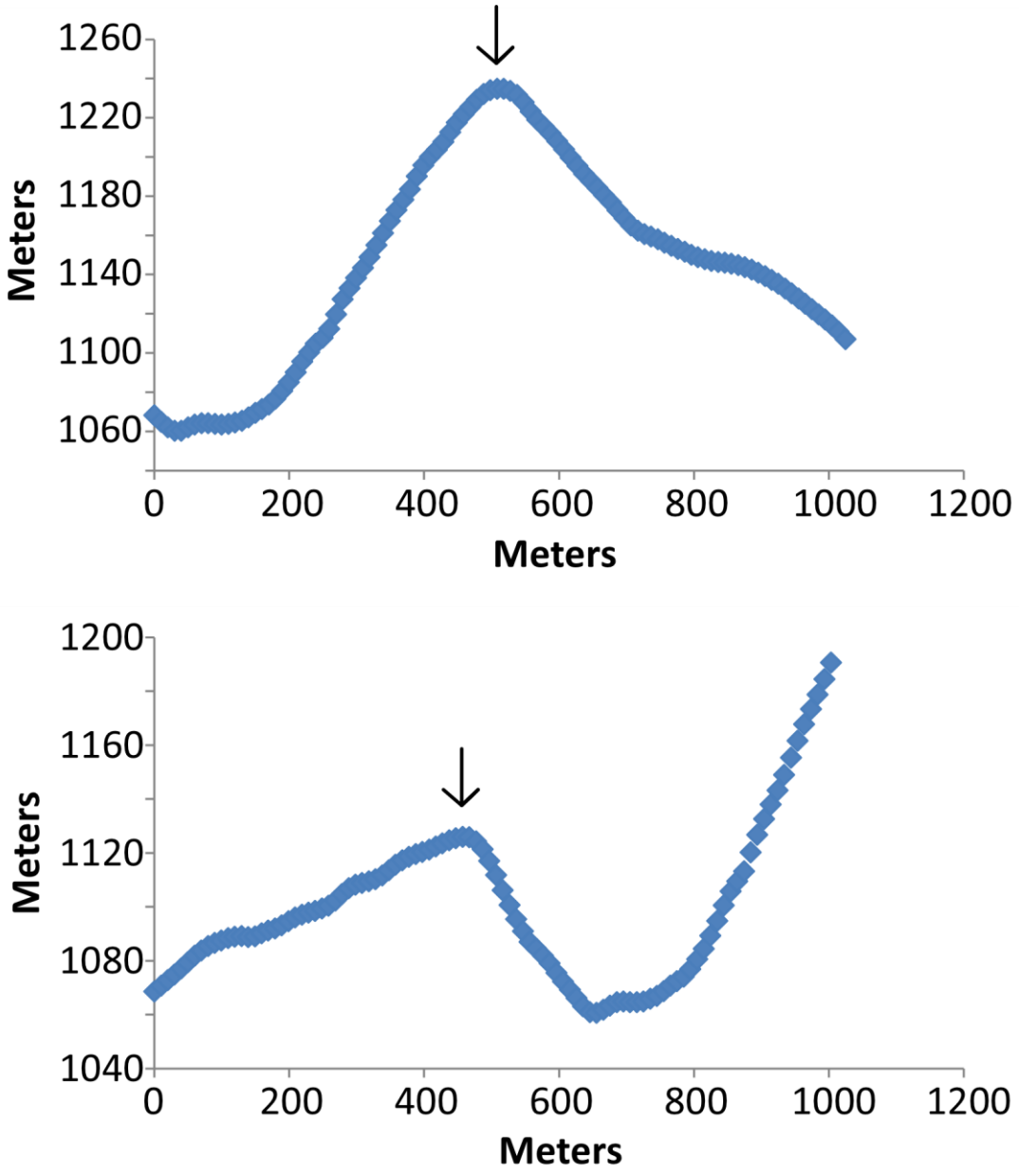

Figure *72*. Topography profiles of the transecting hills of Cluster 94. Hills are denoted with a black arrow.

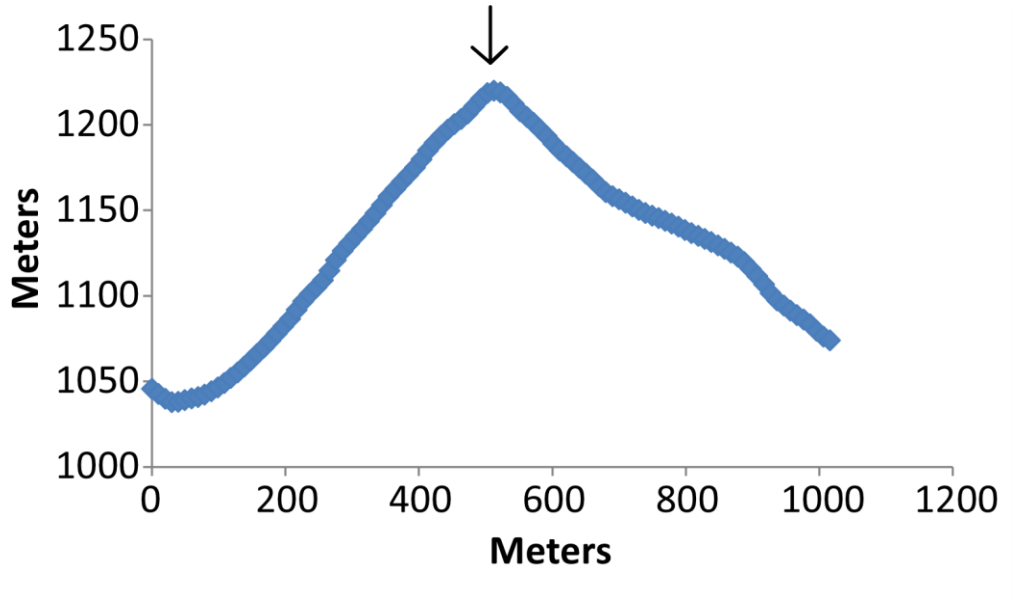

Figure *73*. Topography profiles of the transecting hills of Cluster 95. Hills are denoted with a black arrow.

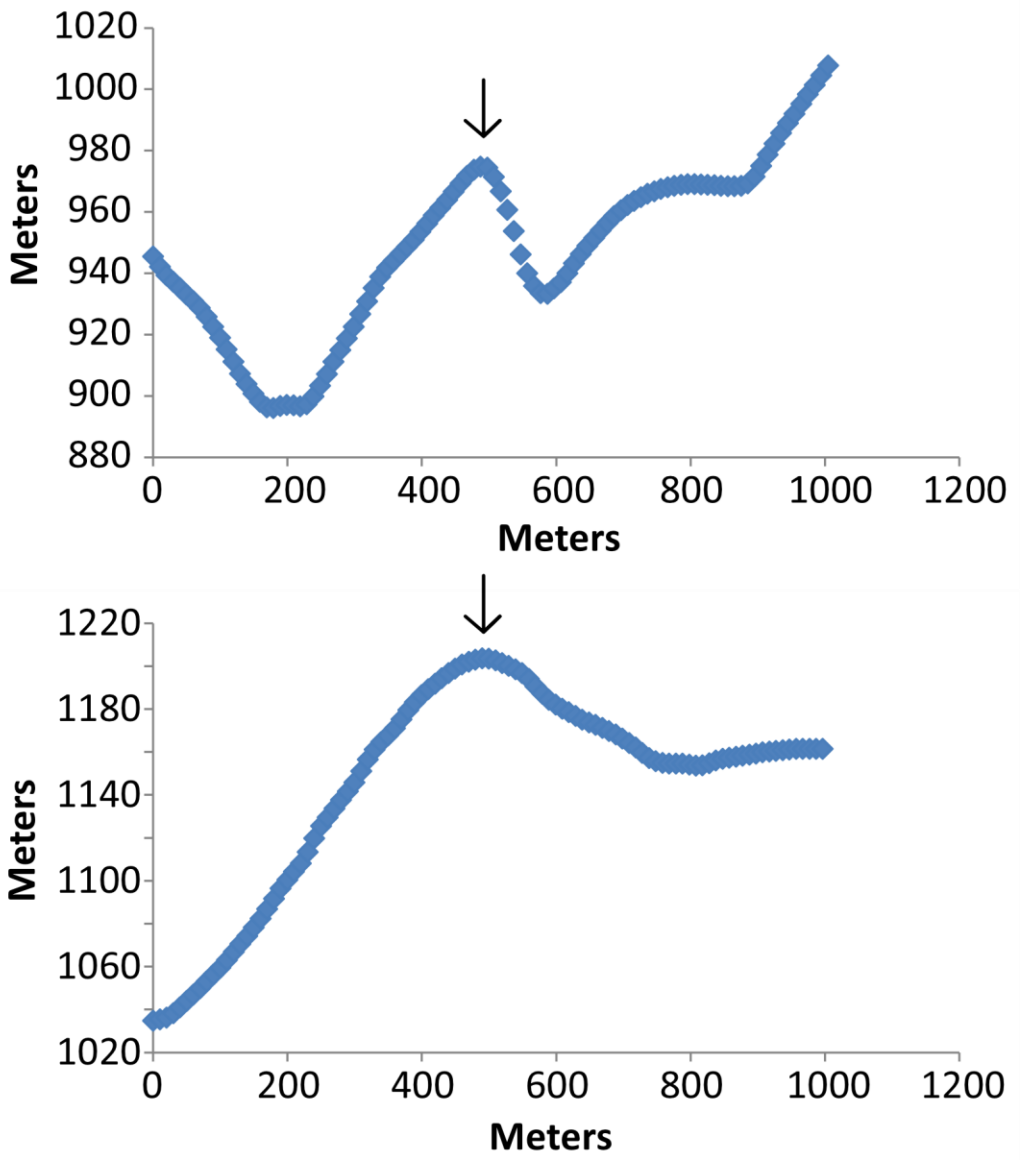

Figure *74*. Topography profiles of the transecting hills of Cluster 96. Hills are denoted with a black arrow.

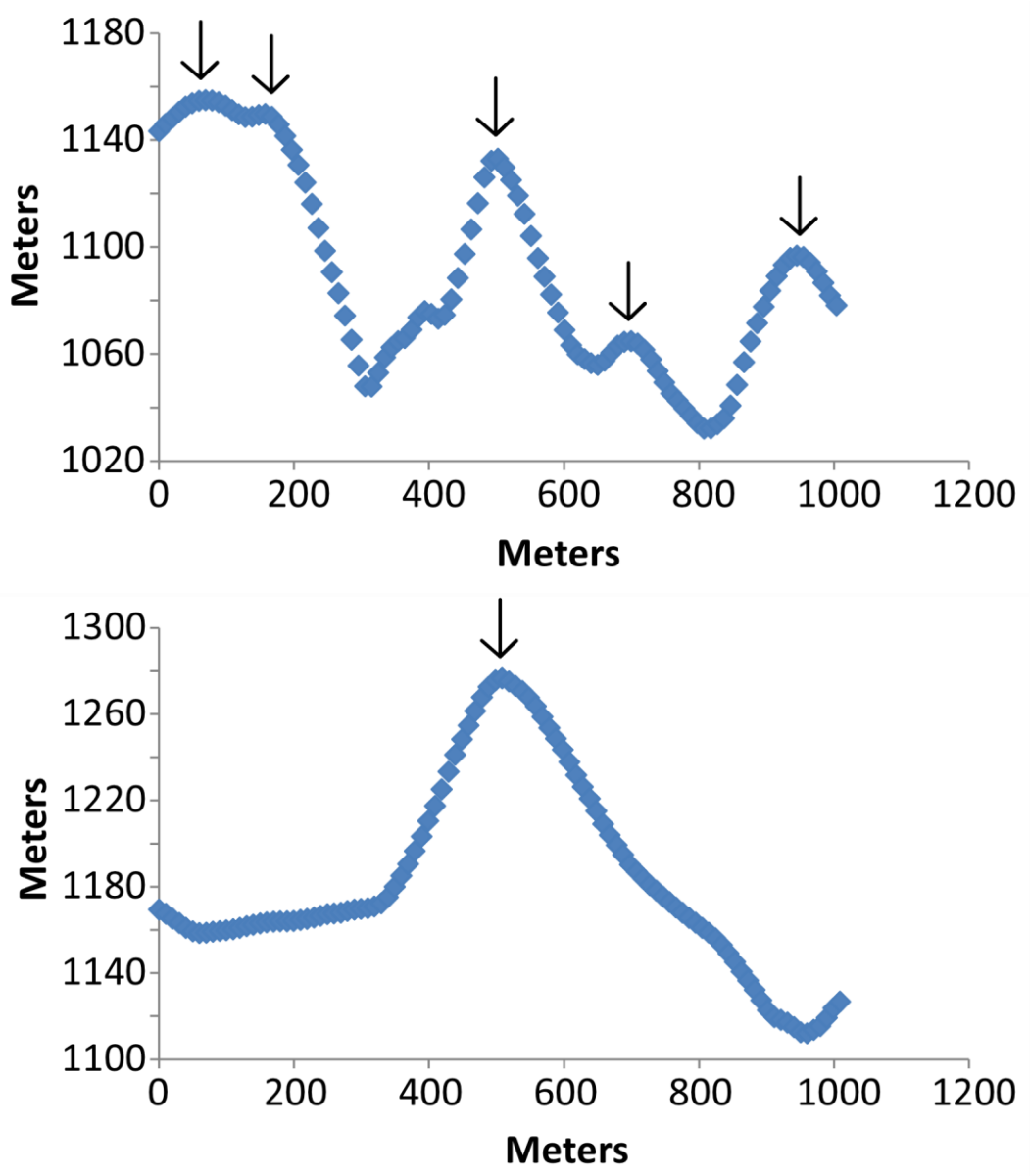

Figure *75*. Topography profiles of the transecting hills of Cluster 97. Hills are denoted with a black arrow.

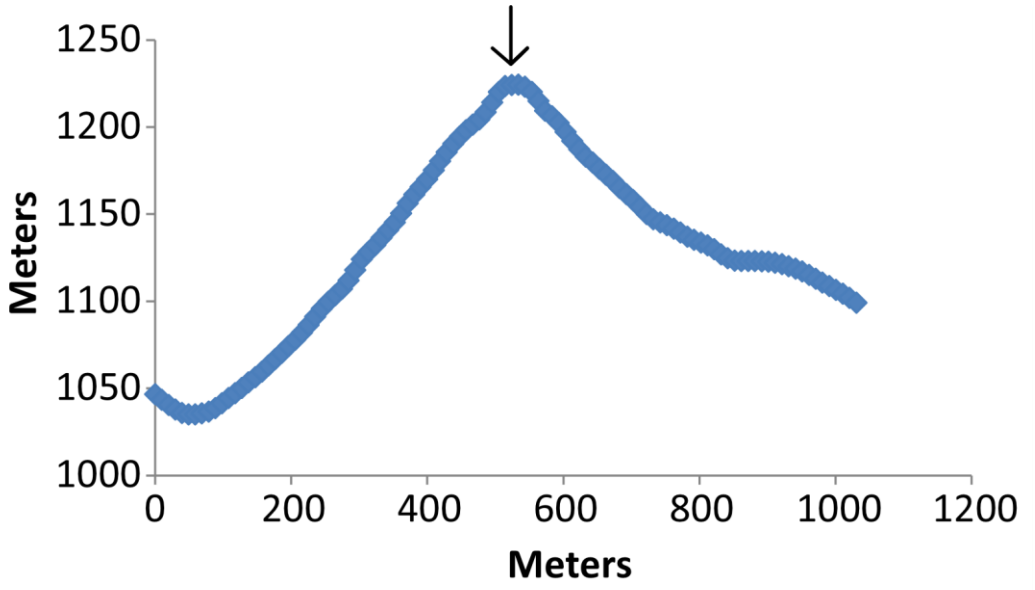

Figure *76*. Topography profiles of the transecting hills of Cluster 98. Hills are denoted with a black arrow.

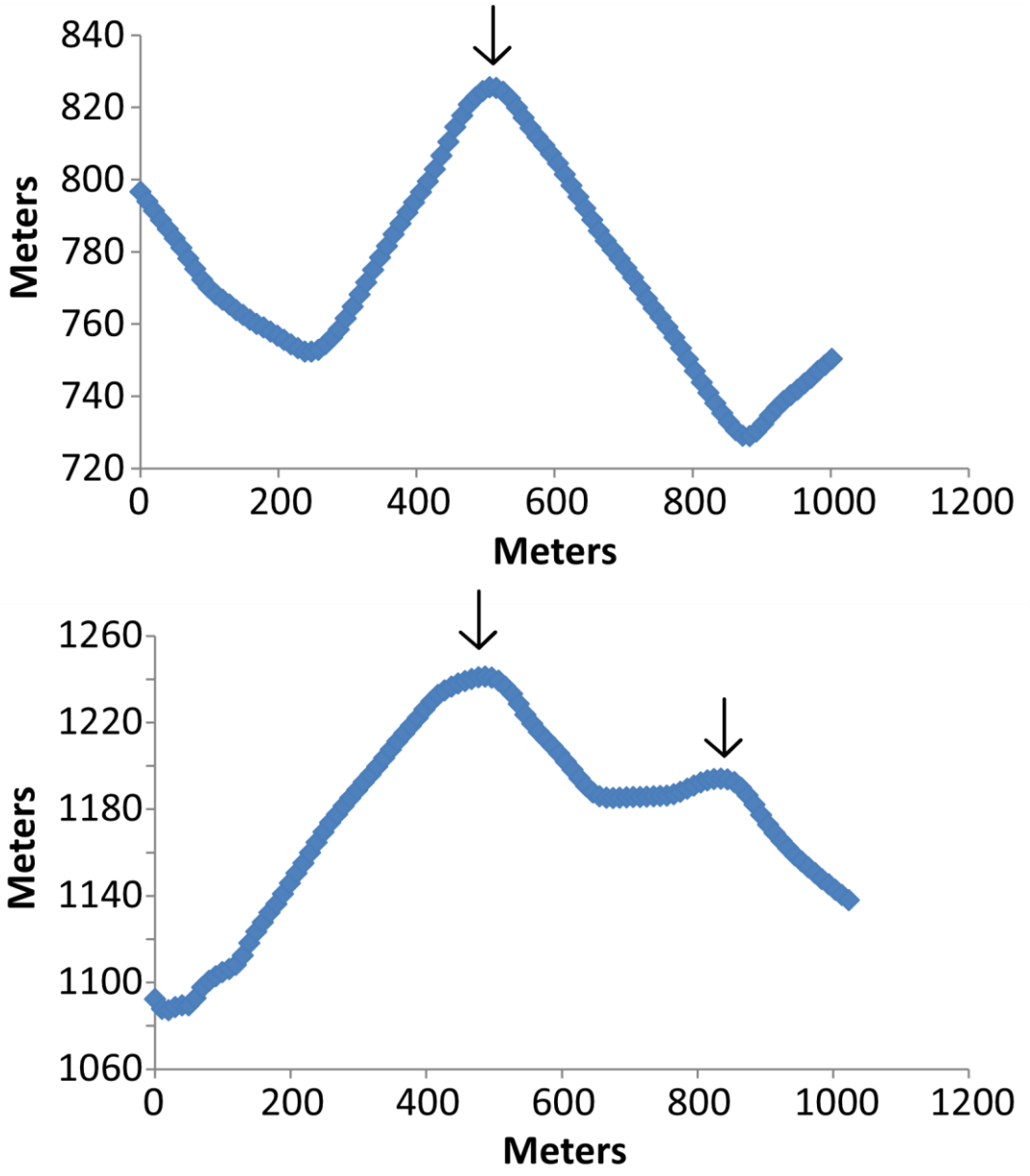

Figure *77*. Topography profiles of the transecting hills of Cluster 99. Hills are denoted with a black arrow.

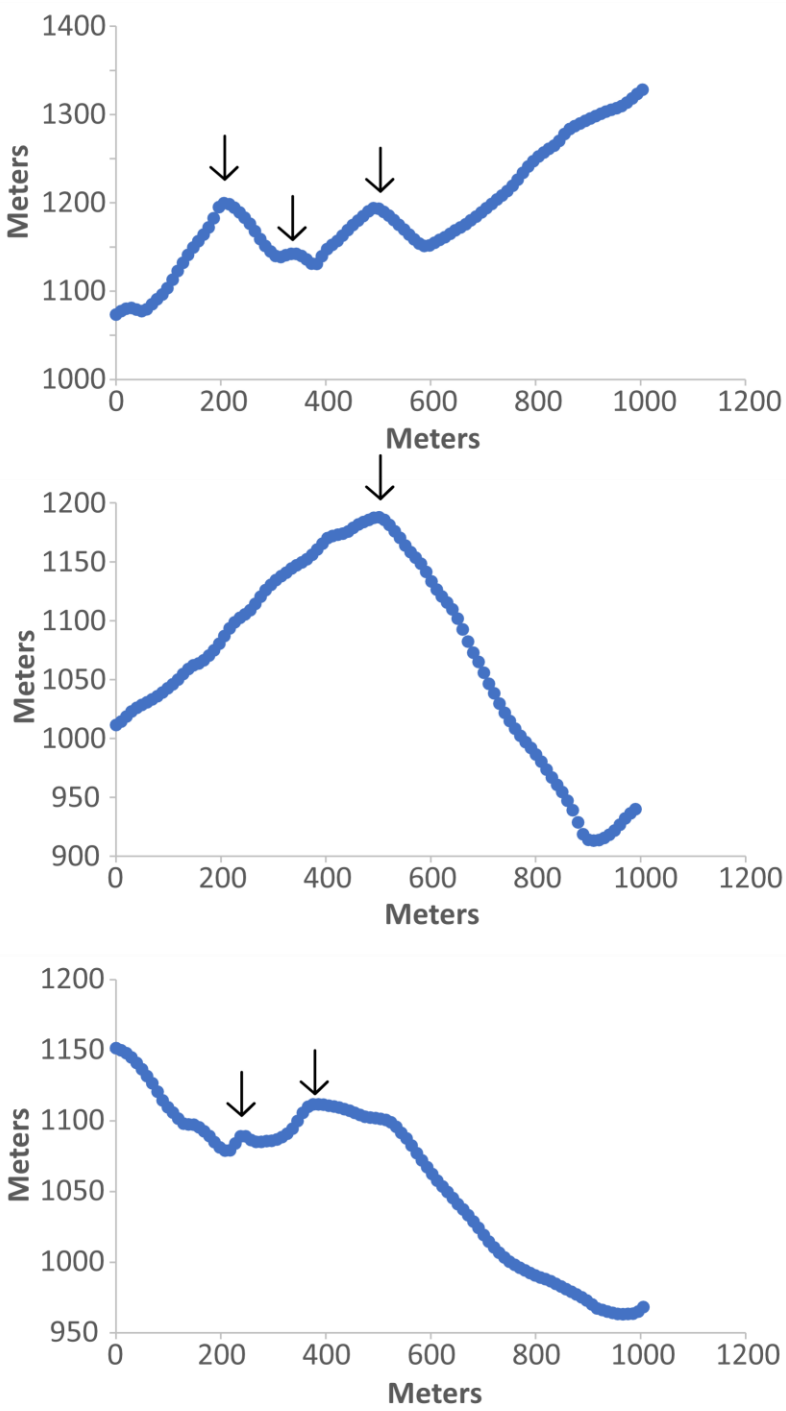

Figure *78*. Topography profiles of the transecting hills of Cluster 101. Hills are denoted with a black arrow.

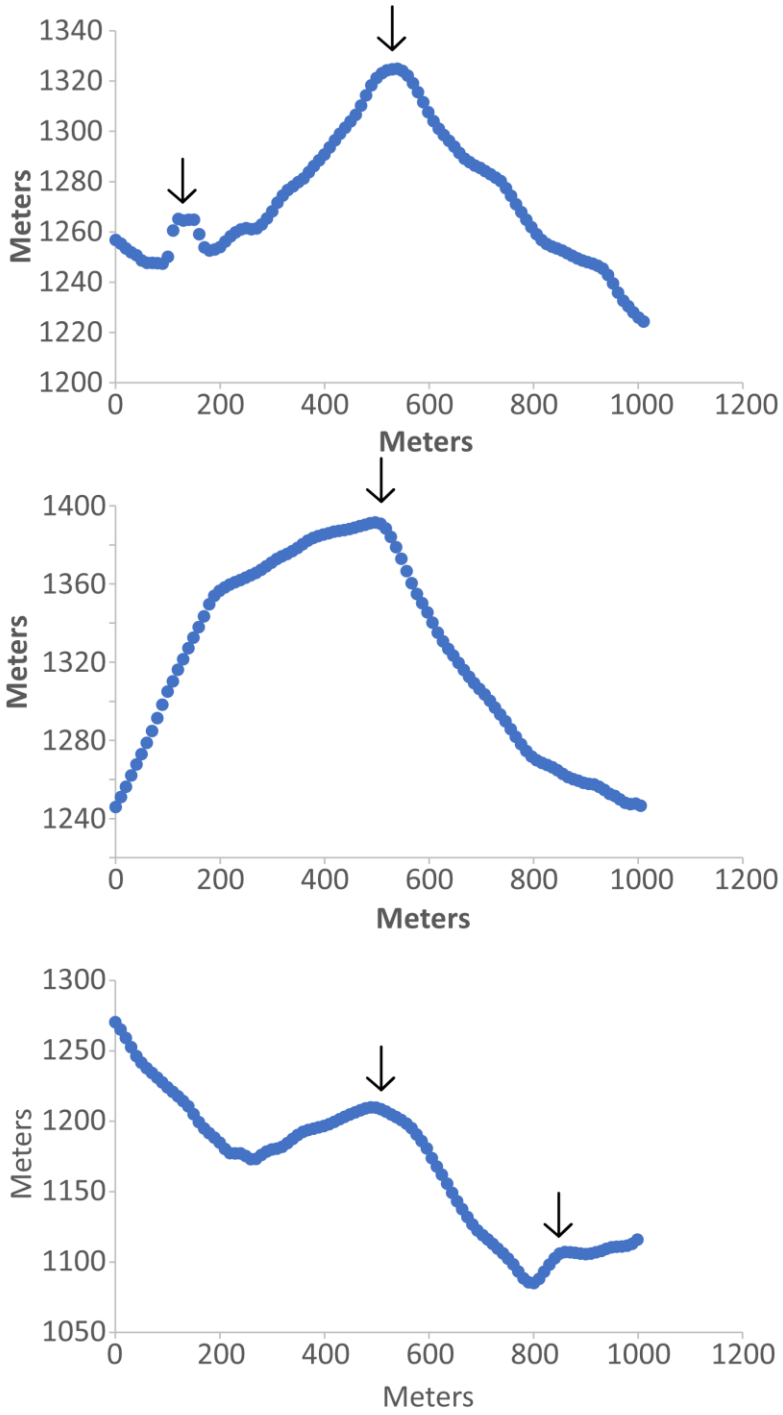

Figure *79*. Topography profiles of the transecting hills of Cluster 102. Hills are denoted with a black arrow.

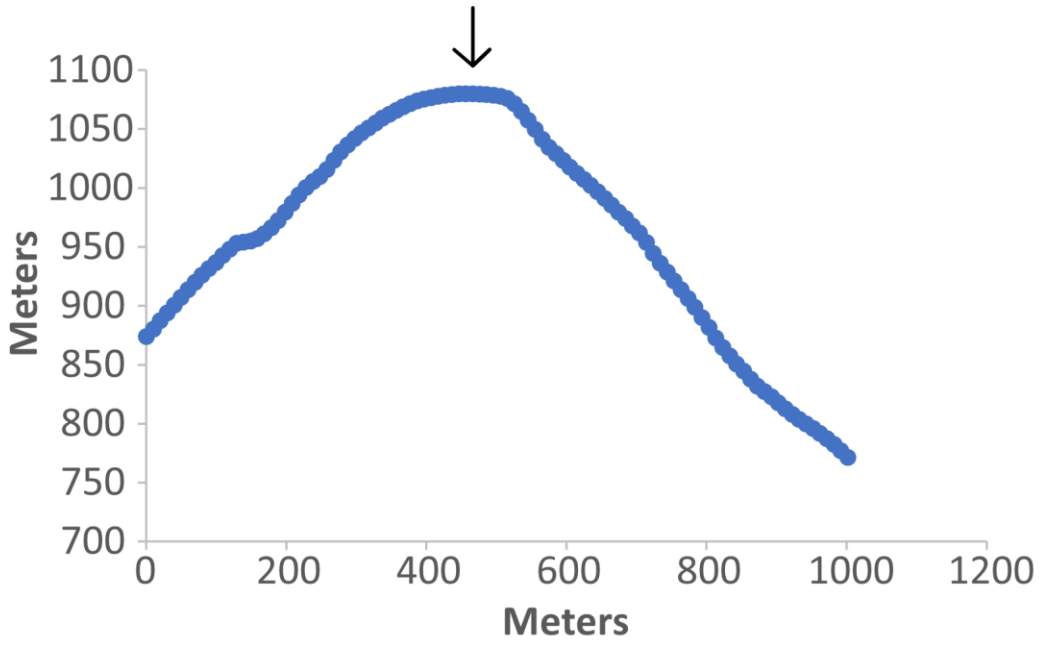

Figure *80*. Topography profiles of the transecting hills of Cluster 104. Hills are denoted with a black arrow.

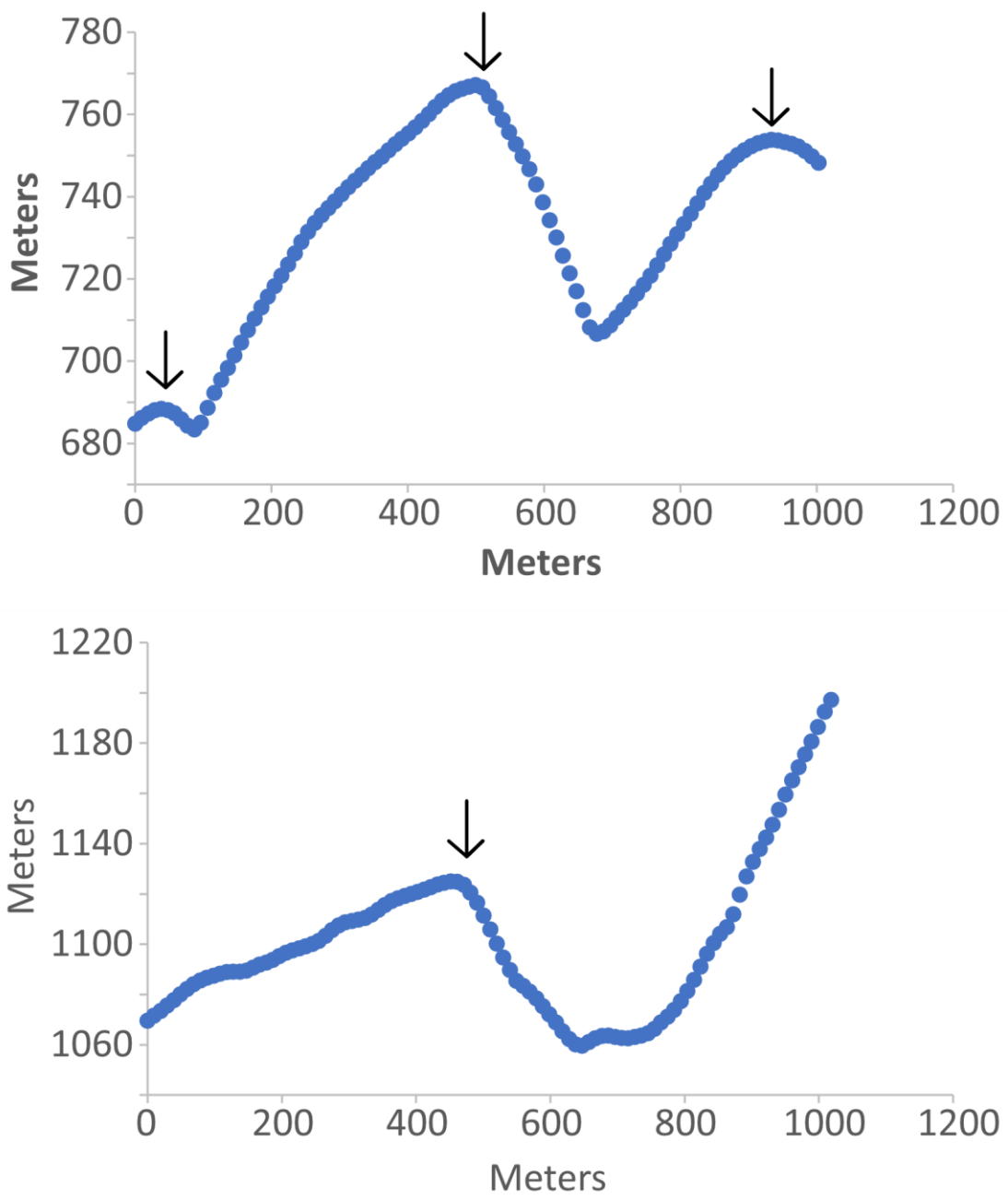

Figure *81*. Topography profiles of the transecting hills of Cluster 106. Hills are denoted with a black arrow.

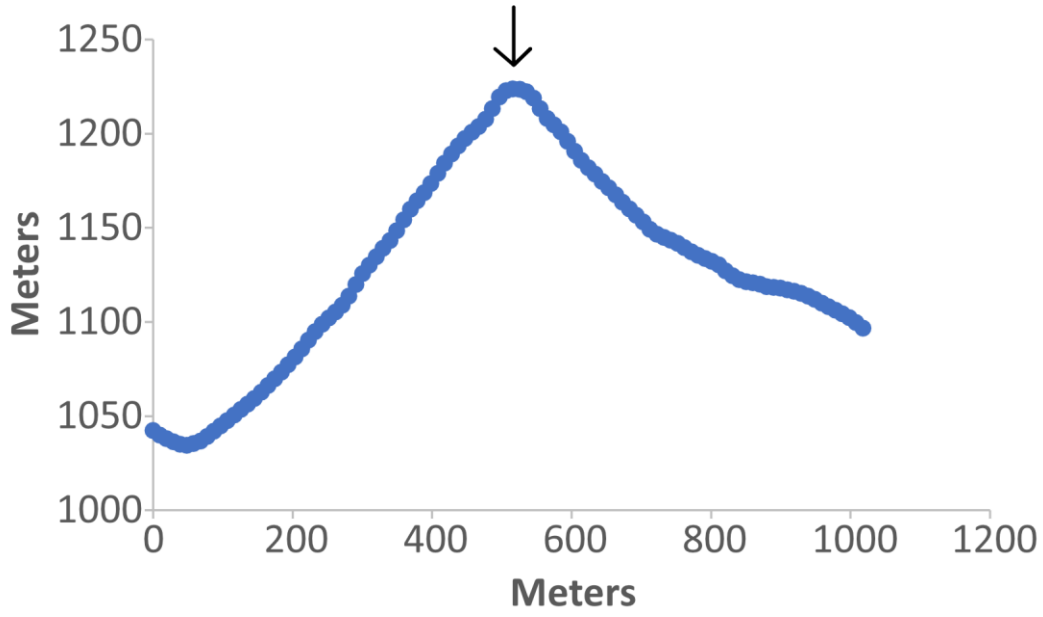

Figure *82*. Topography profiles of the transecting hills of Cluster 107. Hills are denoted with a black arrow.

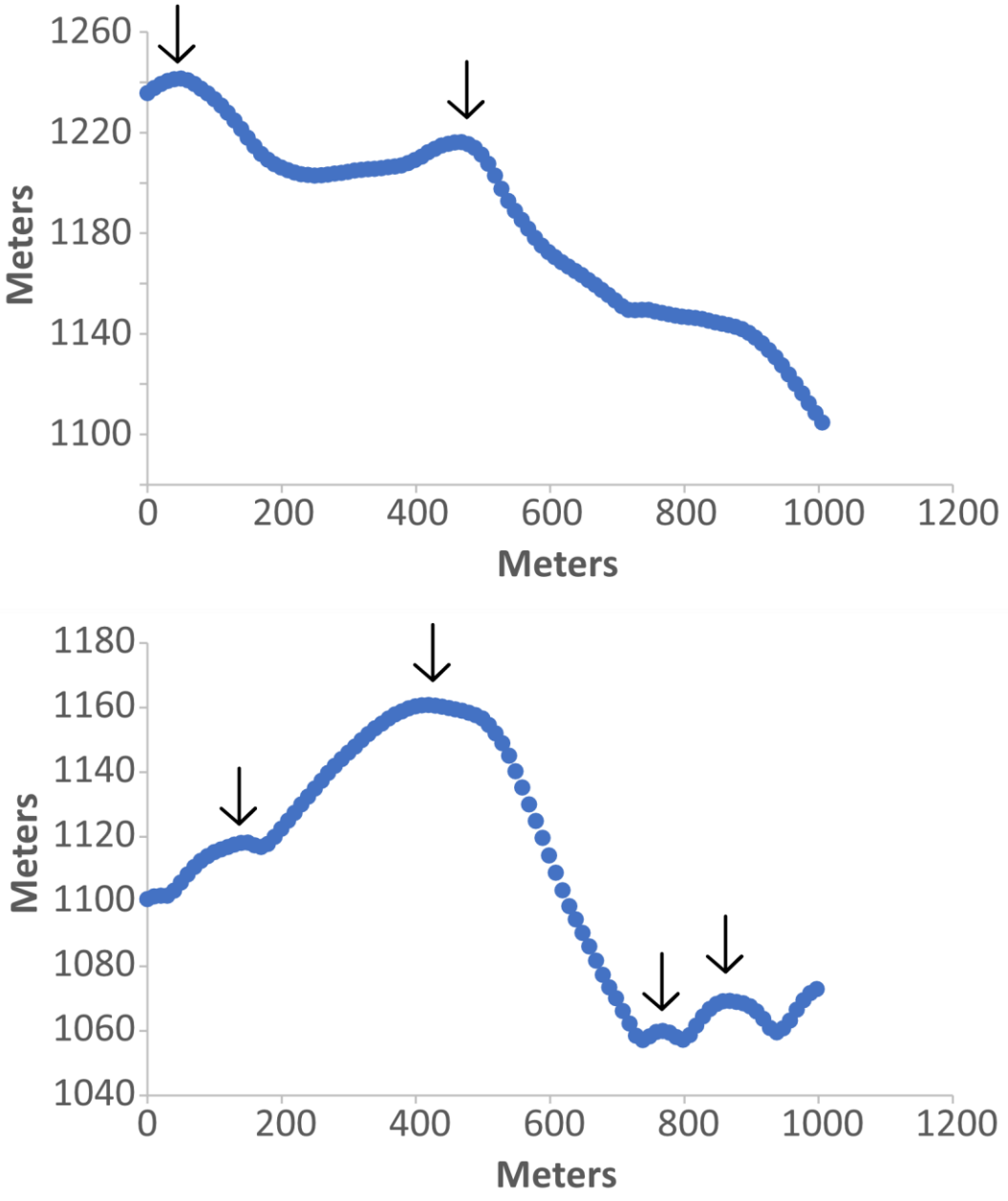

Figure *83*. Topography profiles of the transecting hills of Cluster 108. Hills are denoted with a black arrow.

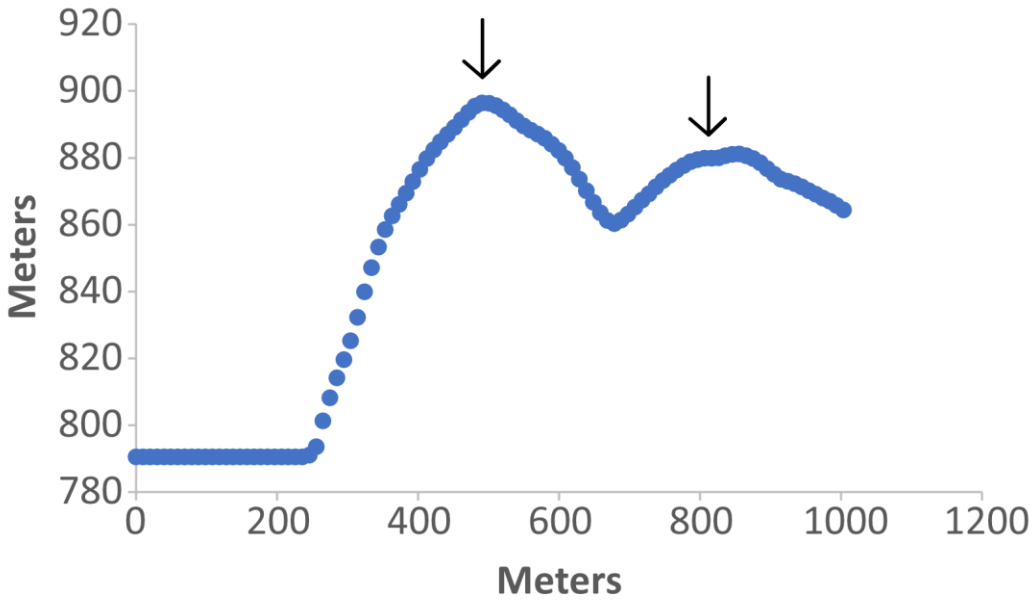

Figure *84*. Topography profiles of the transecting hills of Cluster 109. Hills are denoted with a black arrow.

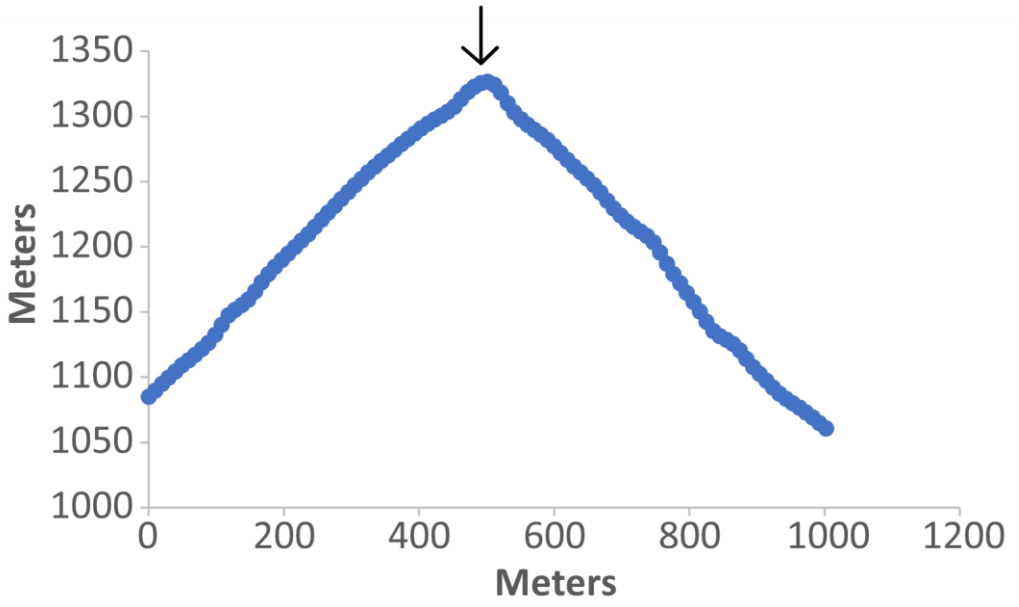

Figure *85*. Topography profiles of the transecting hills of Cluster 110. Hills are denoted with a black arrow.

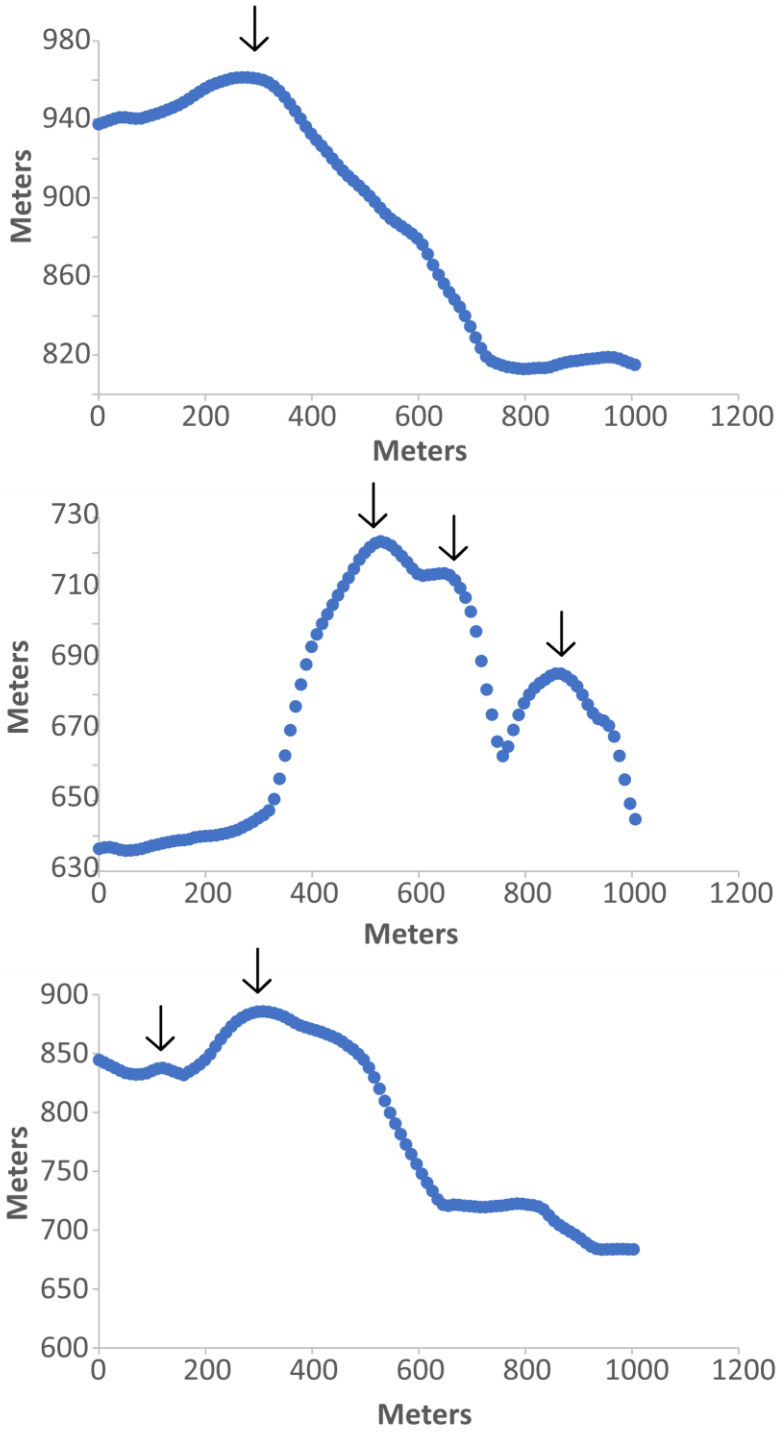

Figure *86*. Topography profiles of the transecting hills of Cluster 111. Hills are denoted with a black arrow.

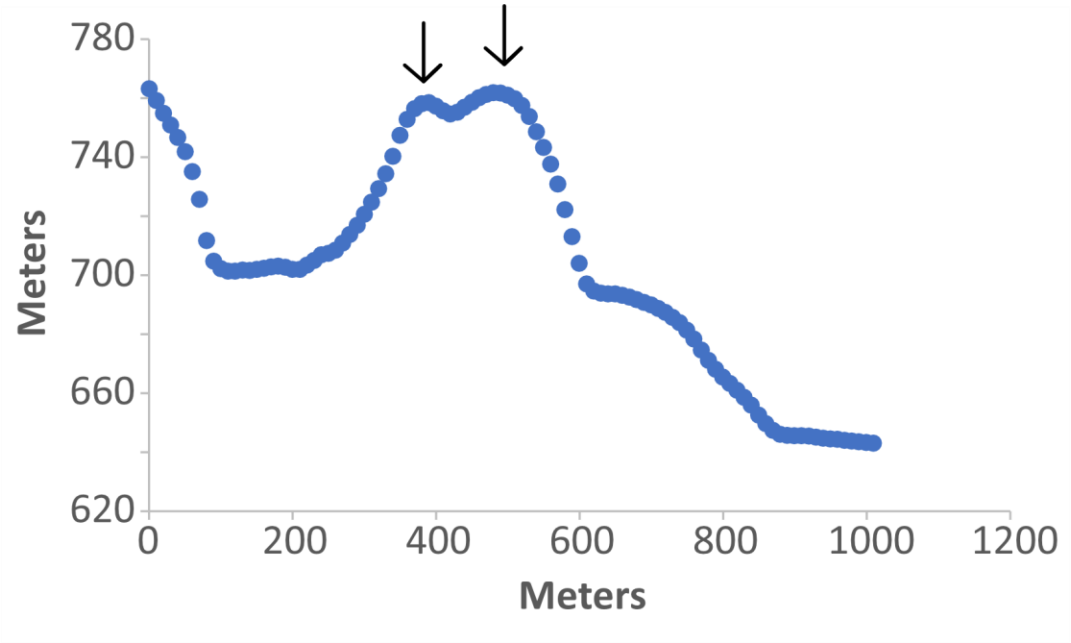

Figure *87*. Topography profiles of the transecting hills of Cluster 112. Hills are denoted with a black arrow.

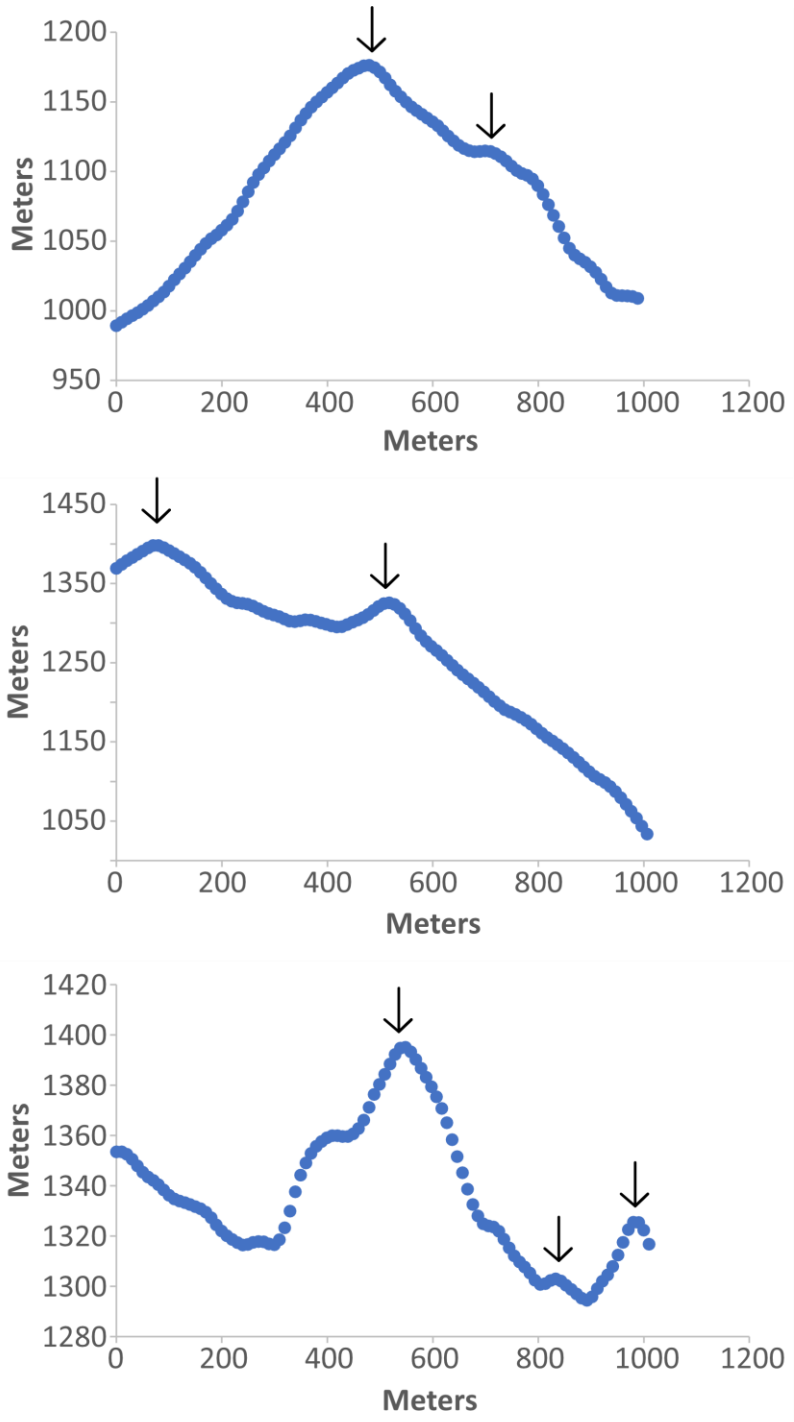

Figure *88*. Topography profiles of the transecting hills of Cluster 113. Hills are denoted with a black arrow.

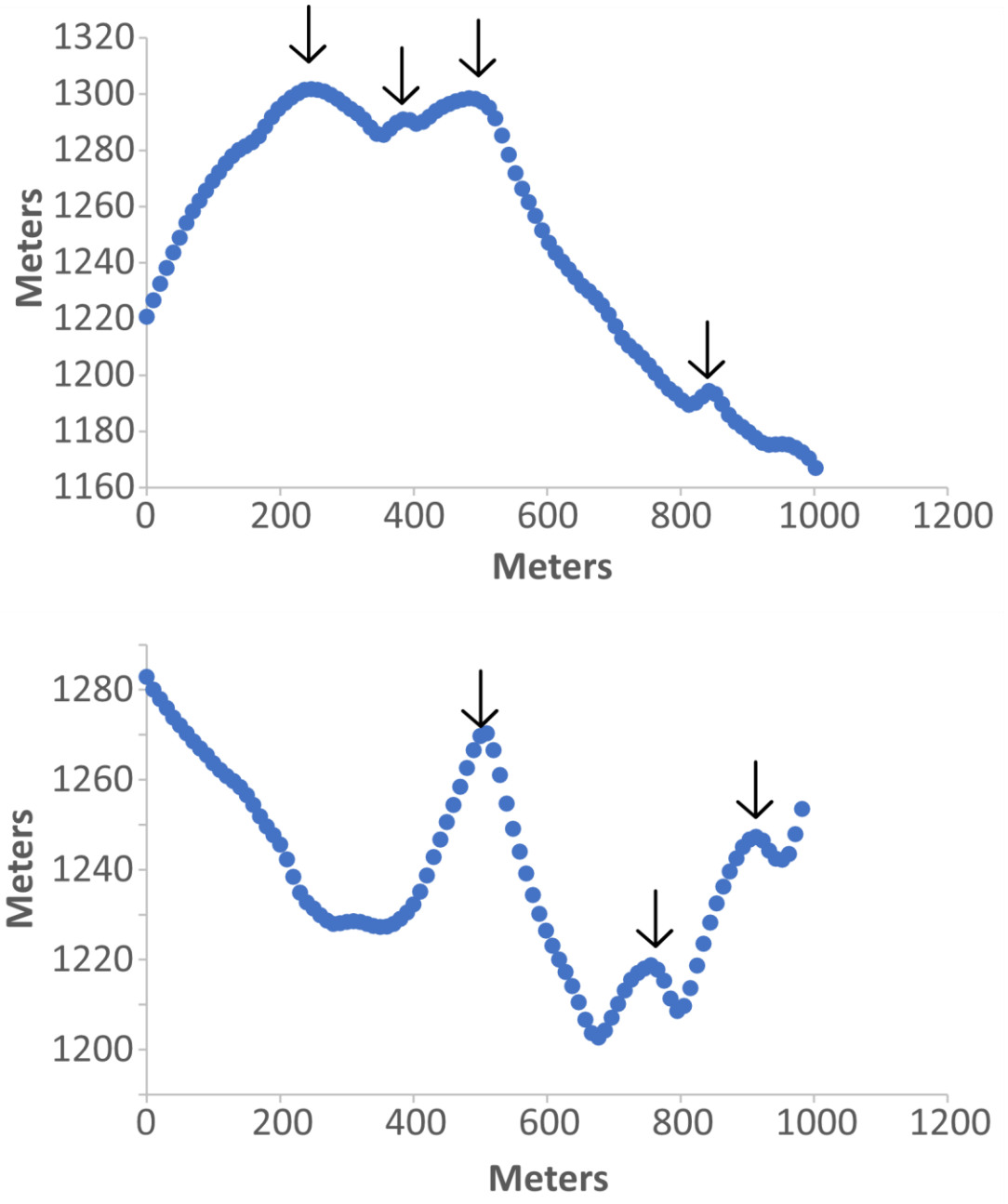

Figure *89*. Topography profiles of the transecting hills of Cluster 115. Hills are denoted with a black arrow.

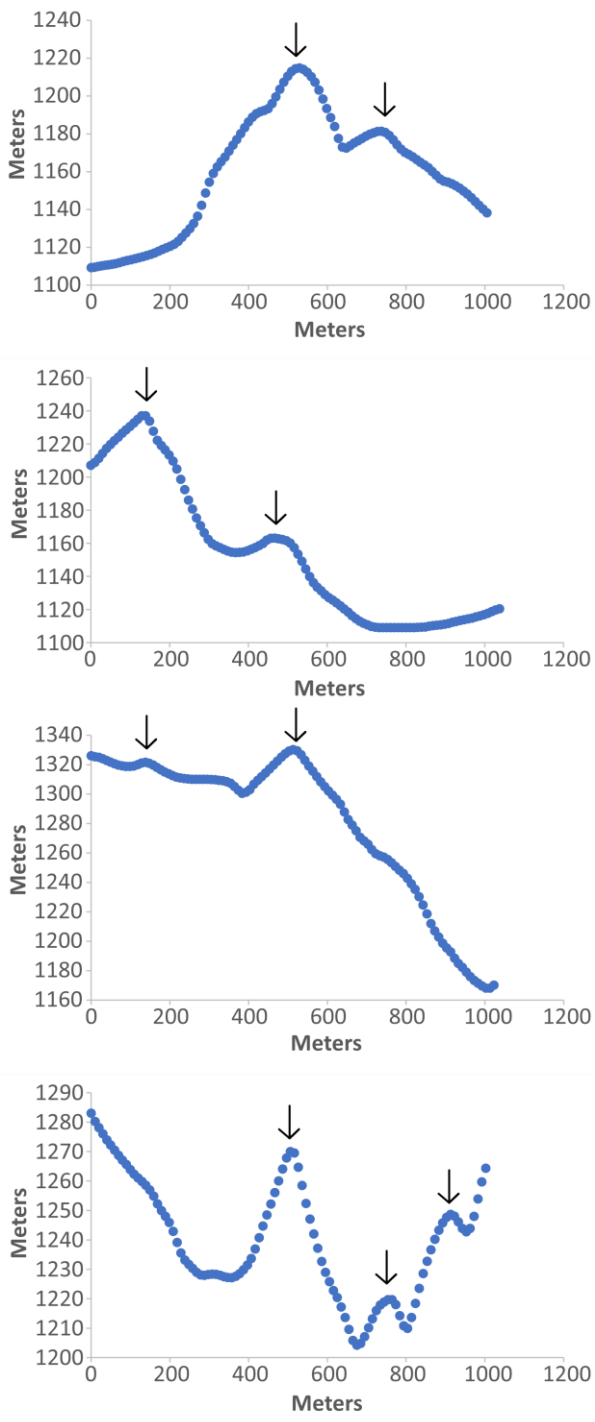

Figure *90*. Topography profiles of the transecting hills of Cluster 116. Hills are denoted with a black arrow.

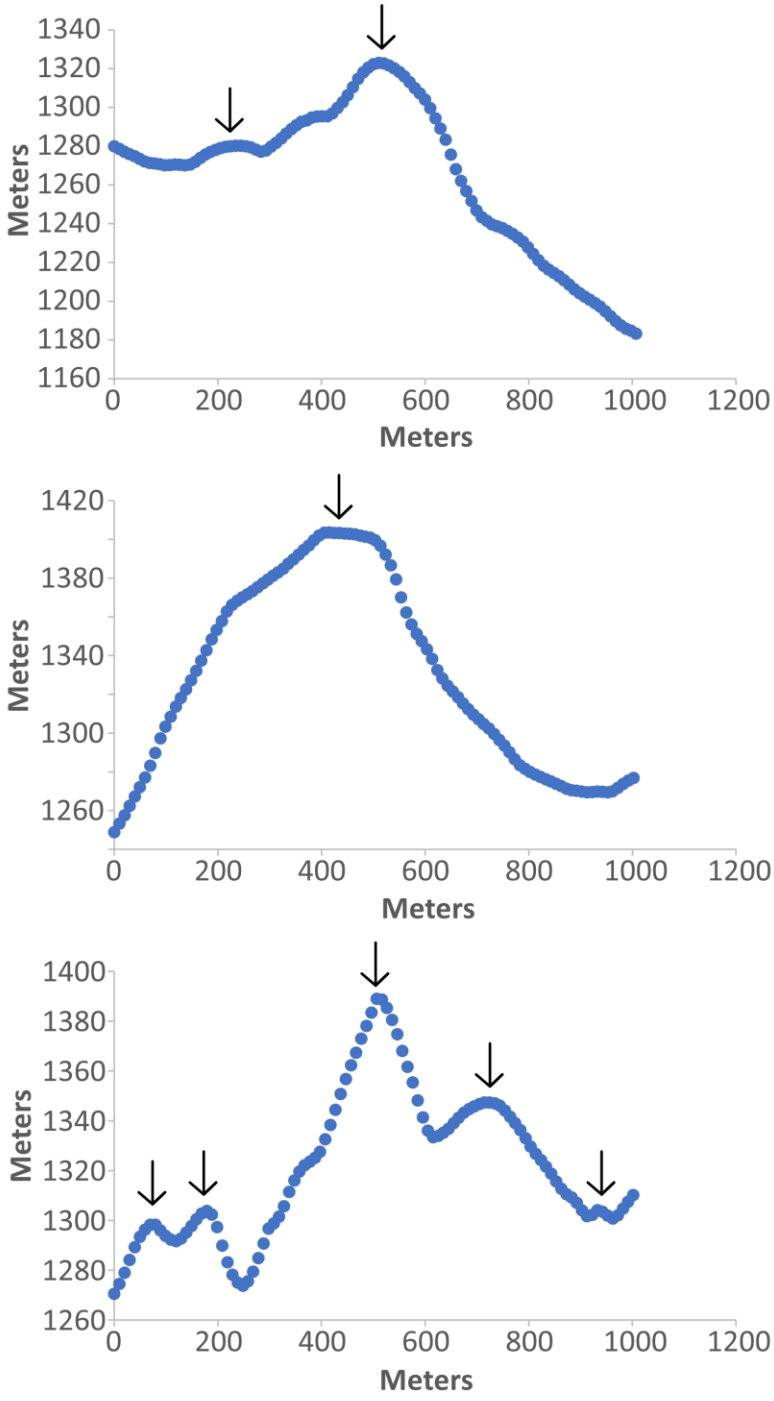

Figure *91*. Topography profiles of the transecting hills of Cluster 117. Hills are denoted with a black arrow.

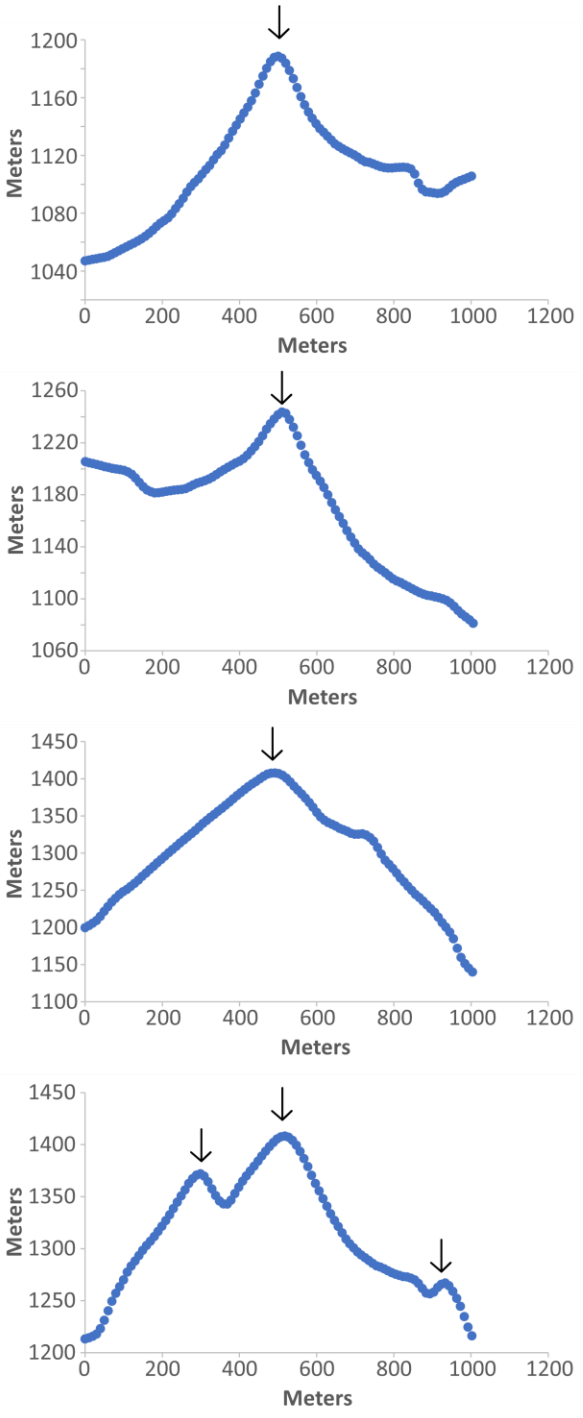

Figure *92*. Topography profiles of the transecting hills of Cluster 118. Hills are denoted with a black arrow.

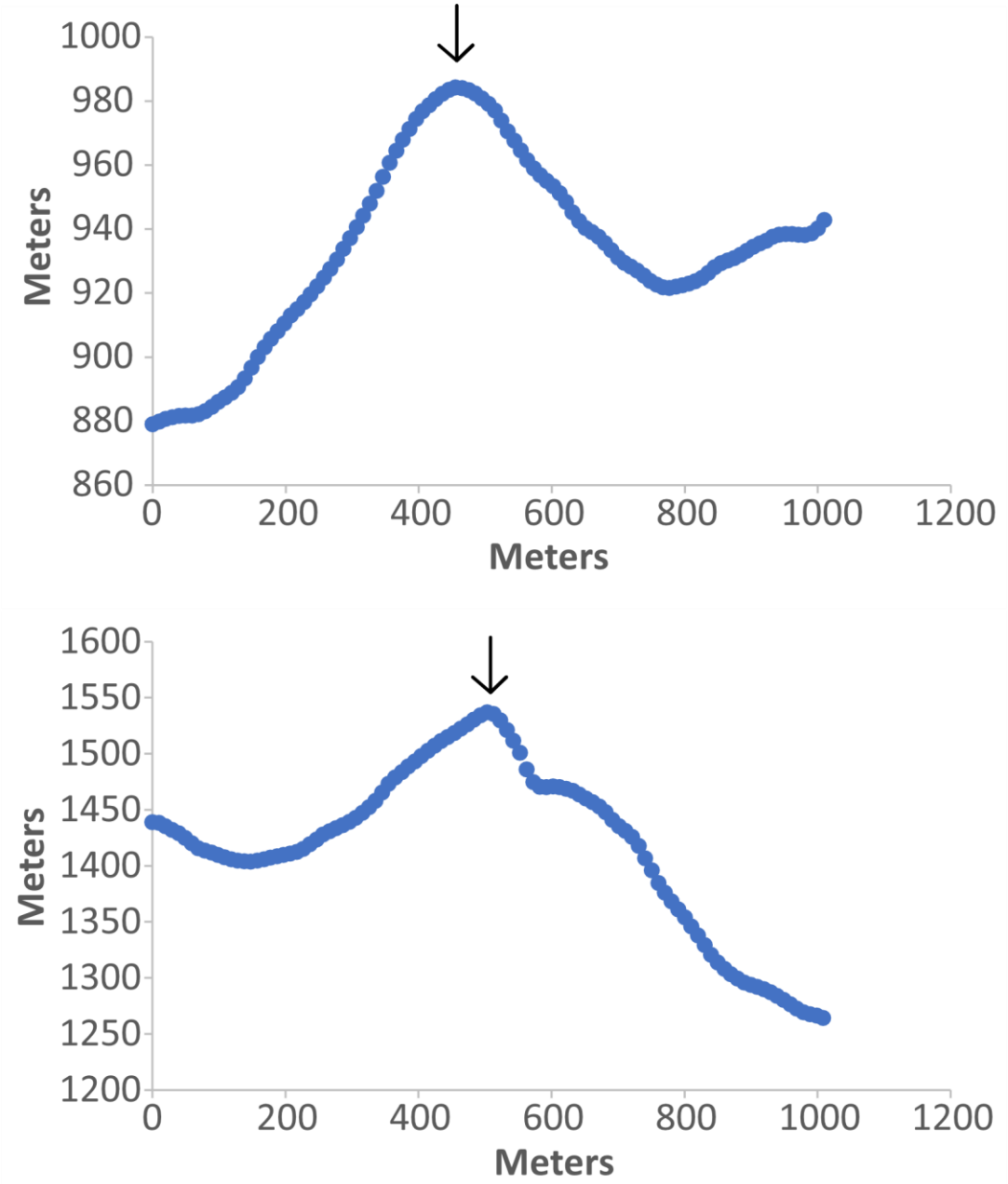

Figure *93*. Topography profiles of the transecting hills of Cluster 119. Hills are denoted with a black arrow.

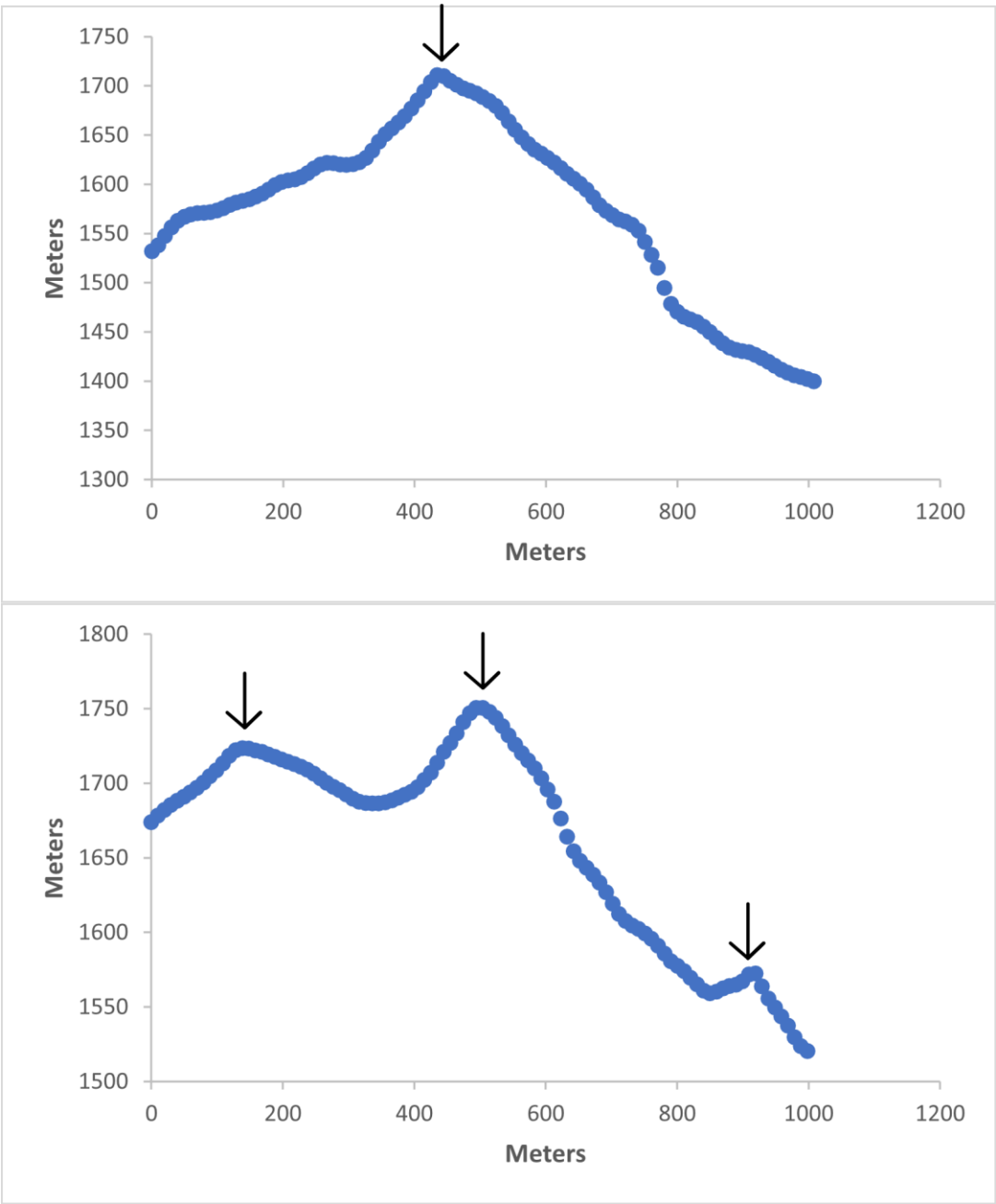

Figure *94*. Topography profiles of the transecting hills of Cluster 120. Hills are denoted with a black arrow.

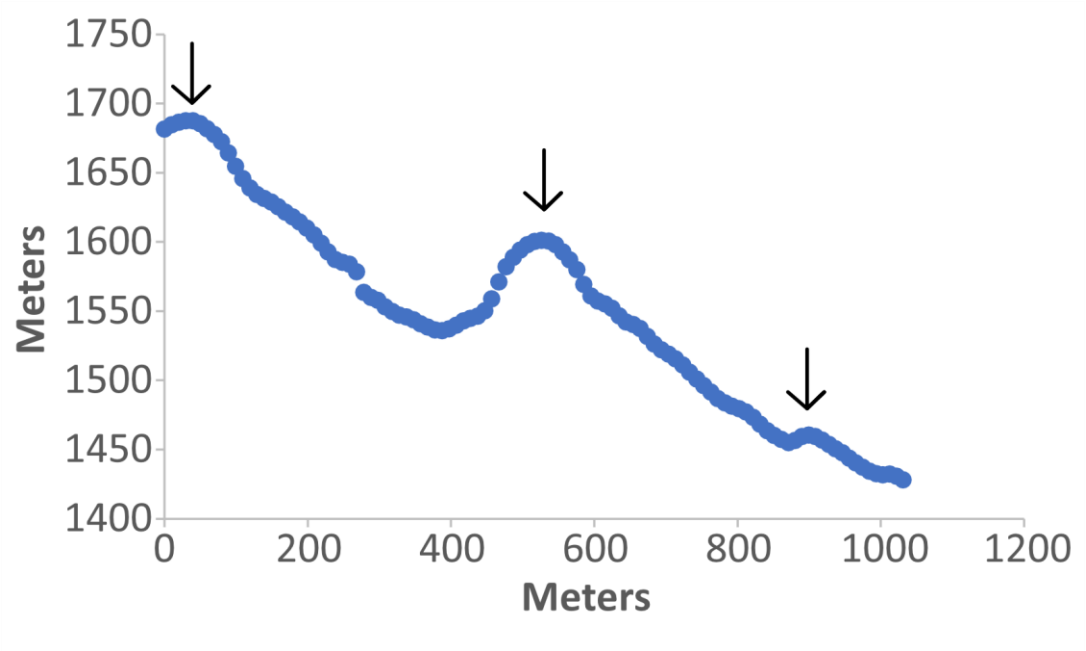

Figure *95*. Topography profiles of the transecting hills of Cluster 121. Hills are denoted with a black arrow.

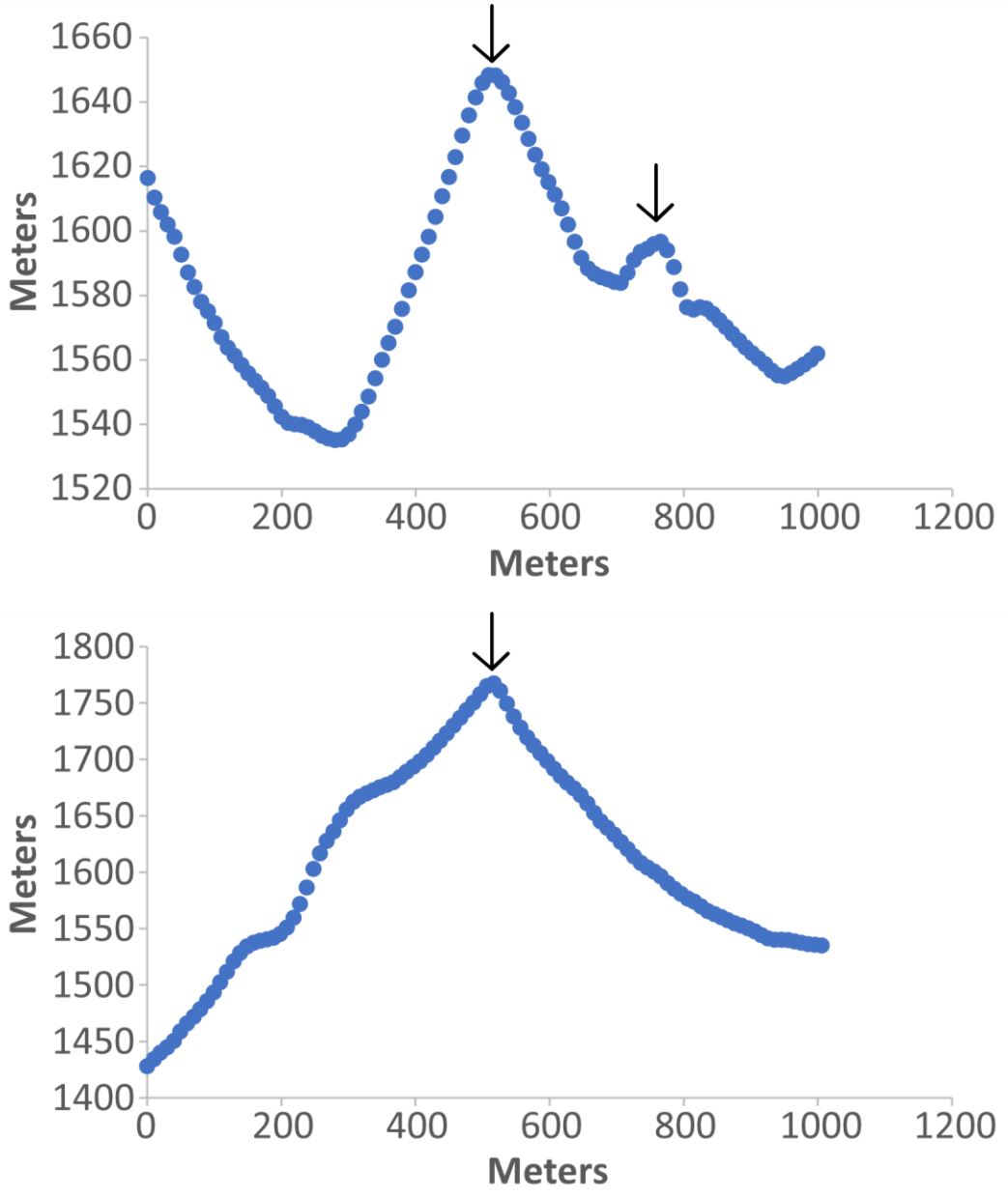

Figure *96*. Topography profiles of the transecting hills of Cluster 122. Hills are denoted with a black arrow.

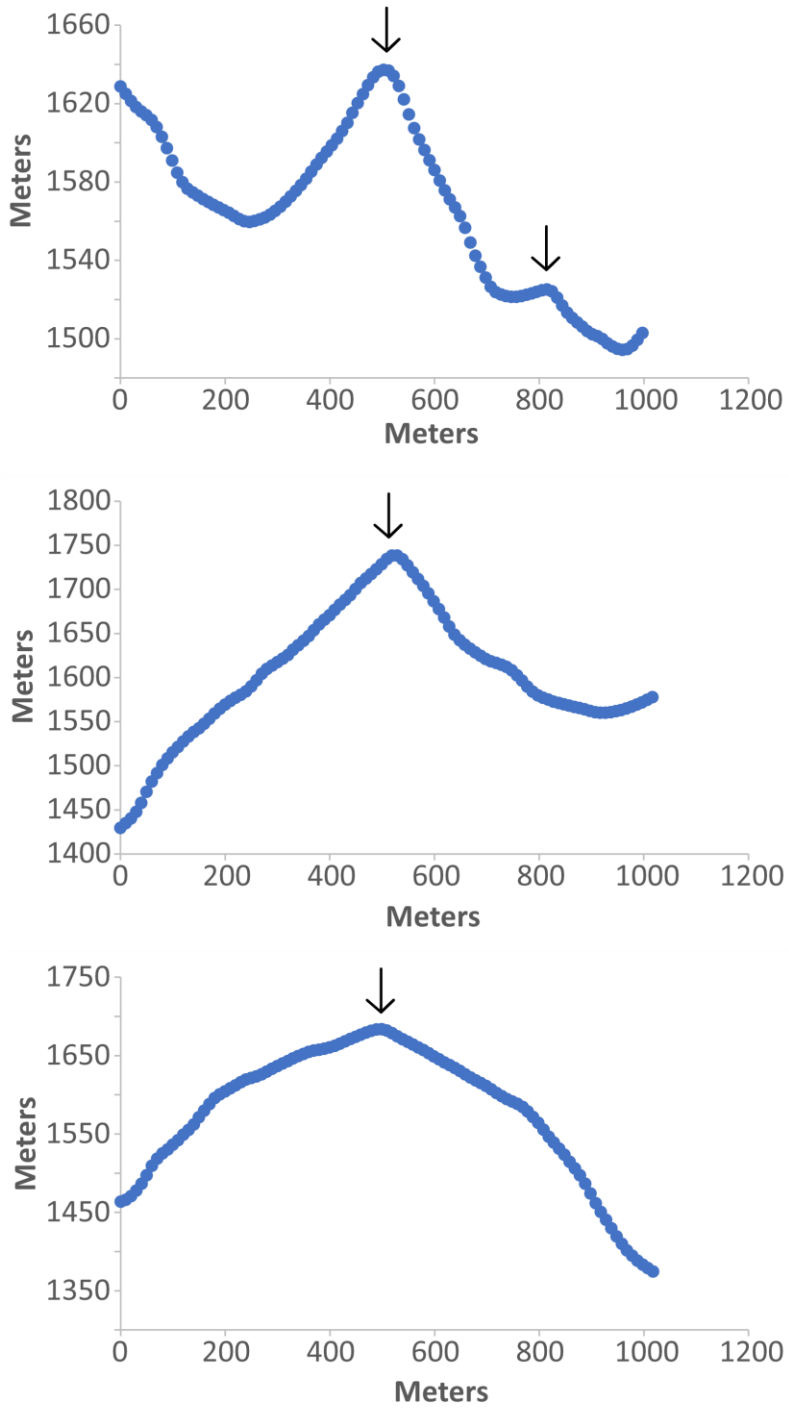

Figure *97*. Topography profiles of the transecting hills of Cluster 123. Hills are denoted with a black arrow.

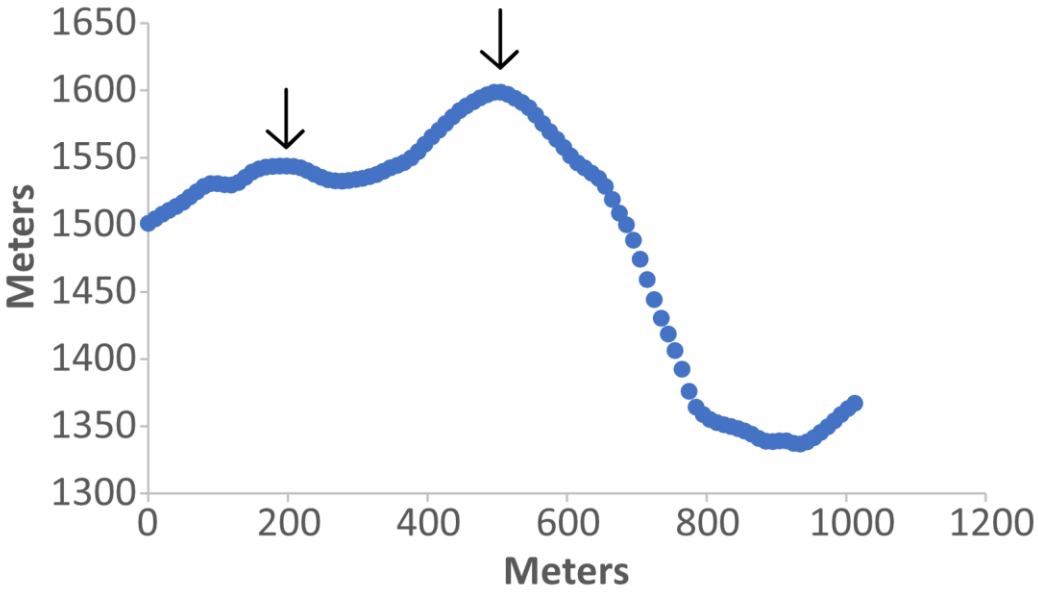

Figure *98*. Topography profiles of the transecting hills of Cluster 124. Hills are denoted with a black arrow.

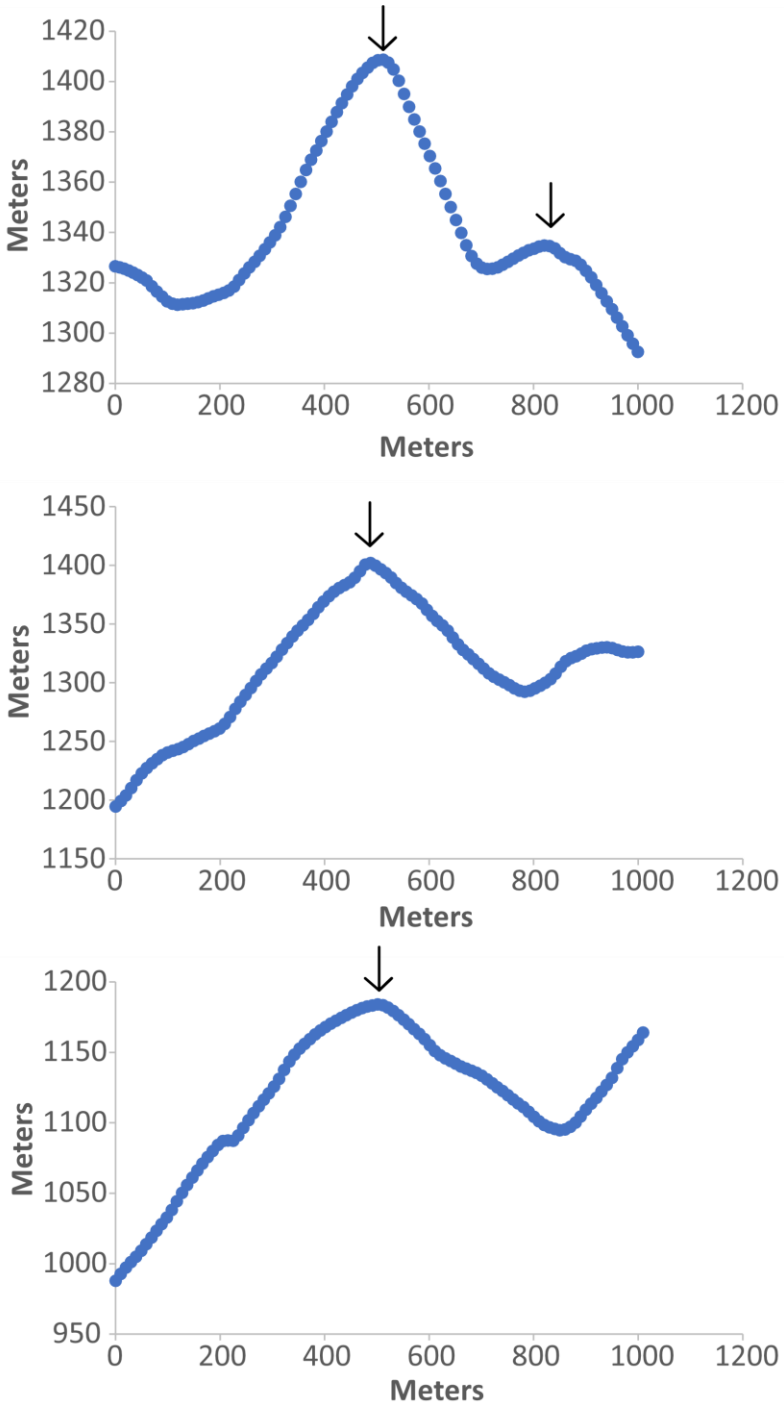

Figure *99*. Topography profiles of the transecting hills of Cluster 125. Hills are denoted with a black arrow.

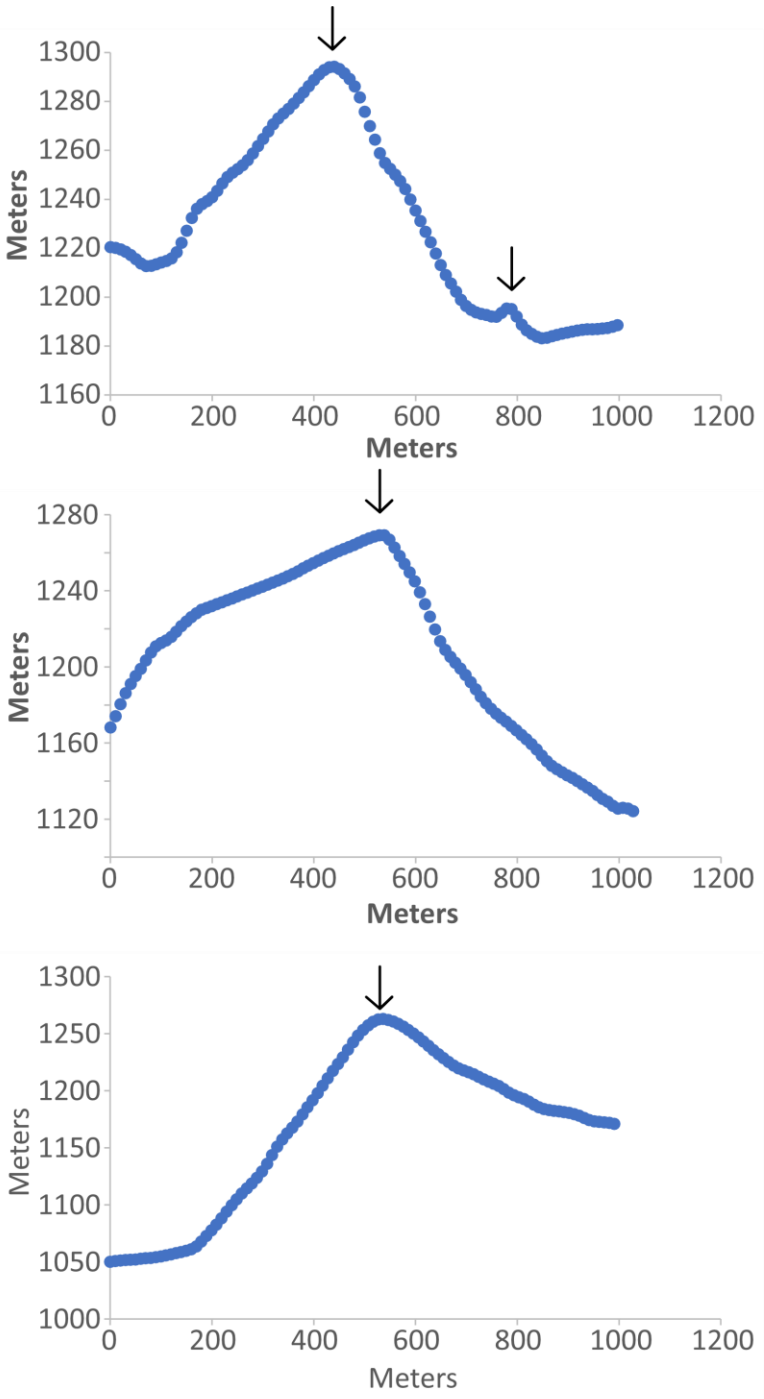

Figure *100*. Topography profiles of the transecting hills of Cluster 126. Hills are denoted with a black arrow.

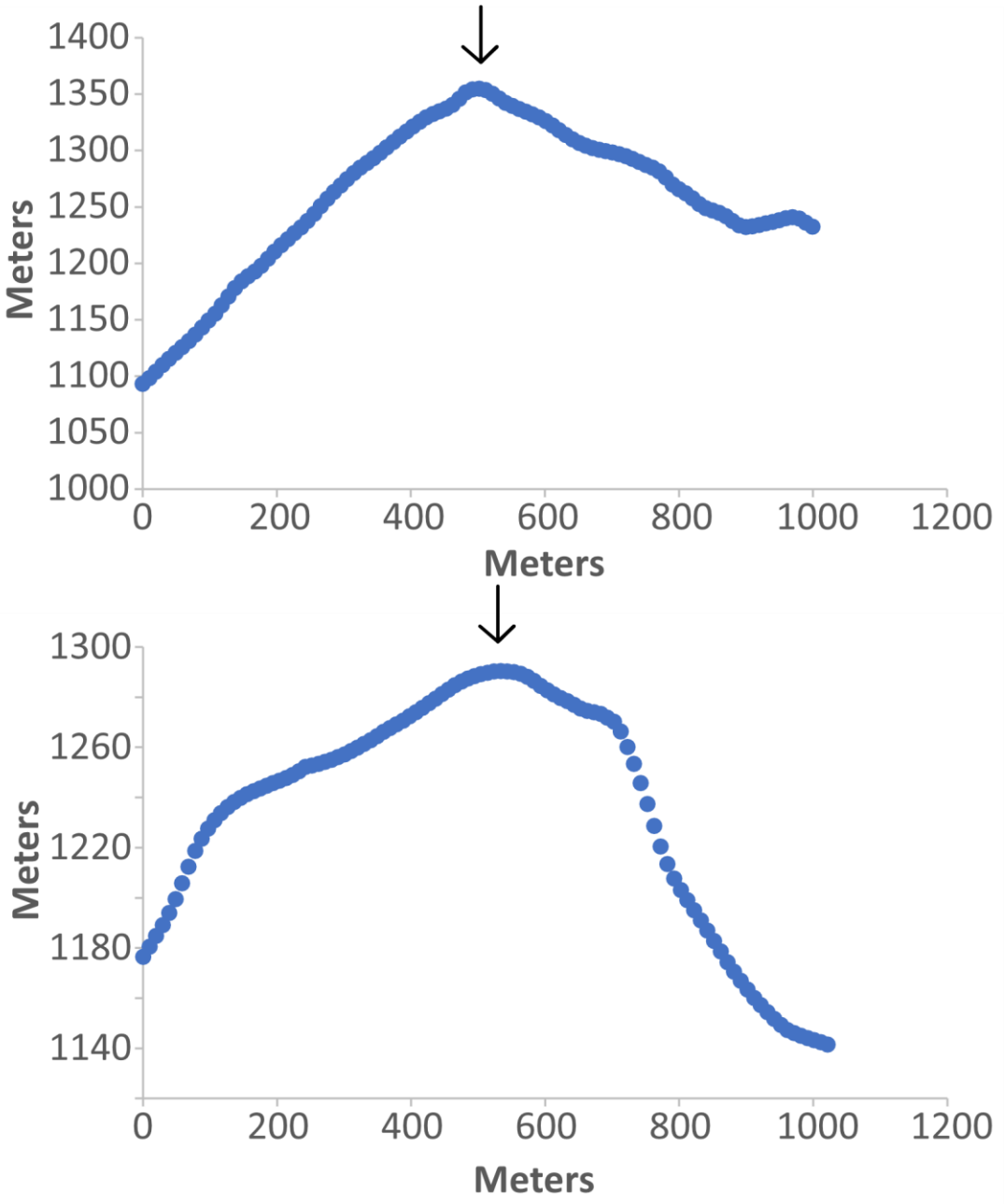

Figure *101*. Topography profiles of the transecting hills of Cluster 127. Hills are denoted with a black arrow.

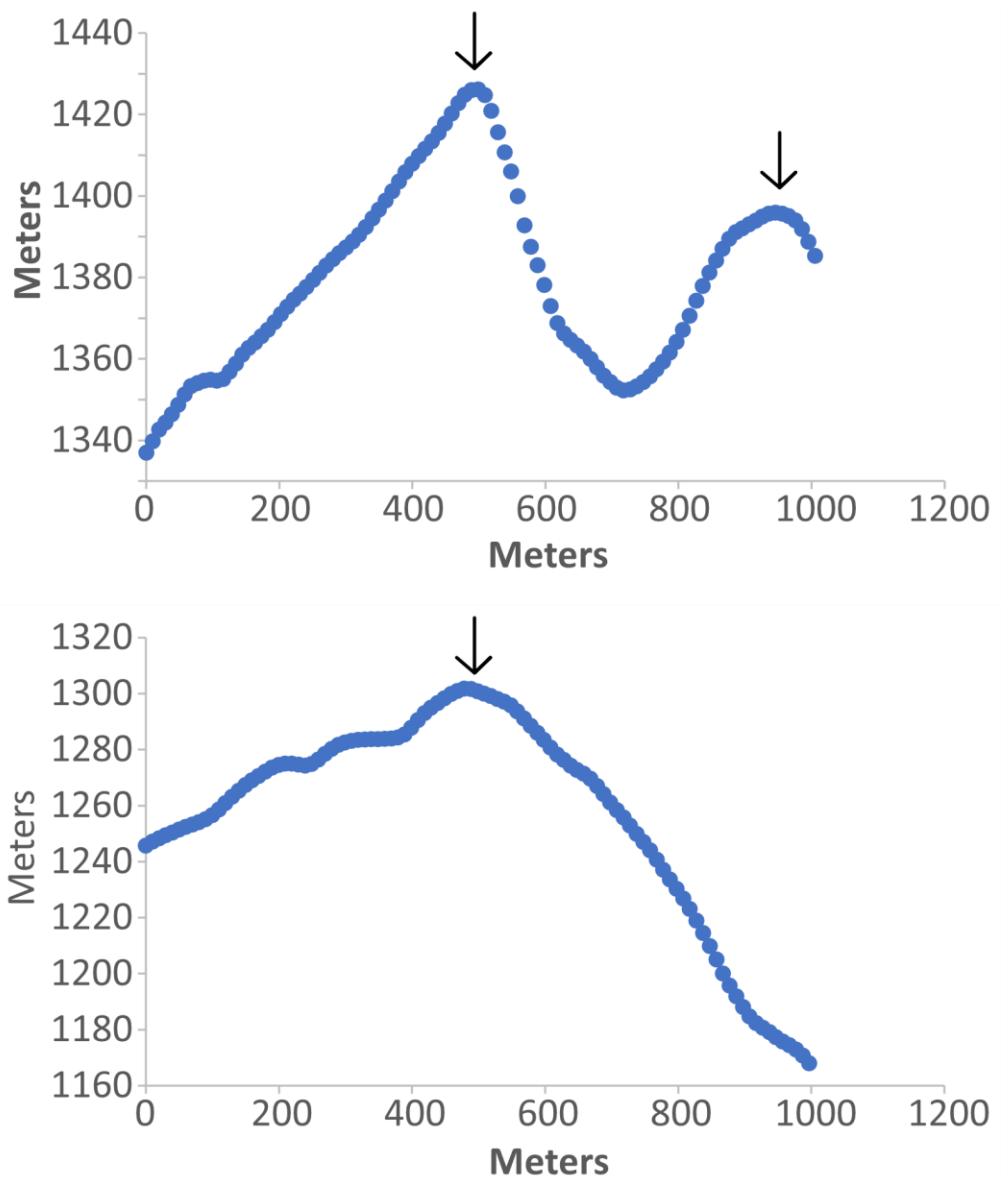

Figure *102*. Topography profiles of the transecting hills of Cluster 128. Hills are denoted with a black arrow.

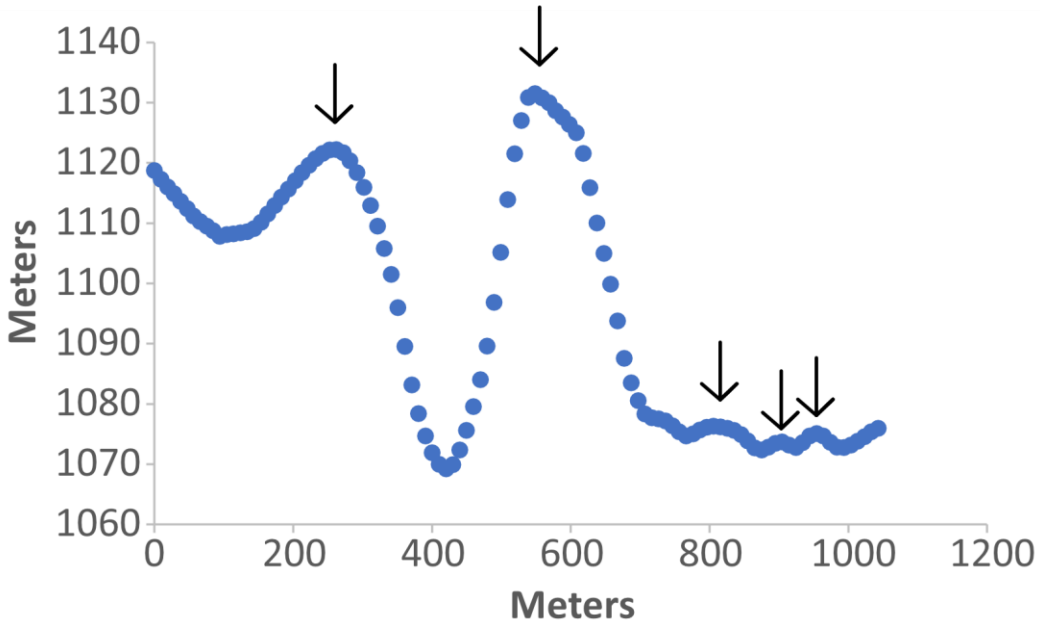

Figure *103*. Topography profiles of the transecting hills of Cluster 131. Hills are denoted with a black arrow.

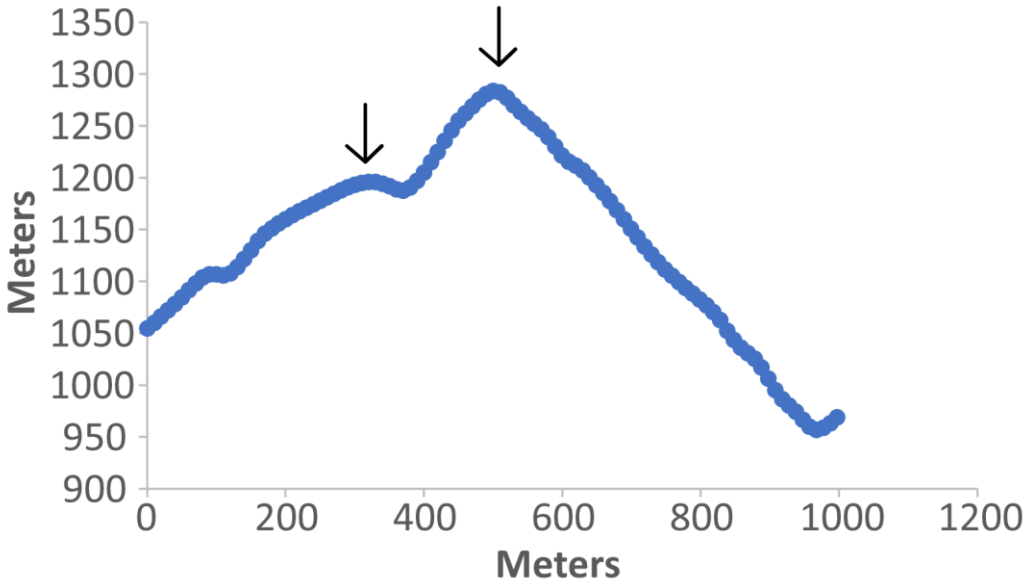

Figure *102*. Topography profiles of the transecting hills of Cluster 132. Hills are denoted with a black arrow.

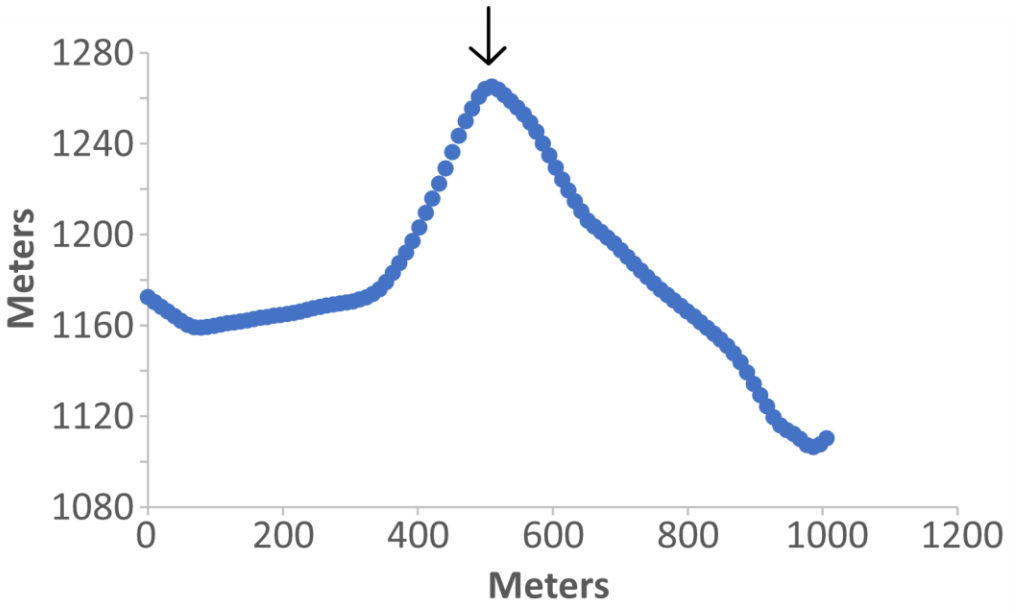

Figure *103*. Topography profiles of the transecting hills of Cluster 133. Hills are denoted with a black arrow.

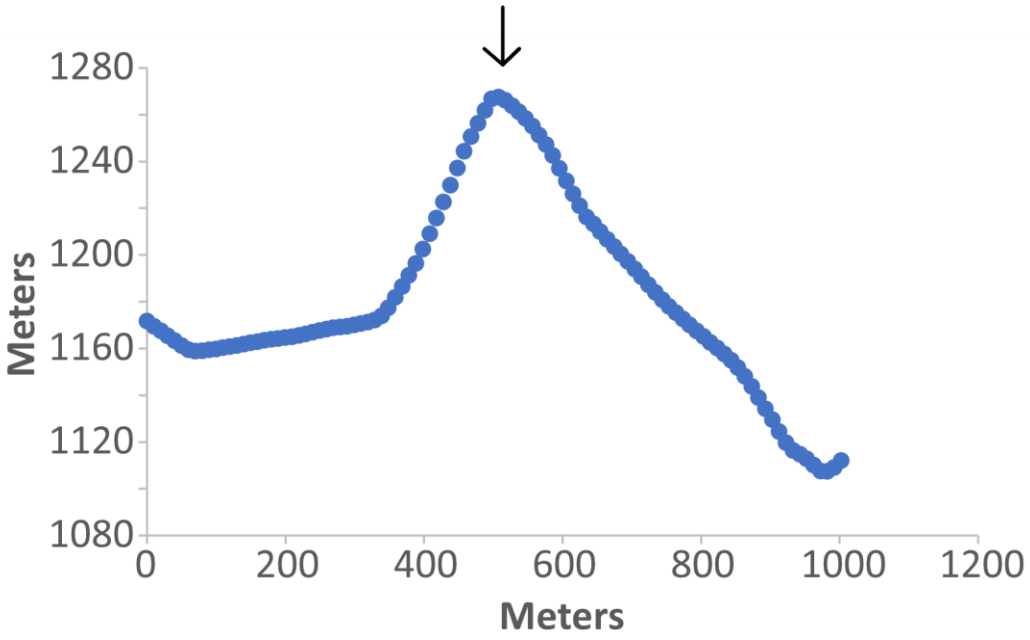

Figure *104*. Topography profiles of the transecting hills of Cluster 134. Hills are denoted with a black arrow.

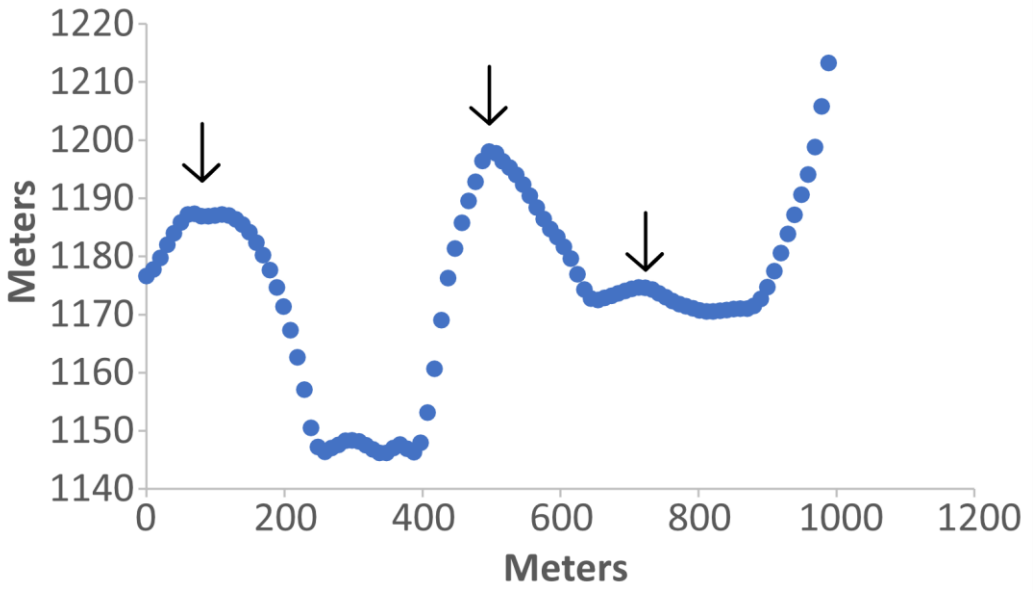

Figure *105*. Topography profiles of the transecting hills of Cluster 135. Hills are denoted with a black arrow.

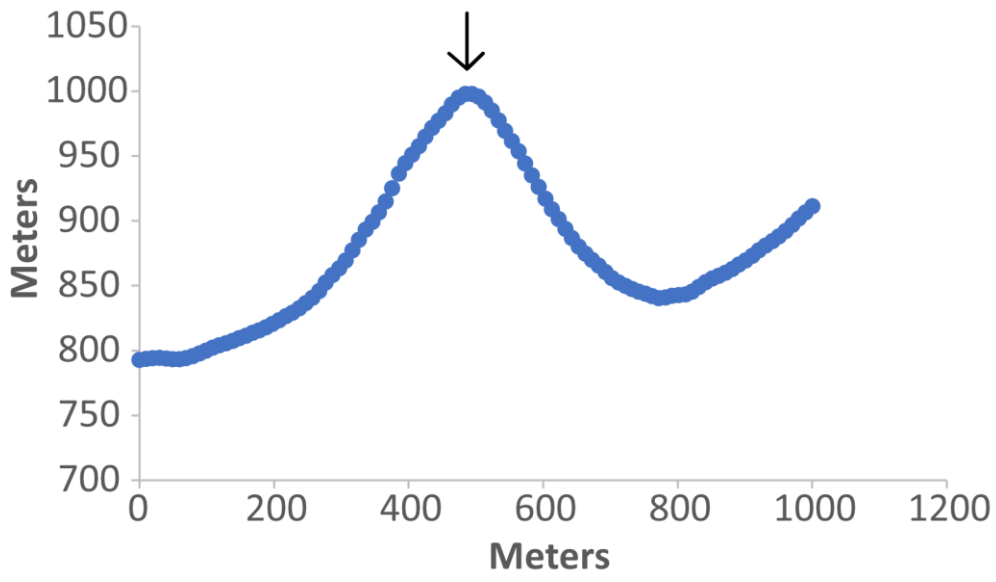

Figure *106*. Topography profiles of the transecting hills of Cluster 137. Hills are denoted with a black arrow.

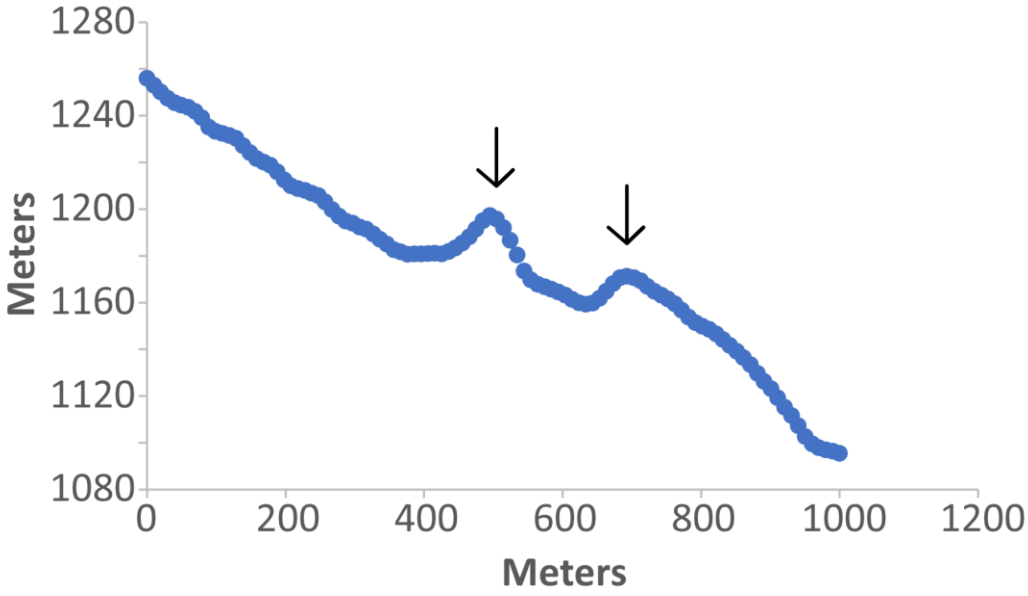

Figure *107*. Topography profiles of the transecting hills of Cluster 138. Hills are denoted with a black arrow.

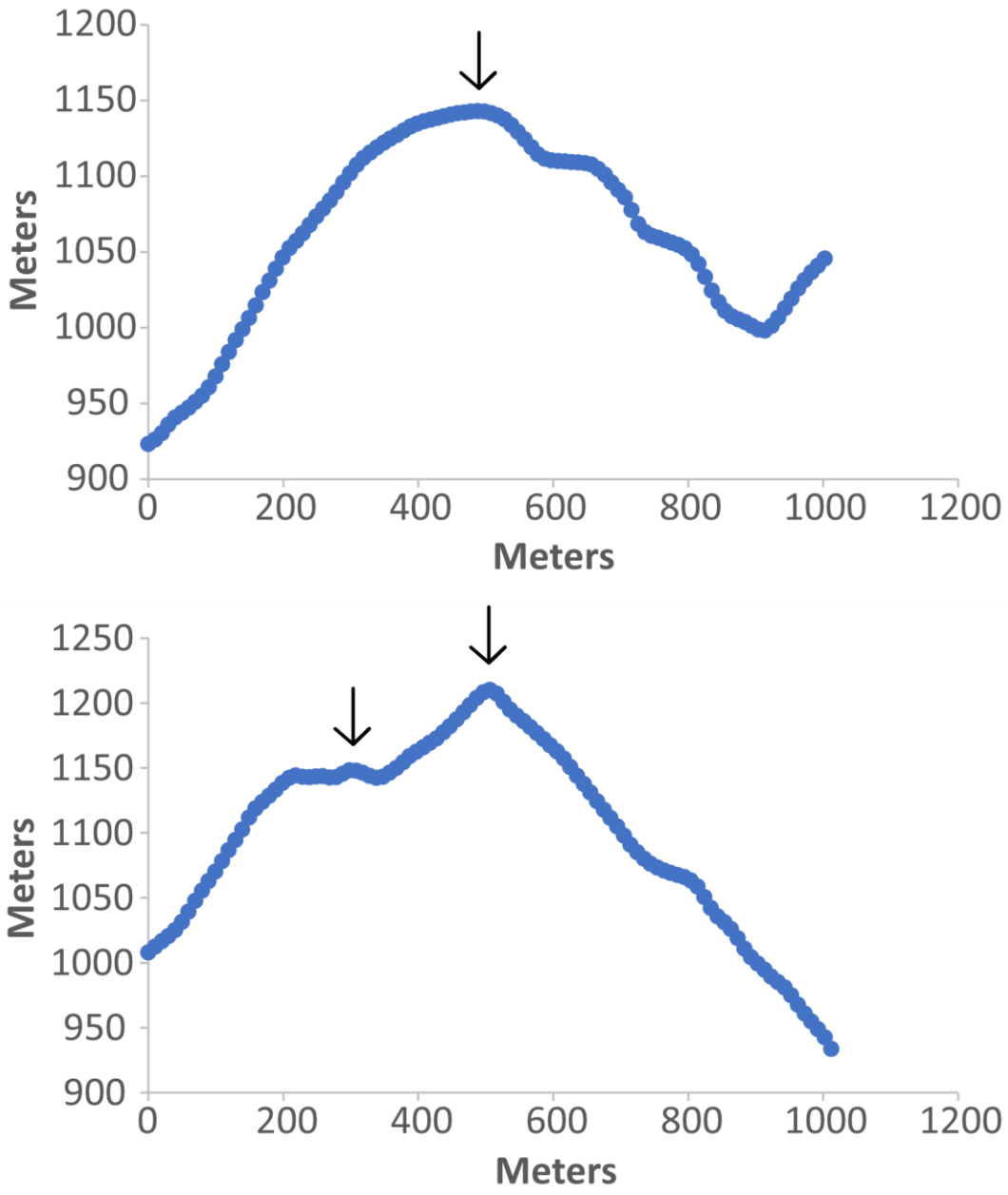

Figure *108*. Topography profiles of the transecting hills of Cluster 139. Hills are denoted with a black arrow.

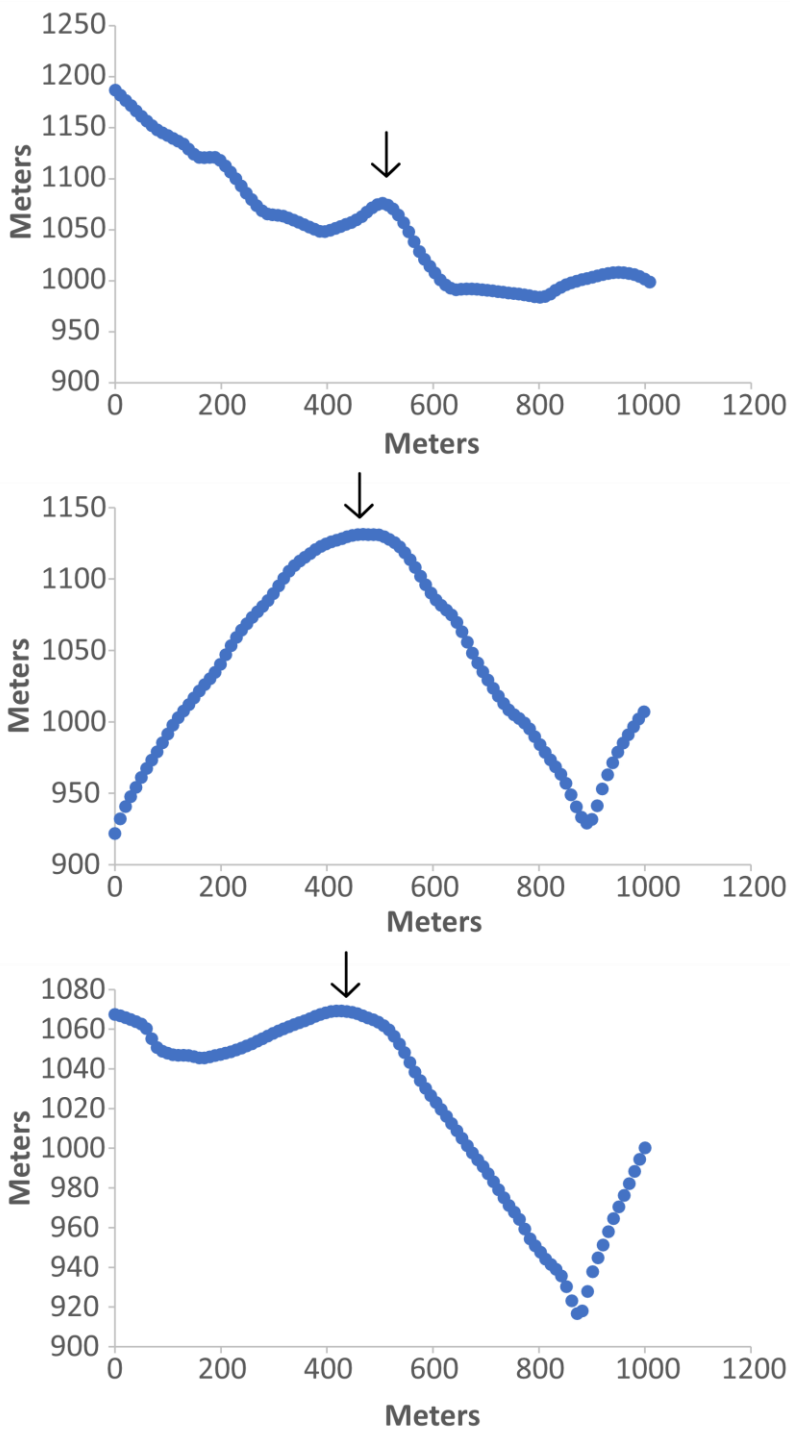

Figure *109*. Topography profiles of the transecting hills of Cluster 143. Hills are denoted with a black arrow.

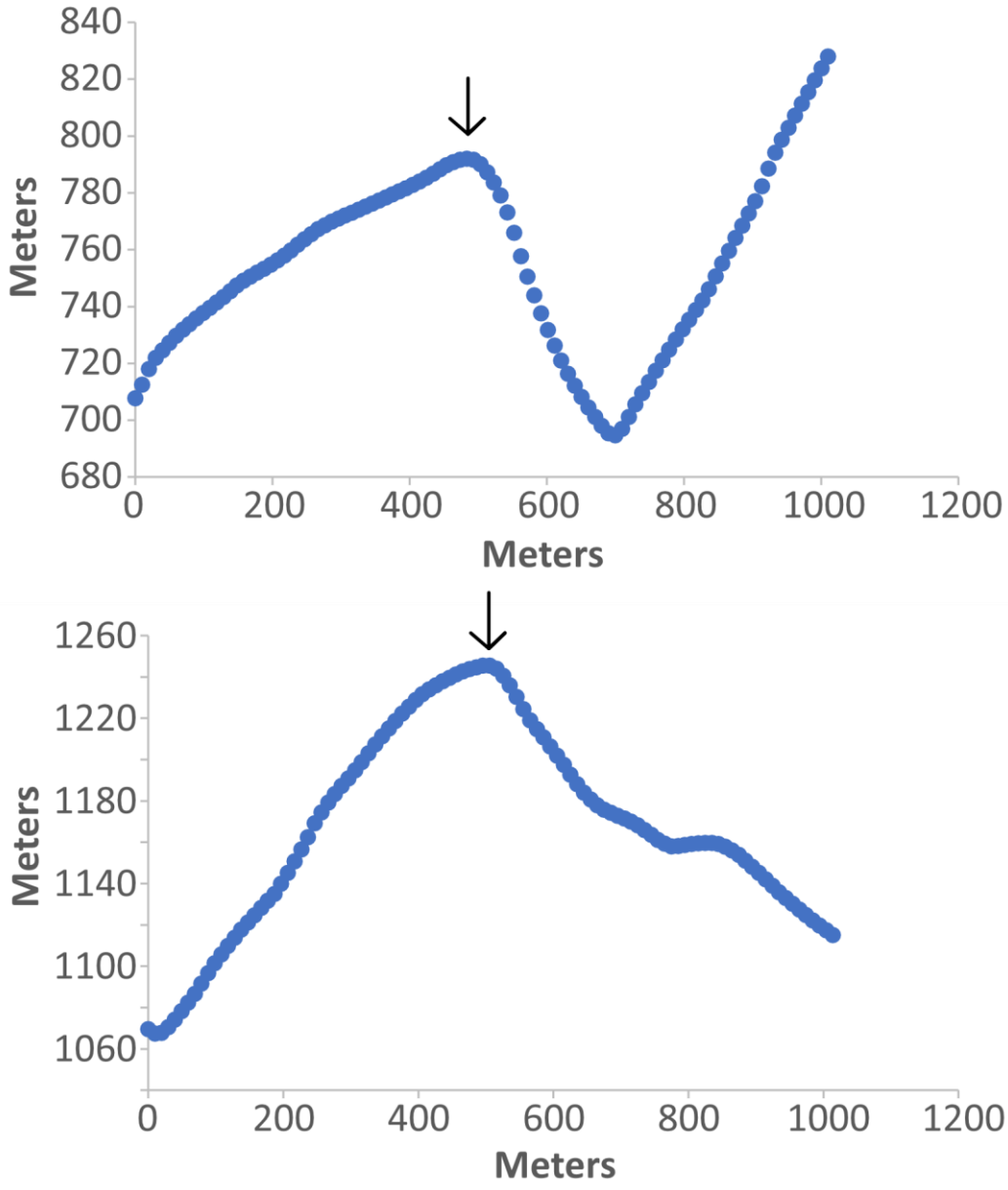

Figure *110*. Topography profiles of the transecting hills of Cluster 144. Hills are denoted with a black arrow.

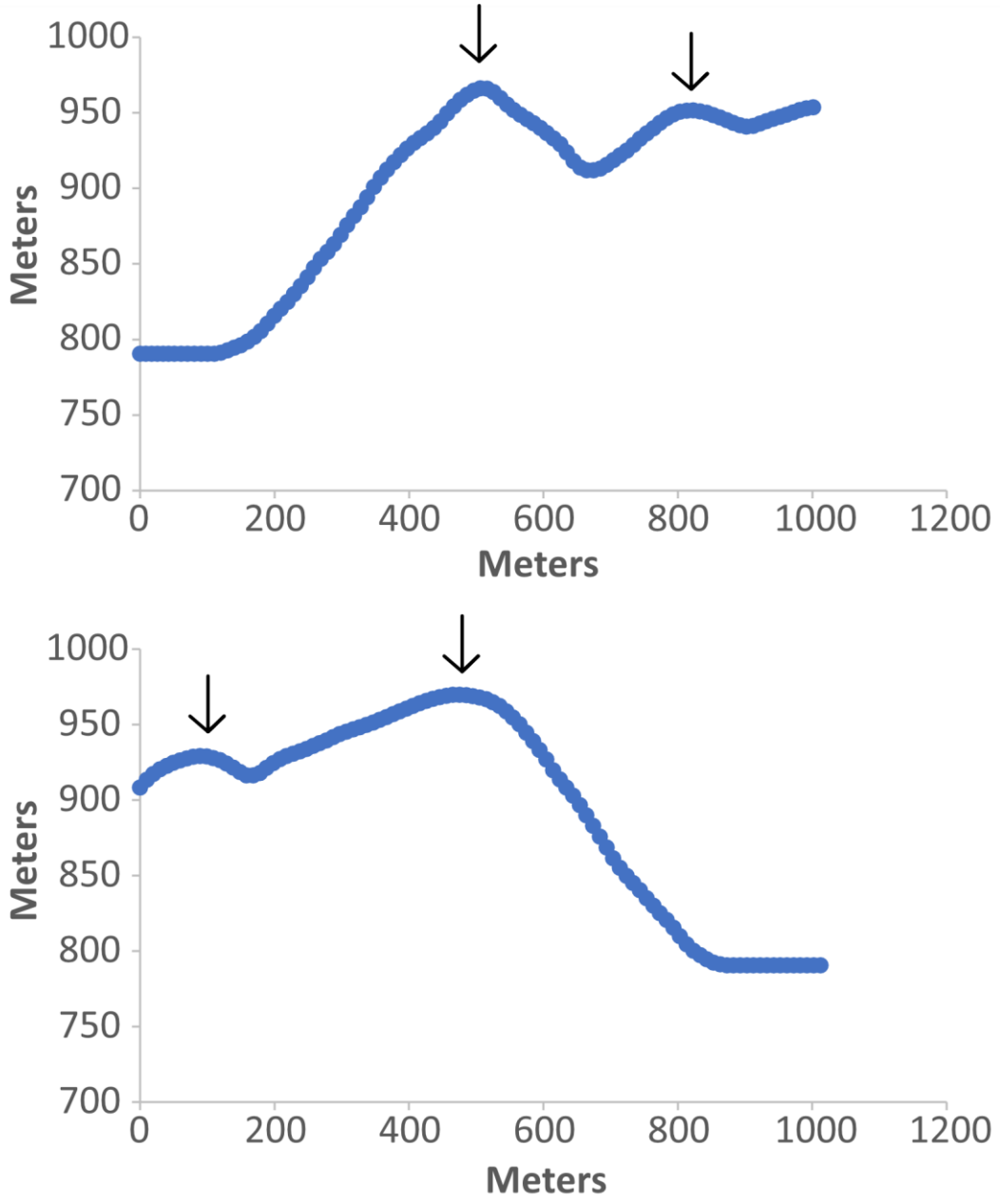

Figure *111*. Topography profiles of the transecting hills of Cluster 145. Hills are denoted with a black arrow.

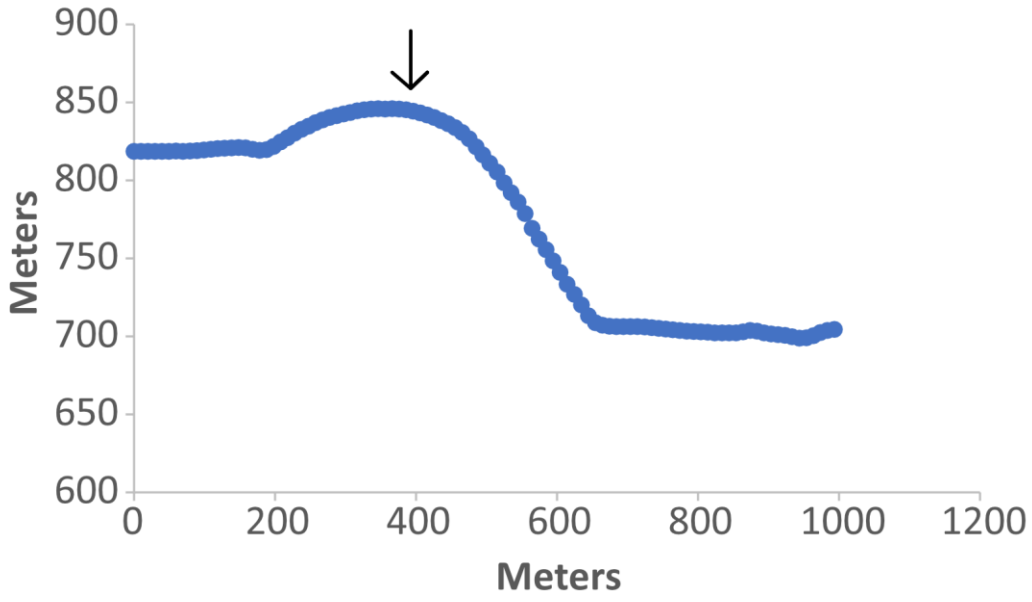

Figure *112*. Topography profiles of the transecting hills of Cluster 146. Hills are denoted with a black arrow.

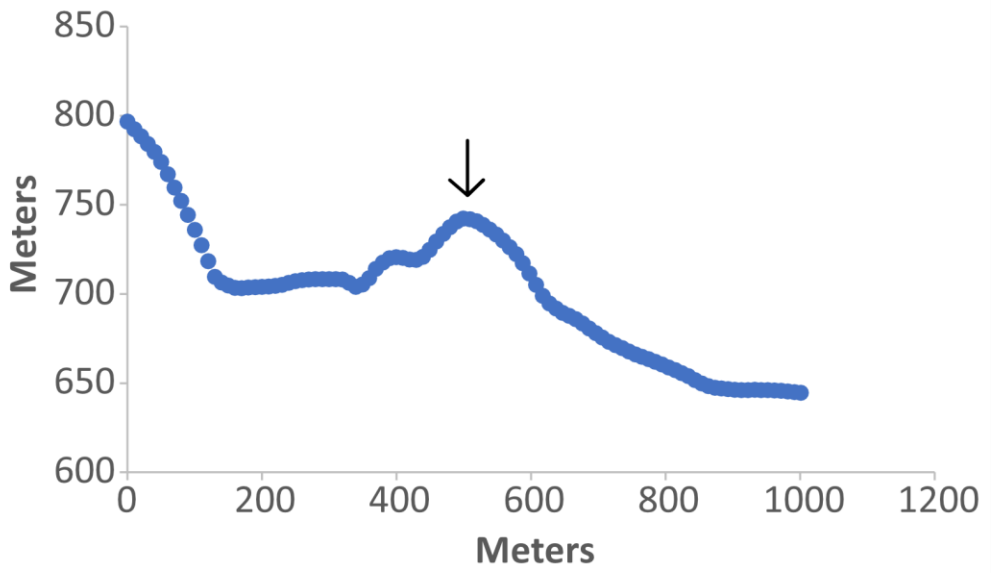

Figure *113*. Topography profiles of the transecting hills of Cluster 147. Hills are denoted with a black arrow.

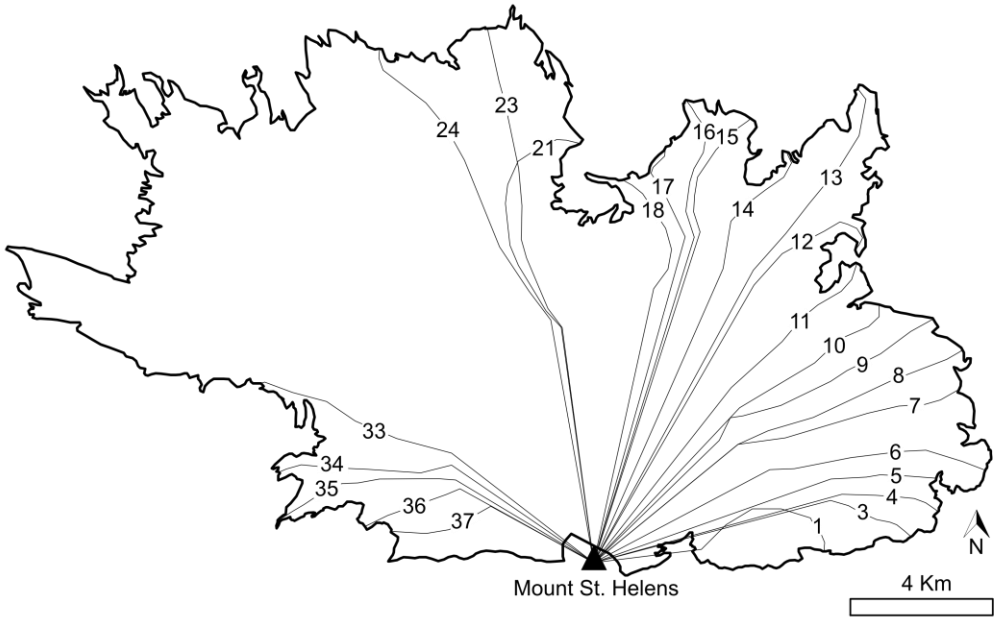

Figure *114*. Numbered flow paths.

Table 8. The top row designates cluster number. Runout % and Tree # pairs represent each flow line in the West zone. Runout percent is the normalized distance along a flow path, taken at the center point of each 200 by 200 m box. Tree # is the number of trees in each 200 by 200 m box.

33		34		35		36		37	
Runout %	**Tree #**	**Runout %**	**Tree #**	**Runout %**	**Tree #**	**Runout %**	**Tree #**	**Runout %**	**Tree #**
98	7	51	2	47	0	61	0	79	4
99	6	52	0	48	0	63	0	96	2
93	3	54	0	50	4	65	0	98	2
94	2	55	0	51	1	68	0	81	1
95	2	57	0	53	0	70	3	54	0
62	1	58	0	54	0	72	0	57	0
73	1	60	0	56	0	74	0	59	0
97	1	62	0	58	0	76	3	62	0
64	0	63	1	59	3	78	1	64	0
65	0	65	0	61	0	80	0	66	0
66	0	66	0	62	0	82	5	69	0
68	0	68	4	64	0	84	5	71	0
69	0	69	1	65	0	86	7	74	0
70	0	71	0	67	0	89	3	76	0
72	0	72	0	68	0	91	3	84	0
75	0	74	0	70	0	93	3	86	0
76	0	75	0	71	0	95	5	89	0
78	0	77	0	73	0	97	12	91	0
79	0	79	0	74	1	99	6	93	0
80	0	80	0	76	0			100	0
82	0	82	0	77	0				
83	0	83	0	79	0				
84	0	85	0	80	0				
86	0	86	0	82	0				
87	0	88	0	83	1				
89	0	89	0	85	1				
90	0	91	1	86	1				
91	0	92	3	88	0				
		94	0	89	1				
		95	0	91	0				
		97	0	92	1				
		98	5	94	4				

Table 8 (continued)

		34		35					
Runout %	**Tree #**	**Runout %**	**Tree #**	**Runout %**	**Tree #**	**Runout %**	**Tree #**	**Runout %**	**Tree #**
		100	5	95	11				
				97	17				
				99	15				
				100	4				

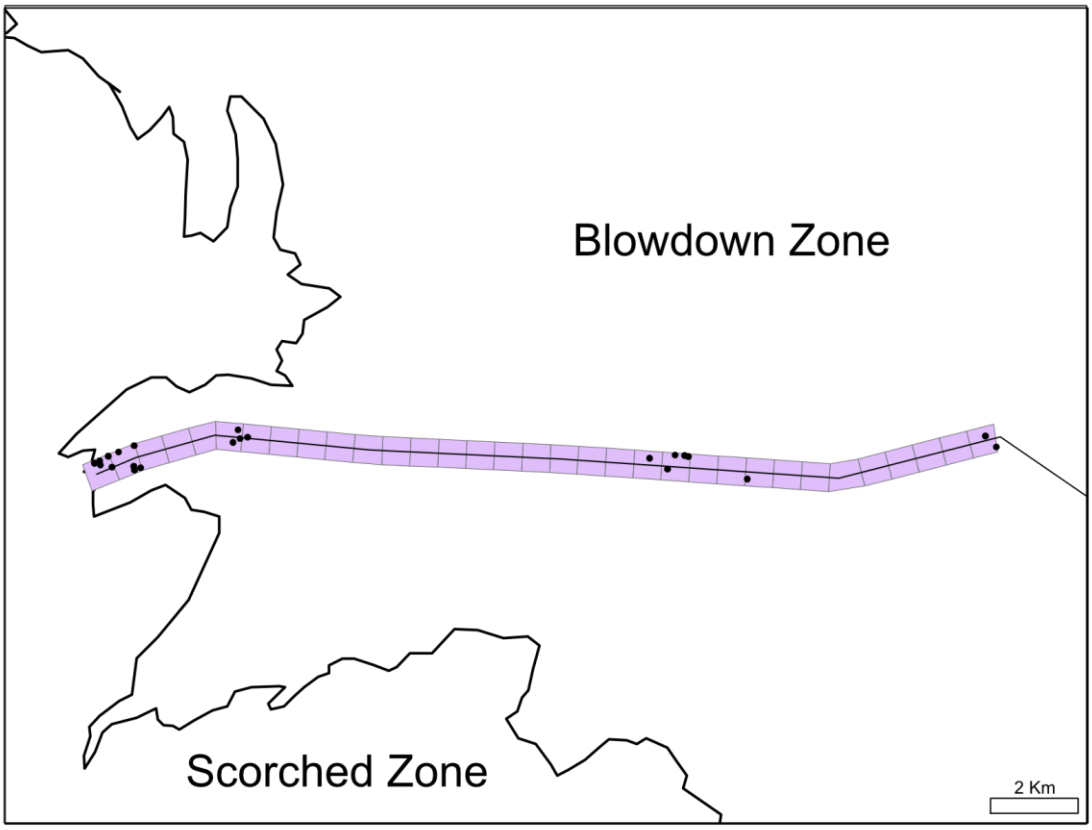

Figure *115*. The thin black line is flow path 34 in the West zone. Light purple boxes represent 200 by 200 m. The black dots are the locations of isolated standing trees. The thicker black line is the boundary between the scorched zone and the blowdown zone.

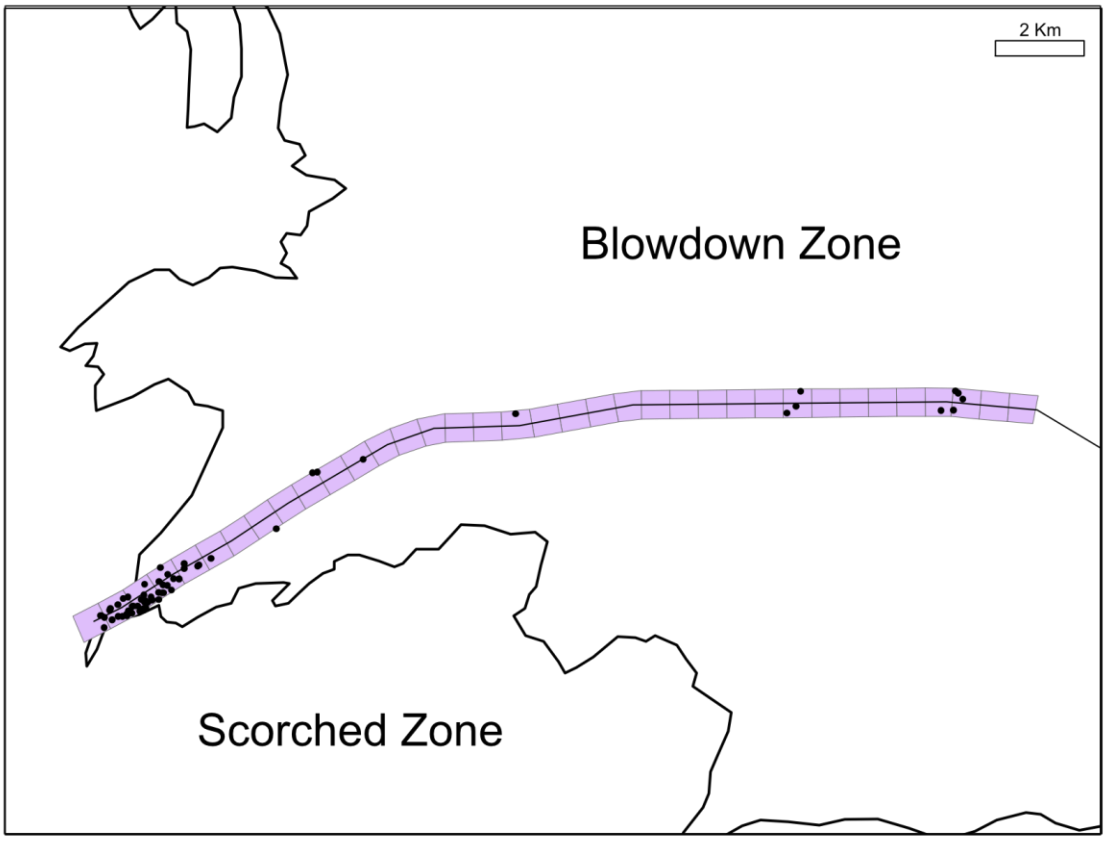

Figure *116*. The thin black line is flow path 35 in the West zone. Light purple boxes represent 200 by 200 m. The black dots are the locations of isolated standing trees. The thicker black line is the boundary between the scorched zone and the blowdown zone.

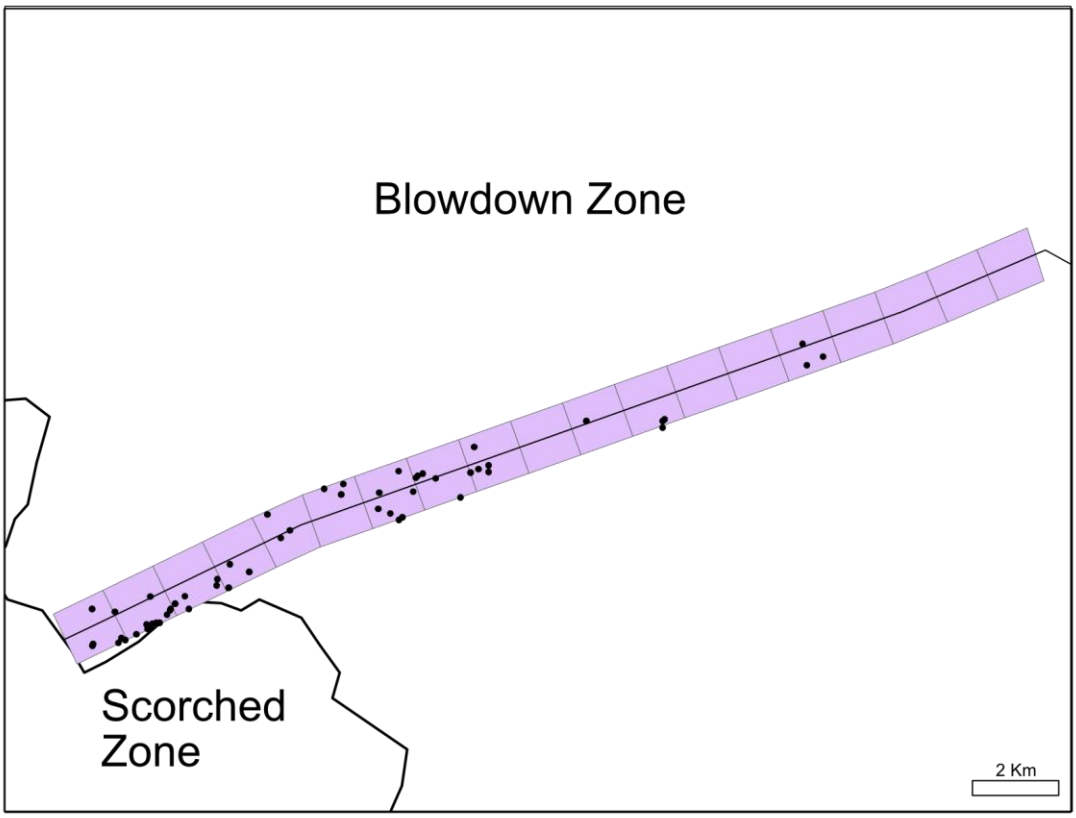

Figure *117*. The thin black line is flow path 36 in the West zone. Light purple boxes represent 200 by 200 m. The black dots are the locations of isolated standing trees. The thicker black line is the boundary between the scorched zone and the blowdown zone.

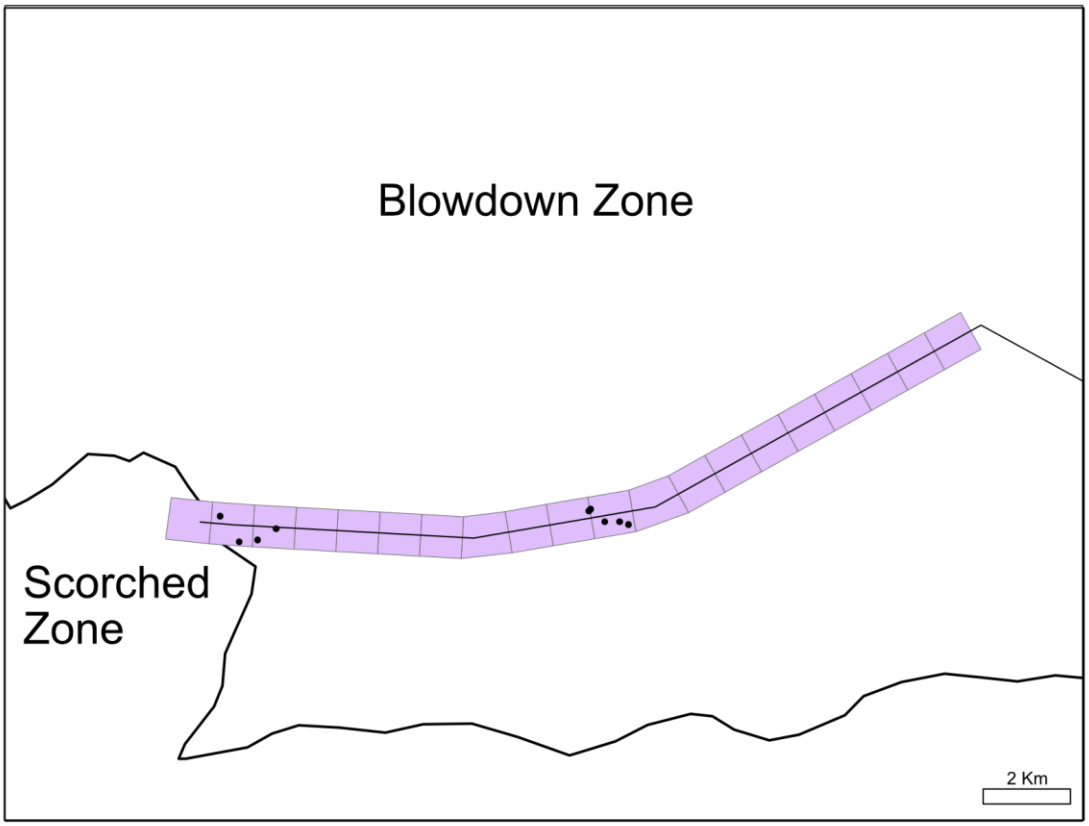

Figure *118*. The thin black line is flow path 37 in the West zone. Light purple boxes represent 200 by 200 m. The black dots are the locations of isolated standing trees. The thicker black line is the boundary between the scorched zone and the blowdown zone.

Table 9. The top row designates cluster number. Runout % and Tree # pairs represent each flow line in the North zone. Runout percent is the normalized distance along a flow path, taken at the center point of each 200 by 200 m box. Tree # is the number of trees in each 200 by 200 m box.

15		16		17		18		21	
Runout %	**Tree #**	**Runout %**	**Tree #**	**Runout %**	**Tree #**	**Runout %**	**Tree #**	**Runout %**	**Tree #**
74	0	71	0	78	0	68	0	51	0
75	0	72	0	79	0	69	0	52	0
76	0	73	0	80	0	71	0	53	0
77	0	74	0	82	0	72	0	54	0
78	0	75	0	83	0	73	0	55	0
79	0	76	0	84	1	75	0	56	0
80	0	77	0	85	0	76	0	58	0
81	0	78	0	86	0	77	0	59	0
82	0	80	0	88	4	79	0	60	0
84	0	81	0	89	0	80	0	61	0
85	0	82	0	90	0	81	0	62	0
86	0	83	0	91	1	82	0	63	0
87	0	84	0	92	2	84	0	64	0
88	0	85	0	94	7	85	0	65	0
89	0	86	0	96	5	86	0	66	0
90	0	87	0	97	31	88	0	67	0
91	0	88	0	98	8	89	0	68	0
92	0	89	0	99	0	90	0	70	0
93	0	90	0	100	5	91	0	71	0
95	0	92	0			93	0	72	0
96	0	93	0			94	0	73	0
97	0	94	0			95	0	74	0
98	0	95	0			97	5	75	0
99	8	96	0			98	10	76	0
100	0	97	0			99	19	77	0
		98	3			100	9	78	0
		99	14					79	0
		100	10					80	0
								82	0
								83	0
								84	0
								85	0

Table 9 (continued)

21		23		24	
Runout %	Tree #	Runout %	Tree #	Runout %	Tree #
86	0	44	0	43	0
87	0	45	0	44	0
88	0	46	0	45	0
89	0	47	0	45	0
91	0	48	0	46	0
92	0	49	0	47	0
93	0	50	0	48	0
95	0	51	0	49	0
96	0	52	0	50	0
97	5	53	0	51	0
98	27	54	0	52	0
99	20	55	0	53	0
100	14	56	0	54	0
		57	0	55	0
		58	0	56	0
		59	0	56	0
		60	0	57	0
		61	0	58	0
		62	0	59	0
		63	0	60	0
		64	0	61	0
		65	0	62	0
		66	0	63	0
		67	0	64	0
		68	0	65	0
		69	0	66	0
		70	0	66	0
		71	0	67	0
		72	0	68	0
		73	0	69	0
		74	0	70	0
		75	0	71	0
		75	0	72	0
		76	0	73	0
		77	0	74	0
		78	0	75	0
		80	1	76	0

Table 9 (continued)

23		24	
Runout %	**Tree #**	**Runout %**	**Tree #**
81	0	77	0
83	0	79	0
84	0	80	0
85	0	81	0
86	0	82	0
87	0	83	0
88	0	84	0
94	1	85	0
90	2	86	0
91	0	87	1
92	1	87	0
93	1	88	0
94	4	89	2
95	4	90	5
96	8	91	5
97	3	92	1
98	0	93	0
99	3	94	0
		95	0
		96	0
		97	0
		98	3

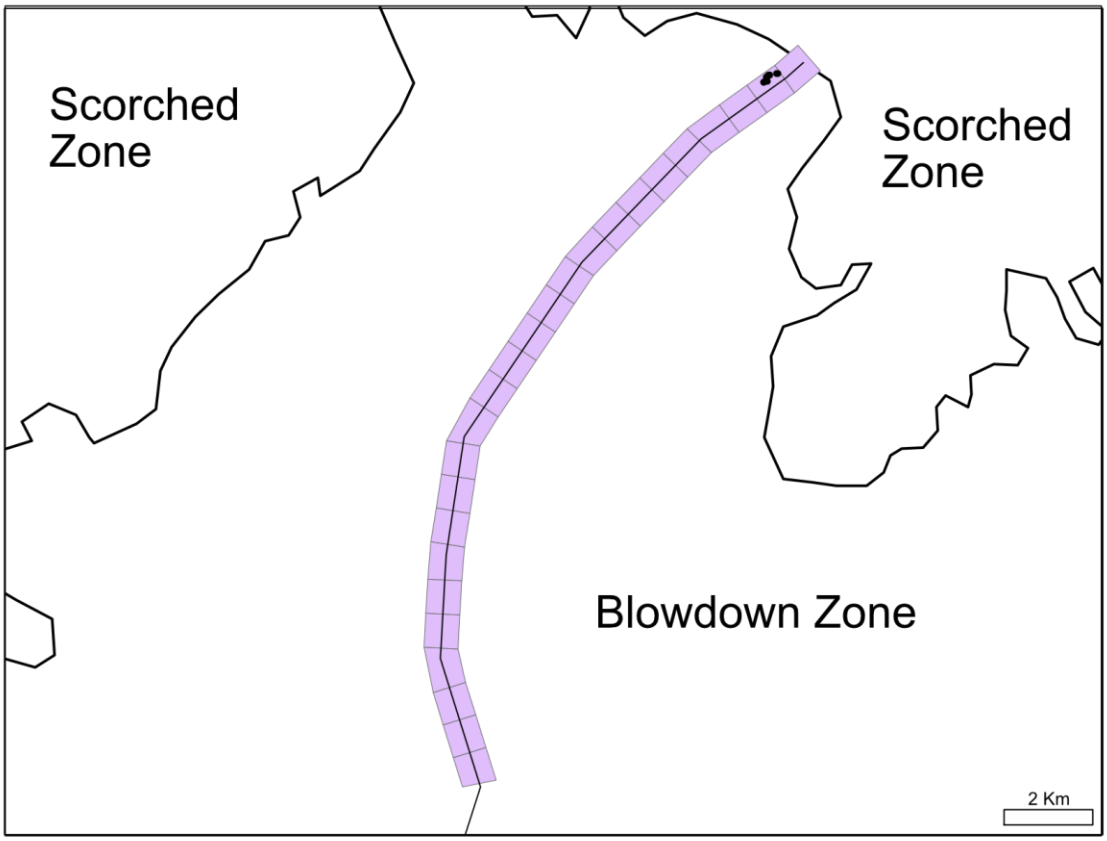

Figure *119*. The thin black line is flow path 15 in the North zone. Light purple boxes represent 200 by 200 m. The black dots are the locations of isolated standing trees. The thicker black line is the boundary between the scorched zone and the blowdown zone.

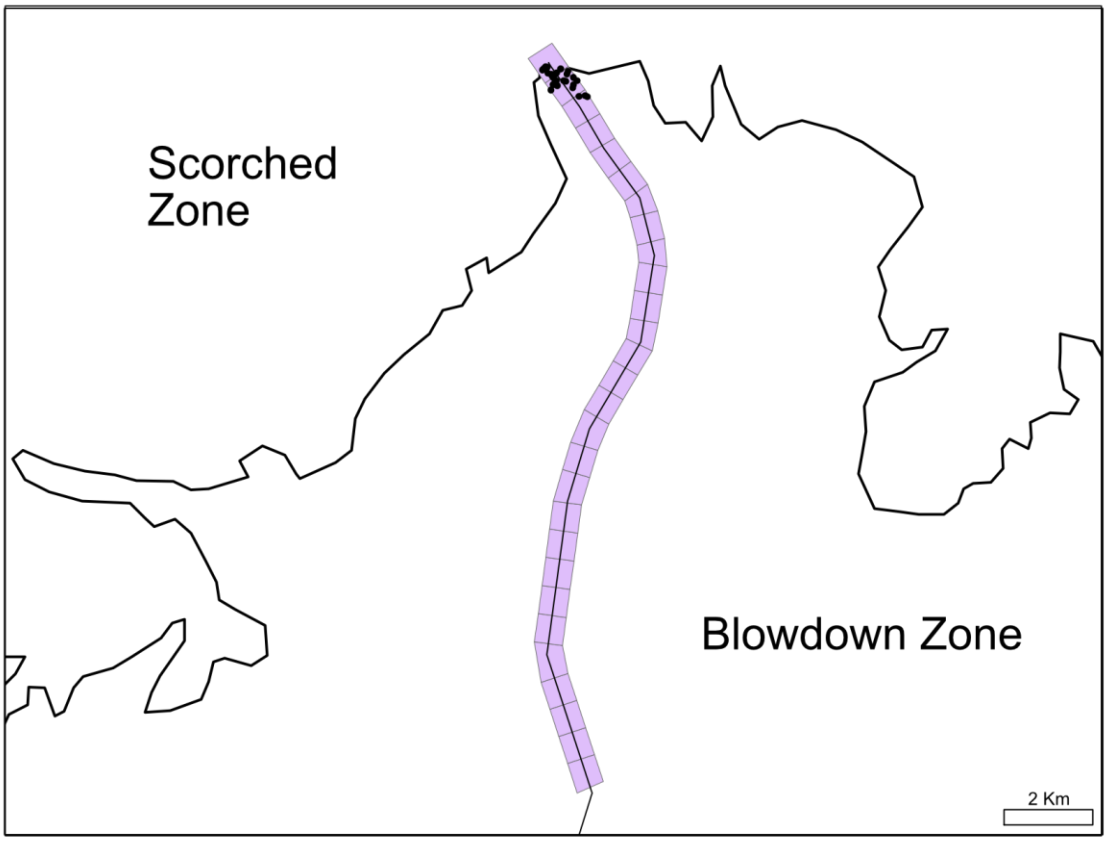

Figure *120*. The thin black line is flow path 16 in the North zone. Light purple boxes represent 200 by 200 m. The black dots are the locations of isolated standing trees. The thicker black line is the boundary between the scorched zone and the blowdown zone.

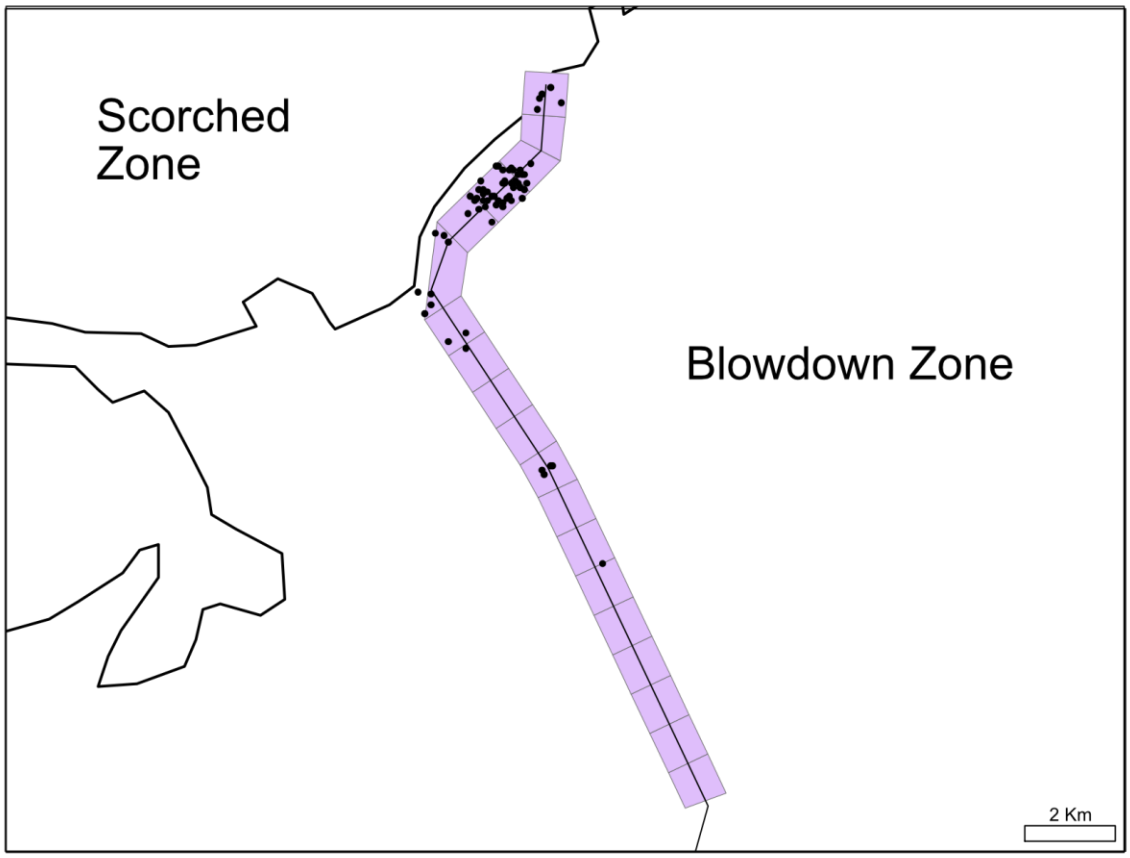

Figure *121*. The thin black line is flow path 17 in the North zone. Light purple boxes represent 200 by 200 m. The black dots are the locations of isolated standing trees. The thicker black line is the boundary between the scorched zone and the blowdown zone.

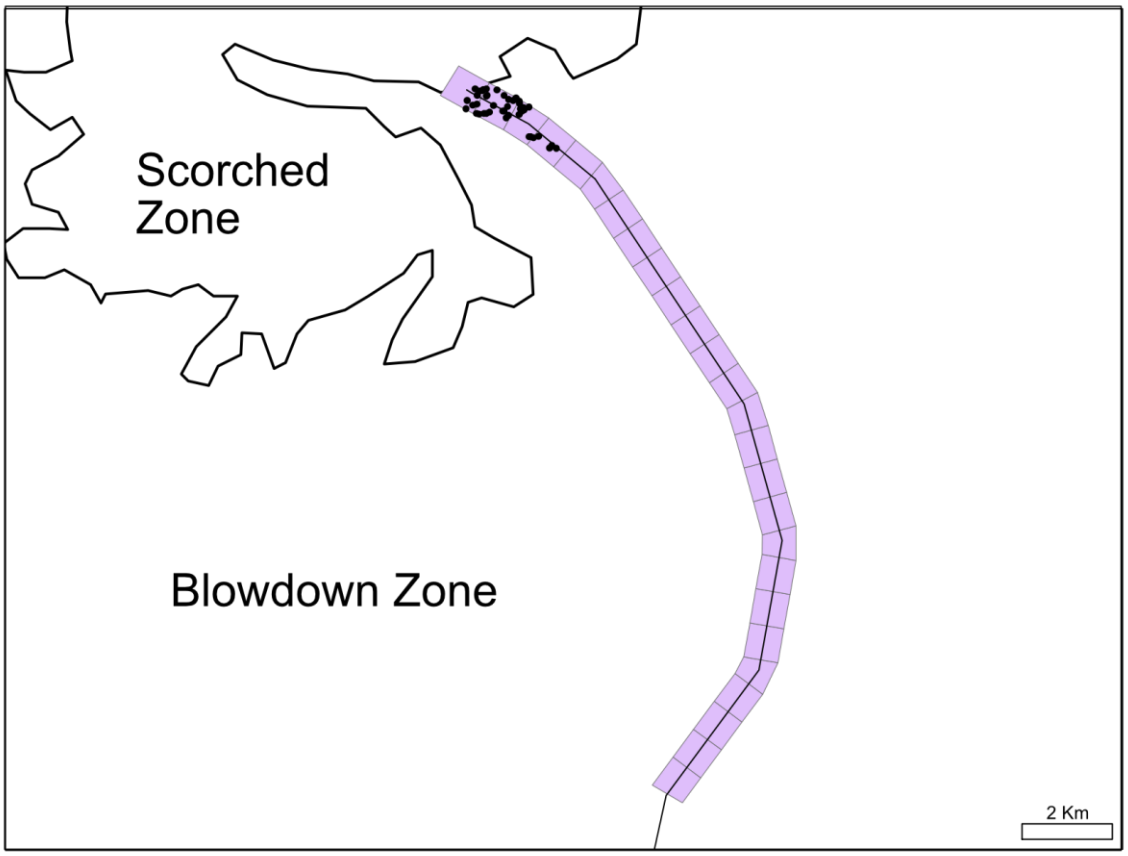

Figure *122*. The thin black line is flow path 18 in the North zone. Light purple boxes represent 200 by 200 m. The black dots are the locations of isolated standing trees. The thicker black line is the boundary between the scorched zone and the blowdown zone.

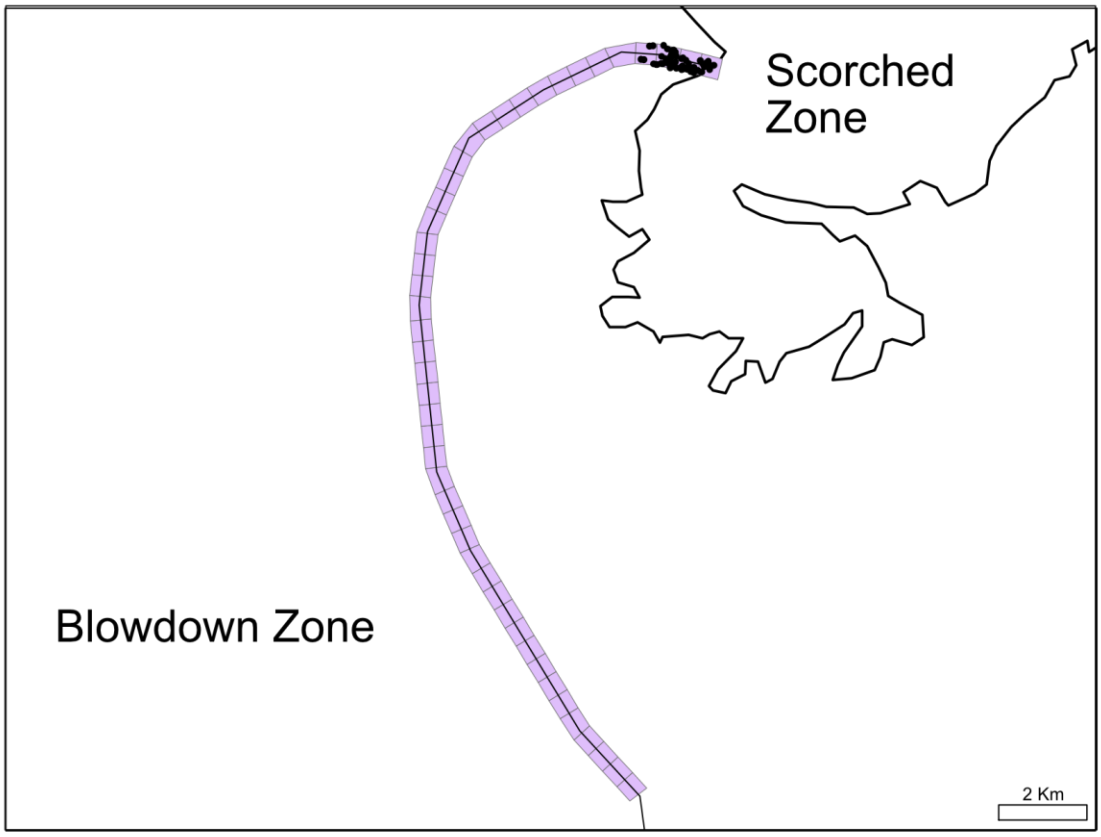

Figure *123*. The thin black line is flow path 21 in the North zone. Light purple boxes represent 200 by 200 m. The black dots are the locations of isolated standing trees. The thicker black line is the boundary between the scorched zone and the blowdown zone.

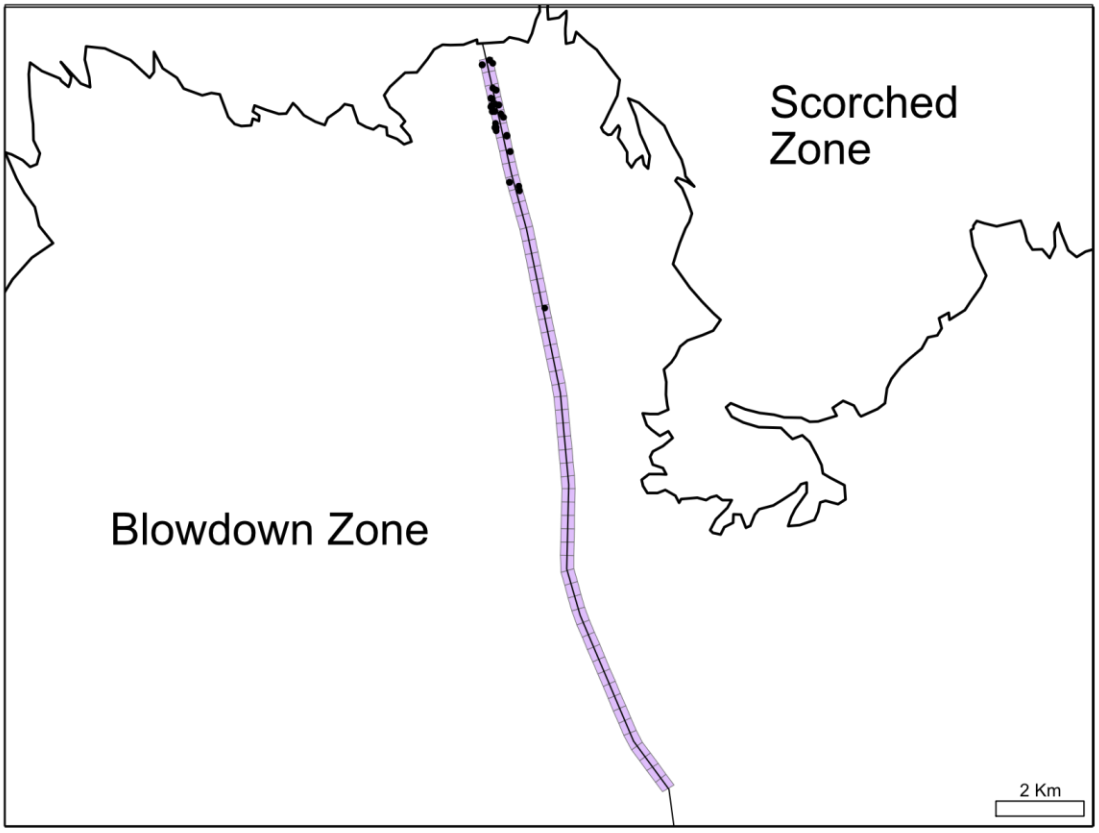

Figure *124*. The thin black line is flow path 23 in the North zone. Light purple boxes represent 200 by 200 m. The black dots are the locations of isolated standing trees. The thicker black line is the boundary between the scorched zone and the blowdown zone.

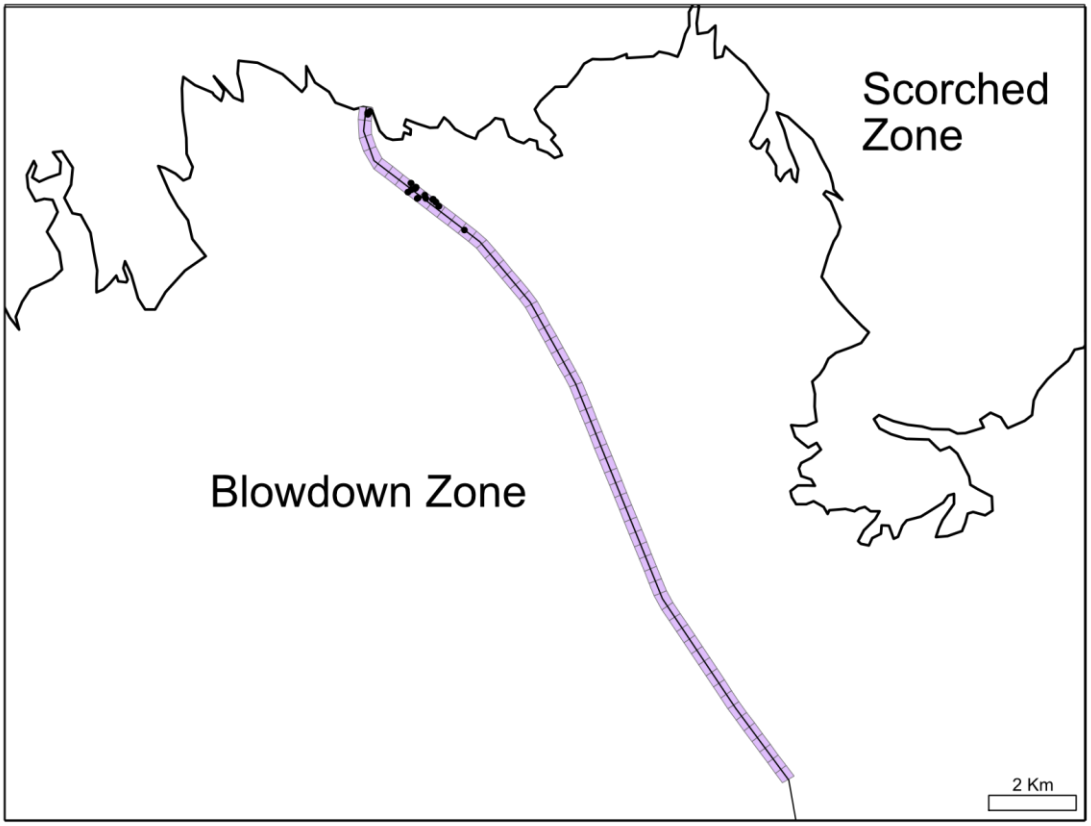

Figure *125*. The thin black line is flow path 24 in the North zone. Light purple boxes represent 200 by 200 m. The black dots are the locations of isolated standing trees. The thicker black line is the boundary between the scorched zone and the blowdown zone.

Table 10. The top row designates cluster number. Runout % and Tree # pairs represent each flow line in the Northeast zone. Runout percent is the normalized distance along a flow path, taken at the center point of each 200 by 200 m box. Tree # is the number of trees in each 200 by 200 m box.

10		11		12		13	
Runout%	Tree #	Runout%	Tree #	Runout%	Tree #	Runout%	Tree #
57	0	56	0	70	0	61	0
58	0	58	0	71	0	62	0
60	0	59	0	72	0	63	0
61	0	60	0	73	0	64	0
62	0	62	0	74	0	65	0
64	0	63	0	75	0	66	0
65	0	64	0	76	0	67	0
66	0	66	0	77	0	68	0
68	0	67	0	79	0	69	0
69	0	68	0	80	0	70	0
71	0	70	0	81	0	71	0
72	0	71	0	82	0	72	0
73	0	72	0	83	0	73	0
75	0	74	0	84	0	73	0
76	0	75	0	85	0	74	0
77	0	76	0	86	0	75	0
79	0	78	0	88	0	76	0
80	0	79	0	89	0	77	0
81	0	80	0	90	0	78	0
83	0	81	0	91	0	79	0
84	0	83	0	92	0	80	0
86	0	84	0	93	0	81	0
87	0	85	0	94	0	82	0
88	0	87	0	95	0	83	0
90	0	88	0	97	0	84	0
91	0	89	0	98	0	85	0
92	0	91	0	99	2	86	0
94	0	92	0	100	3	87	0
95	1	93	0			88	0
96	1	95	0			89	0
98	4	96	0			90	0
99	3	97	8			91	0

Table 10 (continued)

10		11		13		14	
Runout %	Tree #	Runout %	Tree #	Runout%	Tree #	Runout%	Tree #
100	7	99	31	92	0	70	0
		100	11	93	0	71	0
				94	0	72	0
				95	22	74	0
				96	1	75	0
				97	0	76	0
				98	2	77	0
				99	7	78	0
				100	16	79	0
						80	0
						82	0
						83	0
						84	0
						85	0
						86	0
						87	0
						88	0
						90	0
						91	0
						92	0
						93	12
						94	20
						95	21
						96	46
						97	24
						98	19
						99	31
						100	2

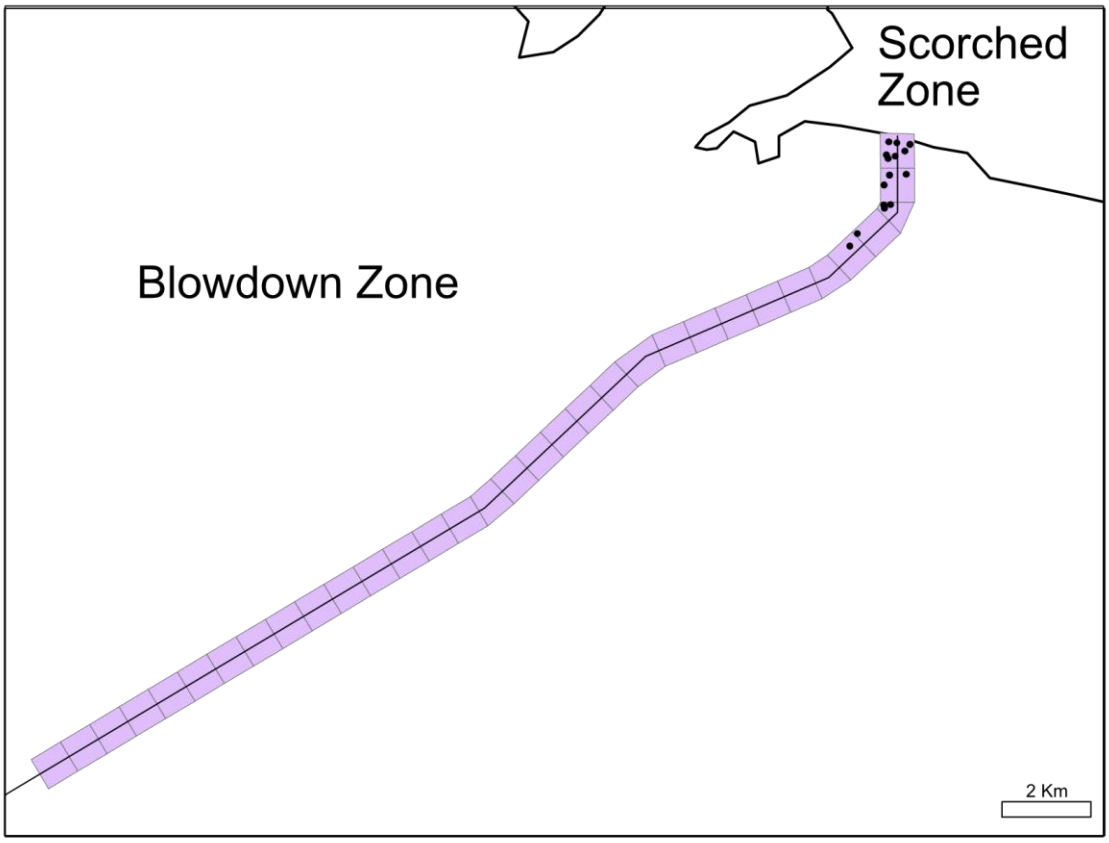

Figure *126*. The thin black line is flow path 10 in the Northeast zone. Light purple boxes represent 200 by 200 m. The black dots are the locations of isolated standing trees. The thicker black line is the boundary between the scorched zone and the blowdown zone.

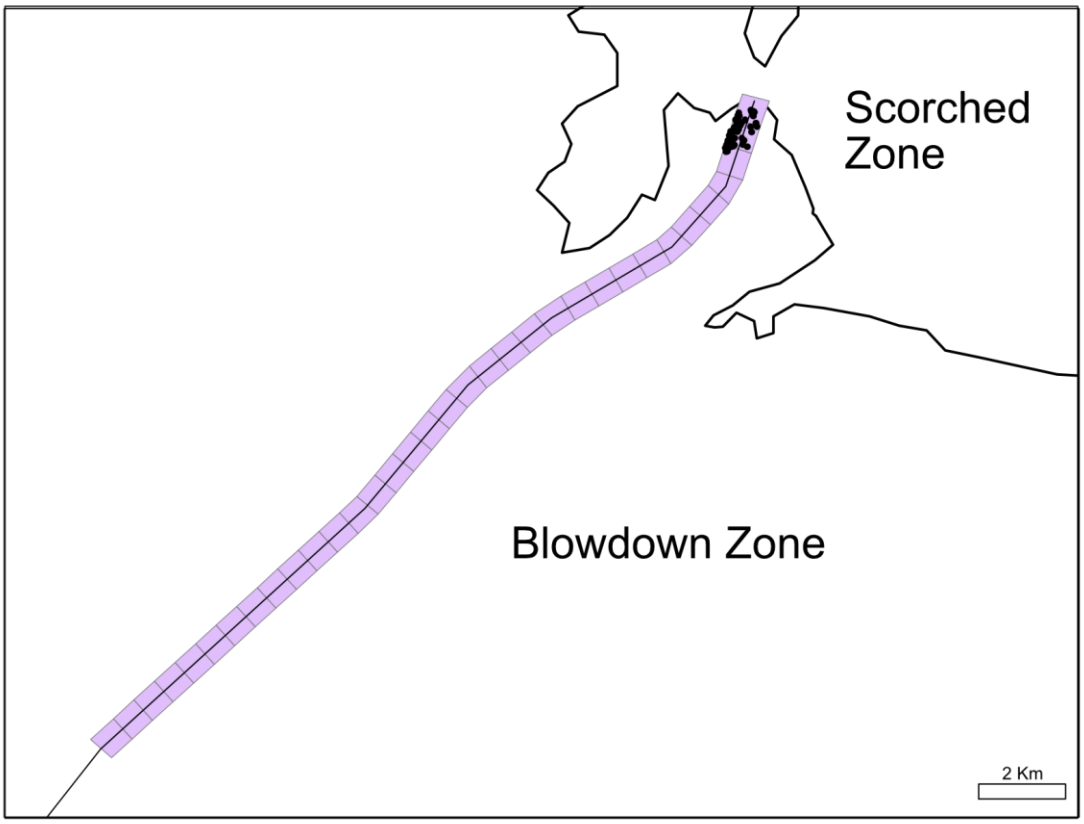

Figure *127*. The thin black line is flow path 11 in the Northeast zone. Light purple boxes represent 200 by 200 m. The black dots are the locations of isolated standing trees. The thicker black line is the boundary between the scorched zone and the blowdown zone.

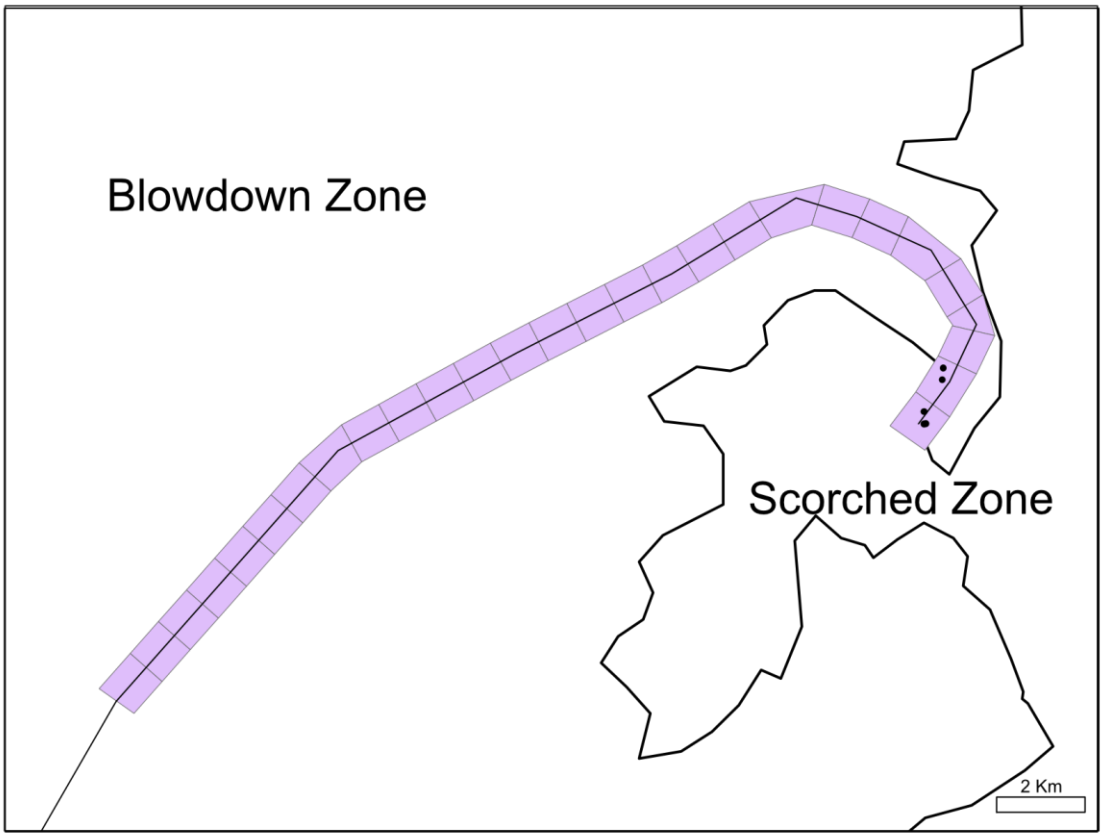

Figure *128*. The thin black line is flow path 12 in the Northeast zone. Light purple boxes represent 200 by 200 m. The black dots are the locations of isolated standing trees. The thicker black line is the boundary between the scorched zone and the blowdown zone.

Figure *129*. The thin black line is flow path 13 in the Northeast zone. Light purple boxes represent 200 by 200 m. The black dots are the locations of isolated standing trees. The thicker black line is the boundary between the scorched zone and the blowdown zone.

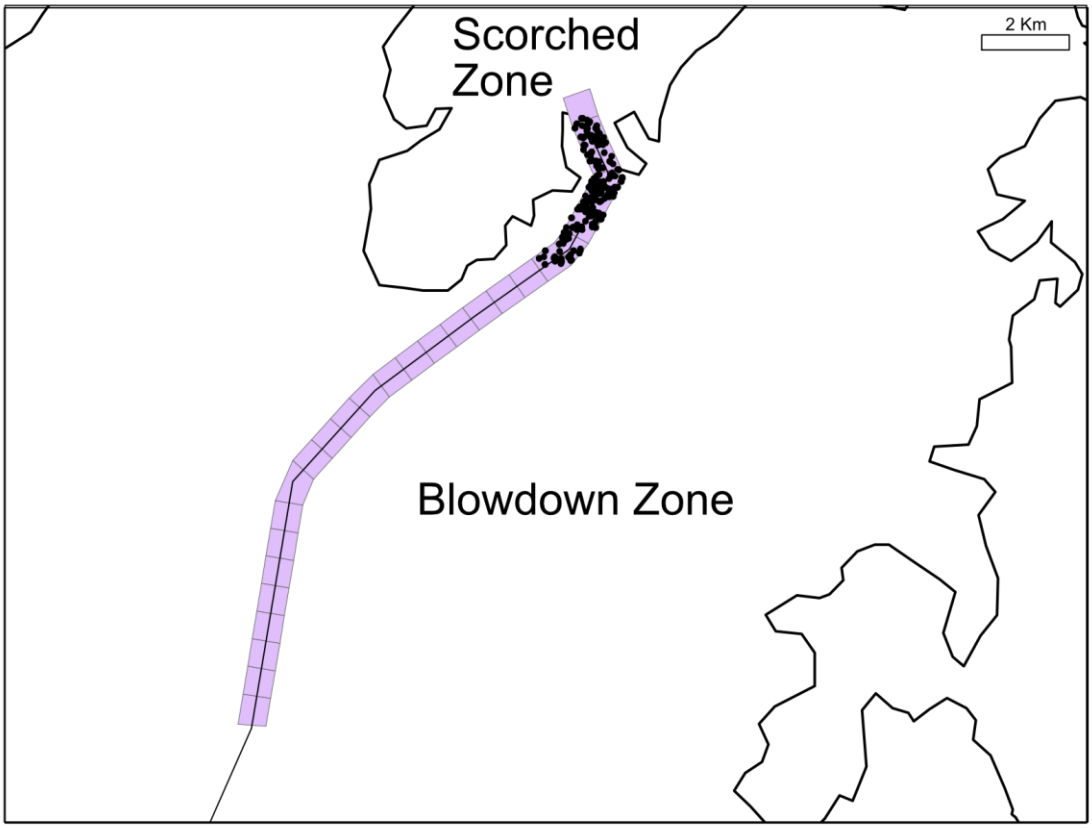

Figure *130*. The thin black line is flow path 14 in the Northeast zone. Light purple boxes represent 200 by 200 m. The black dots are the locations of isolated standing trees. The thicker black line is the boundary between the scorched zone and the blowdown zone.

Table 11. The top row designates cluster number. Runout % and Tree # pairs represent each flow line in the East zone. Runout percent is the normalized distance along a flow path, taken at the center point of each 200 by 200 m box. Tree # is the number of trees in each 200 by 200 m box.

1		3		4		5		6	
Runout %	**Tree #**	**Runout %**	**Tree #**	**Runout %**	**Tree #**	**Runout %**	**Tree #**	**Runout %**	**Tree #**
42	0	74	0	73	0	39	2	48	0
44	0	76	0	74	0	41	3	50	0
46	0	78	0	76	1	42	0	51	0
48	0	79	0	77	4	44	0	52	0
50	0	81	0	79	1	45	0	53	0
52	0	82	0	80	0	47	0	54	0
54	0	84	0	82	0	48	0	56	0
56	0	86	0	83	0	50	0	57	0
58	0	87	0	85	8	51	0	58	0
60	0	89	2	86	2	53	0	60	0
62	0	90	0	88	4	54	0	61	1
64	0	92	0	89	2	56	0	62	0
65	0	94	17	91	2	57	0	63	0
67	0	96	4	93	1	59	0	65	0
69	0	97	0	94	3	60	0	66	0
71	0	99	0	96	12	62	0	67	0
73	0			97	6	63	0	69	0
75	0			99	18	65	0	70	0
77	0			100	5	66	0	71	0
79	0					68	0	72	1
81	0					69	0	74	0
83	0					71	0	75	0
85	0					72	0	76	0
87	0					74	0	77	0
89	0					75	0	79	0
91	0					77	1	80	0
93	0					78	0	81	2
95	0					80	0	83	0
97	4					81	0	84	1
99	8					83	1	85	2
100	4					84	1	87	1
						86	0	88	1
						88	0	89	0

Table 11 (continued)

5		6		7		8		9	
Runout %	Tree #	Runout %	Tree #	Runout %	Tree #	Runout %	Tree #	Runout %	Tree #
89	0	91	0	46	0	44	2	48	0
91	0	92	4	47	0	45	0	49	0
92	5	93	0	48	0	47	0	50	0
94	3	94	0	50	0	48	0	51	0
95	3	96	0	51	0	49	0	53	0
96	5	97	2	52	0	50	0	54	0
99	12			53	0	52	0	55	0
				55	0	53	0	56	0
				56	0	54	0	58	0
				57	0	55	0	59	0
				58	0	57	0	60	0
				60	0	58	0	61	0
				61	0	59	0	63	0
				62	0	60	0	64	0
				64	0	62	0	65	0
				65	0	63	0	66	0
				66	0	64	0	68	0
				67	0	65	1	69	0
				69	0	67	5	70	0
				70	4	68	3	71	0
				71	0	69	0	73	0
				73	1	70	0	74	0
				74	0	72	0	75	6
				75	0	73	0	76	13
				77	1	74	0	78	6
				78	0	75	0	79	3
				79	2	76	0	80	3
				80	4	78	0	81	0
				82	5	79	2	83	0
				83	0	80	0	84	0
				84	12	81	0	85	0
				85	11	83	0	86	0
				89	3	86	0	90	5
				91	4	88	0	91	1
				92	17	89	0	92	0
				93	17	90	0	94	0
				94	15	91	0	95	1

Table 11 (continued)

7		8		9	
Runout %	**Tree #**	**Runout %**	**Tree #**	**Runout %**	**Tree #**
96	6	93	0	96	1
97	5	94	0	98	8
98	7	95	0	99	14
99	10	94	1	100	5
		97	7		
		99	5		
		100	5		

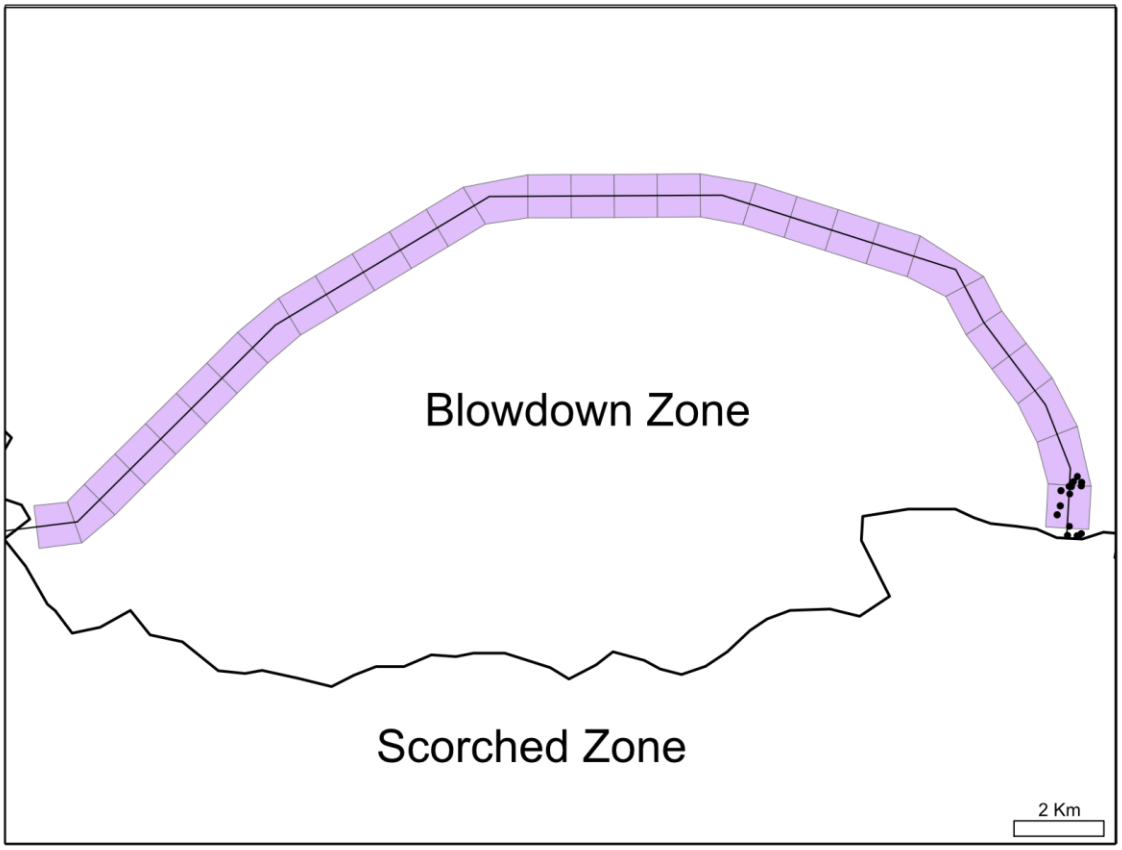

Figure *131*. The thin black line is flow path 1 in the East zone. Light purple boxes represent 200 by 200 m. The black dots are the locations of isolated standing trees. The thicker black line is the boundary between the scorched zone and the blowdown zone.

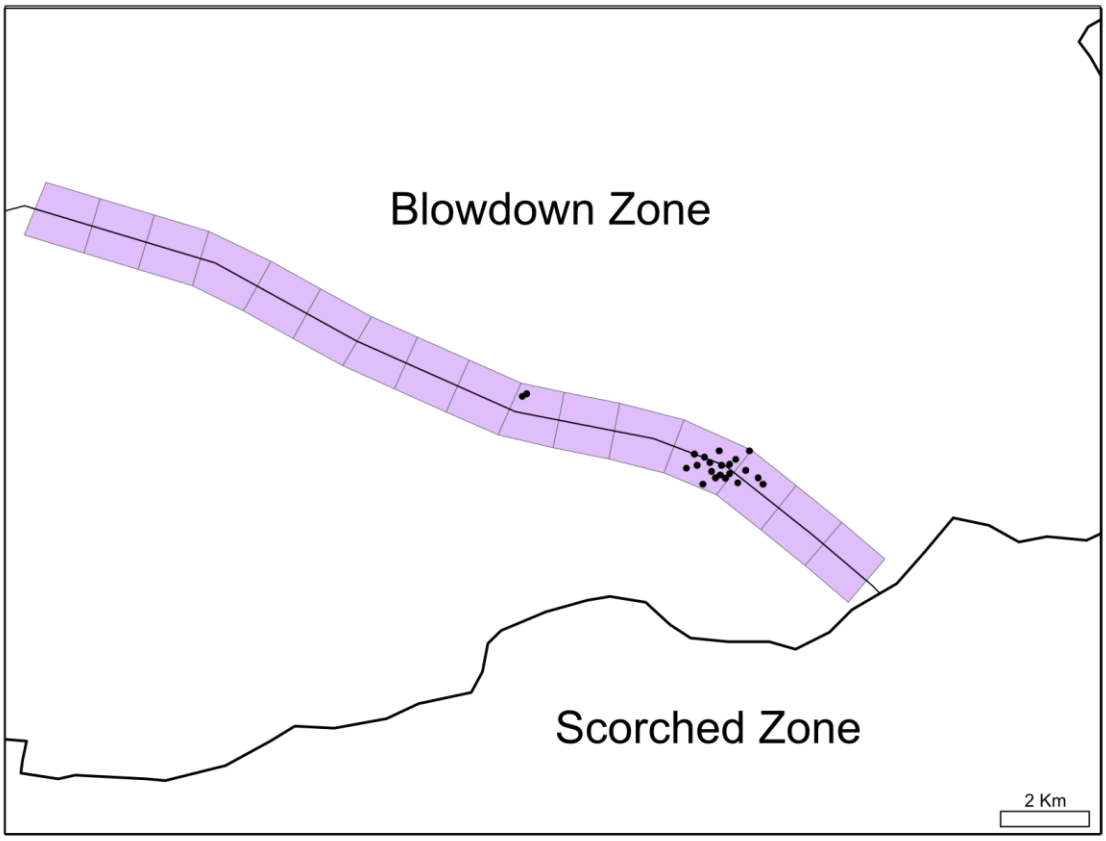

Figure *132*. The thin black line is flow path 3 in the East zone. Light purple boxes represent 200 by 200 m. The black dots are the locations of isolated standing trees. The thicker black line is the boundary between the scorched zone and the blowdown zone.

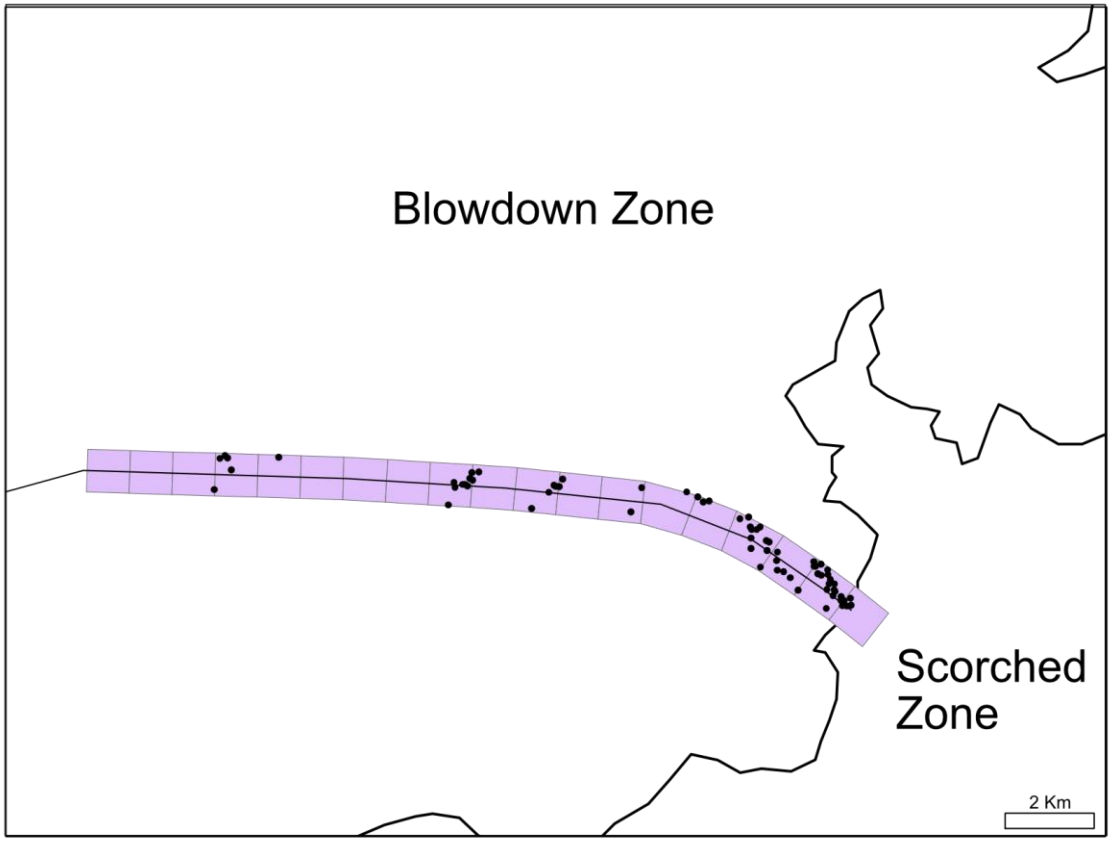

Figure *133*. The thin black line is flow path 4 in the East zone. Light purple boxes represent 200 by 200 m. The black dots are the locations of isolated standing trees. The thicker black line is the boundary between the scorched zone and the blowdown zone.

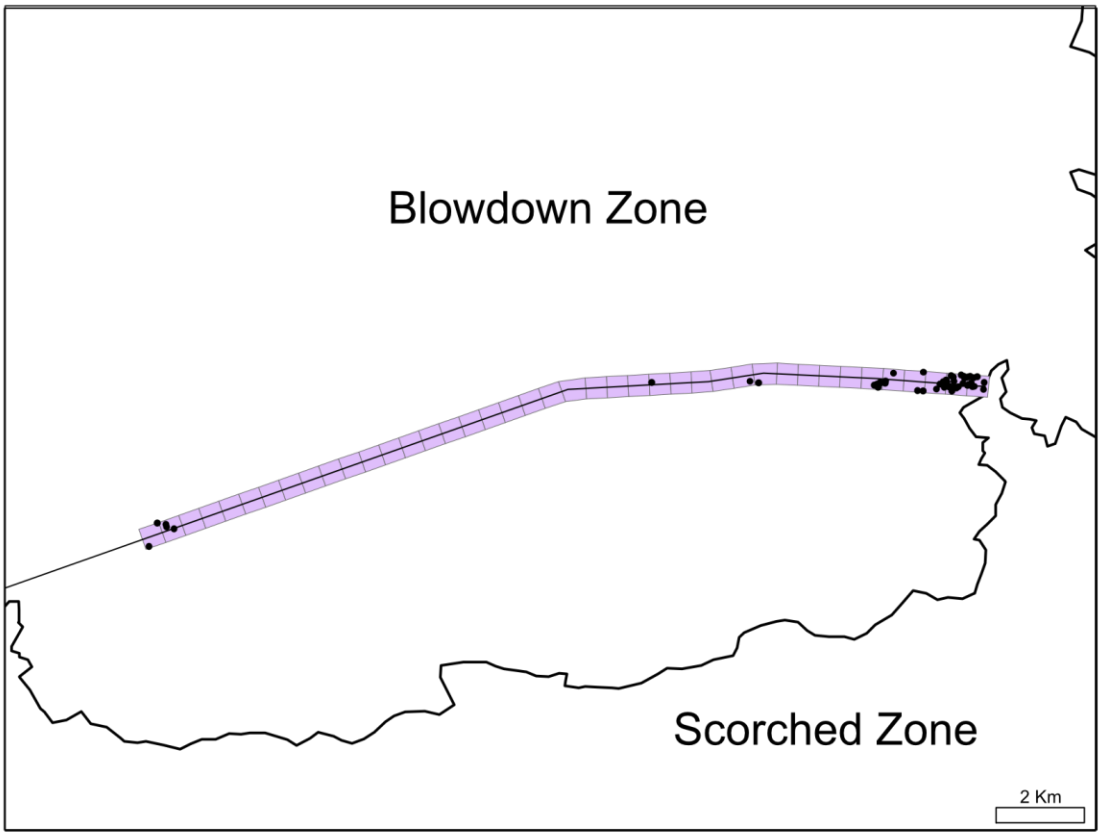

Figure *134*. The thin black line is flow path 5 in the East zone. Light purple boxes represent 200 by 200 m. The black dots are the locations of isolated standing trees. The thicker black line is the boundary between the scorched zone and the blowdown zone.

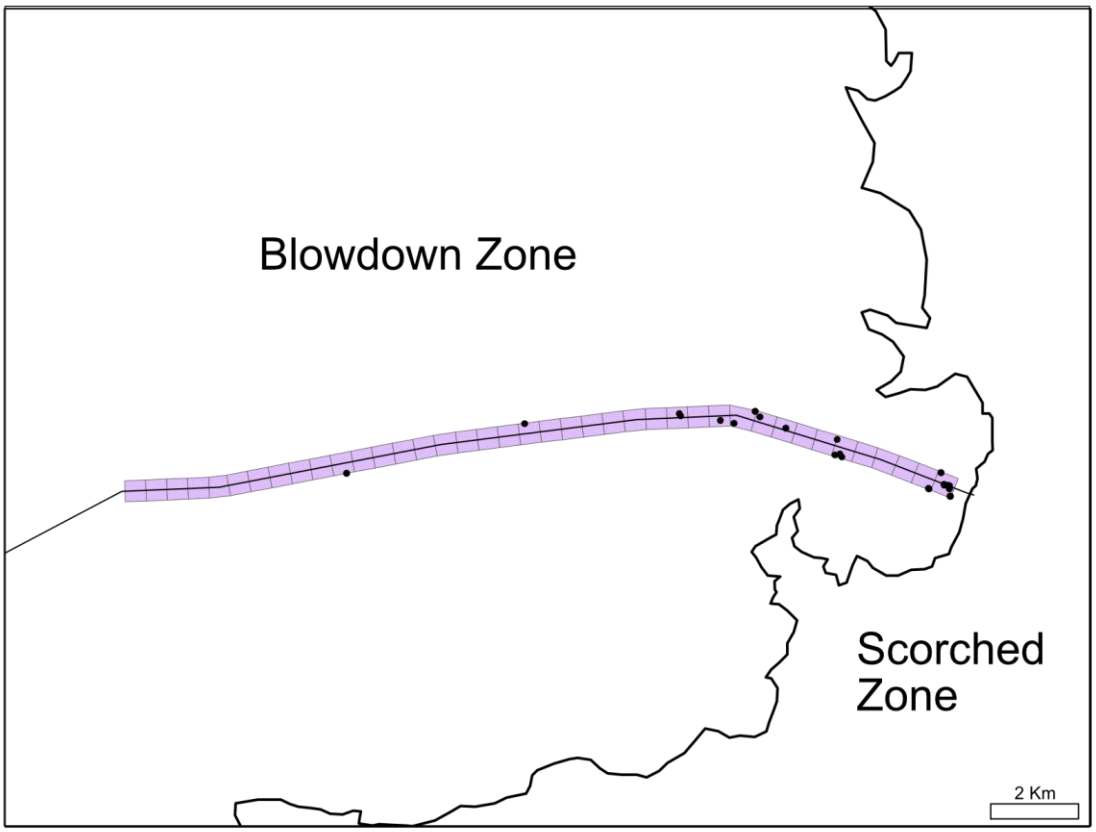

Figure *135*. The thin black line is flow path 6 in the East zone. Light purple boxes represent 200 by 200 m. The black dots are the locations of isolated standing trees. The thicker black line is the boundary between the scorched zone and the blowdown zone.

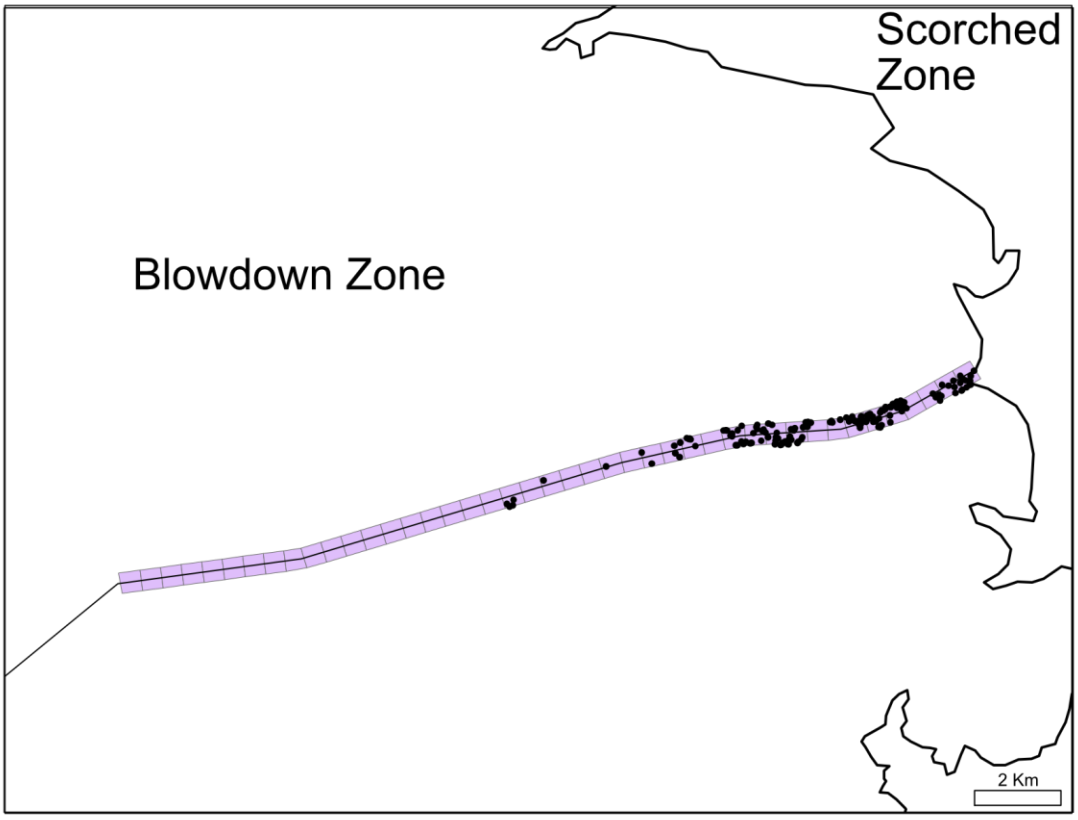

Figure *136*. The thin black line is flow path 7 in the East zone. Light purple boxes represent 200 by 200 m. The black dots are the locations of isolated standing trees. The thicker black line is the boundary between the scorched zone and the blowdown zone.

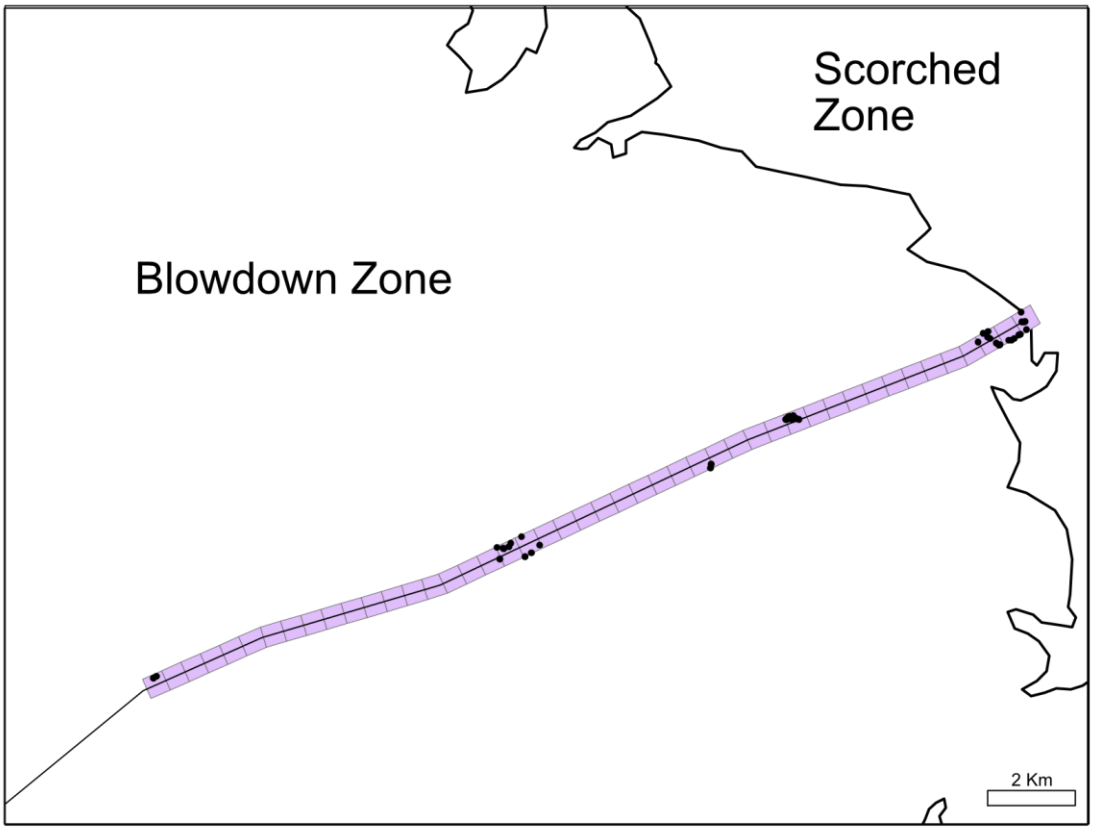

Figure *137*. The thin black line is flow path 8 in the East zone. Light purple boxes represent 200 by 200 m. The black dots are the locations of isolated standing trees. The thicker black line is the boundary between the scorched zone and the blowdown zone.

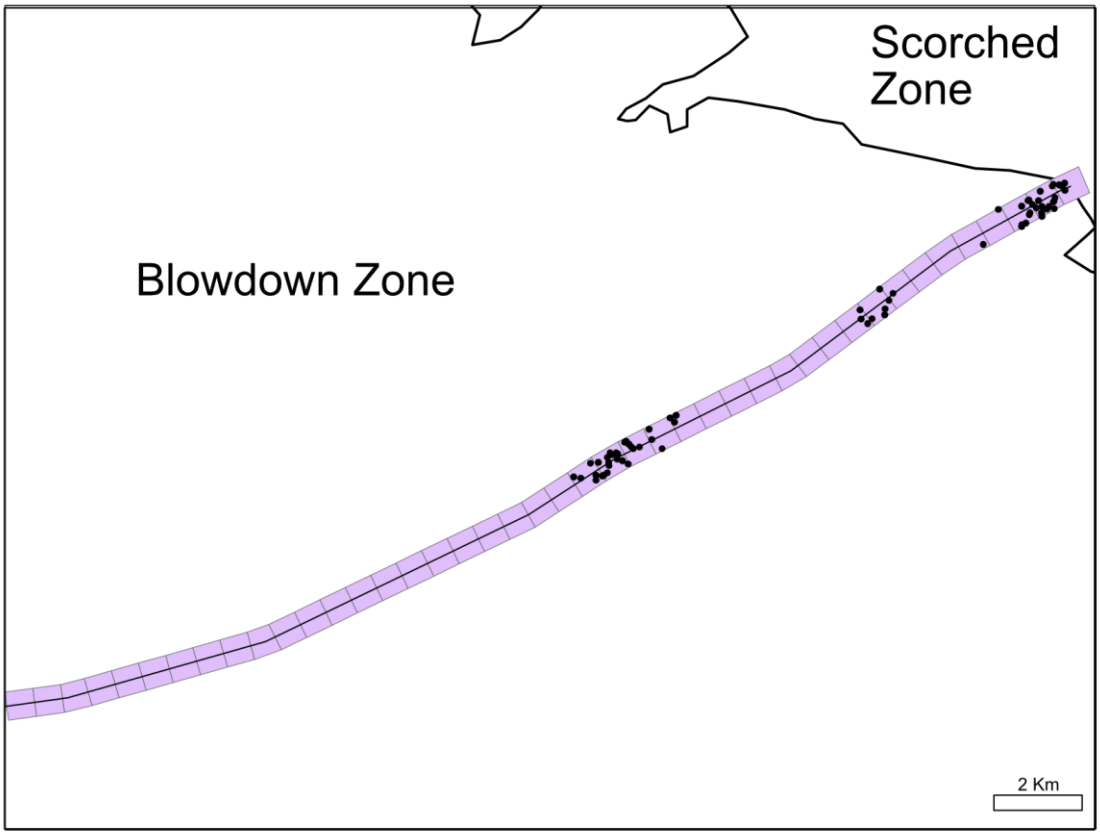

Figure *138*. The thin black line is flow path 9 in the East zone. Light purple boxes represent 200 by 200 m. The black dots are the locations of isolated standing trees. The thicker black line is the boundary between the scorched zone and the blowdown zone.

Table 12. Each row represents an isolated standing tree in the West zone. Length and bearing describe the tree shadow. Aspect and slope describe the ground where the shadow is situated. Height is the height of the tree based on length, bearing, aspect, and slope.

Flow Path	Length	Bearing	Aspect	Slope	Height
33	12	355	13	24.8	21
33	13.9	356	37	30.8	24.2
33	17	352	36	32.9	29.2
33	13.3	354	37	35.2	21.6
33	10.3	358	39	27	18.8
33	24.3	362	131	23.6	61.6
33	17.1	359	187	20.5	43.6
33	9.3	371	191	24	23.8
33	12	354	189	23.9	30.6
33	11.9	358	17	23.2	21.5
33	18.6	355	238	23.2	46.5
33	14.8	354	354	24.3	25.6
33	21.4	359	308	20.1	44.3
33	21.4	362	301	21.1	45.7
33	10.8	368	305	19.7	23.5
33	16.7	346	325	26.3	28.8
33	18.7	359	320	26.7	34.1
33	15.3	339	334	29.1	24.1
33	22.8	362	254	27.3	56.8
33	15.9	357	329	26.6	27.9
33	19.1	348	232	26.6	48
33	16.3	367	355	27.2	27
33	12.2	362	355	30.8	18.6
34	13.8	310	28	27.7	25.9
34	12.7	353	41	28	19.7
34	12.6	346	72	20.5	24.8
34	10.6	321	99	13	22.6
34	10.3	328	104	14.1	22.2
34	12.6	327	107	23.2	27.9
34	15.3	330	111	21.2	33.6
34	10.8	329	95	18.4	23.3
34	20.2	311	120	21.9	44.9
34	11.5	327	179	19.2	25.2
34	10.4	323	186	22.6	22.9

Table 12 (continued)

Flow Path	Length	Bearing	Aspect	Slope	Height
34	10.1	316	224	12.6	20.2
34	12.7	327	223	10.6	25.8
34	14.3	326	224	12.8	29.2
34	10.4	329	232	14.5	21
34	11.2	317	246	16.5	21.3
34	13.3	325	254	20.6	24.8
34	10.4	329	285	24.4	16.5
34	11.3	322	254	18.4	21
34	16.7	308	351	33.3	23
34	13.3	316	356	30.8	18.6
34	10.8	313	357	30.7	15.6
35	16.3	357	342	35.9	17.3
35	11.9	358	332	30.5	15.5
35	11.9	345	319	33.4	14.4
35	16.9	312	310	36.8	16.9
35	25.5	316	309	38.1	24.5
35	14.3	318	309	30	17.7
35	10.5	340	307	30.5	14.2
35	12.4	316	307	31.5	14.8
35	13.8	316	306	39.8	12.6
35	18.3	318	301	40.9	16.4
35	26.3	309	310	42.3	21.2
35	22	315	299	41	19.6
35	17.7	339	320	43.8	14.4
35	16.1	350	309	44.2	16.5
35	26.3	305	292	43	21.2
35	19.9	316	289	42.8	18
35	10.5	316	287	43.5	9.5
35	26.4	313	288	42.5	23.8
35	11.7	315	292	42.4	10.4
35	16.9	321	291	41.9	16.4
35	19.7	310	280	36.6	22.5
35	13.9	357	275	35	26.3
35	14.3	314	277	36.6	17.3
35	15.6	345	269	38.5	27.6
35	18.5	310	267	36.6	23.8
35	15.4	313	266	35.1	21.1
35	10.1	322	268	36	14.6

Table 12 (continued)

Flow Path	Length	Bearing	Aspect	Slope	Height
35	14.7	312	268	30.1	21.5
35	12.1	351	262	30.7	23.9
35	13.1	315	257	42.4	17.7
35	11.2	313	237	29.8	20.6
35	11.5	316	233	24.7	22.2
35	12.4	318	235	26.7	24
35	12.6	325	243	30.1	24
35	12.3	329	240	27.1	24.4
35	15.2	319	274	26.8	23.6
35	11.2	317	290	30.7	14.6
35	13.1	326	230	33	27.1
35	10.7	326	182	33.4	24
35	14.1	321	213	35.1	30.5
35	16.8	317	207	26.7	35.9
35	11	316	215	19.1	22.6
35	15	319	203	26.2	32.4
35	11	316	199	20	23.4
35	13.5	324	200	21.4	29.2
35	10.8	322	197	16.4	23.2
35	20.9	331	185	20.1	46
35	10.8	313	184	24	23.6
35	15.7	314	182	21.8	34.3
35	12.4	331	177	24.6	27.7
35	11.6	355	175	32.1	25.8
35	10.6	321	175	30.4	23.6
35	10.7	324	174	24.7	23.7
35	10.4	329	171	25.4	23.2
35	15.7	319	163	23.8	35
35	12.7	345	153	27	28.3
35	11	330	152	24.8	24.6
35	13.8	330	148	17.3	30.4
35	20.5	321	144	34	45.3
35	10.4	323	142	42.2	22.3
35	18.4	330	141	35.5	40.6
35	14	324	140	22.6	31.1
35	10.7	344	129	22.7	23.6
35	10.1	311	110	19.1	22.3
35	12.2	327	100	23.6	26.8

Table 12 (continued)

Flow Path	Length	Bearing	Aspect	Slope	Height
36	10.3	312	349	11.7	17
36	11.9	312	345	34.2	13.3
36	16.5	322	345	25	21.4
36	19.9	317	340	37.4	18.5
36	14.3	318	335	38	12.5
36	10.4	307	335	8.9	17.5
36	13.2	307	321	19.6	18.7
36	12.4	312	317	35.3	11.5
36	15.9	317	305	21.7	21.5
36	21.2	323	305	16.1	32.1
36	11.3	320	309	16.9	16.7
36	12.5	302	307	10.6	20.3
36	10.3	312	304	4.3	18.2
36	18.7	318	302	18.8	27
36	15.3	309	300	26.2	18.6
36	10.3	320	301	22.8	13.9
36	12.7	319	298	28.2	15.2
36	12.9	314	297	26.7	15.8
36	17.6	319	291	16.9	26.7
36	12.7	321	288	17.2	19.5
36	12.9	318	288	15.2	20.1
36	14.3	326	289	16.4	22.4
36	15	317	288	17.8	22.5
36	14.6	322	285	26.8	19.5
36	10.1	328	284	31.6	13
36	17.1	313	284	29.8	20.4
36	16.2	309	273	21.2	23.6
36	10.8	308	271	14.8	17.3
36	12.2	308	269	22.6	17.7
36	11.1	307	262	22.6	16.5
36	10.8	310	262	37	12.9
36	13.8	318	255	20.7	22.7
36	11.5	311	254	19.5	18.6
36	15.7	319	262	21.9	24.9
36	13.3	318	260	27.5	20.1
36	10.5	316	241	26.2	18
36	13.2	332	236	19.7	24.7
36	10.2	306	241	25.6	16.3

Table 12 (continued)

Flow Path	Length	Bearing	Aspect	Slope	Height
36	20.1	306	262	17	31.9
36	14.1	311	267	10.8	23.8
36	12.6	315	265	18.1	20.2
36	13.8	316	229	28.3	25
36	14.7	306	223	27.2	26.1
36	10.1	316	227	20.1	18.5
36	13.6	317	231	16.7	24.7
36	11.7	328	225	22.7	22.6
36	10.8	308	224	16.6	19.6
36	10.8	315	222	19.9	20
36	15.7	319	209	17.3	30.4
36	14.3	314	193	19.1	28.4
36	14.3	326	180	25.9	29.8
36	13.6	319	155	26.3	28.5
36	13.6	315	144	26	28.4
36	10.5	319	138	25.8	22.1
36	14.7	316	82	22	29.8
36	11.5	319	166	18.9	23.6
37	10.6	325	350	24.2	16.2
37	26.3	356	193	30.7	59.8
37	11.1	339	274	17.8	20.9
37	12.6	325	278	35.9	17.6
37	11.5	321	281	32.4	16.2
37	11.2	313	323	32.5	13.6
37	11.8	322	333	23.7	17.5
37	12.5	323	349	35.3	15
37	11.3	328	113	21.2	25.5

Table 13. Each row represents an isolated standing tree in the North zone. Length and bearing describe the tree shadow. Aspect and slope describe the ground where the shadow is situated. Height is the height of the tree based on length, bearing, aspect, and slope.

Flow Path	Length	Bearing	Aspect	Slope	Height
15	13.1	324	179	18.2	30.5
15	12	335	190	16.9	27.8
15	11.7	335	200	18	27.1
15	10.1	333	207	27.9	23.6
15	11.2	329	209	34.6	26.3
15	10.1	346	212	37	23.8
15	11.3	339	221	32.8	26.5
15	11.2	326	218	30.6	25.7
16	10.7	292	222	8.3	20.7
16	14.9	328	231	11.5	29.9
16	11.4	333	259	13.6	21.9
16	10.8	329	259	14.1	20.5
16	10.8	320	248	13.5	20.6
16	12.8	323	252	14	24.3
16	22.1	325	252	14.4	42.2
16	10.7	334	249	14.3	20.9
16	19.2	316	231	14.2	37.7
16	16	294	223	14.6	30.3
16	11.1	300	221	14.7	21.5
16	10.2	299	244	16.1	18.4
16	15.7	318	234	18.1	30.6
16	14	324	226	18.6	28.3
16	13	322	219	18.6	26.7
16	23.7	320	224	19.3	48
16	13.7	323	232	20.3	27.3
16	12	332	234	20.5	24.4
16	15.5	326	243	20.7	30.1
16	11.3	345	239	21.7	23.6
16	13	322	185	24.7	28.6
16	11	311	156	25.8	24.5
16	11	339	142	26.4	24.5
16	13.2	328	178	30.4	29.4
16	15.8	344	72	30.1	31.1
16	11.1	337	50	27.8	20.1

Table 13 (continued)

Flow Path	Length	Bearing	Aspect	Slope	Height
16	12	339	144	15.9	26.3
17	11.7	324	19	19	21.8
17	14	331	23	23.3	24.8
17	10.1	330	25	22.9	18.2
17	17.3	335	27	25.3	30
17	13.6	323	31	24	26
17	10.9	337	27	29.5	17.8
17	10.1	325	36	20.2	19.8
17	12.8	328	39	23.8	24.9
17	12.7	339	32	31	20.6
17	11.8	333	24	22.3	21
17	15.5	335	33	20.1	28.9
17	12.6	321	36	27.1	24.6
17	10.9	346	43	30.1	18.5
17	12.3	332	44	21.3	24.1
17	14.2	329	44	28.6	27.7
17	12.5	339	54	30.2	24
17	14.9	335	64	28.3	31.1
17	11	336	56	21.4	22.3
17	15.3	332	63	26.8	32.1
17	10.5	335	70	29.4	22.6
17	10.5	326	69	19.9	22.8
17	10.4	308	69	40.1	24.1
17	12.3	337	73	21.3	26.3
17	10.9	321	90	38.2	25.3
17	12	342	94	43.9	27.7
17	13.3	329	69	34.9	29.3
17	11.5	334	58	29.9	23.3
17	11.1	320	103	22.6	25.5
17	11.3	330	105	16.4	25.4
17	13	327	108	17.7	29.6
17	13	327	71	11.1	27.8
17	10.4	333	102	10.1	22.9
17	23.3	331	94	12.9	51.4
17	11.8	331	139	18.5	27.3
17	11.5	334	141	21.3	26.6
17	10.1	330	108	31.7	23.4
17	12	327	109	32.4	27.9

Table 13 (continued)

Flow Path	Length	Bearing	Aspect	Slope	Height
17	14.6	325	113	23.7	33.8
17	10.2	329	115	25.4	23.7
17	10.7	322	115	31.9	24.9
17	11.6	333	138	26.3	26.9
17	11.6	330	150	22	26.9
17	11.6	339	123	30.1	27
17	11.6	330	111	32.3	27
17	14.6	318	129	32.7	33.7
17	16.4	326	131	33.2	37.7
17	11.5	328	134	33.8	26.5
17	13.5	320	150	24.4	31.4
17	10.2	323	153	24	23.7
17	10.3	334	145	31.9	23.8
17	12.2	316	151	22.4	28.2
17	10.3	318	155	14	23.4
17	10.7	316	161	1.3	22.6
17	11.4	324	276	19.1	20.7
17	15.3	332	277	15.5	29.3
17	10.6	325	217	19.1	23.3
17	11.6	325	288	16.3	21
17	14.8	327	283	23.7	25.1
17	13.3	339	248	23.7	28.1
17	14.7	330	303	12.7	27.3
17	11.8	326	325	4	23.9
17	10.5	339	310	10.8	19.9
17	10.1	340	334	14.7	18
17	10.7	322	342	15.5	19.1
17	20	342	355	32	25.4
17	15.1	341	256	30.8	30.8
18	11.1	356	262	32.8	23.7
18	10.4	338	244	33.2	22.1
18	10.4	323	250	28.6	19.8
18	11.1	356	262	32.8	17.2
18	10.4	338	244	33.2	21.3
18	10.4	323	250	28.6	21
18	10.5	311	255	33	22.6
18	10.6	328	249	21.8	23.8
18	10.7	326	257	19.9	26.2

Table 13 (continued)

Flow Path	Length	Bearing	Aspect	Slope	Height
18	10.8	317	228	26.7	26.8
18	11.2	358	266	27.4	26.9
18	11.3	357	223	33.4	24.1
18	11.5	333	191	34.6	27.6
18	11.7	325	210	37.3	28.2
18	11.8	322	236	30.5	27.8
18	12	323	206	32.9	20.8
18	12.1	349	207	30.3	20.1
18	12.3	329	224	38.8	28.9
18	12.3	340	298	23.6	25
18	12.4	326	251	54.9	25.6
18	12.4	331	188	30.9	26.7
18	12.7	327	258	17.6	26.8
18	12.7	319	237	27.2	30.7
18	12.8	325	237	35.4	30.2
18	13.2	332	247	34.1	28
18	13.3	356	215	37.5	24.1
18	13.3	337	189	43	32.4
18	13.6	321	233	43.9	33
18	13.8	320	254	34.3	32
18	14.1	327	208	31.3	32.8
18	14.2	324	182	28.6	32.3
18	14.5	317	211	24.9	36
18	16	320	234	30.5	36.9
18	16	330	247	30.8	33.3
18	16	352	246	34.8	33.4
18	16.1	334	224	39.8	21.9
18	16.2	329	252	8.2	31.7
18	16.3	331	246	28.8	30.7
18	16.9	318	292	33.1	36.3
18	17.4	327	262	28.4	31.8
18	18.4	322	267	30.5	37.5
18	18.7	330	251	35.5	40.9
18	19.8	327	262	41.5	48.6
21	18.2	340	6	13.6	33.8
21	10.8	332	7	15	20.1
21	16	330	6	16	29.4
21	14	335	7	10.8	27

Table 13 (continued)

Flow Path	Length	Bearing	Aspect	Slope	Height
21	20.6	335	7	13.3	38.7
21	15.6	336	8	14.6	28.9
21	23.6	331	12	10.8	46.1
21	20.4	331	14	14	38.9
21	11.9	330	12	13.5	22.7
21	15.6	341	17	16.4	28.4
21	10.5	331	17	21.5	18.7
21	12.1	328	19	20.4	22.2
21	13.8	342	22	13.6	26.2
21	17.3	328	23	9.6	34.7
21	15.1	330	26	11.1	30.2
21	12.4	333	29	11.3	24.7
21	10.9	327	31	9.9	22.2
21	16.7	335	31	10.2	33.5
21	10.3	337	32	11.4	20.5
21	17.2	326	34	10.8	35
21	11.9	345	6	12.1	22.4
21	21.2	322	112	19.2	49.1
21	13.7	324	217	23.9	30.5
21	13.2	327	221	21.8	29.2
21	13.1	340	228	20.5	29.2
21	11.2	328	233	17.2	24.1
21	14.4	328	157	16.8	33.4
21	14.6	319	160	17.4	33.8
21	23.3	333	160	16.2	53.7
21	12.1	337	239	21.2	26.2
21	10.6	326	236	23.8	22.4
21	20.4	333	236	21.1	44.1
21	10.6	333	241	19.6	22.7
21	12.6	336	243	17.9	26.9
21	16.2	335	242	19.9	34.6
21	11.5	333	239	20.6	24.8
21	14.6	338	238	18.5	31.6
21	10.5	349	242	17.7	23.1
21	16.5	336	243	19.2	35.3
21	11	319	241	23.6	22.2
21	18.1	331	240	17.9	38.5
21	18.1	337	240	15.7	38.9

Table 13 (continued)

Flow Path	Length	Bearing	Aspect	Slope	Height
21	12.2	324	241	16.4	25.4
21	13.3	343	241	16.1	28.8
21	12.8	324	243	14.4	26.5
21	11.3	321	244	12.5	23.3
21	11.9	339	246	10.7	25.4
21	13.3	330	250	16.4	27.5
21	14.4	332	246	18	30
21	14.1	328	248	13.5	29.2
21	13.7	334	248	15.9	28.6
21	12.5	329	245	15.7	26
21	13.8	327	246	18.4	28.3
21	10.6	326	248	21	21.4
21	12.1	319	248	25.5	23.4
21	10.1	318	249	26.1	19.4
21	15.6	333	250	13.4	32.6
21	15.7	344	254	18.6	33.2
21	12.9	326	272	14.1	25.1
21	10.7	329	282	5.9	21.8
21	25.6	334	314	6.4	51.1
21	11.1	325	319	7.8	21.8
21	21.4	329	342	9.2	41.3
21	15.7	326	347	10.8	30
21	10.2	339	350	10.6	19.3
21	13.1	331	291	20.7	23.1
23	16.2	323	110	17.6	36.7
23	10.2	323	142	7.6	22.3
23	13.7	326	137	6.4	29.8
23	12.8	328	165	17.2	29.2
23	11.7	335	252	19.9	23.7
23	12.8	328	288	18.4	22.6
23	19.7	329	293	22.7	32.4
23	11.2	333	298	16.6	20
23	11	325	304	25	16.5
23	20.3	327	315	18	33.9
23	10.7	330	313	14	19
23	10.4	330	314	13.4	18.7
23	13	331	315	10.9	24.2
23	23.6	328	324	14.5	41.6

Table 13 (continued)

Flow Path	Length	Bearing	Aspect	Slope	Height
23	11.2	326	326	16.8	19
23	18.4	328	328	18.8	30.2
23	10.9	330	328	8.9	20.7
23	12.3	327	331	8.2	23.4
23	15.2	331	332	7.6	29.2
23	20.3	327	335	14.7	35.6
23	14.4	340	336	19.4	23.4
23	23.9	327	339	14.3	42.4
23	11.6	330	340	14	20.6
23	13	327	337	13.3	23.3
23	11.6	330	345	15.9	20.1
23	11.4	332	346	7.6	21.9
23	10.5	335	357	11.1	19.6
23	10.4	336	189	26.1	23.9
24	22.2	330	8	16.7	41.1
24	13.8	330	9	4.8	28.5
24	12	328	10	3.7	25.1
24	12.1	343	13	29.8	17.8
24	12.5	338	8	28.9	18.6
24	19.4	337	79	31.6	43.6
24	16.7	330	116	33.3	39.4
24	21.2	326	44	20.6	43.6
24	26.5	336	66	19.6	56.6
24	12.2	338	178	16.6	28.3
24	10.8	329	261	23.4	21
24	19.1	332	343	17.7	33.1
24	13.5	329	345	17.6	23.6
24	14.1	327	347	16.2	25.4
24	20.7	331	348	14.6	37.9
24	16	330	354	13.6	29.9
24	21	332	200	25.3	49.1

Table 14. Each row represents an isolated standing tree in the Northeast zone. Length and bearing describe the tree shadow. Aspect and slope describe the ground where the shadow is situated. Height is the height of the tree based on length, bearing, aspect, and slope.

Flow Path	Length	Bearing	Aspect	Slope	Height
10	12.6	362	27	12.3	26.6
10	10.6	356	19	19.6	20.4
10	11.7	368	35	25.9	20.7
10	14.2	360	113	27.7	35.7
10	10.3	360	86	31	23.7
10	12.6	358	8	31.9	18.7
10	10.1	351	11	32.6	15.1
10	13.6	359	24	33.5	20.5
10	11.3	357	33	33.6	18.1
10	13.2	359	33	33.6	20.9
10	13	353	319	34.3	20.2
10	11.3	355	154	41	27.8
10	13.2	360	13	40.6	15.4
10	14.6	355	23	39.5	19.3
10	14.3	364	79	37.4	30.1
10	16.5	361	88	32	38.5
11	4.4	360	103	3.6	10.4
11	3.7	350	211	3.8	8.8
11	3.8	345	167	16.7	9.5
11	3.9	340	156	16.4	9.8
11	4	360	102	5.9	9.4
11	4	360	117	20.7	9.8
11	4.3	360	111	47.9	10.9
11	4.3	337	153	27.1	10.9
11	4.3	337	66	13.7	10
11	4.3	356	124	15.4	10.7
11	4.6	360	90	5.6	10.8
11	4.6	360	99	3.4	10.9
11	4.7	352	102	13.9	11.3
11	4.9	340	213	4.6	11.7
11	4.9	340	113	19.1	12.3
11	5	360	176	23	12.6
11	5	360	156	16.4	12.5
11	5	356	229	4.2	11.8

Table 14 (continued)

Flow Path	Length	Bearing	Aspect	Slope	Height
11	5	356	78	25.1	11.3
11	5.3	364	146	24.9	13.5
11	5.5	346	140	23.6	13.9
11	5.5	346	116	6.5	13.1
11	5.6	315	145	22.7	14.3
11	5.6	360	135	25.5	14.3
11	5.6	357	154	15.2	14.1
11	5.6	357	158	12.1	14
11	10	352	36	29.4	17.8
11	10.4	343	148	17.5	26.2
11	10.6	355	141	17.3	26.7
11	10.7	338	201	30.9	27.2
11	10.7	356	295	26.5	21.9
11	11	365	325	17.6	22.3
11	11	353	145	16.5	27.7
11	11	353	199	11	27.2
11	11.1	350	248	6.8	26.2
11	11.1	358	148	38.4	27.7
11	11.3	367	33	41.4	13.7
11	11.8	349	130	13.5	29.3
11	12.3	357	169	12.3	30.6
11	12.3	365	234	18.6	30.7
11	12.3	366	139	35	31.3
11	12.4	351	249	28.3	30.1
11	12.5	351	253	32	30.1
11	13.6	322	226	14.4	32.1
11	13.6	345	113	27.7	34.4
11	13.6	364	15	3.1	31
11	13.6	364	43	39.8	19.4
11	13.6	366	40	46.5	15
11	13.6	366	148	42.9	33.8
11	15.5	337	231	34.2	38.5
11	15.7	345	226	36.4	39.9
11	18.6	348	249	46.1	46.1
12	11.2	352	237	9.5	26.8
12	13.5	349	258	15.8	31.3
12	14.8	345	263	19.2	33.5
12	12.7	355	265	18.9	29.6

Table 14 (continued)

Flow Path	Length	Bearing	Aspect	Slope	Height
12	12.7	343	261	9	29.3
13	15.7	326	30	14.7	30.6
13	17.8	328	39	17.8	34.9
13	10.3	332	48	16.8	20.5
13	17.6	332	62	4	36.4
13	13.1	331	114	11	29
13	14.8	329	132	14	33.2
13	10.2	339	81	11.3	21.5
13	11	330	100	7.7	23.7
13	12.9	317	237	7.8	26.5
13	11	330	150	11.7	24.6
13	11.2	343	108	14.9	24.6
13	10.7	329	208	9.9	23
13	16.7	329	265	8.6	33.5
13	11.9	362	238	12.5	26
13	18.3	318	244	22.1	35.6
13	12.7	340	248	21.3	26.4
13	14.4	323	252	16.3	28.4
13	12.4	333	248	16.8	25.4
13	16.8	326	256	17.5	32.9
13	15.2	317	262	20.1	27.7
13	18.3	326	268	13.4	35.2
13	10.1	334	273	12.3	19.8
13	26.5	320	282	19.4	45.8
13	13.2	314	278	19.6	22.6
13	23.7	325	287	13.6	43.8
13	16.6	327	291	13.1	30.8
13	13.5	336	291	10.4	26
13	14.9	318	288	13.1	27.4
13	12.9	326	293	9.2	24.7
13	10.7	329	302	10	20.2
13	11.1	345	300	20.1	19.5
13	11.1	339	302	14.9	20.1
13	12.6	332	302	14	22.9
13	10.6	333	298	33.2	14.4
13	11.6	322	304	28.2	16.1
13	14	313	309	9.5	26.4
13	13.9	336	307	12.6	25.6

Table 14 (continued)

Flow Path	Length	Bearing	Aspect	Slope	Height
13	14.6	338	306	15.5	26.1
13	12.9	326	305	13.2	23.3
13	26.4	323	310	14.1	46.8
13	10.3	332	312	11	19.2
13	12.7	328	311	14.9	22.3
13	11	330	318	20	17.8
13	12.1	328	324	8.9	23
13	19.9	329	324	3.5	40
13	11.8	327	335	3	23.8
13	13.5	328	337	5.8	26.6
13	16.7	322	289	10.5	31.6
14	12.1	328	4	43.1	13
14	15	328	7	19.6	26.5
14	11.4	326	7	8.8	22.7
14	20.5	324	7	24.7	34.5
14	15.1	330	7	38	19.1
14	14.6	338	5	42.5	14.8
14	13.1	331	7	42.9	14.3
14	12.5	338	7	23.8	20.1
14	10.8	324	7	24.1	18.3
14	16	333	10	30.5	23.7
14	22.2	341	11	21.3	37.4
14	12.1	337	11	21.7	20.5
14	14.7	333	10	17.7	26.6
14	20.5	338	12	25.8	32.5
14	16.6	343	12	24.2	26.6
14	13.6	339	13	19.9	23.5
14	18.3	336	11	34.4	24.9
14	23.3	330	11	34.8	32.7
14	22.2	331	13	19.9	39.6
14	15.4	334	13	22.1	26.4
14	10.4	320	13	9.5	20.9
14	10.8	336	14	9.5	21.3
14	16.2	338	12	34.9	21.5
14	19.6	339	16	34.7	27
14	19.7	332	18	34.9	28.8
14	15.7	344	18	30.6	22.9
14	21.2	337	18	29.5	32.9

Table 14 (continued)

Flow Path	Length	Bearing	Aspect	Slope	Height
14	15.5	331	18	24	26.8
14	12	326	15	14	23.1
14	21.3	333	14	32.4	31.4
14	14.9	331	18	37.2	21
14	22.2	336	18	37.8	29.6
14	10.3	332	18	38.9	13.9
14	22.3	327	17	42	29.9
14	28.2	332	19	32.4	43.5
14	22.1	327	20	31.6	36
14	17.4	325	18	23.1	31.3
14	12.7	328	17	31	20.4
14	11.2	328	17	27	19
14	11	322	18	31.3	18.5
14	12.3	327	17	39	17.6
14	30	331	18	24	52.1
14	10.8	336	26	24.4	19
14	11.7	332	19	11.5	23
14	11.7	332	12	23.6	19.8
14	13.1	331	19	35.1	19.6
14	16.8	341	20	37.9	21.7
14	13.9	340	24	22.5	24.2
14	29.8	327	24	20.4	56
14	28.4	333	22	30.3	45.7
14	31.8	342	21	27.4	50.6
14	13.2	327	19	33.1	21
14	24.2	337	20	27.4	39.4
14	17	323	22	33	28.8
14	25.7	328	18	25.7	44.2
14	16	333	17	20.5	28.4
14	23.1	341	18	16	42.4
14	15.7	326	17	17.1	29.6
14	10.3	356	22	16.6	18.5
14	13	337	21	31.6	19.9
14	27.3	332	21	28.8	44.9
14	23.8	334	21	26.4	39.9
14	16	318	21	24.2	30
14	36.1	330	22	22.8	64.6
14	19.4	329	23	26.2	34

Table 14 (continued)

Flow Path	Length	Bearing	Aspect	Slope	Height
14	19.7	326	22	28.5	34.3
14	10.4	317	21	26.3	19.3
14	17.2	334	23	31.4	27.5
14	16.9	321	25	31.6	30.1
14	11.4	324	24	34.7	19.1
14	12.8	330	24	18.8	24
14	20.6	322	29	34.1	36.8
14	11.4	326	29	31.4	20.3
14	34.4	329	27	41.8	50.9
14	21	323	28	37.4	35.8
14	22.9	330	28	38	35.9
14	21.7	329	26	37.8	33.8
14	13.8	342	28	26.9	23
14	17.7	316	27	27.7	34
14	11.4	331	26	20.2	21.2
14	14	331	28	25	25.3
14	21.4	338	26	34.7	32
14	25.3	325	24	35	42.2
14	18.9	330	29	14.8	37
14	18.6	318	30	10.9	38.1
14	13.7	334	31	12.8	27
14	21.3	331	31	15.1	41.9
14	11.8	327	32	11.9	23.8
14	21.7	342	31	14.6	41.7
14	16.7	335	31	15.5	32.4
14	20.8	331	29	27.2	36.9
14	20.9	333	35	29.8	37.2
14	25.4	333	37	29	46.2
14	12.3	327	37	21.2	24.2
14	20.8	331	36	14.7	41.3
14	13.3	321	37	11.4	27.4
14	17.2	326	36	13.4	34.8
14	11.7	336	36	21	22.1
14	12.6	336	39	21.3	24
14	13.3	323	41	24.2	26.9
14	14.2	337	41	24.3	26.7
14	18	320	38	39.5	34.5
14	16.1	344	47	29.1	29

Table 14 (continued)

Flow Path	Length	Bearing	Aspect	Slope	Height
14	11.8	320	52	22.2	25.2
14	12.8	334	53	44.9	24.1
14	13	329	48	32.8	25.7
14	12.9	326	42	24.3	25.7
14	18.8	335	61	9.2	39.6
14	18.3	330	50	30.3	36.8
14	22.7	333	39	46.1	35.2
14	14.4	332	45	45.3	25.1
14	13	333	48	39.2	24.3
14	17.4	333	84	24.4	39.1
14	13.5	317	82	26.1	31.1
14	13.7	330	77	33.5	31
14	19.5	336	45	28.6	36.9
14	13.7	330	43	24.1	26.8
14	10.7	338	72	12.2	22.8
14	13.9	329	85	17.9	31
14	11.4	335	72	9	24.3
14	14	331	103	16.1	31.8
14	10.7	345	94	18.3	23.6
14	14.4	328	60	18.9	30.6
14	17.7	333	59	10.8	37.3
14	10	326	91	15.2	22.5
14	14.1	328	96	34.3	32.9
14	14	331	100	30.9	32.7
14	20.9	327	106	32.2	48.9
14	18.6	340	105	32.2	43.3
14	18.3	330	111	26	42.7
14	15.8	332	111	27.9	36.9
14	15.6	336	109	32	36.6
14	10.5	331	109	33.9	24.5
14	17.1	329	109	31.1	40
14	16.7	338	114	26.6	39
14	14.4	328	114	25.8	33.7
14	19.3	328	177	30.8	45.1
14	13.3	333	199	31.7	31.1
14	23.6	327	200	31.4	54.9
14	11.9	330	125	22.6	27.8
14	14.6	327	128	22.1	34.2

Table 14 (continued)

Flow Path	Length	Bearing	Aspect	Slope	Height
14	10.4	320	141	12.4	23.8
14	12.7	321	142	5.6	28
14	12.8	338	132	10.8	28.9
14	14	331	130	14.2	32.1
14	20	326	132	22.2	46.8
14	11.8	320	133	21.8	27.6
14	10.3	328	136	26.2	24.2
14	17.3	323	138	13.2	39.6
14	11.7	342	139	14.1	26.7
14	15.1	337	137	20.8	35.2
14	16.5	336	139	31.5	38.5
14	10.5	323	140	37.8	23.9
14	12.7	328	146	32.5	29.4
14	11.8	320	154	32.5	27.5
14	10.1	329	155	36.8	23.3
14	11.5	333	169	23.9	27
14	14.4	332	181	23.6	33.5
14	18.1	334	268	24.9	34.2
14	12.2	324	265	21.2	23
14	12.4	333	335	29.6	16.7
14	14.7	333	317	29.7	20.2
14	16.9	336	317	31.4	22.5
14	16.5	330	317	31.5	21.6
14	14.1	328	319	30.9	18.5
14	27.3	327	322	30.8	35.8
14	17.1	329	322	30.8	22.4
14	11.2	333	321	30.4	14.9
14	13.2	316	323	31.1	17.2
14	20	326	334	29.7	27
14	18.1	337	340	31.7	23.2
14	18.9	330	341	31.7	24.4
14	19	331	343	32.2	24.2
14	19.5	327	345	35.6	23.2
14	18	329	349	33.8	22.5
14	11.7	325	350	33.4	15.2
14	12.7	328	354	38.1	14.6
14	11.6	329	190	39	26.9

Table 15. Each row represents an isolated standing tree in the East zone. Length and bearing describe the tree shadow. Aspect and slope describe the ground where the shadow is situated. Height is the height of the tree based on length, bearing, aspect, and slope.

Flow Path	Length	Bearing	Aspect	Slope	Height
1	10.7	329	220	7.9	21.2
1	13.1	325	300	15.6	21.5
1	12.3	315	312	18.9	18.7
1	11.6	308	315	19	17.6
1	11.2	315	291	19.5	17.3
1	14.3	326	298	25.9	19.9
1	16.1	322	297	23.7	23.1
1	16.3	315	320	27.3	20.7
1	12.9	317	317	28	16.1
1	10.3	328	317	31.3	12
1	13.3	321	320	34.7	13.6
1	14.6	313	322	36.7	14.2
1	10.7	315	318	35.8	10.6
1	12.7	319	311	39.7	10.9
1	14.3	314	312	42.1	11
1	12.7	319	321	40.6	10.4
3	13.9	357	187	29.5	34.8
3	19	344	317	31.3	29.4
3	17	349	306	31.5	28.8
3	17.6	342	303	32.1	28.7
3	14.4	339	303	32.3	23.1
3	11.6	344	302	32.1	19.3
3	21.5	337	233	31.8	52.3
3	11.6	344	197	31.7	29
3	14.5	351	305	32.6	24.5
3	13.7	343	306	33.4	21.5
3	11	347	301	32.9	18.7
3	18.7	348	228	34.9	46.8
3	10.2	347	192	36.1	25.3
3	18.1	337	311	39.4	22.9
3	12.4	343	318	40.7	15
3	12.4	354	320	39.8	16.5
3	14.2	349	321	39.8	17.8
3	14.6	347	205	39.3	36.3

Table 15 (continued)

Flow Path	Length	Bearing	Aspect	Slope	Height
3	12.6	342	133	38.5	30.9
3	13.3	350	191	40	32.4
3	12.1	343	202	40.1	29.9
3	11.2	352	139	42	27.4
3	20.8	352	253	38.5	50.2
4	16	353	248	11.5	38.5
4	12.9	356	243	20.5	32
4	12.6	355	248	33	31.6
4	16	353	245	25.3	39.6
4	11.2	358	239	21.6	28.2
4	10.9	346	230	22.3	27.2
4	10.7	351	222	14.6	26.6
4	16.6	354	219	21.2	42.2
4	14	355	220	33.8	35.7
4	16.3	354	220	29.8	41.7
4	19.2	358	220	22.7	48.9
4	16	353	199	21.7	40.9
4	18.8	350	207	14.1	47.2
4	13.1	351	207	18.3	33.1
4	13.2	359	215	27.5	33.9
4	13.6	357	227	26.7	34.6
4	13.1	351	224	23.7	33.1
4	14.6	359	216	28.1	37.3
4	16.2	360	217	22.3	41.3
4	15.6	354	216	16.7	39.3
4	13.1	339	212	16.1	32.6
4	11.2	360	220	15.2	28.2
4	10.3	356	224	21.8	26
4	11.3	355	211	28.8	28.9
4	12.1	351	203	20.1	30.7
4	10.6	360	207	28.3	27.1
4	18.9	360	204	12.1	47.2
4	15.9	348	200	18.3	40.3
4	15	352	196	22.7	38.4
4	16.6	363	195	17.9	42.2
4	14.7	352	193	17.2	37.3
4	12.3	365	192	21.3	31.4
4	12	352	193	20.1	30.7

Table 15 (continued)

Flow Path	Length	Bearing	Aspect	Slope	Height
4	10	352	193	14.3	25.3
4	13.3	356	188	18	33.8
4	10.9	357	186	20	27.9
4	10.9	362	185	24.1	27.9
4	11.9	358	186	33.8	30
4	13.7	353	187	19.2	34.9
4	17.6	347	182	17.1	44.9
4	15.2	361	183	12.5	38.3
4	16	353	175	22.7	40.9
4	12.3	363	174	26.8	31.3
4	10.7	351	172	34.5	26.9
4	13.1	350	171	21	33.5
4	14.8	344	166	14.8	37.4
4	13.3	354	164	18.9	33.9
4	12.6	364	156	14.6	31.8
4	15.6	358	126	24.8	39.5
4	12.9	360	115	25.2	32.3
4	11.6	363	131	16.4	29
4	13.9	357	119	22.8	35
4	14.6	359	113	25.9	36.5
4	14.4	369	117	26.2	35.7
4	13.9	361	111	25.2	34.5
4	11.1	350	104	23.6	27.7
4	13.5	349	94	24.3	33.1
4	10.3	366	89	28.7	23.5
4	16.9	359	92	17.9	40
4	10	352	92	11.2	23.9
4	12.9	356	92	21.4	31
4	12.2	358	89	30.2	28.9
4	10.6	358	89	21.7	25
4	10.3	354	90	36	24.9
4	12.7	367	87	23	28.9
4	12.7	353	75	7.6	29.6
4	15.5	360	76	20	35.1
4	12.9	359	69	33.6	26.8
4	15	354	130	24.9	38.2
5	14.9	356	278	43.1	31.4
5	12.5	349	266	43.3	27.5

Table 15 (continued)

Flow Path	Length	Bearing	Aspect	Slope	Height
5	13.8	350	255	38.4	33.1
5	10.1	351	257	33.8	23.9
5	11.7	350	253	32.7	28.4
5	15.1	350	213	24.9	38.3
5	11.6	357	194	23.8	29.5
5	11.6	357	174	28.8	29.4
5	12.3	366	162	37.2	30.7
5	11.3	357	154	41.2	27.6
5	14.4	344	124	29	36.7
5	11.5	321	112	21.7	29.2
5	10.3	358	111	19.3	25.2
5	12.7	319	112	34.4	31.9
5	16	353	101	11.9	38.4
5	13.4	370	94	23.9	30.8
5	22.7	352	101	32.5	56.7
5	11.8	324	107	29.7	30.1
5	27.6	354	101	17.6	66.7
5	12.7	353	95	14.1	30.3
5	14.9	363	93	14	34.8
5	16.4	352	92	9	38.7
5	10.9	357	90	8.6	25.7
5	11	351	89	8.8	26
5	16.9	358	89	16.1	39.6
5	10.2	331	89	33.7	25.8
5	10.4	351	90	7.7	24.5
5	19.6	353	86	17.3	46.3
5	13	354	84	21.1	30.3
5	14.6	354	85	21	34.4
5	10	343	87	8.7	23.8
5	14	353	84	8.8	32.8
5	15.6	358	83	9.1	36.2
5	14.2	360	82	9	32.9
5	23.6	354	81	10.5	55.1
5	10.6	365	81	9.3	24.4
5	14.1	349	80	12	33.1
5	16.5	358	78	11.7	38.1
5	12.7	353	74	10.3	29.3
5	16.6	363	73	9.5	37.7

Table 15 (continued)

Flow Path	Length	Bearing	Aspect	Slope	Height
5	11.2	358	74	10	25.8
5	19.9	355	72	8.9	45.8
5	21.2	356	72	9.8	48.6
5	14.7	351	58	8	33.6
5	16.9	344	55	27.8	35.9
5	16.1	325	45	41	35
5	17.5	358	24	23.9	31.6
5	13.9	364	48	10.9	30.4
6	20.9	350	281	2.1	49.1
6	14.1	344	278	2.1	32.9
6	15.5	357	265	2.2	36.5
6	12.5	349	261	1.9	29.5
6	17.9	360	259	12.1	42.8
6	11.2	348	259	17.3	26.3
6	20.3	364	245	12.4	49.7
6	10.1	349	241	17.9	24.7
6	11.3	350	228	0.8	26.7
6	11.6	354	198	15.8	29.3
6	12.9	359	140	26.7	33
6	10.3	360	134	11.7	25.4
6	13.9	355	167	14.3	35.3
6	10.3	356	160	29.9	26.2
6	10.8	352	146	27.3	27.7
6	10.3	358	123	15.7	25.5
6	10.3	354	98	9.5	24.7
6	10.6	358	89	7.1	25
6	10.9	350	89	14.3	26.1
6	10.6	356	87	24.4	25
6	11.1	358	73	21.1	24.9
6	15.9	360	50	40.8	24.9
6	11.5	356	45	40.2	18.2
6	16.9	369	184	13.5	42.6
7	10.9	360	228	32.9	27.8
7	10.1	358	154	20.1	25.7
7	10.1	363	81	17.5	23
7	10.1	355	96	24.6	24.5
7	10.1	355	150	11	25.1
7	10.3	364	201	15.2	26

Table 15 (continued)

Flow Path	Length	Bearing	Aspect	Slope	Height
7	10.3	359	178	30.9	26.2
7	10.3	357	115	26.7	26.1
7	10.4	351	54	21	22.4
7	10.4	351	170	12.1	26.2
7	10.4	349	170	13.4	26.4
7	10.4	349	60	20.8	23.1
7	10.6	346	62	23.8	23.7
7	10.6	354	80	18.7	24.8
7	10.7	353	67	6	24.8
7	10.7	344	85	28.2	26.2
7	10.7	350	21	30.3	17.8
7	10.8	349	86	26.2	26
7	10.8	347	60	30.4	23.3
7	10.8	360	90	33	25.6
7	10.9	359	76	33.8	23.8
7	10.9	363	163	34.1	27.4
7	10.9	356	254	25	26.5
7	11.1	349	165	21	28.3
7	11.1	352	96	23.1	27.2
7	11.1	359	92	22.3	26.5
7	11.3	364	153	14.3	28.3
7	11.3	357	221	2.1	26.8
7	11.4	356	64	33.7	23.2
7	11.6	348	205	18.2	29.4
7	11.7	353	157	46.7	27.5
7	11.7	356	184	33.7	29.4
7	11.7	354	234	36	29.9
7	11.7	354	216	36	29.9
7	11.7	354	118	30.7	29.9
7	11.9	362	84	17.6	27.5
7	11.9	357	73	7.6	27.7
7	11.9	356	152	19.7	30.4
7	12	354	164	14.2	30.3
7	12.1	351	172	24.5	30.9
7	12.1	370	161	36.5	30.5
7	12.2	360	74	28.1	26.6
7	12.2	358	183	21.3	31.2
7	12.3	345	181	12.8	31

Table 15 (continued)

Flow Path	Length	Bearing	Aspect	Slope	Height
7	12.4	362	70	19.6	27.4
7	12.5	355	71	25.9	27.8
7	12.5	361	192	16.9	31.8
7	12.5	354	155	13.2	31.5
7	12.7	358	22	25.4	22.4
7	12.7	355	42	27.4	24
7	12.9	345	65	19.4	29.6
7	12.9	347	83	27.2	31.1
7	12.9	356	69	25.5	28.4
7	13	354	62	19.7	28.5
7	13	348	55	18.9	28.5
7	13.1	353	62	11.8	29.7
7	13.1	352	146	5.8	31.9
7	13.2	328	132	21.7	33.8
7	13.2	360	80	32.5	29.6
7	13.2	361	112	38	33.6
7	13.2	361	175	38.7	32.6
7	13.2	358	135	24.4	33.8
7	13.5	356	65	19.9	30
7	13.5	356	68	23.2	29.9
7	13.6	356	57	30.9	27
7	13.7	353	78	15.9	31.9
7	13.7	352	161	3.7	33.1
7	13.9	356	159	13.6	35.1
7	14	353	80	24.7	32.6
7	14	359	78	26.9	31.5
7	14.1	352	55	21.8	30.2
7	14.2	363	67	28.8	29.2
7	14.3	357	204	14.6	36.1
7	14.3	356	256	16.2	34.4
7	14.6	360	357	14.8	29.4
7	14.6	357	54	16.7	31.5
7	14.6	356	48	8.6	32.8
7	14.6	356	83	22.7	34
7	14.6	365	148	17	36.9
7	14.6	347	169	9.8	36.5
7	14.7	337	276	3.1	34.2
7	14.8	350	63	11.8	33.9

Table 15 (continued)

Flow Path	Length	Bearing	Aspect	Slope	Height
7	15	354	47	23	30.5
7	15.3	360	48	19.3	31.6
7	15.3	361	45	18.2	31.7
7	15.4	356	58	5.4	35.5
7	15.6	355	92	41.9	38.2
7	15.6	362	50	38.9	25
7	15.6	356	38	20.8	31.2
7	15.7	354	30	29.4	27.1
7	15.9	359	46	23.7	31.2
7	15.9	356	55	36.9	29.2
7	16.1	358	69	31.2	34.1
7	16.2	354	90	16.3	38.6
7	16.4	351	144	8.4	40.3
7	16.5	350	233	1.6	39
7	16.7	359	71	18.9	37.3
7	16.7	356	74	25.1	37.5
7	16.7	351	76	23.7	38.9
7	16.9	358	100	20.9	41
7	16.9	360	89	22.9	39.8
7	17	355	66	23.8	37.4
7	17	354	39	35.8	28.1
7	17.1	350	80	30.5	40.4
7	17.2	357	92	30.3	41.3
7	17.2	363	98	25	41.2
7	17.3	355	151	14.6	43.6
7	17.3	365	168	9.2	42.9
7	17.3	355	115	12.2	42.4
7	17.7	362	132	12.3	43.8
7	17.8	357	154	6.2	43.4
7	17.8	349	139	10.3	44.3
7	17.9	359	77	14.5	41.1
7	18	347	81	15.1	42.6
7	18	362	77	24.9	40
7	18.1	355	78	29.5	41.3
7	18.2	364	108	19.9	44.4
7	18.3	363	109	19.9	44.7
7	18.3	354	201	1.3	43.5
7	18.3	356	159	24.1	46.8

Table 15 (continued)

Flow Path	Length	Bearing	Aspect	Slope	Height
7	18.3	353	240	17.3	45.1
7	18.4	352	275	5.3	42.9
7	18.7	353	279	7	43.3
7	18.9	357	281	5.5	44
7	19.1	359	243	8.5	46
7	19.2	366	141	12.4	47.6
7	19.2	368	73	22.6	41.2
7	19.3	357	65	34.6	39.4
7	19.4	356	81	42.4	44
7	19.5	368	89	39.3	43.2
7	19.7	343	84	28.7	48.1
7	19.9	358	78	21.6	45.3
7	20.4	359	80	22.9	46.6
7	20.6	348	74	26.8	47.8
7	20.8	353	123	20.6	52.5
7	21.1	353	108	18.5	52.1
7	21.5	356	242	1.2	50.9
7	21.8	356	32	26.1	39.7
7	22.1	351	68	26.9	49.4
7	22.4	347	65	30.7	49.6
7	22.8	357	105	24.9	56.4
7	22.8	360	103	26.1	55.9
7	23.2	358	116	19.2	57.6
7	24.8	347	29	37.3	38.5
7	24.8	358	35	30.3	42.3
7	24.9	358	106	27.7	61.8
7	24.9	355	116	23.5	62.6
7	24.9	355	56	0.9	58.4
7	25.2	358	58	21.3	53.4
7	25.8	341	183	7	63.4
7	26.5	356	155	9.6	65.9
7	27.6	369	222	1.7	65.6
8	16.5	355	348	40.3	19
8	11.4	356	343	31.1	17.4
8	11.2	355	320	20.6	21.7
8	13.3	353	303	11.1	29.4
8	12.8	347	282	19.5	27.7
8	15.2	367	255	22.4	37.6

Table 15 (continued)

Flow Path	Length	Bearing	Aspect	Slope	Height
8	11.1	360	253	12	26.7
8	13.6	354	252	8.3	32.3
8	11.8	351	238	10.3	28.5
8	10.7	353	235	17.8	26.4
8	13.8	349	237	16	33.6
8	12	354	234	19.1	29.8
8	11	340	231	18.2	26.8
8	10.1	353	229	19.7	25.3
8	12.4	350	225	24.2	31.2
8	12.2	356	213	18.4	30.8
8	17.8	354	189	12	44.6
8	13.8	355	184	11	34.5
8	13.2	359	108	11.5	31.9
8	17.1	344	190	22	43.6
8	14.8	361	206	18.5	37.6
8	13.8	356	175	18.5	35.1
8	20.6	361	193	27.6	52.6
8	11.6	358	112	27.4	29
8	12.2	358	97	28.3	29.6
8	15.3	326	79	35.6	38.6
8	13	360	67	34.2	26.2
8	10.9	354	64	28.6	23.1
8	11.7	365	54	27.1	22.3
8	13.5	358	57	22.2	28.3
8	10.7	344	57	25	23.5
8	10.9	357	44	34.6	18.4
8	12.4	358	42	34.3	20.9
8	12.5	355	46	34.7	21.9
8	15.7	366	40	32.8	25.2
8	15.6	357	42	30.6	27.9
8	13	361	32	39	17.6
8	12.4	358	23	43.8	14
8	13.5	349	24	52.7	11.9
8	12.7	358	14	52.9	8.5
8	10.3	360	8	40.7	11.8
8	10.9	357	9	30.1	16.9
8	13.8	356	147	21.6	35.2
9	13.5	356	6	18.9	25.9

Table 15 (continued)

Flow Path	Length	Bearing	Aspect	Slope	Height
9	10	348	9	18.8	19.5
9	10.9	357	10	25.8	18.5
9	10.9	359	11	20.6	20.3
9	12.5	355	15	17.3	24.7
9	11.1	356	19	21.7	20.8
9	11.7	356	24	22.7	21.8
9	19.1	3	33	29.8	31.7
9	25.4	359	37	36.1	39.3
9	12.7	4	37	34.1	19.8
9	14.7	9	38	39.4	19.6
9	13.5	359	39	34.8	21.7
9	10.1	6	41	28	17.8
9	10.6	1	43	21.8	20.9
9	10.1	7	54	13.2	22
9	10.7	353	58	14.4	23.8
9	15.4	356	52	24.5	31.3
9	14.8	359	55	28.5	29.2
9	13.8	358	58	23	28.8
9	12.8	352	60	28.6	27.1
9	13.5	1	61	34	25.8
9	13.8	0	62	29.6	27.7
9	11.5	352	66	24	25.5
9	10.6	354	75	40.6	23.4
9	10.8	0	78	48.3	22.5
9	14.3	356	119	19.9	35.9
9	12.2	354	136	13	30.6
9	11.7	355	148	17.8	29.7
9	11.1	359	152	21.3	28.4
9	13.8	358	155	24.2	35.2
9	12.8	7	110	19.4	31.1
9	10.9	3	87	17.7	25.3
9	11.1	0	100	11	26.5
9	13.3	3	219	13.2	33.2
9	10.6	343	240	16	25.7
9	14.6	354	257	14.7	35
9	15.6	349	251	17.3	37.5
9	11.6	359	257	11.6	27.9
9	10.9	346	258	14.1	25.6

Table 15 (continued)

Flow Path	Length	Bearing	Aspect	Slope	Height
9	12.6	342	256	29.7	29
9	11.6	343	260	35.6	26.2
9	14.1	344	264	35.3	31.2
9	15.9	357	262	30.6	38.1
9	10.5	344	265	20.9	23.8
9	11.3	351	272	19.8	25.7
9	15.6	343	274	21.5	34.1
9	11.6	348	270	13.3	26.8
9	15.3	350	268	15.8	35.4
9	13	1	271	16.8	30.6
9	12.5	355	275	21.7	28.5
9	11.2	352	276	25.6	25
9	14.3	356	283	30.2	30.8
9	11.6	336	285	31.1	21.3
9	12.8	349	283	27	26.9
9	11.1	349	291	32.6	21.1
9	16.6	347	296	33.2	29.9
9	17.5	359	294	26.8	36.6
9	11.4	338	295	35.1	18.7
9	18	358	305	41	29.5
9	10.1	358	302	41.5	16.8
9	14.2	342	318	36.2	19.9
9	10.4	354	321	35	15.8
9	15.8	350	337	29.7	24.9
9	14	357	340	28.5	22.9
9	13	4	342	26.5	22.3
9	11.9	359	343	23.7	21.2
9	15.1	4	348	24.1	26.8
9	10.4	354	351	28.1	16.7
9	11.1	357	320	32.1	18.5

Table 16. Each row represents a standing tree in a cluster. Length and bearing describe the tree shadow. Aspect and slope describe the ground where the shadow is situated. Height is the height of the tree based on length, bearing, aspect, and slope.

Cluster #	Length	Bearing	Aspect	Slope	Height
3	16.1	351	89	18	37
3	13.4	351	66	26	29
3	12.8	348	9	34	18
3	14.6	355	15	32	22
3	11.9	0	51	25	24
3	18.6	354	333	15	38
3	13.2	0	111	33	27
3	14.6	357	72	20	33
3	8.6	356	60	33	17
3	15.9	0	81	30	36
3	10.6	0	69	30	22
3	9.9	0	69	25	21
3	10.5	342	60	27	23
3	9.5	348	45	19	20
3	5.4	324	9	35	7
22	16.1	327	333	51	8
22	17.3	328	336	49	11
22	20.4	331	330	44	17
22	16.2	324	339	45	12
22	22.5	324	326	39	21
22	21.8	322	327	37	21
22	24.7	323	329	38	24
22	13.8	309	305	39	9
22	13.8	327	315	36	15
22	12	326	315	29	16
22	19.1	317	237	32	34
22	13.6	322	3	33	18
22	25.9	324	333	49	15
22	21.8	322	330	49	12
22	14.6	331	327	29	20
28	11	8	33	36	15
28	15.2	353	3	36	20
28	13	355	15	36	18
28	6.1	0	6	42	7

Table 16 (continued)

Cluster #	Length	Bearing	Aspect	Slope	Height
28	5.3	342	21	32	8
28	8.3	338	15	34	12
28	13.2	358	6	38	17
28	16.4	356	9	35	23
28	4.6	347	15	38	6
28	14	357	21	35	20
28	8.2	356	15	35	12
28	12.2	354	12	41	14
28	12.3	353	9	38	16
28	10.1	358	12	37	13
28	12	355	9	37	16
28	7.4	356	9	40	9
28	11.9	357	24	41	15
28	10.4	353	18	51	9
28	11.9	347	9	41	14
28	5.7	349	3	37	7
28	9.1	350	9	35	13
28	5	0	21	33	8
28	7.7	0	27	26	13
28	8.7	358	24	25	15
28	8.2	356	21	30	13
28	9.8	355	15	31	15
28	7.5	17	15	33	10
28	6.1	355	15	38	8
28	4.5	353	3	42	5
28	7.3	350	180	41	8
28	6.9	353	3	37	9
28	6.7	353	21	31	11
28	4.6	350	27	32	7
28	8.6	351	15	32	13
28	9.5	358	9	38	12
28	7.9	358	6	43	8
29	11.4	331	275	36	18
29	9	341	177	24	15
29	7.1	345	9	23	13
29	7.7	344	183	24	13
29	14.8	338	339	36	18
29	16.6	335	342	39	18

Table 16 (continued)

Cluster #	Length	Bearing	Aspect	Slope	Height
29	13.9	336	342	36	17
29	9.4	328	348	34	11
29	7.9	340	321	26	13
29	12.2	356	336	25	21
29	6.2	340	345	36	8
29	6.9	353	315	36	11
29	11	333	318	38	12
29	6.4	5	27	45	7
29	15.9	356	351	44	16
29	16.1	351	345	43	17
29	6	315	327	37	5
29	9.1	327	327	41	8
29	13	333	342	40	13
29	7.3	309	324	40	5
29	10.6	346	330	27	17
29	12.1	347	33	42	17
32	14.1	338	300	5	30
32	14.2	330	339	21	24
32	14.8	324	345	24	22
32	10.3	332	252	2	22
32	23.5	323	318	12	41
32	10.1	315	249	2	18
32	14.5	325	219	3	29
32	14.4	323	228	2	29
32	18.8	318	225	3	36
32	14.1	328	321	1	29
32	10.3	332	183	4	21
32	12.1	319	192	4	23
32	10.8	324	171	4	21
32	14.3	326	249	3	29
32	18.2	328	335	20	29
35	4.2	335	273	24	8
35	7.5	328	282	23	13
35	3.8	358	279	27	9
35	5.2	315	285	23	7
35	6.6	328	273	26	11
35	6.6	320	267	21	11
35	4.5	321	279	26	7

Table 16 (continued)

Cluster #	Length	Bearing	Aspect	Slope	Height
35	4.5	357	267	32	10
35	6.3	346	273	24	14
35	5.9	334	255	27	12
35	4.9	329	255	28	9
35	5.3	323	261	32	9
35	2.3	326	255	33	4
35	4.7	321	264	33	7
35	2.3	338	261	27	5
35	4.6	344	261	24	10
36	5.2	339	273	26	10
36	5.4	329	255	25	10
36	6.1	335	261	22	13
36	4	328	231	19	8
36	5.6	347	282	31	11
36	3.5	303	279	31	3
36	4.2	336	231	27	9
36	5	340	249	31	11
36	3.3	345	285	29	6
36	3.4	0	213	23	6
37	3.3	337	123	15	6
37	5.8	331	51	3	12
37	4.6	346	102	11	10
37	6.6	325	78	16	12
37	5.8	332	75	17	12
37	3.5	357	102	16	8
37	4	0	57	13	9
37	2.8	322	27	19	5
37	4.6	0	39	16	10
37	3	344	21	17	6
37	5.4	341	15	17	10
37	4.7	10	15	20	9
37	4.9	354	45	17	10
41	6.8	346	333	20	12
41	7.4	339	333	19	13
41	6.5	336	327	17	12
41	6.2	324	327	17	10
41	4.7	315	321	19	6
41	7.9	338	327	21	14

Table 16 (continued)

Cluster #	Length	Bearing	Aspect	Slope	Height
41	7.1	349	327	28	12
41	4.6	339	333	26	7
41	5.6	332	333	27	8
41	7.5	322	327	25	10
41	5.4	322	324	20	9
41	11.5	333	333	18	20
41	8.7	313	336	19	12
41	6.6	311	327	22	8
41	7.3	5	333	25	13
41	7.5	347	339	20	14
43	5.2	325	111	14	9
43	5.4	318	252	9	10
43	3.8	341	261	17	8
43	4.9	326	249	15	10
43	7.2	310	264	14	11
43	8.4	317	261	12	15
43	6.3	310	273	19	8
43	6.5	319	303	16	10
43	8.6	329	279	12	17
43	5	327	291	14	9
43	4.2	319	291	18	7
43	8.2	342	279	17	17
43	6.8	321	291	16	11
43	6.5	331	291	16	12
43	6.9	333	279	21	13
43	5.7	321	291	26	8
43	8.7	326	294	23	14
43	5.1	336	291	23	9
43	4.6	338	291	21	9
43	5.2	325	297	21	8
43	5.3	323	297	23	8
43	6.6	343	291	24	13
43	6.6	338	306	25	11
43	5.1	322	303	22	8
43	5.1	318	309	26	6
43	7.6	349	303	20	15
43	6.4	326	291	25	10
43	4.2	336	303	26	7

Table 16 (continued)

Cluster #	Length	Bearing	Aspect	Slope	Height
43	7.4	347	189	11	16
43	6.5	331	189	12	13
43	6.4	326	291	24	10
43	7.6	330	303	21	13
43	6.9	322	312	22	10
43	4.6	317	315	19	7
43	7.5	317	177	3	14
43	6.1	324	279	24	10
43	5.7	329	273	15	11
43	12.5	332	183	10	25
43	5.6	331	279	10	11
43	6.4	323	279	22	10
43	8.7	326	273	9	17
43	5	327	285	12	9
43	5.3	337	291	20	10
43	6.7	332	279	16	13
43	5	327	279	22	9
43	6.3	340	285	16	13
46	4.4	327	303	33	6
46	5.8	321	297	31	7
46	6.4	300	300	24	6
46	4.7	322	273	22	8
46	7	335	318	34	9
46	6.2	340	321	36	8
46	6.6	331	213	15	13
46	5.2	315	291	30	6
46	5.6	319	186	18	9
46	3.2	0	315	40	5
46	3.5	333	315	35	4
46	4.5	310	309	35	4
50	7.7	333	231	33	15
50	8.5	2	237	34	16
50	6.9	0	237	36	13
50	5.9	350	234	34	12
50	6.7	326	225	27	13
50	2.9	0	237	28	6
50	6.1	5	237	25	12
50	4.4	335	249	26	9

Table 16 (continued)

Cluster #	Length	Bearing	Aspect	Slope	Height
50	3.4	0	237	25	7
50	4	0	261	31	9
50	3.5	13	231	28	6
50	3.2	0	231	30	6
51	5.9	344	189	41	7
51	6.8	346	177	46	6
51	6.6	354	177	44	7
51	5.5	327	177	42	5
51	6.4	325	177	41	7
51	5.4	322	219	40	10
51	5.6	332	222	42	10
51	5	4	213	44	6
51	4.3	0	183	42	5
51	3.1	302	213	40	5
51	3.9	329	225	43	7
52	8.5	355	273	31	19
52	5	0	282	43	11
52	6.6	358	267	26	16
52	3.7	0	261	29	8
52	6.9	344	252	28	16
52	5.8	357	267	32	14
52	4.4	17	267	31	9
52	4.5	7	267	33	10
52	4.3	6	297	33	9
53	9.9	346	225	38	17
53	8.8	349	231	32	17
53	8.7	353	246	31	18
53	5.3	0	237	36	10
53	10.6	0	225	28	20
53	6.6	354	243	30	14
53	6.6	354	225	27	13
53	9.2	345	225	33	17
53	10.9	346	228	30	21
53	7.6	355	231	32	14
53	10.2	347	222	32	19
53	7.9	346	231	33	15
53	6.7	349	246	26	15
54	4.9	5	12	21	9

Table 16 (continued)

Cluster #	Length	Bearing	Aspect	Slope	Height
54	4.4	353	33	25	8
54	3	13	21	26	5
54	2.2	14	15	25	4
54	1.8	13	45	27	3
54	3.8	346	21	24	7
55	7	341	315	21	13
55	5.3	337	327	16	10
55	6.6	315	333	14	10
55	7.8	331	327	15	14
55	9.5	326	318	14	16
55	4.5	320	333	15	7
55	6.7	315	297	21	9
55	4.9	319	333	20	7
57	12.5	324	63	32	24
57	12.4	317	93	29	17
57	8.9	312	45	36	15
57	6.6	319	78	34	10
57	9.1	314	33	26	15
57	6.2	295	33	44	7
57	8.2	313	54	26	14
57	7.8	332	54	30	16
57	7	315	42	36	12
57	10.8	320	79	39	16
60	3.4	13	339	25	6
60	3.9	358	237	42	7
60	4	6	267	40	9
60	4.1	354	279	43	8
60	4.1	0	321	27	8
60	4.1	357	267	39	10
60	4.1	357	237	42	7
60	4.1	343	243	40	9
60	4.3	306	333	46	2
60	4.4	356	261	39	10
60	4.8	351	297	31	9
60	5.3	13	255	38	10
60	5.3	353	315	26	10
60	5.8	343	309	26	10
60	5.8	340	327	44	5

Table 16 (continued)

Cluster #	Length	Bearing	Aspect	Slope	Height
60	5.9	345	315	23	11
60	5.9	320	321	42	5
60	6	355	273	40	13
60	6.4	344	315	35	9
60	6.5	327	327	48	4
60	6.6	340	321	40	8
60	6.8	353	321	25	12
60	7	353	297	39	12
60	7.4	3	258	39	16
60	7.7	344	297	34	13
60	8.2	339	294	39	12
60	8.8	352	321	37	12
60	8.8	352	306	41	13
60	9.4	355	294	40	17
60	9.5	352	309	30	17
60	9.7	336	297	39	13
60	11.9	354	318	40	16
60	12.1	359	297	40	22
61	14.7	355	108	13	31
61	12.5	349	75	15	29
61	13.5	0	102	26	30
61	11.9	0	105	5	28
61	10.3	356	87	12	23
61	7.2	354	93	10	17
61	10.8	352	114	18	23
61	10	351	123	25	19
61	12.3	331	93	11	25
64	5.5	4	135	5	13
64	5.9	347	135	8	13
64	4.7	36	147	9	9
64	5.1	24	9	12	10
64	5.3	23	243	6	11
64	4.1	39	321	15	8
64	6.4	8	339	17	13
64	5.5	358	357	16	11
64	5.9	358	81	5	14
64	5	12	27	12	10
64	4.5	28	27	24	7

Table 16 (continued)

Cluster #	Length	Bearing	Aspect	Slope	Height
64	4.7	5	63	3	11
64	3	356	153	19	6
64	4.3	9	33	13	9
64	4.3	6	165	7	9
65	14.6	342	333	35	19
65	14.2	348	351	30	21
65	6	357	351	32	9
65	6.6	0	351	31	10
65	13.3	356	342	31	20
65	11.9	3	357	37	15
65	14.7	352	351	31	22
65	17.8	349	351	29	28
65	11.1	343	351	29	17
65	9	354	357	35	12
65	8.8	349	3	33	12
65	6	351	357	41	7
65	15.9	358	357	37	20
65	9	352	342	32	13
65	8.3	337	351	27	13
65	6.7	333	351	29	9
65	9	352	333	34	13
66	5.4	349	309	42	7
66	8.2	347	327	54	5
66	5.8	344	309	32	9
66	4	356	315	36	6
66	4.5	353	297	32	9
66	6	347	303	45	8
66	4	355	294	31	8
66	4.9	0	291	33	10
66	3.7	0	297	31	7
66	4	351	303	32	7
66	5	351	291	33	10
66	3.4	347	303	31	6
66	4.3	345	306	32	7
66	4.3	356	303	30	8
66	4.3	358	297	34	8
66	4.6	358	309	29	9
66	5.2	349	327	33	8

Table 16 (continued)

Cluster #	Length	Bearing	Aspect	Slope	Height
66	4.7	346	327	29	8
66	4	349	321	30	7
66	2.4	307	297	18	3
66	3.7	317	309	20	5
66	3.6	331	303	17	6
66	2.6	335	339	29	4
66	3.5	350	321	28	6
66	2.4	337	315	26	4
66	3.2	341	315	31	5
66	4.4	339	315	36	6
66	4.7	344	303	37	7
66	2.1	342	321	34	3
66	4.4	341	327	45	4
67	3.7	356	45	30	7
67	4.3	353	33	31	7
67	3.2	351	63	29	7
67	3.7	339	57	21	8
67	3.8	326	45	32	7
67	3.4	328	21	33	5
67	3.2	336	33	34	6
67	3.1	329	21	33	5
67	3.7	339	15	27	6
67	3.2	355	15	24	6
67	3.5	333	21	31	6
67	4.4	346	21	33	7
67	3.4	338	357	29	5
67	3.7	336	357	40	4
67	3.1	332	345	32	4
67	3.6	332	339	45	3
67	3.8	344	345	34	5
67	3.2	337	333	48	2
67	5.4	347	333	41	6
67	3.3	345	327	33	5
67	2.8	318	327	35	3
67	3.9	347	327	31	6
67	2.8	318	333	32	3
67	4	317	321	52	1
67	2.9	339	315	41	3

Table 16 (continued)

Cluster #	Length	Bearing	Aspect	Slope	Height
67	2.9	324	324	42	2
67	4	337	327	32	6
67	3.6	312	309	31	4
67	3.6	306	303	34	3
67	3.6	312	309	36	3
67	6	337	297	36	9
67	3.5	297	303	33	2
67	3.3	331	297	26	5
67	5.1	317	303	37	5
67	3.8	321	303	32	4
67	5.2	336	339	40	6
67	4.8	351	345	47	4
67	3.1	301	339	23	3
68	3.2	342	243	22	7
68	3.2	349	231	24	7
68	3	354	324	33	5
68	3.2	0	321	39	5
68	3.5	342	333	28	5
68	3.5	350	333	34	5
68	3.9	348	327	33	6
68	2.2	339	327	35	3
68	3.5	350	333	25	6
68	4.1	358	327	31	7
68	2.7	350	321	27	5
68	4.9	347	303	21	10
68	4.7	350	315	26	8
68	3.2	351	333	26	5
68	3.7	342	291	20	7
68	4.4	341	279	17	9
68	3.4	349	273	21	8
68	4.9	2	285	7	11
68	2.9	351	219	1	7
68	4.8	4	285	3	11
68	4	4	177	0	9
68	4	351	315	21	8
68	5	353	300	13	11
69	4.5	355	285	15	10
69	3.3	345	303	23	6

Table 16 (continued)

Cluster #	Length	Bearing	Aspect	Slope	Height
69	3.8	344	306	15	8
69	4.8	345	303	18	10
69	4	354	315	19	8
69	4.3	349	324	18	8
69	3.4	353	309	15	7
69	3.4	353	309	15	7
69	3.1	336	321	9	6
69	3	357	183	37	4
69	3.2	349	243	12	7
69	2.4	354	177	17	5
69	2.9	357	183	27	5
69	3	356	267	17	7
69	3.6	0	249	26	8
69	3.2	352	267	22	7
69	2.8	0	249	18	6
69	3	352	267	25	7
70	3.4	18	297	42	7
70	3.3	13	297	43	7
70	3.6	345	303	43	5
70	4.5	352	303	40	7
70	4.1	0	303	42	7
70	3.2	356	291	36	6
70	6.4	343	258	29	14
71	4.6	358	219	0	11
71	3.2	353	105	0	7
71	4.1	356	351	0	10
71	5.4	359	315	12	12
71	4.8	357	183	7	11
71	7.7	357	213	1	18
71	3.8	356	282	2	9
71	5.4	356	333	19	11
71	4.8	355	333	16	10
71	3.2	358	318	25	6
71	3.6	358	309	21	7
71	4.4	0	327	22	8
71	4.8	355	327	26	8
71	6.5	355	327	22	12
71	4.3	355	225	11	9

Table 16 (continued)

Cluster #	Length	Bearing	Aspect	Slope	Height
71	5.5	350	288	11	12
71	4	0	270	9	9
71	4.1	354	315	21	8
71	5.4	344	186	12	11
71	5	0	207	10	11
71	4.3	0	297	24	9
71	4.9	356	249	14	11
71	4.4	347	213	10	9
71	4.3	358	267	37	10
71	4.6	354	189	20	9
71	3.7	353	225	14	8
71	4.2	351	213	16	9
71	3.8	348	189	6	8
71	5.5	353	312	11	12
71	4.4	353	303	20	9
74	6.2	65	87	29	5
74	6.8	47	87	35	7
74	4.6	30	81	34	7
74	7.7	40	69	37	9
74	7.1	53	81	29	7
74	4.3	43	93	34	6
74	6	52	75	37	5
74	4.1	27	63	34	6
75	27.5	344	29	39	41
75	19.5	354	78	38	44
75	8.4	355	93	40	19
75	12.4	353	354	49	10
75	11.1	2	117	48	19
75	11.6	352	96	33	25
75	22.4	347	105	51	34
75	10.3	344	78	7	22
75	12.6	336	57	7	28
75	12	352	63	46	23
75	10.8	349	75	31	25
75	15.2	348	33	54	14
75	13	348	60	12	29
75	12.3	353	21	25	22
75	16.9	0	331	35	25

Table 16 (continued)

Cluster #	Length	Bearing	Aspect	Slope	Height
75	11	343	102	3	25
75	12.3	353	81	6	29
75	9.2	347	81	3	21
75	14.1	347	198	2	32
75	9.2	347	42	29	18
75	8.1	349	78	22	19
75	18.1	345	93	15	40
76	4	344	63	38	8
76	4.3	325	54	45	8
76	2.9	330	51	44	6
76	5	321	57	42	9
76	3.2	319	69	43	5
76	2.9	309	63	44	3
76	3.5	322	45	43	6
76	2.5	317	45	43	5
76	3.6	330	63	38	8
77	8.6	337	261	20	18
77	8.2	339	261	20	18
77	6	13	273	19	13
77	7.4	356	279	19	16
77	7.2	332	279	20	14
77	5.8	317	279	19	9
77	6.7	315	273	20	10
77	5.8	313	273	19	8
77	4.7	313	273	20	7
77	5.6	329	267	19	10
77	7.6	346	267	19	17
77	8.4	332	267	18	17
77	4.4	343	261	20	10
78	17.3	328	127	14	31
78	5.3	318	345	18	8
78	11	319	306	18	17
78	8.8	278	342	6	7
78	10.8	324	345	28	14
78	6.9	336	342	10	14
78	15	328	289	21	25
78	15.3	316	275	29	20
78	14	331	276	36	22

Table 16 (continued)

Cluster #	Length	Bearing	Aspect	Slope	Height
78	17.3	329	267	35	29
78	26.5	323	281	45	27
78	17.9	321	275	41	21
78	14.9	328	279	46	17
78	15.7	332	261	41	28
79	12.2	319	354	39	13
79	9.9	323	351	40	10
79	9.8	327	351	39	10
79	12.6	325	351	43	11
79	13	324	342	49	8
79	13.6	334	351	40	15
79	17.5	327	351	43	16
79	14	329	357	37	16
79	14.7	314	357	38	15
80	4.3	0	261	21	10
80	4.6	347	273	27	10
80	4.8	308	267	23	6
80	5.2	325	267	24	9
80	5.9	322	267	23	10
80	4.6	313	267	25	6
80	3	321	267	26	5
80	6.5	322	291	24	10
80	3.5	335	285	23	6
80	3.3	333	243	10	7
80	4.6	304	243	10	7
80	4.5	323	237	11	9
80	4.9	270	255	12	2
80	4.1	351	309	9	9
80	3	348	279	10	7
80	3.1	304	339	9	4
80	4.1	309	351	8	6
80	4.3	303	357	8	6
80	4.1	348	285	12	9
80	5.8	294	285	31	4
80	4.2	323	273	16	7
80	3.2	349	267	15	7
80	4.4	337	273	26	9
81	6.5	330	39	7	13

Table 16 (continued)

Cluster #	Length	Bearing	Aspect	Slope	Height
81	5.2	325	33	16	10
81	6.5	15	51	18	13
81	2.6	0	9	21	5
81	6.6	3	39	15	14
81	4	9	33	20	8
81	3.3	66	321	12	4
81	4.6	356	57	14	10
82	4.5	353	357	26	8
82	6.4	351	357	22	11
82	5.9	324	357	38	7
82	7.9	334	357	39	9
82	4.9	331	357	29	7
82	7.2	324	357	35	9
82	6.3	327	357	25	10
82	3.4	337	357	31	5
82	3.8	348	357	25	6
82	5.7	349	351	17	11
83	6.5	346	315	26	11
83	5	348	327	23	9
83	5.7	356	324	13	12
83	6.2	344	342	13	12
83	5.7	338	345	29	8
83	5.5	353	315	2	13
83	5.5	358	333	32	9
83	5.3	344	330	28	8
83	7.6	355	336	21	14
83	5.1	343	213	11	11
83	5.6	351	231	5	13
83	5.2	346	240	3	12
83	5.4	351	336	31	8
83	5.3	358	147	11	11
83	5.4	334	147	6	11
83	4	317	171	13	7
83	3.4	317	177	5	6
83	4.7	0	255	9	11
83	7	358	315	1	16
83	4.2	357	333	9	9
84	4.4	347	183	2	10

Table 16 (continued)

Cluster #	Length	Bearing	Aspect	Slope	Height
84	6.5	345	45	11	14
84	3.7	355	51	15	8
84	3.9	340	51	15	8
84	4.5	349	3	12	9
84	5.3	358	27	10	11
84	2.5	0	39	8	6
84	2.3	0	357	11	5
84	5.3	355	27	15	11
85	4.8	339	327	15	9
85	3.9	341	327	14	8
85	4.3	333	327	13	8
85	4.8	326	333	15	8
85	6.6	345	333	17	13
85	4.9	331	333	17	8
85	4.6	347	27	14	10
85	7.4	336	33	14	15
85	5.3	333	33	13	11
85	8.9	348	333	17	17
85	5.6	335	333	16	10
85	6.7	326	333	15	11
85	6	337	336	19	11
85	5.7	326	333	16	9
85	4.7	317	336	17	7
85	6.2	317	327	17	9
85	4.7	322	327	18	7
85	6.8	324	330	16	11
85	5.3	323	333	16	9
85	5	328	333	17	8
85	5.2	345	339	16	10
85	8.8	321	341	19	14
85	4.6	324	339	22	7
85	5	328	345	15	9
85	4.3	349	333	16	9
85	5.9	333	339	18	10
85	5.8	336	321	19	10
86	5.6	350	252	32	12
86	5.3	340	264	33	11
86	5.3	356	255	34	12

Table 16 (continued)

Cluster #	Length	Bearing	Aspect	Slope	Height
86	2.8	349	261	30	7
86	3.9	6	279	29	9
86	4	348	273	25	9
86	4.4	348	279	26	9
86	4.6	345	285	22	9
86	4.6	338	315	18	8
86	3.5	351	303	17	7
86	4	348	3	10	8
86	5.4	0	21	25	9
86	5.4	355	15	27	9
86	7	357	27	39	9
86	8	352	27	39	11
86	6.2	354	27	37	9
86	6.7	355	15	31	10
86	5	353	348	27	8
86	4.9	0	357	36	7
86	5.6	0	3	42	6
86	7.1	359	15	44	7
86	5.9	354	15	43	7
86	7.2	357	327	37	10
86	7	352	333	34	10
86	5.3	353	327	31	8
86	5.6	358	309	25	11
86	5.3	351	279	24	12
86	6.7	351	357	43	7
86	3.6	345	261	29	8
86	4	354	255	24	9
86	3.5	351	249	20	8
86	5.9	352	303	34	10
86	4.5	348	321	37	6
86	4.4	350	321	23	8
87	29.5	334	351	32	39
87	28.8	337	349	36	35
87	22	326	287	9	42
87	20.9	333	345	45	17
87	17	323	348	33	21
87	21	338	357	14	41
87	21.1	334	180	14	40

Table 16 (continued)

Cluster #	Length	Bearing	Aspect	Slope	Height
87	28.6	335	243	23	62
87	18.1	327	63	45	35
87	22	337	39	18	45
87	17.6	342	285	13	37
87	19	331	12	40	24
87	23.4	344	345	47	20
87	20.3	336	339	13	39
89	7.2	341	285	21	14
89	7.7	356	291	22	17
89	3.3	342	297	22	6
89	4.5	332	285	23	8
89	3.7	315	279	17	6
89	4.4	346	228	16	9
89	5.9	328	234	21	12
89	6.5	346	264	12	15
89	6.2	329	237	16	13
89	6.1	342	249	16	14
89	8.2	347	285	16	18
89	5.6	357	273	14	13
89	4.8	354	297	20	10
89	5.3	342	285	23	10
89	5.3	333	276	18	10
89	4.8	341	291	19	9
89	4.8	354	300	22	10
89	6.5	348	306	20	13
89	4.7	344	309	20	9
89	4.6	350	303	22	9
91	3.2	42	219	12	5
91	4.9	41	219	12	8
91	6	337	243	12	13
91	4.8	0	219	11	10
91	6.1	358	201	19	12
91	3.7	339	237	20	8
91	5.6	0	213	15	12
92	6.7	42	225	15	11
92	4.2	0	231	15	9
92	4.6	336	213	15	9
92	6.8	39	213	20	10

Table 16 (continued)

Cluster #	Length	Bearing	Aspect	Slope	Height
92	5.6	357	219	18	11
92	3.9	344	219	17	8
92	3.4	4	219	14	7
92	2.7	354	207	13	6
92	5.7	349	201	15	12
94	9.5	327	13	15	17
94	6.5	313	18	13	11
94	7.7	339	291	24	14
94	7.8	330	324	22	12
94	6.7	332	27	15	13
94	7	313	33	14	12
94	8.8	324	27	17	16
94	6.6	327	291	21	11
94	8.2	346	276	16	18
94	5.6	332	279	14	11
94	7.5	331	273	16	15
94	6.8	337	315	15	13
94	9.3	333	312	12	18
94	7.9	327	315	13	14
94	7.1	347	339	11	15
94	8.6	332	330	11	16
94	6.3	342	333	12	13
94	4.6	330	285	16	9
94	7.4	333	273	16	15
94	6.3	342	303	16	12
94	6.7	340	309	14	13
94	5.1	345	303	9	11
94	7	355	291	15	16
94	7.3	342	321	16	14
94	7.3	342	243	16	16
94	8.9	333	294	20	16
94	6.1	342	21	13	13
94	7.5	343	27	17	15
95	5.2	341	315	9	11
95	7.5	315	315	9	12
95	5.2	328	309	9	10
95	5.2	328	312	9	10
95	6.1	346	312	10	13

Table 16 (continued)

Cluster #	Length	Bearing	Aspect	Slope	Height
95	4.4	325	294	11	8
95	3.7	329	291	10	7
95	4.4	337	303	10	9
95	6.6	315	303	9	11
95	3	335	297	8	6
95	3.6	320	309	9	6
96	5	348	339	19	9
96	5.4	349	345	19	10
96	8.4	321	354	18	14
96	7.2	328	12	28	11
96	7.2	320	15	15	13
96	4.8	315	21	23	8
96	4.8	331	15	25	8
96	6.3	327	15	15	11
96	5.9	319	3	14	10
96	3.4	313	3	16	5
96	5.2	328	357	16	9
96	5.3	326	351	10	10
96	3.2	337	30	9	7
96	6	337	33	10	13
96	5.2	341	6	14	10
96	6.8	340	9	16	13
96	8.5	346	3	15	17
96	5.7	345	3	14	11
96	3.6	332	327	12	7
96	6.3	334	354	11	12
96	5.4	334	351	11	10
96	5.2	341	345	16	10
96	7.2	332	345	13	13
96	5	340	345	14	10
96	4.2	330	333	17	7
96	5.7	329	333	15	10
96	5.1	330	339	18	9
96	3.7	336	339	19	6
96	4.1	321	345	19	6
97	7.5	354	213	43	10
97	11.5	328	147	32	14
97	7.6	324	189	35	10

Table 16 (continued)

Cluster #	Length	Bearing	Aspect	Slope	Height
97	10.3	320	201	36	16
97	10.3	328	183	34	14
97	8.4	328	163	25	12
97	11.5	323	137	37	12
97	12	327	180	34	16
97	12.2	326	222	41	22
97	9.4	317	225	43	17
97	10.1	315	225	37	18
97	6.6	313	225	35	11
97	6.7	312	210	38	10
97	9.2	311	213	33	15
97	9.1	322	225	36	17
98	7.4	0	306	21	15
98	5.9	13	303	19	13
98	5.4	351	315	27	10
98	5.5	337	309	26	9
98	3.6	0	315	29	7
98	4.6	336	297	10	10
98	6.9	337	303	24	12
98	4.7	342	309	34	7
98	5.9	352	162	20	11
98	6.5	349	303	23	13
98	4.9	2	303	31	10
98	6.4	356	297	29	13
98	7.7	354	285	13	17
98	3.8	341	291	16	8
98	4.9	353	285	16	11
98	8.4	350	291	21	17
98	4.2	357	291	20	9
98	4.9	353	291	30	10
98	5.4	349	291	33	10
98	6	337	291	32	10
99	7.9	327	321	25	11
99	6.8	331	315	30	9
99	8.3	323	315	29	10
99	8.2	320	327	21	12
99	4	336	321	33	5
99	8.7	323	321	29	11

Table 16 (continued)

Cluster #	Length	Bearing	Aspect	Slope	Height
99	8.1	333	315	30	11
99	6.4	325	303	20	10
99	9.7	322	309	22	14
99	6.8	317	315	16	10
99	5.9	322	315	25	8
99	5.9	322	315	25	8
99	2.5	337	285	28	5
99	5.9	333	321	28	9
101	8.6	0	52	27	7
101	11.9	335	65	25	7
101	11.9	347	58	27	8
101	9.5	346	86	36	7
101	14.6	335	78	34	1
101	16.8	350	57	32	13
101	13.3	354	60	27	7
101	10.8	349	38	30	16
101	9.4	352	68	13	0
101	7	355	57	5	3
101	12.7	353	60	10	5
101	15.2	347	61	26	8
101	13	341	57	22	9
101	12.5	348	63	30	6
101	6.8	346	85	15	5
102	9.5	345	62	29	6
102	15.1	1	76	21	5
102	5.3	342	65	27	2
102	6.6	335	79	24	2
102	6.6	357	80	32	3
102	6.6	357	80	32	3
102	4.9	335	85	12	4
102	2.8	335	36	30	5
102	2.8	335	36	30	5
102	10.3	1	85	12	8
102	5.7	342	48	25	6
102	6.7	343	39	26	10
102	5.7	1	47	25	5
102	6.7	1	63	29	2
102	5.6	348	88	33	5

Table 16 (continued)

Cluster #	Length	Bearing	Aspect	Slope	Height
102	3.8	344	53	14	3
104	30.5	336	327	41	73
104	29.6	333	328	43	68
104	20.4	331	316	43	47
104	8	312	315	41	14
104	18.9	335	297	47	45
104	18.9	335	297	47	45
104	28.1	333	284	35	53
104	7.2	326	274	19	9
104	19.5	332	304	30	45
104	21.9	331	310	17	50
104	6.6	323	345	36	14
104	24.1	328	325	51	51
104	17.5	331	308	45	41
104	14.9	328	282	32	26
104	13.1	315	276	49	27
104	15.2	326	306	44	34
106	8.9	348	341	19	22
106	8	342	7	19	17
106	4.3	340	345	16	10
106	7.4	329	344	17	16
106	6.2	333	341	14	14
106	5.6	347	322	15	14
106	7.4	355	323	23	18
106	6.2	352	357	22	15
106	2.4	345	185	18	5
106	5	343	313	16	12
107	5	338	16	18	10
107	5	332	44	22	7
107	6.5	324	33	14	9
107	6.1	326	348	23	13
107	5.4	318	10	13	10
107	5	306	327	10	9
107	4.2	319	1	19	8
107	6.8	328	340	17	15
107	5.1	318	338	16	11
107	4.7	321	335	14	10
107	4.9	317	337	16	12

Table 16 (continued)

Cluster #	Length	Bearing	Aspect	Slope	Height
107	7.5	313	322	15	15
107	4.2	315	319	17	9
107	5.9	322	318	22	14
108	7	327	197	9	12
108	8.3	330	196	8	15
108	5.4	321	197	8	9
108	7	327	200	3	12
108	5	327	196	9	9
108	5.4	321	199	14	9
108	3.2	328	192	16	6
108	5.7	321	198	4	10
108	5.9	319	197	4	10
109	2.8	328	358	35	6
109	5	332	2	40	11
109	4.2	315	2	40	8
109	2.7	321	6	34	5
109	2.6	325	355	41	5
109	3.9	331	13	32	8
109	6.6	345	353	32	16
109	5.8	354	21	34	11
109	3	321	3	19	6
109	3.6	310	345	32	6
110	6.1	5	324	31	15
110	5.4	351	304	25	12
110	4	352	305	27	9
110	5.6	335	312	30	13
110	5.3	354	329	28	14
110	6.4	355	326	28	15
110	6.9	353	332	26	18
110	4.8	0	303	22	10
110	4.2	0	305	26	10
110	4.3	11	317	30	10
110	3.1	340	298	24	7
110	3.4	337	322	24	8
111	3.5	9	322	25	9
111	3.5	351	331	21	9
111	4.8	351	27	25	9
111	4.6	350	346	28	11

Table 16 (continued)

Cluster #	Length	Bearing	Aspect	Slope	Height
111	4	337	11	24	8
111	5.9	339	325	30	15
111	5	335	343	21	12
111	1.7	321	340	20	4
111	3	322	340	19	6
111	7.7	322	339	23	16
111	6.6	317	331	31	13
111	5.7	323	350	24	13
111	3.2	325	352	26	7
111	5.1	332	334	33	12
111	6.2	329	338	29	14
111	2.8	338	336	18	7
112	4.8	351	1	24	11
112	3.4	356	346	29	8
112	5.9	350	347	29	15
112	4.6	350	16	19	9
112	4.3	338	65	23	2
112	4.5	332	352	21	10
112	4.9	331	16	18	9
112	4.4	327	354	21	9
112	4.5	320	354	26	9
112	3.4	321	49	17	4
112	4.4	346	28	28	8
112	3.2	325	359	24	6
113	9.7	350	285	36	17
113	5.4	11	315	35	13
113	5.6	320	319	36	12
113	5.3	353	335	33	14
113	6.5	336	350	39	15
113	5.6	332	320	39	13
113	5.9	322	313	40	13
113	5.4	313	348	33	10
113	3.3	323	301	38	7
113	3.8	308	324	30	6
115	4.6	344	87	30	4
115	5.2	358	83	32	4
115	4.3	356	83	33	3
115	5.2	358	171	4	13

Table 16 (continued)

Cluster #	Length	Bearing	Aspect	Slope	Height
115	5	9	133	3	12
115	4.5	356	102	22	7
115	2.9	351	99	23	4
115	4.5	356	256	27	2
115	3.2	340	187	4	7
115	3.8	315	145	10	8
115	1.9	357	64	39	1
115	3.2	11	73	21	1
116	8.8	5	23	30	16
116	7.2	354	23	34	14
116	12.3	357	7	29	28
116	6	354	28	34	11
116	14.4	0	39	35	20
116	11	0	24	31	20
116	10.2	0	14	39	22
116	9.1	348	22	39	18
116	11.5	355	12	42	25
116	14.4	354	30	57	29
116	17.6	348	17	46	37
116	14.6	356	27	32	24
116	11.9	356	57	38	10
116	18.7	352	7	46	42
116	26.1	359	14	44	56
116	10.8	356	24	37	21
116	15.7	1	30	36	27
117	9.3	356	6	34	20
117	12.6	354	349	36	31
117	6.2	0	357	34	15
117	3.3	358	25	38	6
117	8.7	357	28	35	16
117	8.5	358	334	41	22
117	10.5	359	347	35	26
117	11	1	28	31	19
117	13.7	356	346	34	32
117	4.9	358	322	38	12
117	6.4	358	325	42	16
117	9.3	359	340	35	24
117	9.1	359	317	43	23

Table 16 (continued)

Cluster #	Length	Bearing	Aspect	Slope	Height
117	3.7	4	352	33	9
117	9.1	358	318	46	23
117	5.7	358	28	35	10
118	11	2	31	43	19
118	11.4	2	48	33	11
118	11.5	4	47	34	12
118	11.2	2	23	33	21
118	18.7	6	10	40	41
118	13.8	5	127	43	33
118	8.9	5	36	19	12
118	7.4	358	46	30	8
118	10.2	355	69	32	1
118	7.8	3	21	26	15
118	9.5	0	50	30	9
118	11.9	0	38	31	16
118	13.8	0	40	32	18
118	12.3	359	50	27	11
118	14.4	0	55	20	9
118	8.3	359	49	14	7
118	13.5	359	83	21	10
118	8.7	357	41	23	11
118	8.5	357	340	31	22
118	6.4	356	346	34	16
118	11.7	3	289	23	21
118	5.7	356	62	29	2
118	13.3	359	36	21	19
118	12.5	1	20	28	24
118	18.5	5	50	29	16
118	13.7	9	20	33	26
118	7.4	355	14	30	16
119	11.4	331	20	35	22
119	8.2	331	8	51	17
119	10.1	333	357	38	22
119	6.5	325	18	38	12
119	6.7	315	18	39	12
119	9.1	330	17	43	18
119	8.2	324	16	37	16
119	9	332	181	21	19

Table 16 (continued)

Cluster #	Length	Bearing	Aspect	Slope	Height
119	5.9	322	26	46	12
119	8.5	316	10	41	16
120	11.2	337	290	46	25
120	7.9	319	325	26	17
120	14.7	341	319	32	36
120	8.2	337	322	31	20
120	6.4	300	329	36	10
120	5.3	297	283	15	9
120	6.3	325	297	41	14
120	10	335	303	50	24
120	9.7	334	280	44	18
120	9.9	335	324	35	24
120	9	304	282	26	16
120	6.6	320	307	32	15
121	14.5	339	50	24	15
121	15.2	330	31	38	28
121	8.7	321	44	37	15
121	17.9	333	57	14	12
121	12.7	334	44	37	20
121	11.3	327	22	20	20
121	8.5	330	57	28	9
121	13.5	330	43	27	19
121	8.3	341	65	33	5
121	10.2	320	58	45	19
121	16.3	334	38	36	28
121	12.9	324	43	31	20
121	7.2	320	51	39	12
121	8.5	324	64	33	9
121	10.4	329	74	33	3
122	7.6	337	56	44	11
122	5.8	323	43	44	11
122	5.7	322	50	42	10
122	5.3	355	29	40	10
122	6.3	339	179	44	14
122	3.5	344	28	52	7
122	7.7	322	340	39	16
122	2.7	350	97	51	4
122	4.6	354	346	29	12

Table 16 (continued)

Cluster #	Length	Bearing	Aspect	Slope	Height
123	13.5	335	21	51	28
123	14.5	352	3	60	34
123	5.5	344	13	54	12
123	5.6	326	14	57	11
123	34	327	341	27	74
123	25.2	334	345	26	58
124	9.6	336	41	25	14
124	7	335	50	16	7
124	4.1	320	146	12	9
124	5.7	338	168	28	13
124	5.7	338	168	28	13
124	15.1	341	110	28	30
124	11.9	321	75	26	3
124	8.8	331	42	26	12
124	8	343	89	35	8
124	9.6	346	169	36	23
124	6.7	334	186	53	14
124	5.7	326	179	35	12
125	4.8	331	181	16	10
125	5.5	328	1	15	11
125	4.7	321	4	16	9
125	7.8	313	36	16	11
125	7.8	313	36	16	11
125	6.6	318	82	21	2
125	4	317	62	15	3
125	4.4	325	50	16	4
125	8.3	330	92	23	9
125	9.1	332	81	29	3
125	14.4	327	53	25	16
125	17.1	333	66	34	13
125	16.6	328	63	32	15
125	7.4	333	83	36	3
125	13.2	338	25	11	22
125	14.9	334	49	24	17
125	4.6	326	135	30	10
125	6.8	324	55	5	4
125	5.1	315	63	39	8
126	7.5	328	342	26	16

Table 16 (continued)

Cluster #	Length	Bearing	Aspect	Slope	Height
126	5.1	321	340	25	11
126	4.6	340	291	23	9
126	6.3	325	311	27	14
126	5	329	3	37	10
126	4	315	0	29	7
126	4.8	319	304	24	11
126	6.1	319	288	22	12
126	7.3	326	320	22	16
126	2.6	338	270	26	3
126	4.2	331	278	24	6
126	3.4	347	295	22	7
126	5	325	309	23	11
127	8	338	64	42	8
127	11.3	330	65	45	16
127	12.3	321	80	43	12
127	6.3	318	73	45	11
127	14.6	338	74	37	3
127	11.4	331	76	35	2
127	10.1	313	92	48	15
127	7.3	332	77	43	3
127	7.2	339	116	29	15
127	5.8	352	88	30	5
127	18	332	70	45	18
127	15.1	342	41	31	22
128	8.1	349	355	37	19
128	9.4	350	12	25	20
128	9.4	350	12	31	20
128	7.7	358	358	22	18
128	8.5	358	44	30	10
128	7.2	6	5	38	16
128	4.8	354	299	37	11
128	8.1	349	300	39	18
128	7	351	304	36	16
128	7.2	354	340	35	18
128	10.6	356	327	44	27
128	7.7	0	339	38	19
128	8.2	356	324	40	21
128	6.1	353	27	28	11

Table 16 (continued)

Cluster #	Length	Bearing	Aspect	Slope	Height
128	5	0	346	42	13
129	17.1	319	285	34	36
129	14.3	316	283	36	30
129	5.9	317	266	30	3
129	7.3	321	254	30	4
129	7.8	324	272	31	9
129	11.3	322	249	30	8
129	13.4	322	258	22	2
129	7.3	321	291	22	15
129	7.5	319	230	23	10
129	16.5	327	271	27	18
129	11.4	324	251	22	3
129	8.1	325	47	28	11
129	12.2	322	27	12	19
129	9.8	312	254	25	5
129	9.3	325	272	25	11
129	14.8	310	271	14	15
129	9.1	316	38	29	14
129	17.9	321	267	26	14
129	16.6	317	228	25	22
130	10.7	328	330	35	24
130	10.8	324	336	38	23
130	6.6	320	344	45	13
130	7.2	315	344	43	13
130	7.5	325	337	39	16
130	9.5	310	334	41	16
130	6.4	323	334	37	13
130	9.1	316	336	39	17
130	4.7	324	337	39	10
131	10.4	320	285	24	20
131	8	333	307	23	18
131	7.6	321	286	17	14
131	9.3	310	269	23	9
131	10.1	315	277	27	16
131	11.5	314	272	30	14
131	10.9	314	246	29	12
131	11.8	320	290	29	25
131	5.9	312	279	29	11

Table 16 (continued)

Cluster #	Length	Bearing	Aspect	Slope	Height
131	6.6	327	263	33	3
131	8	303	262	32	11
131	14.6	315	272	27	18
132	9	323	227	31	13
132	6.6	314	218	23	10
132	3.7	320	208	20	6
132	8.3	328	186	17	16
132	6.5	313	173	21	12
132	5.1	330	167	16	11
132	4	318	205	20	7
132	5.6	310	218	14	7
132	5.6	323	162	17	12
132	3.7	313	201	29	6
132	7.2	313	262	16	3
132	3.7	313	274	17	5
132	6.2	320	180	11	12
132	5.6	325	275	17	7
132	4.2	317	232	21	5
132	4.9	324	226	26	7
133	4.4	327	187	29	9
133	3.3	309	190	29	5
133	7.1	320	201	35	13
133	3.8	318	198	33	7
133	3.3	325	184	31	7
133	4.3	324	160	33	9
133	3.3	329	162	34	7
133	3.1	330	181	34	7
133	4.6	311	211	32	7
133	3	317	222	38	5
133	2	309	259	39	3
133	4.4	308	194	27	7
134	9.7	316	255	42	15
134	15.1	317	240	38	24
134	12.1	313	253	44	20
134	14.5	310	264	38	20
134	8	304	265	45	2
134	13.7	311	269	42	7
134	6.9	320	197	37	13

Table 16 (continued)

Cluster #	Length	Bearing	Aspect	Slope	Height
134	8.8	316	233	37	14
134	12.4	312	247	40	20
134	6.7	312	273	41	13
134	18	317	246	43	31
135	6	309	212	27	9
135	5.2	305	182	27	8
135	8.8	316	245	29	9
135	10.6	317	241	26	11
135	6.5	319	227	23	9
135	5.9	311	257	24	2
135	2.9	300	257	29	4
135	3.3	333	228	31	4
135	5.4	321	226	27	8
135	5.5	313	242	26	6
137	10	323	149	20	22
137	10.3	314	141	21	21
137	4.7	308	150	23	8
137	12.6	309	135	18	24
137	7.9	323	136	20	18
137	7.3	327	137	21	17
137	12.5	324	194	25	23
137	7.7	311	197	25	12
137	8.2	324	196	33	15
137	10.3	318	153	27	21
137	10	320	197	20	18
137	7.9	318	199	25	14
137	6.2	313	201	28	10
137	9.4	320	211	32	16
137	10.2	323	204	31	18
137	5.8	317	131	24	12
137	9.1	322	147	21	20
137	10.7	320	207	27	18
137	11.8	329	194	29	23
137	6.4	315	200	31	11
137	6.8	321	149	24	15
137	4.9	315	108	32	10
137	3.4	302	176	25	5
137	6.6	317	191	27	12

Table 16 (continued)

Cluster #	Length	Bearing	Aspect	Slope	Height
137	9.7	313	118	29	20
137	9.9	318	191	27	18
137	7.4	325	238	29	8
137	9.6	321	195	30	18
137	9.9	316	190	31	18
138	14	349	268	21	13
138	14.6	347	268	23	13
138	6	352	261	21	3
138	6.6	345	254	37	0
138	7.1	348	258	19	3
138	11.2	343	261	41	3
138	9.6	336	265	41	5
138	12.3	356	262	38	7
138	10.6	347	278	41	16
138	22	347	301	28	49
138	10.8	332	339	33	25
138	12.9	349	317	34	32
138	9.2	353	287	40	17
138	9.4	345	266	41	6
139	15.3	350	348	22	38
139	11	347	266	21	9
139	8.3	357	256	27	3
139	7.3	347	283	31	12
139	10.4	342	277	32	14
139	9.3	340	288	35	18
139	10.8	352	264	25	7
139	12.9	349	272	22	14
139	8.5	349	280	28	13
139	12.3	339	282	30	21
139	13.2	344	271	26	14
139	9.5	343	287	29	17
139	19.2	353	284	30	32
139	9.7	351	318	13	23
140	4.3	338	121	15	9
140	7.1	336	119	16	15
140	6	320	120	13	12
140	3.5	342	121	15	7
140	3.9	333	121	15	8

Table 16 (continued)

Cluster #	Length	Bearing	Aspect	Slope	Height
140	2.9	354	79	12	1
140	3.1	345	7	22	7
140	5.4	355	95	11	7
140	4	344	89	10	4
140	5.5	336	81	11	3
140	3.9	328	126	14	9
140	4.4	330	89	11	4
140	3.8	338	57	7	2
141	4.6	344	351	28	11
141	2.6	353	352	27	6
141	3.3	321	360	22	6
141	1.9	0	357	28	5
141	1.9	24	353	30	4
141	2.2	4	360	28	5
141	3.1	332	2	21	6
141	2.8	355	351	21	7
142	6.2	342	41	26	9
142	3.8	332	28	29	7
142	6	342	57	25	5
142	5.5	342	60	26	4
142	5.9	322	33	26	10
142	6.2	345	32	22	10
142	2.9	326	88	17	3
142	5.4	322	69	19	2
142	5.5	319	26	26	9
142	6.8	336	56	8	4
142	2.9	344	65	13	1
142	6.2	333	60	25	5
142	5.2	339	63	25	3
143	7	323	342	9	15
143	10.3	331	283	14	16
143	3.3	331	303	15	7
143	8.9	323	286	17	16
143	4	328	284	16	7
143	4.6	347	298	17	10
143	3.9	332	281	17	6
143	5.2	330	282	18	8
143	5.3	342	283	20	8

Table 16 (continued)

Cluster #	Length	Bearing	Aspect	Slope	Height
143	5.1	332	315	8	12
143	4.9	331	162	11	11
143	3.9	340	282	18	6
143	4.6	329	273	22	5
143	8	343	353	16	19
143	3.1	340	39	11	4
144	4.2	356	287	5	7
144	5.5	342	315	4	13
144	5.9	341	295	18	12
144	4.9	324	335	20	11
144	4.5	328	306	8	10
144	4	333	314	4	9
144	5.5	327	306	5	12
144	6.9	330	347	20	15
144	3.4	330	336	10	8
144	5.3	320	354	14	11
144	4.2	319	328	16	9
144	5.9	339	303	10	13
144	2.7	327	246	8	0
144	4.5	339	291	11	8
144	3.9	346	287	13	7
144	5.6	333	291	15	10
145	3.3	333	1	27	7
145	5.1	317	359	33	10
145	3.7	328	357	39	8
145	2.8	335	4	35	6
145	4.4	340	310	31	10
145	5	337	330	36	12
145	3.5	340	336	42	8
145	3	337	328	28	7
145	7	351	297	27	15
145	3.4	355	325	16	9
145	2.8	341	300	30	6
145	2.9	339	358	5	7
145	4.6	345	339	40	11
145	3.1	350	332	38	8
145	3.4	353	5	46	8
145	4.4	348	339	41	11

Table 16 (continued)

Cluster #	Length	Bearing	Aspect	Slope	Height
146	4.7	328	344	31	10
146	3.6	350	351	23	9
146	5	343	22	20	9
146	4.4	339	343	29	10
146	4.6	342	337	27	11
146	3.9	336	10	23	8
146	2.8	329	46	29	4
146	4.9	338	352	27	11
146	5.5	340	1	23	12
146	3.5	335	338	25	8
146	3.8	340	11	12	8
146	3	333	36	30	5
147	5	332	20	26	9
147	3.3	335	21	27	6
147	2.5	332	46	20	3
147	2.4	328	83	28	1
147	2	339	61	23	1
147	3.5	325	21	27	6
147	3.3	325	79	25	1
147	2.6	330	54	24	3

Table 17. Table contains the flow path of the downed tree along with the length.

Flow Path	Length
4	18
4	16
4	12
4	28
4	23
4	15
4	15
4	19
4	16
4	20
4	22
4	14
4	20
4	15
4	20
4	19
4	22
4	21
4	31
4	33
4	20
4	20
4	15
4	22
4	33
4	22
4	23
4	16
4	22
4	19
4	22
4	22
4	19
4	14
4	14
4	20
4	16

Table 17 (continued)

Flow Path	Length
4	13
4	24
4	19
4	21
7	18
7	17
7	27
7	24
7	19
7	31
7	29
7	18
7	19
7	24
7	21
7	17
7	16
7	29
7	15
7	14
7	16
7	21
7	21
7	16
7	20
7	20
7	21
7	17
7	23
7	27
7	20
7	22
7	19
7	23
7	25
7	31
7	19
7	21

Table 17 (continued)

Flow Path	Length
7	21
7	18
7	25
7	33
7	33
7	46
7	40
7	30
7	34
7	36
7	29
7	34
9	21
9	24
9	16
9	19
9	16
9	28
9	15
9	25
9	23
9	18
9	19
9	25
9	21
9	17
9	25
9	29
9	23
9	20
9	19
9	22
9	22
9	26
9	15
9	16
9	18
9	21

Table 17 (continued)

Flow Path	Length
9	17
9	19
9	24
9	19
9	25
9	23
9	18
9	30
9	34
9	17
9	29
9	27
9	24
9	28
9	13
9	17
9	29
9	25
9	39
9	20
9	21
9	15
9	15
9	18
9	25
9	20
9	20
9	28
9	19
13	26
13	31
13	19
13	20
13	26
13	17
13	22
13	37
13	21

Table 17 (continued)

Flow Path	Length
13	18
13	26
13	21
13	21
13	15
13	21
13	35
13	25
13	27
13	27
13	28
13	35
13	22
13	20
13	30
13	17
13	17
13	13
13	16
14	24
14	20
14	23
14	21
14	23
14	25
14	15
14	23
14	18
14	20
14	24
14	21
14	25
14	13
14	16
14	17
17	17
17	17
17	14

Table 17 (continued)

Flow Path	Length
17	17
17	16
17	13
17	17
17	28
17	18
17	18
17	18
17	24
17	17
17	22
17	21
17	25
17	23
17	26
17	22
17	22
17	17
17	28
17	22
17	19
17	26
17	25
17	18
17	18
17	20
17	25
17	24
23	26
23	27
23	34
23	16
23	32
23	21
23	18
23	29
23	22
23	22

Table 17 (continued)

Flow Path	Length
23	24
23	22
23	28
23	19
23	16
23	12
23	22
23	21
23	16
23	23
23	21
23	24
23	22
23	26
23	15
23	23
23	19
23	36
23	28
23	22
23	25
23	27
23	35
23	15
23	17
23	21
23	36
23	51
23	41
23	35
23	48
23	43
23	29
23	28
23	25
23	44
23	19
23	19

Table 17 (continued)

Flow Path	Length
23	26
23	14
35	26
35	21
35	25
35	31
35	27
35	13
35	13
35	20
35	14
35	22
35	15
35	27
35	15
35	21
35	25
35	27
35	19
35	27
35	25
35	21
35	21
35	18
35	29
35	23
35	15
35	23
35	34
35	27
35	26
35	26
36	35
36	35
36	23
36	24
36	27
36	23

Table 17 (continued)

Flow Path	Length
36	19
36	28
36	21
36	29
36	21
36	22
36	21
36	40
36	32
36	23
36	18

References

Anderson, J.D. (1991). Fundamentals of Aerodynamics. McGraw-Hill, Inc., 772.

Andrews, B. J., & Manga M. (2012). Experimental study of turbulence, sedimentation, and coignimbrite mass partitioning in dilute pyroclastic density currents. Journal of Volcanology and Geothermal Research, 225-226, 30-44. https://doi.org/10.1016/j.jvolgeores.2012.02.011

Andrews, B.J. (2014). Dispersal and air entrainment in unconfined dilute pyroclastic density currents. Bulletin of Volcanology, 76, 852. https://doi.org/10.1007/s00445-014-0852-4

Auker, M. R., Sparks, R. S. J., Siebert, L., Crosweller, H. S., & Ewert, J. (2013). A statistical analysis of the global historical volcanic fatalities record. Journal of Applied Volcanology, 2(2), https://doi.org/10.1186/2191-5040-2-2

Baer, E. M., Fisher, R. V., Fuller, M., & Valentine, G. A. (1997). Turbulent transport and deposition of the Ito pyroclastic flow: Determinations using anisotropy of magnetic susceptibility. Journal of Volcanology and Geothermal Research, 102(10), 22565-22586. https://doi.org/10.1029/96JB01277

Bardintzeff, J. M. (1984). Merapi volcano (Java, Indonesia) and Merapi-type Nuée ardente. Bulletin of Volcanology, 47, 433-446. https://doi.org/10.1007/BF01961217

Baxter, P. J. (1990). Medical effects of volcanic eruptions. Bulletin of Volcanology, 52, 532-544. https://doi.org/10.1007/BF00301534

Baxter, P. J., Boyle, R., Cole, P., Neri, A., Spence, R., & Zuccaro, G. (2005). The impacts of pyroclastic surges on buildings at the eruption of the Sourfrière Hills volcano, Montserrat. Bulletin of Volcanology, 67(4), 292-313. https://doi.org/10.1007/s00445-004-0365-7

Baxter, P. J., Jenkins, S., Seswandhana, R., Komorowski, J. C., Dunn, K., Purser, D., Voight, B., & Shelley, I. (2017). Human survival in volcanic eruptions: Thermal injuries in pyroclastic surges, their causes, prognosis and emergency management. Burns, 43(5), 1051-1069. https://doi.org/10.1016/j.burns.2017.01.025

Benage, M. C., Dufek, J., & Mothes, P. A. (2016). Quantifying entrainment in pyroclastic density currents from the Tungurahua eruption, Ecuador: Integrating field proxies with numerical simulations. Geophysical Research Letters, 43(13), 6932-6941. https://doi.org/10.1002/2016GL069527

Blong, R. J. (1984). Volcanic Hazards: A Sourcebook on the Effects of Eruptions. Academic Press. 424.

Bogoyavlenskaya, G. E., Braitseva, O. A., Meleketsev, I. V., Kirianov, V. Y., & Miller, C. D. (1985). Catastrophic eruptions of the directed-blast type at Mount St. Helens, bezymianny and Shiveluch volcanoes. Journal of Geodynamics, 3(3-4), 189-218.

Brand, B. D., Gravley, D. M., Clarke, A. B., Lindsay, J. M., Bloomberg, S. H., Agustin-Flores, J., & Németh, K. (2014). A combined field and numerical approach to understanding dilute pyroclastic density current dynamics and hazard potential: Auckland Volcanic Field, New Zealand. Journal of Volcanology and Geothermal Research, 276, 215-232. https://dx.doi.org/10.1016/j.volgeores.2014.01.008

Branney, M. J., & Kokelaar, P., 2002, Pyroclastic Density Currents and the Sedimentation of Ignimbrites. Geological Society of London, 27, https://doi.org/10.1086/427850

Bursik, M. I, & Woods, A. W. (1996). The dynamics and thermodynamics of large ash flows. Bulletin of Volcanology, 58, 175-193. https://doi.org/10.1007/s004450050134

Cas, R. A. F., & Wright, J. V. (1988). Volcanic Successions: Modern and Ancient. Springer Netherlands.

Clarke, A. B., & Voight, B. (2000). Pyroclastic current dynamic pressure from aerodynamics of tree or pole blow-down. Journal of Volcanology and Geothermal Research, 100(1-4), 395-412. https://doi.org/10.1016/S0377-0273(00)00148-7

Cole, P. D., Calder, E. S., Druitt, T. H., Hoblitt, R., Robertson, R., Sparks, R. S. J., & Young, S. R. (1998). Pyroclastic flows generated by gravitational instability of the 1996-97 Lava Dome of the Soufriere Hills Volcano, Montserrat. Geophysical Research Letters, 25(18), 3425-3428. https://doi.org/10.1029/98GL01510

Cole, P. D., Calder, E. S., Sparks, R. S. J., Clarke, A. B., Druitt, T.H., Young, S.R., Herd, R. A., Harford, C. L., & Norton, G. E. (2002). Deposits from dome-collapsed and fountain-collapse pyroclastic flows at Sourfriere Hills Volcano, Montserrat. In Druitt, T. H., & Kokelaar, B. P. (Eds), The Eruption of Soufrière Hills Volcano, Montserrat, from 1995 to 1999. Geological Society, 21(1), 231-262. https://doi.org/10.1144/GSL.MEM.2002.021.01.11

Dade, B. W., & Huppert, H. E. (1996). Emplacement of the Taupo ignimbrite by a dilute turbulent flow. Nature, 381, 509-512. https://doi.org/10.1038/381509ao

Dobran, F., Neri, A., & Macedonio, G. (1993). Numerical simulation of collapsing volcanic columns. Journal of Geophysical Research, 98(3), 4231-4259. https://doi.org/10.1029/92JB02409

Druitt, T. H. (1998). Pyroclastic density currents. Geological Society, 145, 145-182. https://doi.org/10.1144/GSL.SP.1996.145.01.08

Fisher, R. V. (1966). Mechanism of deposition from pyroclastic flows. American Journal of Science, 264(5), 350-363. https://doi.org/10.2475/ajs.264.5.350

Fisher, R. V. (1990). Transport and deposition of a pyroclastic surge across an area of high relief: The May 1980 eruption of Mount St. Helens, Washington. Geological Society of America Bulletin, 102(8), 1038-1054. https://doi.org/10.1130/0016-7606(1990)102<1038:TADOAP>2.3.CO;2

Fisher, R. V., & Heiken, G. (1982). Mt. Pelée, martinique: may 8 and 20, 1902, pyroclastic flows and surges. Journal of Volcanology and Geothermal Research, 13(3-4), 339-371. https://doi.org/10.1016/0377-0273(82)90056-7

Gardner, J. E., Andrews, B. J., & Dennen, R. (2016). Liftoff of the 18 May 1980 surge of Mount St. Helens (USA) and the deposits left behind. Bulletin of Volcanology, 79(8), https://doi.org/10.1007/s00445-016-1095-3

Gardner, J. E., Nazworth, C., Helper, M. A., & Andrews, B. J. (2018). Inferring the nature of pyroclastic density currents from tree damage: The 18 May 1980 blast surge of Mount St. Helens, USA. Geology, 46(9), 795-798. https://doi.org/10.1130/G45353.1

Hoblitt, R. P., Miller, C. D., & Vallance, J. W. (1981). Origin and stratigraphy of the deposit produced by the May 18 directed blast. In Lipman, P. W., & Mullineaux, D. R. (Eds.), The 1980 Eruptions of Mount St. Helens, Washington. United States Geological Survey Professional Paper, 1250, 401-420.

Hoblitt, R. P. (1986). Observations of the eruptions of July 22 and August 7, 1980, at Mount St. Helens, Washington. United States Geological Survey Professional Paper, 1335, https://doi.org/10.3133/pp1335

Hoblitt, R. P. (2000). Was the 18 May 1980 lateral blast at Mt St Helens the product of two explosions? Philosophical Transaction of the Royal Society a Mathematical, Physical and Engineering Sciences, 358(1770), 1639-1661. https://doi.org/10.1098/rsta.2000.0608

Iangum, C. E., Yadama, V., & Iowell, E. C. (2009). Physical and mechanical properties of young-growth Douglas-fir and western hemlock from western Washington. Forest Products Journal, 59(11/12), 37-47.

Jenkins, S., Komorowski, J. C., Baxter, P. J., Spence, R., Picquout, A., Lavigne, F., & Surono (2013). The Merapi 2010 eruption: An interdisciplinary impact assessment methodology for studying pyroclastic density current dynamics. Journal of Volcanology and Geothermal Research, 261, 316-329. https://dx.doi.org/10.1016/j.volgeores.2013.02.012

Kelfoun, K., Legos, F., & Gourgaud, A. (2000). A statistical study of trees damaged by the 22 November 1994 eruption at Merapi Volcano (Java, Indonesia): relationships between ash-cloud surges and block-and-ash flows. Journal of Volcanology and Geothermal Research, 100(1-4), 379-393. https://doi.org/10.1016/S0377-0273(00)00147-5

Kieffer, S.W. (1981). Fluid dynamics of the May 18 blast at Mount St. Helens. In Lipman, P. W., & Mullineaux, D. R. (Eds.), The 1980 Eruptions of Mount St. Helens, Washington, United States Geological Survey Professional Paper 1250, 379-400.

Kneller, B., Buckee, C. (2000). The structure and fluid mechanics of turbidity currents: a review of some recent studies and their geological implications. Sedimentology, 47(1), 62-94. https://doi.org/10.1046/j.1365-3091.2000.047s1062.x

Lipman, P. W., & Mullineaux, D. R. (1981). The 1980 Eruptions of Mount St. Helens, Washington. United States Geological Survey Professional Paper, 1250.

McPherson, G. E., van Doorn, N. S., & Peper, P. J. (2016), Urban tree database, Fort Collins, CO. Forest Service Research Data Archive, Updated 21 January 2020. https://doi.org/10.2737/RDS-2016-0005

Middleton, G. V. (1970). Experimental studies related to the problems of flysch sedimentation. Geological Association of Canada Special Paper, 7, 253-272.-

Moore, J. G., & Albee, W. C. (1981). Topographic and structural changes, March-July 1980 – photogrammetric data. In Lipman, P. W., & Mullineaux, D. R. (Eds.), The 1980 Eruptions of Mount St. Helens, Washington, United States Geological Survey Professional Paper 1250, 123-134.

Moore, J. G., & Sisson, T. W. (1981). Deposits and effects of the May 18 pyroclastic surge. In Lipman, P. W., & Mullineaux, D. R. (Eds.), The 1980 Eruptions of

Mount St. Helens, Washington. United States Geological Survey Professional Paper 1250, 421-439.

Moore, J. G., & Rice, C. (1984). Chronology and character of the May 18, 1980 explosive eruption of Mount St. Helens, In National Research Council (Eds.), Explosive Volcanism: Inception, Evolution and Hazard. National Academy Press, 133-142.

Panton, R. L. (1996). Incompressible Flow. Wiley, New York, 837.

Pitarri, A., Cas, R. A. F., Monaghan, J. J., & Martí, J. (2007). Instantaneous dynamic pressure effects on the behavior of lithic boulders in pyroclastic flows: the Abrigo Ignimbrite, Tenerife, Canary Islands. Bulletin of Volcanology, 69, 265-279. https://doi.org/10.1007/s00445-006-0072-7

Rae, W. H., & Pope, A. (1984). Low-speed wind tunnel testing. Wiley, New York, 534.

Rose, W. I., Pearson, T., & Bonis, S. (1977). Nuée ardente eruption from the foot of a dacite lava flow, Santiaguito volcano, Guatemala. Bulletin Volcanologique, 40, 23-38. https://doi.org/10.1007/BF02599827

Rosenbaum, J. G., Waitt, R. B. (1981). Summary of eyewitness accounts of the May 18 eruption. In Lipman, P. W., & Mullineaux, D. R. (Eds.), The 1980 eruptions of Mount St. Helens, Washington. United States Geological Survey Professional Paper 1250, 53-68.

Rosenfeld, C. L. (1980). Observations of the Mount St. Helens eruption. American Scientist, 68, 494-509.

Simpson, J. (1997). Gravity currents in the environmental and the laboratory, 2nd edition. Cambridge University Press.

Snellgrove, T. A., Kendall Snell, J. A., & Max, T. A. (1983). Damage to National Forest timber on Mount St. Helens. Journal of Forestry, 81(6), 368-371. https://doi.org/10.1093/jof/81.6.368

Sparks, R. S. J., & Walker, G. P. L. (1973). The Ground Surge Deposit – a Third Type of Pyroclastic Rock. Nature Physical Science, 241, 62-64. https://doi.org/10.1038/physci241062a0

Sparks, R .S. J., & Walker, G. P. L. (1977). The significance of vitric-enriched air-fall ashes associated with crystal-enriched ignimbrites. Journal of Volcanology and

Geothermal Research, 2(4), 329-341. https://doi.org/10.1016/0377-0273(77)90019-1

Sparks, R. S. J., Bonnecaze, R. T., Huppert, H. E., Lister, J. R., Hallworth M. A., Mader, H., & Phillips, J. (1993). Sediment-laden gravity currents with reversing buoyancy. Earth and Planetary Science Letters, 114(2-3), 243-257. https://doi.org/10.1016/0012-812X(93)90028-8

Sparks, R. S. J., Bursik, M. I., Carey, S. N., Gilbert, J. S., Glaze, L. S., Sigurdsson, H., & Woods, A. W. (1997). Volcanic Plumes. John Wiley & Sons Ltd.

Sulpizio, R., Dellino, P., Doronzo, D. M., & Sarocchi, D.(2014). Pyroclastic density currents: state of the art and perspectives. Journal of Volcanology and Geothermal Research, 283, 36-65. https://doi.org/10.1016/j.jvolgeores.2014.06.014

Tilling, R. I., Swanson, T. L., Swanson, D. A. (1990). Eruptions of Mount St. Helens: Past, Present, and Future. United States Geological Survey Special Interest Publication, 56. https://web.archive.org/web/20111026174423/http://vulcan.wr.usgs.gov/Volcanoes/MSH/Publications/MSHPPF/MSH_past_present_future.html

Ui, T., Matsuwo, N., Sumita, M., & Fujinawa, A. (1999). Generation of block and ash flows during the 1990-1995 eruption of Unzen volcano, Japan. Journal of Volcanology and Geothermal Research, 89(1-4), 123-127. https://doi.org/10.1016/S0377-0273(98)00128-0

Valentine, G. A. (1987). Stratified flow in pyroclastic surges. Bulletin of Volcanology, 49, 616-630. https://doi.org/10.1007/BF01079967

Valentine, G. A. (1998). Damage to structures by pyroclastic flows and surges, inferred from nuclear weapons effects. Journal of Volcanology and Geothermal Research, 87(1-4), 117-140. https://doi.org/10.1016/0377-0273(86)90026-0

Vortman, L. J. (1980). Deduced physical characteristics of the May 18, 1980, eruption [abs.]. EOS, American Geophysical Union, 61, 1135-1136.

Waitt, R. B. (1981). Devastating pyroclastic density flow and attendant air fall of May 18 – stratigraphy and sedimentology of deposits, In Lipman, P. W., & Mullineaux, D. R. (Eds.), The 1980 eruptions of Mount St. Helens, Washington. United States Geological Survey Professional Paper 1250, 601-616.

Waitt, R. B. (2015). In the Path of Destruction: Eye-witness Chronicles of Mount St. Helens. Washington State University Press.

Wilson, C. J. N. (2008). Supereruptions and supervolcanoes: processes and products. Elements, 4(1), 29-34. https://doi.10.2113/GSELEMENTS.4.1.29

Woods, A. W., & Wohletz, K. (1991). Dimensions and dynamics of co-ignimbrite eruption columns. Nature, 350, 225-227. https://doi.org/10.1038/35022a0

Woods, A. W., & Bursik, M. I. (1994). A laboratory study of ash flows. Journal of Geophysical Research. 99(B3), 4375-4394. https://doi.org/10.1029/93JB02224

Yamamoto, T., Takarado, S., & Suto, S. (1993). Pyroclastic flows from the 1991 eruption of Unzen volcano, Japan. Bulletin of Volcanology, 55, 166-175. https://doi.org/10.1007/BF00301514

Vita

Nicole Kristen Guinn was born in Plano, Texas. She moved to Richmond, Virginia with her family when she was eight years old. After graduating from Deep Run High School, she attended the University of Mary Washington in Fredericksburg, Virginia where she received her Bachelor of Science in Geology and GIS Certificate in May 2016. Nicole spent a two-year stint at Mapcom Systems in Richmond, Virginia, working as a project coordinator and GIS trainer. In August 2018, she entered the Jackson School of Geosciences at the University of Texas at Austin and is currently a Research Assistant and Master of Science candidate. Nicole plans on attending the University of Houston starting in August 2020 for a Doctor of Philosophy in Geosensing Systems Engineering and Science, focusing on volcanic monitoring.

Email: nicole.guinn1@gmail.com

This thesis was typed by the author.